

UC San Diego

UC San Diego Electronic Theses and Dissertations

Title

Polymer integrated protein crystalline materials

Permalink

<https://escholarship.org/uc/item/41z9p7sn>

Author

Zhang, Ling

Publication Date

2021

Peer reviewed|Thesis/dissertation

UNIVERSITY OF CALIFORNIA SAN DIEGO

Polymer integrated protein crystalline materials

A dissertation submitted in partial satisfaction of the requirements

for the degree Doctor of Philosophy

in

Chemistry

By

Ling Zhang

Committee in charge:

Professor F. Akif Tezcan, Chair
Professor Seth M. Cohen
Professor Neal K. Devaraj
Professor Y. Shirley Meng
Professor Michael J. Sailor

2021

©

Ling Zhang, 2021

All rights reserved

The Dissertation of Ling Zhang is approved, and it is acceptable in quality and form for
publication on microfilm and electronically:

Chair

University of California San Diego

2021

TABLE OF CONTENTS

SIGNATURE PAGE	iii
TABLE OF CONTENTS.....	iv
LIST OF ABBREVIATIONS.....	viii
LIST OF TABLES.....	xii
LIST OF FIGURES	xiii
ACKNOWLEDGEMENTS.....	xvi
VITA.....	xviii
ABSTRACT OF THE DISSERTATION.....	xx
Chapter 1 : Design of protein hybrid materials.....	1
1.1 Introduction.....	1
1.2 Protein and polymer hybrid materials.....	2
1.3 Protein nanoparticle hybrids	9
1.4 DNA protein hybrids.....	16
1.5 Dissertation objectives.....	25
1.6 Reference	26
Chapter 2 : Hyperexpandable, self-healing macromolecular crystals with integrated polymer networks.....	40
2.1 Abstract.....	40
2.2 Introduction.....	41
2.3 Results.....	45
2.3.1 Polymer formation inside the crystal lattice	45
2.3.2 Characterization of the dynamic behavior of ferritin crystal-hydrogel hybrids	47
2.3.3 Atomic-level structural characterization of ferritin crystal-hydrogel hybrids	55
2.3.4 Self-healing behavior and functionalization of ferritin crystal-hydrogel	59
2.4 Discussion.....	62
2.5 Methods.....	63
2.5.1 Protein expression, purification and characterization.....	63
2.5.2 Determination of zeta potentials.....	64

2.5.3	Formation of crystal-hydrogel hybrids	64
2.5.4	Measurement of the rate of diffusion into ferritin crystals.	65
2.5.5	Determination of in crystallo polymerization dynamics.....	65
2.5.6	Scanning electron microscopy of ferritin crystals	66
2.5.7	Polymer quantification with ¹⁹ F NMR.....	66
2.5.8	Monitoring crystal expansion-contraction using light microscopy	67
2.5.9	Monitoring crystal expansion using confocal microscopy	68
2.5.10	Quantification of protein release during expansion.....	68
2.5.11	Multi-crystal expansion monitored using SAXS	68
2.5.12	Multi-crystal SAXS at elevated temperatures.....	70
2.5.13	Single-crystal SAXS	70
2.5.14	Single-crystal XRD at room temperature	71
2.5.15	Single-crystal XRD at 100 K.....	71
2.5.16	Nanoindentation measurements of crystals	72
2.5.17	Preparation of iron-loaded ferritin	72
2.5.18	Formation of core-shell ferritin crystals	73
2.6	Data availability	73
2.7	Acknowledgments.....	74
2.8	References.....	75
Chapter 3	: Towards a comprehensive understanding of the material properties of polymer integrated crystals	79
3.1	Abstract.....	79
3.2	Introduction.....	80
3.3	Results and discussion	82
3.3.1	On the effects of ferritin packing on PIX behavior.....	82
3.3.2	On the effects of electrostatic interactions on PIX behavior	87
3.3.3	Exploring PIX formation with other proteins	99
3.3.4	Atomistic simulations of ferritin cages in the presence of polymer chains	104
3.3.5	Coarse-grained simulations of ferritin PIX in the presence of polymer chains	109
3.4	Conclusions.....	118
3.5	Methods.....	119
3.5.1	Design of ferritin variants	119

3.5.2 Purification of ferritin variants.....	120
3.5.3 Crystallization of ferritin variants.....	123
3.5.4 Acquisition of all non-ferritin proteins	124
3.5.5 Crystallization of all non-ferritin proteins	124
3.5.6 PIX formation using ferritin variants.....	126
3.5.7 PIX formation using non-ferritin proteins	127
3.5.8 Determination of zeta potentials	127
3.5.9 Monitoring PIX dynamics using light microscopy.....	127
3.5.10 Monitoring PIX dynamics using SAXS.....	128
3.5.11 MD simulations.....	128
3.6 Acknowledgments.....	130
3.7 References.....	132
 Chapter 4 : Polymer integrated protein crystals as a general platform for controlled protein encapsulation and release.....	 136
4.1 Abstract.....	136
4.2 Introduction.....	137
4.3 Results and Discussion	139
4.3.1 Encapsulation of GFP within ferritin PIX	139
4.3.2 Characterization of pH effects on GFP encapsulation by PIX	145
4.3.3 Quantification of cargo loading within GFP-encapsulated PIX	148
4.3.4 Controlled release of GFP from PIX	151
4.3.5 Size-selective encapsulation of other proteins within PIX	153
4.4 Conclusions.....	157
4.5 Methods.....	158
4.5.1 GFP expression and purification.....	158
4.5.2 Rhodamine labeling of streptavidin, catalase, and lysozyme	159
4.5.3 Formation of polymer integrated crystals.....	159
4.5.4 Protein encapsulation within PIX	160
4.5.5 Confocal microscopy imaging of protein-encapsulated PIX.....	160
4.5.6 Protein release from PIX.....	161
4.5.7 Quantification of total encapsulated GFP via UV-Vis absorbance	161
4.5.8 Quantitation of protein concentrations in PIX via HPLC.....	161
4.6 Acknowledgments.....	161

4.7 References..... 162

LIST OF ABBREVIATIONS

1D	one dimensional
2D	two dimensional
3D	three dimensional
Ac	acrylate
AFM	atomic force microscopy
aFT	apo ferritin
Am	acrylamide
APS	ammonium persulfate
AuNPs	gold nanoparticles
Bis-Tris	2-[Bis(2-hydroxyethyl)amino]-2-(hydroxymethyl)propane-1,3-diol
C2	2-fold symmetry
C3	3-fold symmetry
C4	4-fold symmetry
CAT	catalase
CCMV	cowpea chlorotic mottle virus
CFP	cyan fluorescent protein
CG	coarse-grained
CHES	N-cyclohexyl-2-aminoethanesulfonic acid
cyt c	cytochrom c
DI water	deionized water
DLS	dynamic light scattering

DMAEMA	2-(Dimethylamino)ethyl methacrylate
DMF	Dimethylformamide
DNA	deoxyribonucleic acid
DPS	DNA protection during starvation protein
DTT	dithiothreitol
EDTA	2,2',2'',2'''-(Ethane-1,2-diyl)dinitrilo)tetraacetic acid
FAD	flavin adenine dinucleotide
<i>fcc</i>	face centered cubic
FESEM	field emission scanning electron microscope.
FPLC	fast protein liquid chromatography
GFP	green fluorescent protein
GOx	glucose oxidase
HEPES	(4-(2-hydroxyethyl)-1-piperazineethanesulfonic acid)
HPLC	high pressure liquid chromatography
HuHF	human heavy-chain ferritin
IPTG	Isopropyl β -D-1-thiogalactopyranoside
LB media	Luria–Bertani medium
MD	molecular dynamics
MES	2-(N-morpholino)ethanesulfonic acid
MOF	metal-organic framework
MPD	methylpentanediol
MRI	magnetic resonance imaging

MS	mass spectrometry
NIPAm	N-Isopropylacrylamide
NMR	nuclear magnetic resonance
NP	nanoparticle
OD	optical density
p(Ac-Am)	poly(acrylate-co-acrylamide)
P4VP	poly(4-vinylpyridine)
pAc	poly-acrylate
PAFA	polyaspartic acid
PAGE	polyacrylamide gel electrophoresis
pAm	poly-acrylamide
PAMAM	poly(amidoamine)
PEG	poly(ethylene glycol)
PIX	polymer integrated crystals
PMSF	phenylmethanesulfonyl fluoride
PNIPAm	poly(N-isopropylacrylamide)
PPG	polypropylene glycol
PVF	polyvinylformal
QD	quantum dots
RDF	radial distribution function
RFP	red fluorescent protein
RhuA	L-rhamulose 1-phosphate aldolase

RNA	ribonucleic acid
Rnase	ribonuclease
SAV	streptavidin
SAXS	small angle X-ray scattering
sc-XRD	single-crystal X-ray diffraction
SDS	Sodium dodecyl sulfate
SEC	size exclusion column
TEM	transmission electron microscopy
TEMED	N,N,N',N'-tetramethylethane-1,2-diamine
TRIS	tris(hydroxymethyl)aminomethane
TYMV	turnip yellow mosaic virus
XRD	X-ray diffraction
YFP	yellow fluorescent protein

LIST OF TABLES

Table 2.1 X-ray data collection and refinement statistics.....	58
Table 3.1 Properties of ferritin variants used in this study.....	91
Table 3.2 Crystal packing information for all other proteins tested as new scaffolds for PIX...	101
Table 3.3 Polymer composition in coarse-grained simulation.....	111
Table 3.4 Crystallization conditions for ferritin variants.....	123
Table 3.5 Crystallization conditions of other protein variants.....	125

LIST OF FIGURES

Figure 1.1 Formation of 0- and 1-dimensional protein-polymer hybrid materials.	4
Figure 1.2 Formation of 2-dimensional polymer-protein hybrid materials.	7
Figure 1.3 Formation of 3D polymer-protein hybrid materials.	8
Figure 1.4 Protein self-assembly templated nanoparticle arrays.	10
Figure 1.5 Templated assembly of nanoparticles encapsulated in protein cages	13
Figure 1.6 Protein-nanoparticle hybrid materials in interfacial electron transfer.	14
Figure 1.7 Functional protein-nanoparticle hybrid materials.	17
Figure 1.8 Designed protein-DNA hybrid materials.....	19
Figure 1.9 Design of protein-DNA hybrid materials.....	20
Figure 1.10 Designed protein-DNA hybrid materials.....	22
Figure 1.11 Functional protein-DNA hybrid materials.....	23
Figure 2.1 Packing arrangement in ferritin crystals and their expansion–contraction mediated by the infused hydrogel network.....	43
Figure 2.2 Distribution of electrostatic charge on the surface of ferritin and size distribution of ferritin in solution.	44
Figure 2.3 Molecular diffusion and polymerization in ferritin crystals, monitored using confocal microscopy.....	46
Figure 2.4 Quantification of an acrylic acid analogue using ^{19}F NMR.....	47
Figure 2.5 Characterization of the expansion and contraction behavior of ferritin crystal–hydrogel hybrids.....	49
Figure 2.6 Isotropic hyperexpansion of ferritin crystal–hydrogel hybrids.	51
Figure 2.7 Expansion and contraction behavior of crystal–hydrogel hybrids in the presence of different metal ions.	52
Figure 2.8 Successive expansion–contraction cycles for a single ferritin crystal–hydrogel hybrid.	53

Figure 2.9 Alternative hydrogel formulations.	54
Figure 2.10 SAXS imaging of a single crystal–hydrogel hybrid in a microfluidic chip.	56
Figure 2.11 Atomic-level structural characterization of ferritin crystal–hydrogel hybrids by XRD.	57
Figure 2.12 Self-healing behavior and functionalization of ferritin crystal–hydrogel hybrids. ...	60
Figure 2.13 Mechanical and thermal properties of ferritin crystal–hydrogel hybrids.	61
Figure 3.1 Crystal lattice packing and protein-protein interaction in the lattice.	83
Figure 3.2 Light microscope profiles of ferritin crystals expansion and contraction.	84
Figure 3.3 Polymer precursors tested in this study.	88
Figure 3.4 Behavior of DMAEMA-based PIX.	89
Figure 3.5 Electrostatic maps of all ferritin variants, as viewed down the 4-fold axis.	91
Figure 3.6 Initial characterization of F432 symmetry crystals for the different charged ferritin variants.	93
Figure 3.7 Expansion behavior of F432-symmetry poly(acrylate-acrylamide) infused PIX constructed from different negatively charged ferritin variants.	94
Figure 3.8 Expansion behavior of negatively charged PIX variants as determined by SAXS.	95
Figure 3.9 Characterization of POS2 variant PIX.	98
Figure 3.10 Alternative proteins explored as new scaffolds for PIX.	100
Figure 3.11 Light microscope images of the different protein crystals tested for the systematic variation of protein scaffold.	103
Figure 3.12 Atomistic simulations of HuHF- ΔC^* in the presence of polymer chains.	106
Figure 3.13 Coarse-grained modeling of ΔC^* -based PIX.	111
Figure 3.14 Analysis of coarse-grained simulations.	113
Figure 3.15 Coarse-grained simulation profiles for PIX.	114
Figure 3.16 Analysis of the effect of polymer chain length in coarse-grained simulation.	116

Figure 3.17 Coarse-grained simulations of positively charged cage (POS2)-pAc PIX.....	117
Figure 4.1 Schematic representation of protein immobilization using PIX.....	140
Figure 4.2 Encapsulation of GFP within PIX.	142
Figure 4.3 Time-dependent encapsulation of GFP by PIX.....	144
Figure 4.4 Optimization of GFP encapsulation.	146
Figure 4.5 Confocal profiles of GFP-encapsulated PIX constructed from different ferritin variants.	147
Figure 4.6 Workflow for the quantification of ferritin and GFP in PIX via HPLC and UV-Vis absorption.....	149
Figure 4.7 Quantification of GFP in PIX with quantitative HPLC and UV-Vis measurements.	150
Figure 4.8 Cargo release from GFP-loaded PIX.....	152
Figure 4.9 Confocal profiles of lysozyme-encapsulated PIX.	155
Figure 4.10 Streptavidin and catalase encapsulation within PIX.	156

ACKNOWLEDGEMENTS

First of all, I would like to thank my PI Professor Akif Tezcan for his support and guidance throughout graduate school.

I have been fortunate to work in the Tezcan Lab and meet many enthusiastic scientists and friends. I would like to thank Julian Esselborn, Eyal Golub, Cedric Owens, and Jon Rittle for their help in scientific discussions, their knowledge of science motivated me to learn more. Thanks to Lewis Churchfield for training me with a lot of things in the lab and helping me design all my molecular biology experiments. Thanks to Nicole Avakyan for being a very supportive and caring friend. Thanks to Tae Su Choi for being a sweet uncle and friend for Miumiu. Thanks to Zhiyin Zhang and Yiyang Li for always sharing their young spirits. Many thanks to Rohit Subramanian for being a good friend and for his help in many ways throughout graduate school as well as “torturing the dog” as a routine activity. I can’t say enough thanks to Jie Zhu and Tina Li (together with Jojo and Potato) for all the things you have done for me! I have been very lucky to work in the ferritin subgroup with Jake Bailey, Kenneth Han and Yui Na for their creative ideas and collaborative environment. Special thanks to Jake who has been a very supportive mentor in my projects and provide all help necessary, as well as a good friend who always cheered me up.

The unlimited love and support from my family is always what keeps me moving forward, though my parents are far away, their love and care never fade. Can’t say enough thanks to my husband Robert Alberstein, your positive attitude and unlimited support always make my life brighter! Last but not least, thanks to my cute smart baby Miumiu, who brings pure joy and love to me and everyone around!

This dissertation was funded in part by UCSD's Teddy Traylor Award and Distinguished Graduate Student Fellowship. Additional funding from the US Department of Energy (BES, Division of Materials Sciences) and National Science Foundation (Department of Materials Research) is acknowledged and detailed at the end of individual chapters.

Chapter 2 is reproduced, in part, with permission, from: Zhang, L., Bailey, J. B., Subramanian, R. H., Groisman, A., Tezcan, F. A. "Hyperexpandable, self-healing macromolecular crystals with integrated polymer networks" *Nature* **557**, 86–91 (2018). The dissertation author was the primary author on all reprinted materials.

Chapter 3, in part, is currently being prepared for submission for publication: Zhang, L., Jimenez-Angeles, F., Alberstein, R. G., de la Cruz, M. O., Tezcan, F. A. "Towards a comprehensive understanding of the material properties of polymer integrated crystals". The dissertation author was the primary investigator and author of this manuscript.

Chapter 4, in part, is currently being prepared for submission for publication: Zhang, L., Han, K., Na, Y., Tezcan, F. A. "Polymer integrated protein crystals as a general platform for controlled protein encapsulation and release". The dissertation author was the primary investigator and author of this manuscript.

VITA

EDUCATION

2013 B.S., Chemistry, Zhejiang University
2017 M.S., Chemistry, University of California, San Diego
2021 Ph.D., Chemistry, University of California, San Diego

HONORS AND AWARDS

2018 Teddy Traylor Award
2019 UCSD Distinguished Graduate Student Fellowship
2019 Chinese Government Award for Outstanding Self-financed Students

PUBLICATIONS

Han, K., Bailey, J. B., **Zhang, L.**, Tezcan, F. A. “Anisotropic Dynamics and Mechanics of Macromolecular Crystals Containing Lattice-Patterned Polymer Networks” *Journal of the American Chemical Society*, **142**(45), 19402–19410 (2020)

Zhang, L., Bailey, J. B., Subramanian, R. H., Groisman, A., Tezcan, F. A. “Hyperexpandable, self-healing macromolecular crystals with integrated polymer networks” *Nature* **557**, 86–91 (2018)

Subramanian, R. H., Smith, S. J., Alberstein, R. G., Bailey, J. B., **Zhang, L.**, Cardone, G., Suominen, L., Chami, M., Stahlberg, H., Baker, T., Tezcan, F. A. “Self-Assembly of a Designed Nucleoprotein Architecture through Multimodal Interactions” *ACS Central Science*, **4**(11), 1578–1586 (2018)

Bailey, J. B., **Zhang, L.**, Chiong, J. A., Ahn, S., Tezcan, F. A. “Synthetic Modularity of Protein–Metal–Organic Frameworks” *Journal of the American Chemical Society*, **139**(24), 8160–8166 (2017)

Li, Z., Tang, Y., **Zhang, L.**, Wu, J. “Label-free study of the function of ion channel protein on a microfluidic optical sensor integrated with artificial cell membrane” *Lab on a Chip*, **14**(2), 333–341 (2014)

FIELDS OF STUDY

Major Field: Chemistry

Studies in Inorganic Chemistry, Polymer Chemistry, Bioinorganic Chemistry

Professor F. Akif Tezcan

ABSTRACT OF THE DISSERTATION

Polymer integrated protein crystalline materials

by

Ling Zhang

Doctor of Philosophy in Chemistry

University of California San Diego, 2021

Professor F. Akif Tezcan, Chair

From only 20 amino acid building blocks, nature has designed and refined protein structures for a wide variety of specific purposes. Each protein molecule carries out a specific function in nature (structural component, transportation, catalysis, among myriad others) that is directly related to the structure of protein. Despite this impressive diversity, many proteins do not operate alone, but combine with other molecules—lipids, carbohydrates, nucleic acids, co-factors, and other proteins—to fulfill their functional roles. Consequently, understanding the structural properties of proteins and their interactions with other types of macromolecules provides insights for creating advanced protein-based hybrid components with tunable properties. Synthetic

polymers are a large class of macromolecules that stand out in terms of their chemical diversity, tunable composition, controlled length (and thus physical properties) and easy acquisition. Thus, synthetic polymers have been commonly employed to augment the functional properties of proteins as well as creating hybrid materials with different proteins. Here, we have utilized synthetic polymers in a new context, namely in combination of protein crystals, to create a novel form of materials that seamlessly combine the advantages of proteins (functional diversity and atomically precise tailorability), crystalline materials (structural order and coherence) with those of synthetic polymers (flexibility, dynamics and stimuli-responsiveness).

In this dissertation, we first report the combination of rigid/ordered ferritin crystals with superabsorbent polymers to create dynamic, self-healing, stimuli-responsive polymer-integrated-crystals (PIX). The so-formed hybrid materials possess the flexibility of the polymer components and the structural order of the protein crystals, and the macroscopic dynamicity arising from these two components can be controlled by changing the pH and ionic strength (Chapter 2). Following the initial success of the first PIX, we sought to expand the scope of utility for PIX materials by investigating the behavior of PIX by systematically varying polymer composition, ferritin surface charge, crystal packing, and identity of the crystallized protein. We carried out experiments and simulations to understand the individual effect of different components on the system. With a better understanding of the PIX system, we demonstrated that the properties of the PIX can be tuned by controlling pH and ionic strength, as mentioned above (Chapter 3). Finally, we showed that the original PIX system can be used as a platform for controlled encapsulation/release of target biomolecules in a size-selective fashion (Chapter 4). Overall, we have created a novel class of materials with unique physical and mechanical properties that possess tremendous potential for use in applications such as molecular storage/delivery and compartmentalized chemical reactions.

Chapter 1 : Design of protein hybrid materials

1.1 Introduction

Proteins are biological macromolecules composed of 21 distinct building blocks - amino acids, whose specific sequence defines the primary structure of a given protein. The interactions between the amino acids help fold the protein into its secondary structures (alpha helices, beta sheets), and the inter- and intra-molecular hydrogen bonding forms the basis of the tertiary and quaternary structure of protein molecules.¹⁻³ The unique sequences and structures of each protein molecule gives rise to its special properties, allowing them to perform roles as structural components (*e.g.*, actin, myosin, and microtubules),⁴⁻⁶ molecular transporters/storage units (*e.g.*, ferritin, membrane transporters and kinesin),⁷⁻¹⁰ messengers (*e.g.*, growth hormone),¹¹⁻¹² catalysts (*e.g.*, nitrogenase, ATPases, and photosystem II),¹³⁻¹⁶ to name just a few. Due to their unique structures and properties (biocompatibility, biodegradability, structure-based functionality)¹⁷ and the advanced development of molecular biology and biotechnology,¹⁸ protein-based materials have attracted significant attention and have found applications in numerous areas, for example food processing,¹⁹⁻²⁰ medication,²¹⁻²² and catalysis.²³ Constructing new protein related materials can help surpass the current limitations of individual soluble proteins for specific applications, such as low stability or the restriction to amino acid chemical groups. Thus, significant effort has focused on designing protein hybrid materials to introduce properties that could not otherwise be easily obtained by proteins alone.²⁴⁻²⁷

Protein-based hybrid materials combine the advantages of proteins and a secondary component. For example, conjugation of polymer chains to protein molecules has been applied to improve the stability of the proteins²⁸⁻³⁰ and the structural order of protein lattices has been utilized for the patterning of inorganic nanoparticles.³¹⁻³⁴ DNA-protein hybrids allow the combination of

specific protein functional properties (*e.g.*, catalysis) with the programmability of DNA base-pairing³⁵⁻³⁶ to yield DNA-scaffolded enzymes with controlled catalytical properties.³⁷ This chapter will provide an introductory discussion of the design of protein-based hybrid materials as well as their existing and potential applications.

1.2 Protein and polymer hybrid materials

Polymers, which have molecular structures consisting of a large number of repeating units, exist everywhere in our daily life. Due to the diversity and flexibility in both chain length and side chain groups, polymers have found wide application across all areas of technology,³⁸⁻⁴³ exemplified most famously by the ubiquity of plastics. Seeking to take advantage of these diverse properties, significant research has been done to combine polymers and proteins together to form materials with new emergent characteristics or to mitigate the drawbacks of one component via the other.⁴⁴⁻⁴⁶ Protein-polymer hierarchical structures have been built using various binding modes, including covalent, host-guest, co-factor, multivalent, and electrostatic interactions. Structures of protein-polymer hybrids like 0D spheres, 1D tubes, 2D membranes and 3D lattices have been constructed, as we shall see in the upcoming sections.

Polymer-protein particles can be formed through multiple reactions. Li et. al. utilized the hydrogen bonding between P4VP and plant virus turnip yellow mosaic virus (TYMV) to form icosahedral colloidal particles by tuning the mass ratio of P4VP to TYMV to control the diameters of the close-packed particles (**Figure 1.1a–d**).⁴⁷ Petkau-Milroy et al. achieved dynamic protein assembly along supramolecular columnar polymers via site-specific covalent attachment.⁴⁸ This dynamic and bioorthogonal assembly allowed the exchange of protein-functionalized discotics between different self-assembled polymers, enabling self-optimization of the protein arrangements and distances (**Figure 1.1e–g**).⁴⁸ Covalent attachment of polymer to protein has been used not only

to stabilize the protein in both aqueous²⁸ and non-aqueous⁴⁹ solution for different purposes, it also essentially forms new di-block co-polymers that have properties of both the protein and the polymer when utilized to form new materials. Wan et al. conjugated the heme cofactor of myoglobin to the thermoresponsive polymer poly(*N*-isopropylacrylamide) (polyNIPAm) and upon binding of the heme group, the so-formed myoglobin/polyNIPAm complex formed stabilized micelles. The assembly/disassembly of the micelles could be controlled by changing the temperature, reflecting the role of polyNIPAm (**Figure 1.1h, i**).⁵⁰ Hirayama et. al. constructed thermoresponsive micellar assemblies with polyNIPAm towards an artificial light-harvesting system (**Figure 1.1j, k**).⁵¹ In this work, thiol-reactive polyNIPAm was crosslinked to the surface of tyrosine-coordinated heme protein (HTHP), which formed micellar assemblies upon increasing the temperature (**Figure 1.1k**). This thermoresponsive hybrid assembly was shown to be capable of light-harvesting after substitution of heme with Zn-protoporphyrin as a photosensitizer. Aggregation of polyNIPAm can also be strategically utilized to assist the assembly of protein-polymer hybrids into larger structures. When polyNIPAm was covalently attached to the fluorescent protein mCherry, this new protein-polymer conjugate was shown to form particles in solution due to the distinct solvation preferences of each component. Furthermore, by solvent annealing at different temperatures, these mCherry-polyNIPAm block copolymers could be manipulated to form 2D layered structures and hexagonally perforated lamellae in bulk samples (**Figure 1.2a, b**).⁵² Subsequent research using the same building blocks showed that multiple morphologies could be attained depending on the polymer coil fraction. Under specific conditions, cylinders, perforated lamellae, lamellae, and aggregated micelles could be synthesized (**Figure 1.2c**).⁵³⁻⁵⁴ The same group later used this method to fabricate nanostructured biocatalysts that exhibited higher protein loading and activity per unit area than previous examples.⁵⁵

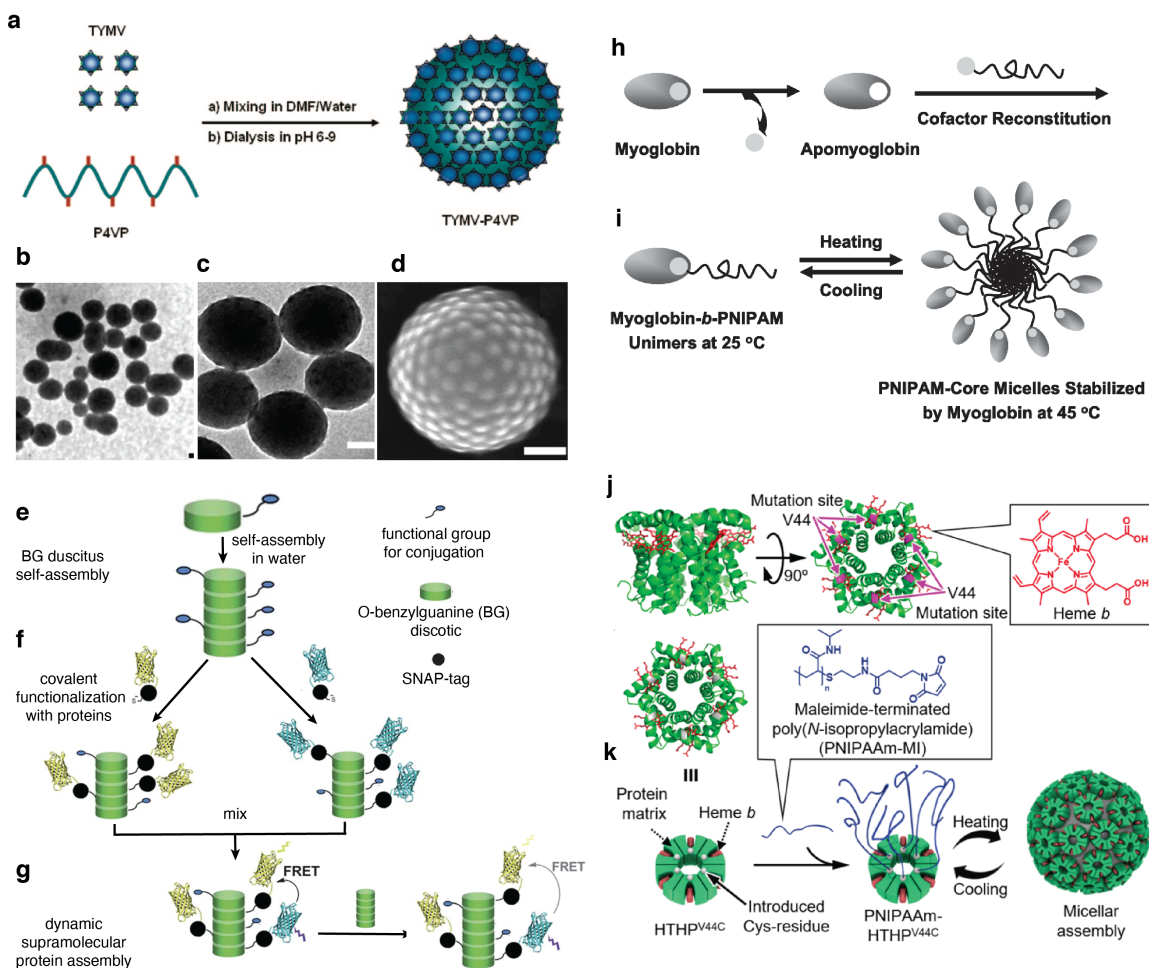


Figure 1.1 | Formation of 0- and 1-dimensional protein-polymer hybrid materials. **a**, Schematic illustration of the formation of TYMV-P4VP raspberry-like colloids. **b**, **c**, TEM images of the colloids in **a**. **d**, SEM image of TYMV-P4VP. **e**, Structure of the O-benzylguanine (BG) discotic 2 carrying a single moiety for conjugation to SNAP-tag fusion proteins. In water these discotics self-assembled to form auto-fluorescent columnar stacks with externally displayed conjugation groups. **f**, Site-selective covalent functionalization of the supramolecular polymer with SNAP-tag-containing cyan and yellow fluorescent proteins (CFP and YFP). **g**, Dynamic intermixing of the discotics between these supramolecular protein assemblies was demonstrated via the detection of efficient Förster resonance energy transfer (FRET) between CFP and YFP. Intercalation by inert discotics enabled tuning of the distance between the fluorescent proteins. **h**, Schematic representation of the construction of the thermoresponsive DHBC copolymer myoglobin-b-PNIPAM₉₀ via the reconstitution of apo protein with heme-containing polymer chains. **i**, Cartoon depiction of reversible assembly/disassembly of myoglobin-b-PNIPAM₉₀ upon changes in temperature. **j**, Reported HTHP structure (PDB ID: 20YY). Red molecules in the protein represent heme. Pink arrows indicate the mutation site. **k**, Schematic representation of attachment of the Cys-reactive polyNIPAm molecule onto the surface of HTHP to produce a thermoresponsive micellar assembly. **Figure 1.1a-d** adapted from ref. 47, **Figure 1.1e-g** adapted from ref. 48, **Figure 1.1h, i** adapted from ref. 50, **Figure 1.1j, k** adapted from ref. 51.

Low-dimensional 2D materials can be manufactured using templated self-assembly onto interfaces (*e.g.*, as used to fabricate ultra-thin protein-polymer membranes with size-selective properties⁵⁶), and these materials can be used as new substrates for the creation of multilayer films via subsequent rounds of deposition, assembly, and curing for each layer. Suci et al. prepared such films by first adsorbing biotin-functionalized cowpea chlorotic mottle virus (CCMV) particles onto a solid interface, creating a planar template onto which streptavidin interlayers could form (via the high-affinity streptavidin/biotin interactions), creating a binary alternating composition of layers in the film (**Figure 1.2d-h**).⁵⁷

Multivalent interactions have been utilized to form 3D structures from protein-polymer hybrids, especially dendrimers (spherical highly branched polymeric structures), which can be prepared at a wide range of diameters and charges while remaining monodisperse. Akin to the close-packing of spheres, oppositely charged dendrimers and spherical proteins or virus capsids have been shown to readily crystallize into 3D lattices via favorable electrostatic interactions from their binary A-B packing.⁵⁸⁻⁵⁹ When incorporated into hybrid materials, stimuli-responsive dendrimers have been shown to endow the resulting structure with unique properties. Kostianen et al. reported the use of optically degradable dendrons to mediate assembly and disassembly of close packed lattices formed with CCMV.⁵⁹ The positively charged dendrons “glue” the negatively charged virus particles together through multivalent interactions, but light-induced decomposition of dendrons led to the disassembly of the material (**Figure 1.3a-c**). Analogous studies have been reported using negatively charged ferritin cages in place of CCMV for dendrimer-mediated crystallization. Synthesis of dendrimers are highly controllable (by iterative growth of their size over multiple “generations”) and highly tunable, enabling the size ratio of dendrimers to protein

to be tuned, which can selectively produce of cocrystals with different symmetries (**Figure 1.3d-g**).⁶⁰

In summary, extensive efforts to create new multi-dimensional and multi-scale protein-polymer hybrid materials have produced myriad methodologies and strategies to do so. The immense chemical and structural diversity characteristic of both proteins and polymers makes the combination of these two components highly attractive for designing new hybrid materials with desirable properties for application in a wide variety of fields spanning catalysis, sensing, medicine, bio-/cascading-enzyme reactors, and stimuli-responsive materials.

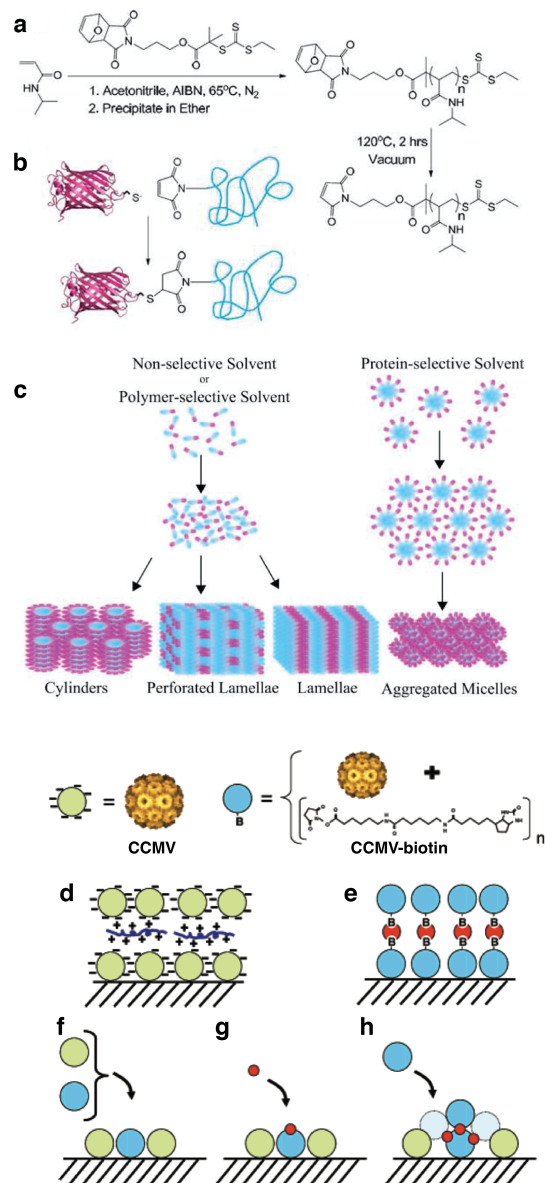


Figure 1.2 | Formation of 2-dimensional polymer-protein hybrid materials. **a**, Synthesis of maleimide-polyNIPAm and **b**, its conjugation to mCherryS131C via thiol reactivity to create a protein-polymer diblock copolymer. **c**, Schematic depicting two pathways observed during self-assembly of protein-polymer block copolymers. The first occurs in a good solvent for the polymer block and can produce a variety of morphologies depending on the polymer coil fraction. The second is obtained by using a poor polymer solvent, which leads to aggregation into micelles. Schematic representation of three types of multilayer films: **d**, Polylysine interlayer between adlayer of CCMV. **e**, Streptavidin interlayer between adlayers of CCMV-biotin. **f–h**, Heterogeneous adlayers formed by adsorption of a mixture of CCMV-biotin and nonbiotinylated CCMV onto a matrix of CCMV (**f**) followed by the addition of streptavidin (**g**) and subsequent addition of CCMV-biotin, leading to selective binding (**h**). **Figure 1.2a, b** adapted from ref. 52, **Figure 1.2c** adapted from Ref 53, **Figure 1.2d-h** adapted from ref. 57.

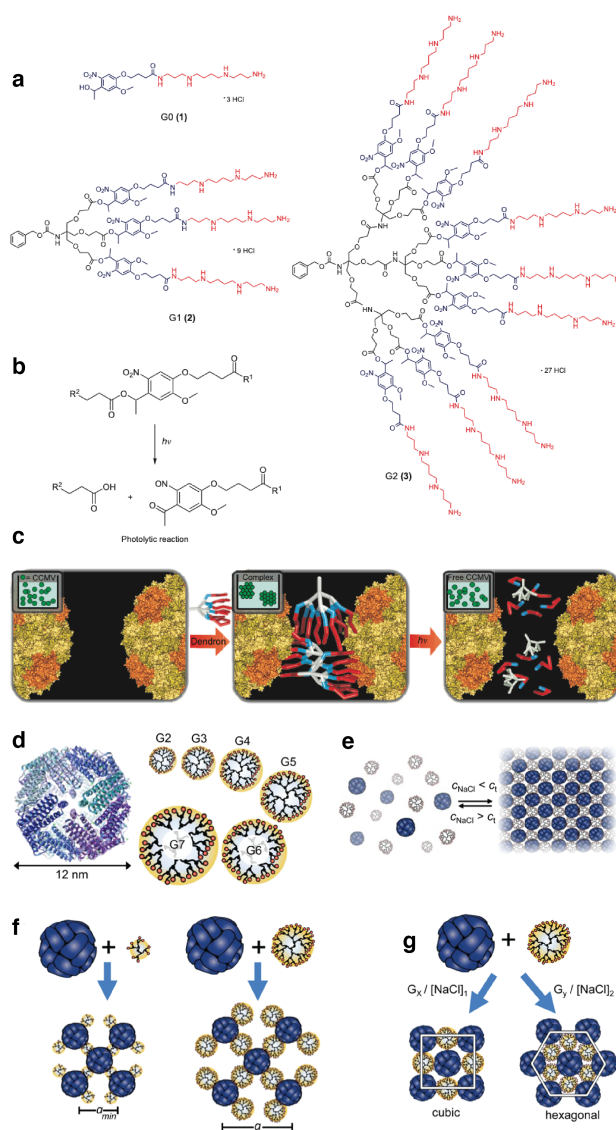


Figure 1.3 | Formation of 3D polymer-protein hybrid materials. **a**, Molecular structures of the optically degradable dendrons G0 (1), G1 (2) and G2 (3) used in the assembly and disassembly studies. **b**, Schematic of the photolytic cleavage reaction. **c**, Depiction of the assembly and disassembly process. Negatively charged virus particles initially exist as individual entities in solution but assemble upon addition of a cationic dendron. Then, irradiation destroys the dendrimer (thus breaking the multivalent binding interactions), leading to release of the virus particles. **d**, The spherical cage protein ferritin, aFT, and PAMAM dendrimers generations G2-G7 drawn to scale. **e**, At low ionic strength anionic ferritin forms a cocrystal together with the cationic PAMAM dendrimer via strong charge interactions. At high ionic strength, free counterions screen electrostatic interactions, leading to dissolution of the crystals. **f**, Dendrimer size can be used to control the lattice constant a . **g**, The dendrimer generation (*i.e.*, size) and ionic strength during assembly can modulate the resulting crystal symmetry. **Figure 1.3a-c** adapted from 59, **Figure 1.3d-f** adapted from ref. 60.

1.3 Protein nanoparticle hybrids

Nanoparticles are (typically inorganic) particles with sizes between 1–100 nm in diameter.⁶¹⁻
⁶² Due to their limited size,⁶³ nanoparticles often possess properties that are very different than bulk materials,⁶⁴ such as large surface area/volume ratios,⁶⁵⁻⁶⁶ defined geometric structures,⁶⁷⁻⁶⁸ and unique catalytic or electronic properties.⁶⁹⁻⁷⁰ Extensive research has been done to understand nanoparticle related materials and their functionalities, with numerous advances being made over the last few decades. Hybrid nanoparticle materials have found many applications in biosensing,⁷¹⁻
⁷³ medicine,⁷⁴⁻⁷⁷ and catalysis.⁷⁸⁻⁸² By combining proteins tailored for specific functions (*e.g.*, by protein engineering) with nanoparticles, various new hybrid materials have been created⁸³⁻⁸⁵ that extend the functionality and transferability beyond what either component could achieve alone.

Proteins have been utilized for the synthesis of nanoparticles as well as templating the arrangement of nanoparticle arrays or lattices.^{31,86-88} Compared to traditional methods for nanoscale array fabrication, the tunability of protein lattices for templating nanoparticle arrays showed great potential for controlling the properties of the nanoarrays,⁸⁹⁻⁹⁴ 1D arrays can be formed by using linear protein or peptide amyloids as the template, as shown by Deschaume et al., who demonstrated that lysozyme amyloid nanofibers deposited onto substrates (*e.g.*, glass or silicon) could induce self-assembly of gold nanoparticle onto the proteins via controlled interaction at pH range 5-6 (**Figure 1.4a-d**).⁸⁷ Two dimensional nanoparticle arrays have also been achieved by templated assembly onto 2D protein lattices. McMillan et al. engineered chaperonin protein templates to assemble synthesized quantum dots onto its 2D crystalline architecture (**Figure 1.4e-h**),³¹ and further demonstrated that introduced cysteine residues enabled the binding of differently sized nanoparticles, highlighting the general applicability and tunability of protein frameworks for directing the organization of nanoparticles with wholly separate functionalities.

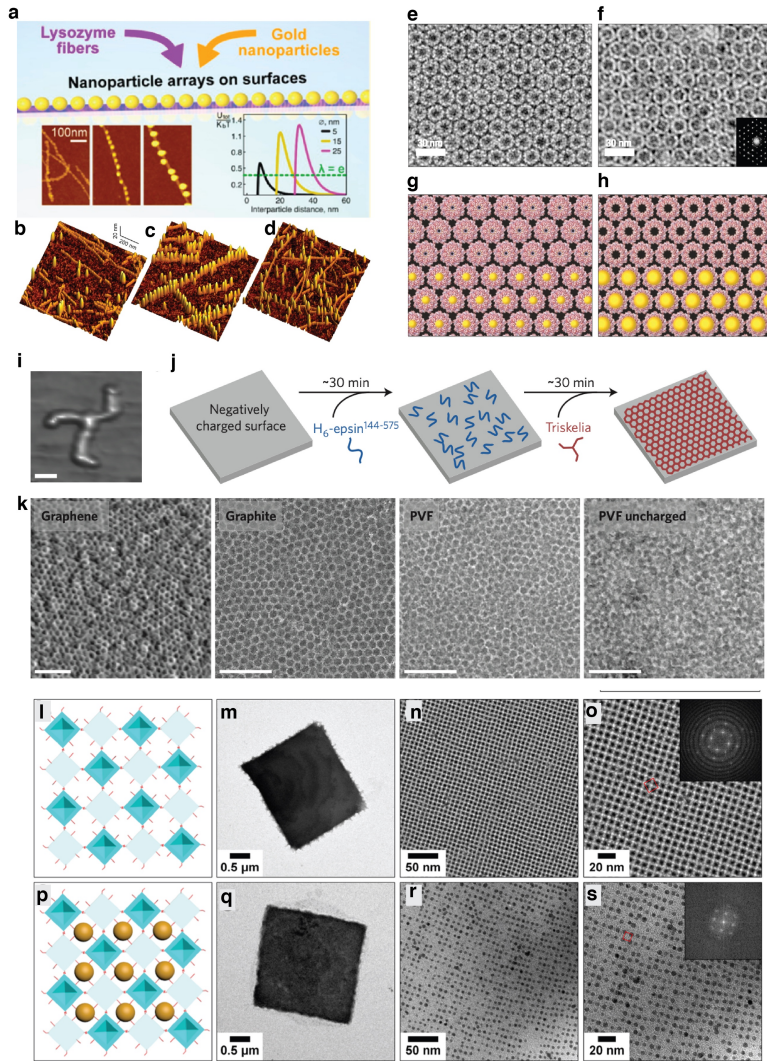


Figure 1.4 | Nanoparticle arrays templated by protein assemblies. **a**, Schematic of lysozyme amyloid-scaffolded 1D nanoparticle arrays using 15 nm diameter AuNPs. These arrays exhibited different structuring and optical properties when deposited onto silicon substrates using nanoparticle suspensions diluted in **b**, HCl pH 2, **c**, ultrapure water, or **d**, 0.1 M MES pH 6.5. **e**, TEM image of a negatively stained 2D crystal of beta chaperonin with cysteine substitutions at the central pores. **f**, 2D crystals of the loop-deletion chaperonin reveals an apparent increase in pore size (from 3 to 9 nm), reflected by changes in electron density within the pores. **g**, Graphical representation of 5 nm AuNP binding within the 3 nm pores of chaperonin 2D crystals and **h**, 10 nm AuNP binding within the 9 nm pores of the loop-deletion variant. **i**, Individual clathrin triskelion imaged by AFM in liquid. **j**, Schematic of the assembly of clathrin lattices on surfaces. **k**, TEM images of clathrin lattices assembled onto graphene, graphite, polyvinylformal (PVF) and uncharged PVF. **l**, Cartoon of the assembled 2D C^{98}/C^{264} RhuA lattices. **m-o**, TEM images of 2D C^{98}/C^{264} RhuA lattices. **p**, Cartoon of 2D AuNP lattices templated onto C^{98}/C^{264} RhuA crystal, in which the AuNPs were bound in the inter-RhuA space. **q-s**, TEM images of 2D AuNP lattices on C^{98}/C^{264} RhuA. Insets (**o**, **s**): Fast Fourier Transforms (FFTs) of the TEM images. **Figure 1.4a-d** adapted from ref. 87, **Figure 1.4e-h** adapted from ref. 31, **Figure 1.4i-k** adapted from ref 96, **Figure 1.4l-s** adapted from ref. 99.

Self-assembled materials are often limited to nanoscale sizes due to the stochasticity of nucleation and growth processes, however Allred et al. described a method to fabricate nanoparticle arrays on S-layer protein (*Deinococcus radiodurans*) over macroscopic substrates.⁹⁵ Dannhauser et al. have also synthesized macroscale nanoparticle arrays using self-assembled clathrin proteins,⁹⁶ which can form extended multi-millimeter wide 2D crystals on a variety of substrates with a periodicity of 30 nm. More importantly, the lattice can be stored for months after crosslinking and stabilized with uranyl acetate and can be dehydrated and rehydrated without affecting the integrity of the lattice (**Figure 1.4i-k**). Precise fabrication of nanoparticles is very important for constructing functional hybrid materials, as the properties of nanoparticles depend strongly on their exact composition and size. Zhang et al. reported the rational design of the disk-shaped TMV protein to display functional groups along its surface that enabled highly controlled assembly of the discrete nanoparticles and TMV monolayer structure, achieving organization of both homogeneous and heterogeneous nanoparticle lattices.⁹¹ Recently, a dynamic 2D nanoparticle lattice was achieved by using flexible 2D crystals of the tetrameric protein ^{C98}RhuA, whose square shape is connected to four neighbors through flexible disulfide bonds, allowing the lattice to open and close through mechanical disturbance.⁹⁷⁻⁹⁸ Upon binding of gold nanoparticles onto these crystals, a framework structure with variable interparticle spacings was achieved (**Figure 1.4l-s**).⁹⁹

The aforementioned methods form protein arrays first and then utilize the interactions between the nanoparticles and protein molecules to guide assembly of the former. Another approach to templating nanoparticle assemblies is to directly utilize protein chemistry to modify the associated nanoparticles. For example, Cheung-Lau et al. encapsulated 5 nm AuNPs into thermophilic ferritin (8 nm internal diameter) by changing the ionic strength of the solution.¹⁰⁰ Subsequent addition of gold ions and mild reductant produced 8-nm gold nanoparticles within the

ferritin cages, demonstrating exquisite control over nanoparticle size due to the physical limitations of the protein shell (**Figure 1.5a, b**). Not only can the protein cage template nanoparticle formation inside the cavity, nanoparticle binding to the outside of proteins has also been used to form binary 3D crystals of both components. Okuda et al. showed that a ferritin variant loaded with Fe_3O_4 magnetic nanoparticles assembled into the same 3D lattice as apo-ferritin, thus achieving a new magnetic superstructure (**Figure 1.5c-e**).¹⁰¹ The complexity of such lattices was further increased by Künzle et al, who engineered the surface of human heavy-chain ferritin (HuHF) to produce two variants with opposite surface charges¹⁰² that could be co-crystallized into tetragonal 3D crystals through complementary electrostatic interaction. When each variant was first loaded with different nanoparticles (CeO_2 and Co_3O_4), binary 3D nanoparticle lattices were achieved upon crystallization of the nanoparticle-loaded protein cages (**Figure 1.5f-h**). In our lab, we have also utilized nanoparticle-loaded ferritin to form hydrogel-infused crystals to achieve a dynamic hybrid system where the interparticle distance is tuned by ionic strength or pH (**Figure 1.5i**).¹⁰³

Electron transfer is another area of great interest for both proteins and nanoparticles. Attempts to introduce electron flow between enzymes and electrodes has been conducted through chemical modification of the proteins as well as by embedding enzymes into redox-active polymers.⁴⁵ However, due to nonoptimal positioning and the lack of alignment of the catalyst with the electrode, electron transfer rates measured for these systems are typically significantly lower compared to natural redox proteins.¹⁰⁴ Xiao et al. demonstrated that by attaching a redox-active enzyme (glucose oxidase) to electrodes through FAD modified gold nanoparticles, rapid electron transfer kinetics were achieved that exceeded the original substrate (**Figure 1.6a**).¹⁰⁵ Utilizing gold nanoparticles as connectors not only improves the electron transfer rates, they have also been shown to improve the efficiency of long-range charge transfer.

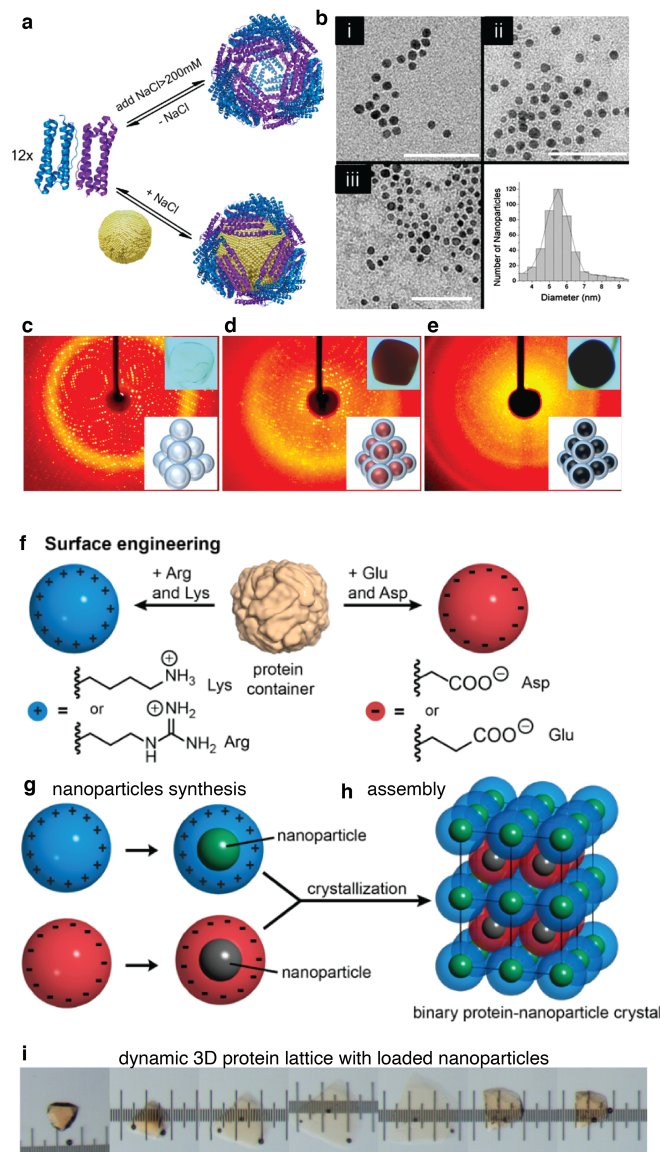


Figure 1.5 | Templated assembly of nanoparticles encapsulated within protein cages. a, Cartoon depiction of thermophilic ferritin dimer (reversible) self-assembly into spherical 24mer cages with/without 5 nm AuNPs. **b,** TEM images of (i) 5-nm BSPP AuNPs alone, (ii) ferritin-(BSPP)AuNPs incubated for 24 h and (iii) for 48 h. Encapsulation was confirmed by detailed SEC analysis. Single-crystal x-ray diffraction patterns from **c**, apoferritin, **d**, ferritin, and **e**, Fe₃O₄-ferritin crystals. Inset top: optical images of the crystal, inset bottom: model of the crystal. **f,** The native ferritin was engineered to produce containers with either positively charged (left) or negatively charged surfaces (right). **g,** Nanoparticle synthesis was carried out separately within each protein container variant. **h,** Self-assembly of the oppositely charged ferritin-nanoparticle composites yielded highly ordered three-dimensional superlattices. **i,** Light-microscopy images showing the expansion and contraction of a crystal–hydrogel hybrid containing Fe-loaded ferritin molecules. **Figure 1.5a, b** adapted from ref. 100, **Figure 1.5c-e** adapted from ref. 101, **Figure 1.5f-h** adapted from ref 102, **Figure 1.5i** adapted from ref. 103.

Jensen et al. demonstrated that long-range (>50 Å) interfacial electron transfer between the heme protein cytochrome *c* and a gold electrode was enhanced when the two components were bridged (electrostatically) by a gold nanoparticle (**Figure 1.6b-d**).¹⁰⁶ In addition to single nanoparticle

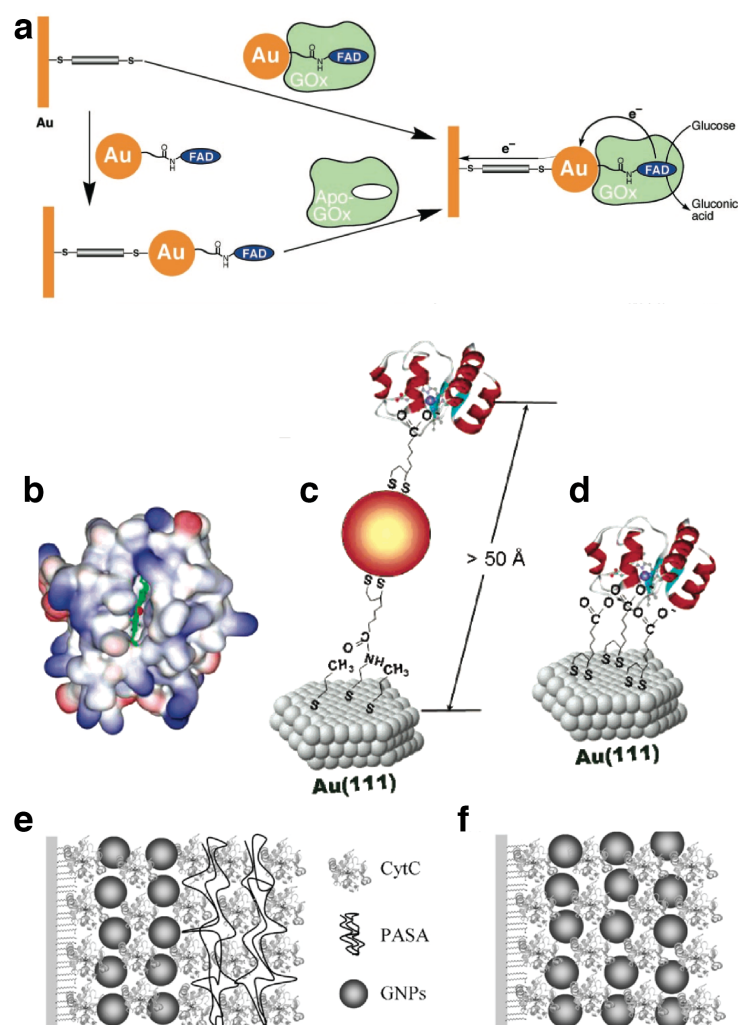


Figure 1.6 | Protein-nanoparticle hybrid materials in interfacial electron transfer. a, Assembly of Au-AuNP-GOx electrode by the binding of AuNP-bound GOx to a dithiol monolayer associated with a gold electrode or via adsorption of FAD-functionalized AuNPs onto the gold electrode followed by the reconstitution of apo-GOx with FAD. Schematic illustration of the molecular assembly of cyt *c* on Au(111) surfaces: **b**, 3D structure of cyt *c*, with surface charge distribution indicated in blue for positive charge and red for negative charge. **c**, Cyt *c*-AuNP hybrid structure on the Au(111) surface and **d**, reference system without AuNPs. Depictions of different types of multilayer assemblies prepared on monolayer electrodes: **e**, combined layer structure [GNPs/cyt *c*]₂-[PASA/cyt *c*]_n, **f**, assembly of AuNPs and cyt *c* only [AuNPs/cyt *c*]_n (n = 2, 4, 6). **Figure 1.6a** adapted from ref. 105, **Figure 1.6b-d** adapted from ref. 106, **Figure 1.6e, f** adapted from ref. 107.

binding to the electrodes, a layered structure of gold nanoparticles with protein (cytochrome *c*) and polymers (PASA) was also obtained, which also showed full electro-activity (**Figure 1.6e, f**).¹⁰⁷

To review, nanoparticles have been intensely investigated for a wide variety of applications in catalysis, biosensing, biology, and medicine, for example as fluorescent biological labels,¹⁰⁸ drug and gene delivery,¹⁰⁹ detection of proteins,¹¹⁰ tissue engineering,¹¹¹ tumor destruction via heating,¹¹² and MRI contrast enhancement,¹¹³ highlighting their broad utility as nanoscale components. When combined with proteins to form new materials, the resulting hybrids can yield new properties otherwise not easily achieved by either component alone, making them suitable to new applications. For example, Kapur et al. used the fluorescent protein mCherry together with gold nanoparticles to enable the detection of thiol derivatives (**Figure 1.7a**).¹¹⁴ Upon protein binding to the surface of the gold nanoparticles through metal coordination, the fluorescence signal was quenched, but when thiol derivatives displaced the protein, fluorescence was restored, resulting in a high accuracy biosensor active both free in solutions and in cell cultures. Want et al. applied a biotemplate of self-assembled nanofibers to regulate gold nanoparticle self-assembly that could be used for improving the photothermal effect in cancer therapy (**Figure 1.7b**).¹¹⁵ Xie et al. developed a simple and general light-inducible method for the assembly of protein-inorganic nanoparticles.¹¹⁶ In addition to *in vivo* targeting, nanoparticle-protein hybrids have also been applied to *in vivo* imaging. Magnetic nanoparticles have been encapsulated inside ferritin cages through various methods and formed into ordered structures through protein crystallization (**Figure 1.7c, d**).¹⁰¹ Valero et al. utilized magnetic nanoparticle-protein complexes as *in vivo* MRI nanoprobes¹¹⁷ whereby magnetic nanoparticles were encapsulated within the protein cage through pH-controlled disassembly/reassembly followed by protein cage functionalization with two carbohydrates. MRI measurements suggested that the resulting hybrid materials (termed

“apomaghemites”) are promising contrast agents (**Figure 1.7e, f**). With higher complexity, hybrid materials can achieve more advanced functionalities. Ghosh et al. showed that M13 filamentous bacteriophage could be used as a scaffold to display targeting ligands and localize nanoparticles, resulting in enhanced MRI contrast via delivery of large numbers of nanoparticles into cancer cells and tumors in mice (**Figure 1.7 g, h**).¹¹⁸

1.4 DNA protein hybrids

DNA self-assembly has been used to create an incredible variety of nanoscale structures, including polyhedra,¹¹⁹ simple machines,¹²⁰⁻¹²¹ one-dimensional wires or tubes,¹²²⁻¹²⁴ two-dimensional arrays,¹²⁵⁻¹²⁷ and three-dimensional structures.¹²⁸⁻¹²⁹ Rapid development of DNA nanotechnology has had a great impact on applications in areas including biophysics, diagnostics, nanoparticle and protein assembly, biomolecule structure determination, drug delivery and synthetic biology.³⁶ DNA-protein hybrid materials exist abundantly in nature as important part of life functions, for example nucleosomes,¹³⁰ T7 RNA polymerase and DNA substrate complex,¹³¹ Cas9 and target DNA complex,¹³² to name just a few. These natural machines cooperatively utilize their DNA and protein components to efficiently conduct their sophisticated biological tasks,¹³³ inspiring great interest in constructing artificial DNA-protein hybrid structures towards a variety of applications (*e.g.*, biological studies, nanofabrication, biomedical research). The unique properties of DNA, including its programmable self-assembly,^{129,134} nanoscale dimensions,^{128,135-136} structural diversity,¹³⁷⁻¹³⁸ and biocompatibility^{134,139-140} make the construction of protein-DNA hybrid materials highly accessible. Functional self-assembled oligomers appended with both a binding and a reporting face have already been shown to hold great promise in the area of multivalent protein targeting.^{126,141-142}

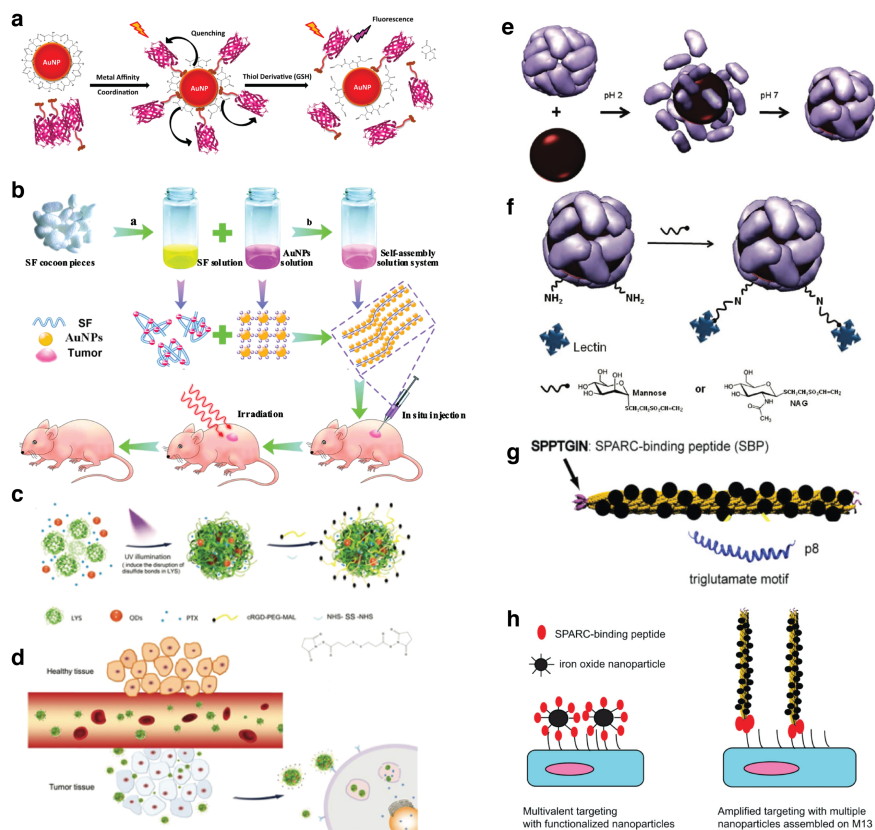


Figure 1.7 | Functional protein-nanoparticle hybrid materials. **a**, Schematic representation of a conjugation and release strategy based on metal coordination between citrate AuNPs and His-tagged mCherry, producing AuNP-mCherry conjugates with quenched fluorescence. Addition of thiolate molecules led to competitive displacement of mCherry, as detected by recovery of its fluorescence. **b**, Schematic of the templated assembly of AuNPs onto SF nanofibers and their use in photothermal breast tumor destruction. **c**, Schematic of the synthesis of Lys-based multi-functional drug delivery system. The first synthetic step involves the assembly of protein-based nanoparticles incorporating both quantum dots (QDs) and the anticancer drug PTX. The second step is the addition of the tumor targeting ligand cyclic RGD-PEG-maleimide to the free thiols on the surface of these Lys-PTX-QD NPs, and the addition of NHS-SS-NHS for crosslinking, yielding the final structure. **d**, Illustration of the *in vivo* delivery pathway for drug encapsulated protein-inorganic hybrid nanoparticles. **e**, Schematic encapsulation and **f**, glycosylation of Apomagemite nanoparticles by reaction of N-acetyl-D-glucosamine or D-mannose vinyl sulfone derivatives with the amine group naturally present in the Apomagemite nanoparticles, making them recognizable by lectins. **g**, Schematic of M13 (yellow) with SPARC binding peptide displayed on p3 protein of virus (in pink). p8 proteins displaying triglutamate motifs enabled multivalent assembly and display of iron oxide nanocrystals (denoted as black circles) along the viral coat. **h**, Left: schematic of SPARC-binding peptide direction of nanoparticles to targets via multivalent interactions. Right: M13 assembles multiple nanoparticles along its coat to deliver a higher cargo of nanoparticles per SPARC target than the ligand functionalized nanoparticles (left). **Figure 1.7a** adapted from ref. 114, **Figure 1.7b** adapted from ref. 115, **Figure 1.7c, d** adapted from ref 101, **Figure 1.7e, f** adapted from ref 117, **Figure 1.7g, h** adapted from ref. 118.

One major application of DNA nanotechnology is the use of self-assembled DNA lattices to scaffold assembly of other molecular components.¹²⁶ The specificity of the interactions between complementary base pairs make DNA a very useful construction material. Highly complex nanoscale shapes and patterns of DNA can be created through the design of its sequences.¹⁴³

Attachment of proteins to patterned DNA would allow novel biological experiments aimed at modeling complex protein assemblies.^{134, 143} DNA origami technology has enabled the creation of highly precise structures, with extra interaction between the DNA strands and protein molecules, creating a very useful strategy for spatial protein assembly. Zhang et al. generated multiple 3D DNA structures modified with biotin molecules, allowing streptavidin binding through host-guest interactions (**Figure 1.8a**).¹⁴⁴ Various covalent (*e.g.*, unnatural amino acids, site-specific modification of proteins, small-molecule labels) and noncovalent (*e.g.*, sequence-specific DNA recognition motifs, DNA aptamers, affinity peptides, electrostatic and hydrophobic) interactions between protein and DNA have been utilized for the construction of DNA-protein hybrids. DNA-templated self-assembly of protein arrays and nanowires have been developed for the assembly of different protein molecules for different purposes. Yan et al. developed a method utilizing 4×4 DNA tiles for the assembly of periodic protein nanoribbons and nanogrids (**Figure 1.8b, c**).¹²⁶ Malo et al. engineered a 2D protein-DNA lattice that, upon incorporation of the protein RuvA, produced a different lattice than the DNA-only structure (**Figure 1.9a–c**).¹⁴⁵ More recently, computational methods have been applied for designing biomolecular self-assembly.¹⁴⁶⁻¹⁴⁸ *De novo* design of protein-DNA co-assemblies was reported by Mou et al, where an homodimerization interface installed onto *Drosophila* Engrailed homeodomain (ENH) allowed the now-dimeric protein complex to bind to two double-stranded DNA molecules. The engineered protein-DNA

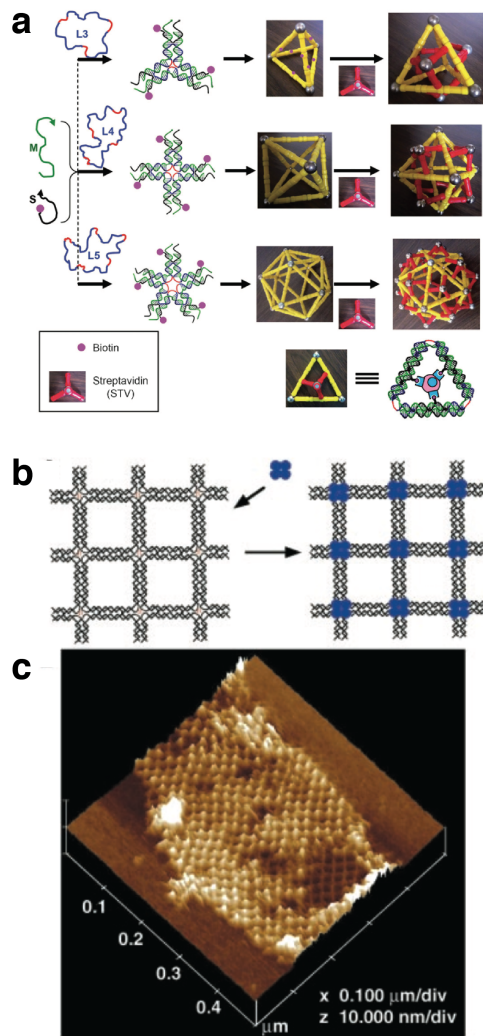


Figure 1.8 | Designed protein-DNA hybrid materials. **a**, Schematic representation of 3D protein organization directed by DNA nanostructures. DNA strands L (blue and red), M (green), and S (black; conjugated to a biotin at its 5' end) self-assemble by maximizing the base pairing between complementary DNA segments into star-shaped nanomotifs that further assemble into symmetric DNA polyhedra: tetrahedron (TET), octahedron (OCT), and icosahedron (ICO). Each vertex is composed of a corresponding DNA star-shaped motif. All faces of the DNA polyhedra are identical triangles and display three biotin moieties. Upon incubation with streptavidin (STV) protein, each polyhedral face obtains a STV protein via biotin binding by STV, resulting in well-structured TET/STV, OCT/STV, and ICO/STV complexes. Lower right: illustrative model of the trivalent binding between a STV protein and a triangular face of the DNA polyhedra. **b**, Self-assembly of 4x4 DNA nanogrids (left) and their use for scaffolded assembly of streptavidin (right), where biotin groups displayed at the center of each tile controls the binding of streptavidin (represented by a blue tetramer) to produce protein nanoarrays. **c**, AFM image of the self-assembled protein arrays in **b**. **Figure 1.8a** adapted from ref. 144, **Figure 1.8b, c** adapted from ref. 126.

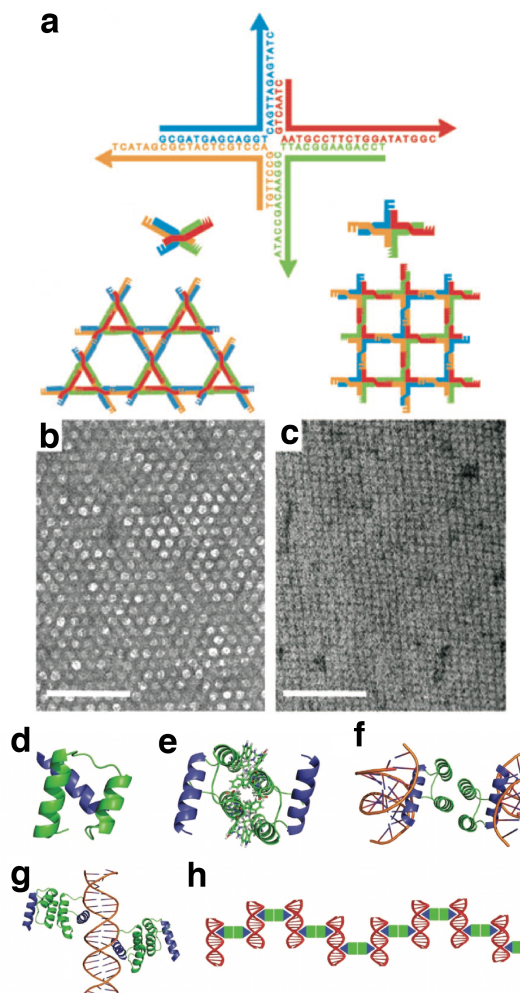


Figure 1.9 | Design of protein-DNA hybrid materials. **a**, Four oligonucleotides hybridize to form a Holliday junction (HJ) with two pairs of complementary “sticky ends” that can be used to create Kagome (lower left) and square (lower right) lattices. Negative-stain TEM images of the Kagome lattice (**b**; DNA is positively stained (dark); scale bar: 100 nm) and the square lattice (**c**) formed from HJs held in a square-planar configuration by the protein RuvA (protein is lighter than background; scale bar: 100 nm). **d–h**, 1D protein–DNA nanomaterial design strategy. **d**, Helix 1 and helix 2 (green) of ENH were engineered into a homodimerization domain, and helix 3 (blue) is the native DNA-binding domain. The interface of the docked model was designed for homodimerization (**e**). **f**, The designed homodimer (dualENH) binds two dsDNA fragments on its outward faces, as modeled by aligning the homodimer model in **e** with the ENH–DNA co-crystal structure. **g**, Two protein-binding sites were engineered onto a dsDNA fragment so that two dualENH dimers would bind 180° apart along the double helix. **h**, Together, the dualENH protein and dsDNA fragments co-assemble into protein–DNA nanowires, as shown in this illustrative cartoon. **Figure 1.9a–c** adapted from 145, **Figure 1.9d–h** adapted from ref 149.

complex could form irregular bulk nanoparticles or nanowires of single-molecule width (**Figure 1.9d-h**).¹⁴⁹ On a different front, DNA-modified protein molecules were assembled into a 3D lattice structure, as shown by Brodin et al., who covalently attached complementary DNA oligos to the surface of separate catalases that could then hybridize to produce body-centered-cubic crystals upon mixing the two modified protein-DNA complexes (**Figure 1.10a**).¹⁵⁰ By changing the DNA oligos used, they could obtain different lattice unit cells. DNA molecules can similarly be used to control nanoparticle superlattice architectures. McMillan et al. showed that two different protein-nanoparticle lattices could be obtained from the same protein and DNA oligos depending on the spatial distribution of conjugated DNA strands on the protein surface: isotropic distributions produced simple cubic crystals, while localized distributions produced hexagonal crystals (**Figure 1.10b-f**).¹⁵¹ Subramanian et al. demonstrated cooperative self-assembly of a synthetic protein-DNA crystal through three types of intermolecular interactions (**Figure 1.10 g, h**).¹⁵² In this work, two complementary DNA fragments were covalently attached to the protein through site-specific labeling, then the two protein-DNA complexes were co-assembled into a 3D lattice through protein-metal coordination, protein-DNA interactions, and Watson-Crick base pairing.

DNA self-assembly not only enables the precise structural organization of nanoparticles or proteins, it can also provide control over enzyme activity. Willner et al. introduced the use of hexagonal DNA scaffolds for the topological organization of different enzymes (**Figure 1.11a, b**).³⁷ By combining two complementary enzymes (or a cofactor-enzyme pair) on DNA scaffolds, a catalytic cascade was formed and the biocatalytic process proceeded more efficiently compared to that observed in diffusion-controlled mixtures. Dutta et al. created a DNA-directed light-harvesting/reaction center system.¹⁵³ In their research, a three-arm-DNA nanostructure served as an antenna conjugated to a photosynthetic center when multiple organic dyes were attached to the

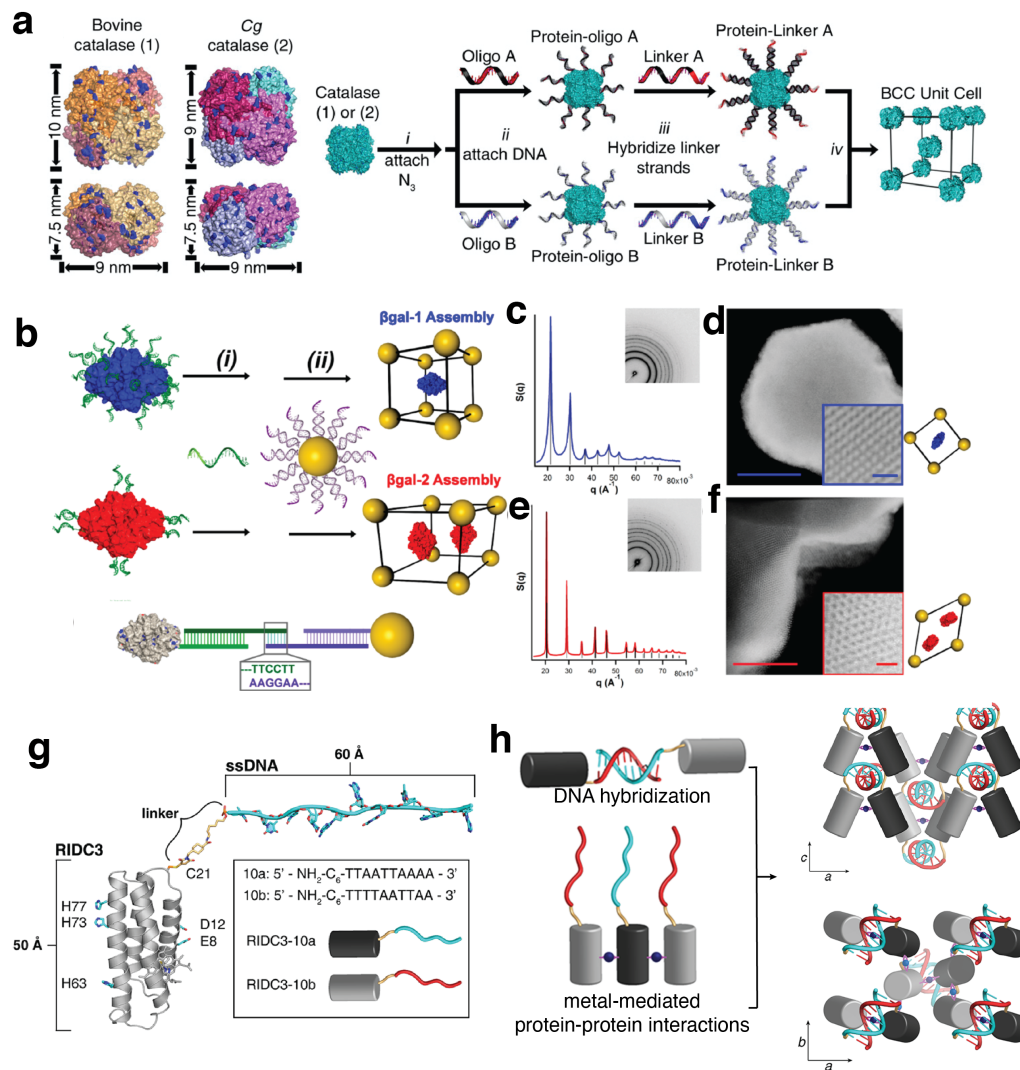


Figure 1.10 | Designed protein-DNA hybrid materials. **a**, Design and intended assembly of protein–DNA conjugates created from bovine and Cg catalases. Surface-accessible amines (shown in blue) are modified with azide-NHS-functionalized DNA strands through copper-free “click chemistry” reactions. Hybridization of the protein-conjugated DNA strands via complementary linkers results in the assembly of the proteins into BCC lattices. **b**, Scheme depicting the functionalization of β gal proteins with DNA (β gal-1 via lysine conjugation, top; β gal-2 via cysteine conjugation, bottom) and their assembly into superlattices with DNA-functionalized AuNPs. **c**, **d**, SAXS patterns of binary superlattices prepared from β gal-1 and -2, respectively. Insets: diffraction patterns. STEM images of the simple cubic (**e**) (scale bar = 1 μ m (50 nm inset)) and simple hexagonal (**f**) (scale bar = 0.5 μ m (50 nm inset)) superlattices, with top view (001 plane) of the unit cells shown. **g**, Design of the protein-DNA conjugate RIDC3–10a/b. Metal-binding residues are shown as cyan sticks on the RIDC3 surface, with the single stranded DNA attached to surface Cys residues. **h**, Indicated interactions responsible for formation of the material (left) and a cartoon schematic of the final crystal (right). **Figure 1.10a** adapted from ref. 150, **Figure 1.10b-f** adapted from ref. 151, **Figure 1.10g, h** adapted from ref. 151.

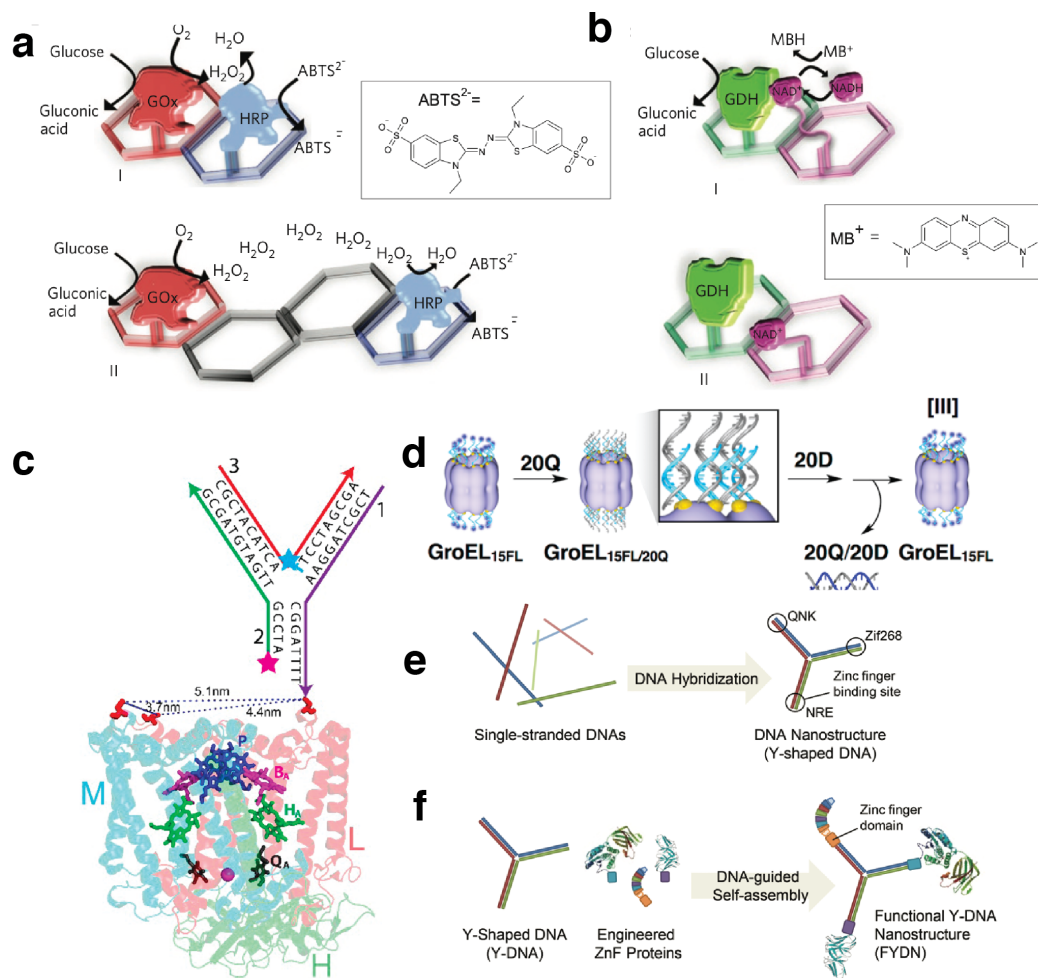


Figure 1.11 | Functional protein-DNA hybrid materials. **a**, Assembly of GOx and HRP enzymes onto two-hexagon (I) and four-hexagon (II) DNA strips to form a coupled, spatially organized, enzymatic system. **b**, Analogous design of an NADH/GDH system using a two-hexagon scaffold with different lengths of tethers linking the NAD cofactor to the scaffold. **c**, Modified structure of the reaction center (RC) from the purple bacterium functionalized with DNA strands to bring fluorophores in proximity to the protein chromophores. **d**, Schematic illustration of the hybridization and displacement of fully and/or partially complementary DNA strands attached to GroEL variants. Fluorophore labeled 15-mer DNA (15FL) was attached to the protein to yield GroEL_{15FL} that, when mixed with 20-mer DNA containing a quenching group (20Q), produced GroEL_{15FL/20Q}. Controlled release of 20Q was induced by addition of the 20-mer DNA 20D, which is complementary to 20Q, by liberation of 20Q/20D dimers. **e**, Schematic representation of the design and construction of functional Y-shaped DNA nanostructures (FYDN) via sequence-specific hybridization of three DNA strands. These Y-DNA molecules were designed to display three different ZnF binding sites (QNK, Zif268, and NRE) at the end of each arm. **f**, When ZnF-fused functional proteins were added to the solution, they could be site-specifically bound to the Y-DNA scaffolds to spatially organize the protein activity. **Figure 1.11a, b** adapted from ref 37, **Figure 1.11c** adapted from ref. 153, **Figure 1.11d** adapted from ref. 154, **Figure 1.11e, f** adapted from ref. 155.

DNA (**Figure 1.11c**). This construction extended the absorbance cross section of the complex into a spectral range where the reaction center has only weak absorbance, rendering it a useful model system for potential applications in nanophotonics. Kashiwagi et al. showed that when the chaperone protein GroEL was labeled with complementary DNA strands (10a/10b, complementary pair) at each end of its structure (**Figure 1.11d**), the hybrid assembled into one-dimensional nanotubes via strong multivalent interactions from DNA hybridization.¹⁵⁴ When asymmetric DNA strands (15c/10d, only 10 pairs matching) were used instead, the nanotubes could be disassembled upon the addition of 15d (fully complementary to 15c) due to the greater stability of the 15c/15d DNA complex, thus demonstrating controlled release of the protein, which itself is capable of serving as a container that toggles between open/closed conformations. More recently, protein-DNA nanostructures have found great potential as functional materials for biomedical applications. To highlight one example, Ryu et al. developed a modular DNA-protein hybrid nanostructure as a targeted drug delivery platform¹⁵⁵ constructed from designed Y-shaped DNA structures containing three distinct zinc-finger protein (ZnF) binding sequences (one on each arm) onto which different ZnF-fused functional proteins could bind (**Figure 1.11e, f**). When one of these ZnF-fusions contained a cellular targeting moiety, these hybrid structures were shown to bind to the surface of cells and deliver protein cargo into the cytosol with negligible cytotoxicity. This underscores the functional utility associated with highly controlled spatial organization of different proteins, a technical requirement that is readily met using DNA nanotechnology, but would be significantly more difficult with proteins alone.

Above, we have highlighted numerous examples of designed protein-based hybrid materials and discussed the many demonstrated (and potential) applications of these materials in biosensing, drug delivery, in-vivo imaging, catalysis, medicine, and several areas of

nanotechnology. The immense space of possible building blocks means that much more remains to be investigated for protein hybrid materials. As is evident from the examples in this Chapter, combining two distinct components can not only be used to complement their individual properties, it can also create new properties (*i.e.*, not achievable with a single component) that emerge directly from their specific construction, significantly broadening the scope of potential applications for this class of materials.

1.5 Dissertation objectives

In this dissertation, we report the creation of a novel hybrid material (polymer-infused protein crystals) that possesses a unique suite of properties (self-healing behavior, dynamism, crystallinity) not previously achieved simultaneously within a single material (Chapter 2). As the fine-tuning of a material's properties is facilitated by a molecularly detailed understanding of their origins, we then set out to characterize this relationship by systematically testing the impact of different variables (*e.g.*, choice of components, protein electrostatics, protein identity) on the bulk-scale material properties (Chapter 3). Finally, we report that the unique characteristics of this protein-polymer hybrid material (namely its ability to dramatically expand and contract its porous structure) enable it to selectively encapsulate and release macromolecular cargos, making it potentially useful for storage and delivery of proteins and/or therapeutic biologics (Chapter 4).

1.6 Reference

1. Marsh, J. A.; Teichmann, S. A., Structure, dynamics, assembly, and evolution of protein complexes. In *Annual review of biochemistry, vol 84*, Kornberg, R. D., Ed. Annual Reviews: Palo Alto, 2015; Vol. 84, pp 551-575.
2. Goodsell, D. S.; Olson, A. J., Structural symmetry and protein function. *Annual Review of Biophysics and Biomolecular Structure* **2000**, *29*, 105-153.
3. Shi, J.; Jiang, Y.; Wang, X.; Wu, H.; Yang, D.; Pan, F.; Su, Y.; Jiang, Z., Design and synthesis of organic-inorganic hybrid capsules for biotechnological applications. *Chemical Society Reviews* **2014**, *43* (15), 5192-5210.
4. Pollard, T. D.; Weihing, R. R., Actin and myosin and cell movement. *Critical Reviews in Biochemistry* **1974**, *2* (1), 1-65.
5. Hall, A., Rho gtpases and the actin cytoskeleton. *Science* **1998**, *279* (5350), 509-514.
6. Janke, C.; Bulinski, J. C., Post-translational regulation of the microtubule cytoskeleton: Mechanisms and functions. *Nature Reviews Molecular Cell Biology* **2011**, *12* (12), 773-786.
7. Theil, E. C., Ferritin - structure, gene-regulation, and cellular function in animals, plants, and microorganism. *Annual Review of Biochemistry* **1987**, *56*, 289-315.
8. Levi, S.; Luzzago, A.; Cesareni, G.; Cozzi, A.; Franceschinelli, F.; Albertini, A.; Arosio, P., Mechanism of ferritin iron uptake - activity of the h-chain and deletion mapping of the ferro-oxidase site - a study of iron uptake and ferro-oxidase activity of human-liver, recombinant h-chain ferritins, and of 2 h-chain deletion mutants. *Journal of Biological Chemistry* **1988**, *263* (34), 18086-18092.
9. Woehlke, G.; Schliwa, M., Walking on two heads: The many talents of kinesin. *Nature Reviews Molecular Cell Biology* **2000**, *1* (1), 50-58.
10. Veenhoff, L. M.; Heuberger, E.; Poolman, B., Quaternary structure and function of transport proteins. *Trends in Biochemical Sciences* **2002**, *27* (5), 242-249.
11. Corpas, E.; Harman, S. M.; Blackman, M. R., Human growth-hormone and human aging. *Endocrine Reviews* **1993**, *14* (1), 20-39.

12. Carroll, P. V.; Christ, E. R.; Growth Hormone Res Soc Sci, C., Growth hormone deficiency in adulthood and the effects of growth hormone replacement: A review. *Journal of Clinical Endocrinology & Metabolism* **1998**, *83* (2), 382-395.
13. Burgess, B. K.; Lowe, D. J., Mechanism of molybdenum nitrogenase. *Chemical Reviews* **1996**, *96* (7), 2983-3011.
14. Rutledge, H. L.; Tezcan, F. A., Electron transfer in nitrogenase. *Chemical Reviews* **2020**, *120* (12), 5158-5193.
15. McEvoy, J. P.; Brudvig, G. W., Water-splitting chemistry of photosystem ii. *Chemical Reviews* **2006**, *106* (11), 4455-4483.
16. Kaplan, J. H., Biochemistry of na,k-atpase. *Annual Review of Biochemistry* **2002**, *71*, 511-535.
17. Tomii, K., Protein properties. In *Encyclopedia of bioinformatics and computational biology*, Ranganathan, S.; Gribskov, M.; Nakai, K.; Schönbach, C., Eds. Academic Press: Oxford, 2019; pp 28-33.
18. Rapley, R.; David Whitehouse, e., Molecular biology and biotechnology. *Royal Society of Chemistry* **2015**.
19. James, J.; Simpson, B. K., Application of enzymes in food processing. *Critical Reviews in Food Science and Nutrition* **1996**, *36* (5), 437-463.
20. Yada, R. Y. e., Proteins in food processing. *Woodhead publishing* **2017**.
21. Basu, S. K.; Govardhan, C. P.; Jung, C. W.; Margolin, A. L., Protein crystals for the delivery of biopharmaceuticals. *Expert Opinion on Biological Therapy* **2004**, *4* (3), 301-317.
22. Shah, R. B.; Patel, M.; Maahs, D. M.; Shah, V. N., Insulin delivery methods: Past, present and future. *International Journal of Pharmaceutical Investigation* **2016**, *6* (1), 1-9.
23. Cooper, G. M.; Hausman, R. E., The cell: Molecular approach. *Medicinska naklada* **2004**.
24. Kickelbick, G., (Ed.), Hybrid materials: Synthesis, characterization, and applications. *John Wiley & Sons* **2007**.

25. Koshiyama, T.; Kawaba, N.; Hikage, T.; Shirai, M.; Miura, Y.; Huang, C. Y.; Tanaka, K.; Watanabe, Y.; Ueno, T., Modification of porous protein crystals in development of biohybrid materials. *Bioconjugate Chemistry* **2010**, *21* (2), 264-269.
26. Obermeyer, A. C.; Olsen, B. D., Synthesis and application of protein-containing block copolymers. *Acs Macro Letters* **2015**, *4* (1), 101-110.
27. Cobo, I.; Li, M.; Sumerlin, B. S.; Perrier, S., Smart hybrid materials by conjugation of responsive polymers to biomacromolecules. *Nature Materials* **2015**, *14* (2), 143-159.
28. Maikawa, C. L.; Smith, A. A. A.; Zou, L.; Meis, C. M.; Mann, J. L.; Webber, M. J.; Appel, E. A., Stable monomeric insulin formulations enabled by supramolecular pegylation of insulin analogues. *Advanced Therapeutics* **2020**, *3* (1), 9.
29. Ye, C.; Chi, H., A review of recent progress in drug and protein encapsulation: Approaches, applications and challenges. *Materials Science & Engineering C-Materials for Biological Applications* **2018**, *83*, 233-246.
30. Perez, C.; Castellanos, I. J.; Costantino, H. R.; Al-Azzam, W.; Griebenow, K., Recent trends in stabilizing protein structure upon encapsulation and release from bioerodible polymers. *Journal of Pharmacy and Pharmacology* **2002**, *54* (3), 301-313.
31. McMillan, R. A.; Paavola, C. D.; Howard, J.; Chan, S. L.; Zaluzec, N. J.; Trent, J. D., Ordered nanoparticle arrays formed on engineered chaperonin protein templates. *Nature Materials* **2002**, *1* (4), 247-252.
32. Nikitin, M. P.; Zdobnova, T. A.; Lukash, S. V.; Stremovskiy, O. A.; Deyev, S. M., Protein-assisted self-assembly of multifunctional nanoparticles. *Proceedings of the National Academy of Sciences of the United States of America* **2010**, *107* (13), 5827-5832.
33. Naik, R. R.; Stringer, S. J.; Agarwal, G.; Jones, S. E.; Stone, M. O., Biomimetic synthesis and patterning of silver nanoparticles. *Nature Materials* **2002**, *1* (3), 169-172.
34. Sleytr, U. B.; Schuster, B.; Egelseer, E. M.; Pum, D., S-layers: Principles and applications. *Fems Microbiology Reviews* **2014**, *38* (5), 823-864.
35. Wang, P.; Ko, S. H.; Tian, C.; Hao, C.; Mao, C., Rna-DNA hybrid origami: Folding of a long rna single strand into complex nanostructures using short DNA helper strands. *Chemical Communications* **2013**, *49* (48), 5462-5464.

36. Seeman, N. C.; Sleiman, H. F., DNA nanotechnology. *Nature Reviews Materials* **2018**, *3* (1).
37. Wilner, O. I.; Weizmann, Y.; Gill, R.; Lioubashevski, O.; Freeman, R.; Willner, I., Enzyme cascades activated on topologically programmed DNA scaffolds. *Nature Nanotechnology* **2009**, *4* (4), 249-254.
38. Young, R. J.; Lovell, P. A., *Introduction to polymers*. CRC press: 2011.
39. Strobl, G. R.; Strobl, G. R., *The physics of polymers*. Springer: 1997; Vol. 2.
40. Mark, J.; Ngai, K.; Graessley, W.; Mandelkern, L.; Samulski, E.; Wignall, G.; Koenig, J., *Physical properties of polymers*. Cambridge University Press: 2004.
41. Chandra, R.; Rustgi, R., Biodegradable polymers. *Progress in Polymer Science* **1998**, *23* (7), 1273-1335.
42. Carothers, W. H., Polymers and polyfunctionality. *Transactions of the Faraday Society* **1936**, *32*, 39-49.
43. Vroman, I.; Tighzert, L., Biodegradable polymers. *Materials* **2009**, *2* (2), 307-344.
44. Szleifer, I., Polymers and proteins: Interactions at interfaces. *Current Opinion in Solid State & Materials Science* **1997**, *2* (3), 337-344.
45. Gerard, M.; Chaubey, A.; Malhotra, B. D., Application of conducting polymers to biosensors. *Biosensors & Bioelectronics* **2002**, *17* (5), 345-359.
46. Shin, H.; Jo, S.; Mikos, A. G., Biomimetic materials for tissue engineering. *Biomaterials* **2003**, *24* (24), 4353-4364.
47. Li, T.; Ye, B.; Niu, Z. W.; Thompson, P.; Seifert, S.; Lee, B.; Wang, Q., Closed-packed colloidal assemblies from icosahedral plant virus and polymer. *Chemistry of Materials* **2009**, *21* (6), 1046-1050.
48. Petkau-Milroy, K.; Uhlenheuer, D. A.; Spiering, A. J. H.; Vekemans, J.; Brunsveld, L., Dynamic and bio-orthogonal protein assembly along a supramolecular polymer. *Chemical Science* **2013**, *4* (7), 2886-2891.

49. Panganiban, B.; Qiao, B. F.; Jiang, T.; DelRe, C.; Obadia, M. M.; Nguyen, T. D.; Smith, A. A. A.; Hall, A.; Sit, I.; Crosby, M. G.; Dennis, P. B.; Drockenmuller, E.; de la Cruz, M. O.; Xu, T., Random heteropolymers preserve protein function in foreign environments. *Science* **2018**, *359* (6381), 1239-1243.
50. Wan, X. J.; Liu, S. Y., Fabrication of a thermoresponsive biohybrid double hydrophilic block copolymer by a cofactor reconstitution approach. *Macromolecular Rapid Communications* **2010**, *31* (23), 2070-2076.
51. Hirayama, S.; Oohora, K.; Uchihashi, T.; Hayashi, T., Thermoresponsive micellar assembly constructed from a hexameric hemoprotein modified with poly(n-isopropylacrylamide) toward an artificial light-harvesting system. *Journal of the American Chemical Society* **2020**, *142* (4), 1822-1831.
52. Thomas, C. S.; Glassman, M. J.; Olsen, B. D., Solid-state nanostructured materials from self-assembly of a globular protein-polymer diblock copolymer. *Acs Nano* **2011**, *5* (7), 5697-5707.
53. Thomas, C. S.; Xu, L. Z.; Olsen, B. D., Kinetically controlled nanostructure formation in self-assembled globular protein-polymer diblock copolymers. *Biomacromolecules* **2012**, *13* (9), 2781-2792.
54. Lam, C. N.; Kim, M.; Thomas, C. S.; Chang, D.; Sanoja, G. E.; Okwara, C. U.; Olsen, B. D., The nature of protein interactions governing globular protein-polymer block copolymer self-assembly. *Biomacromolecules* **2014**, *15* (4), 1248-1258.
55. Huang, A.; Qin, G. K.; Olsen, B. D., Highly active biocatalytic coatings from protein-polymer diblock copolymers. *Acs Applied Materials & Interfaces* **2015**, *7* (27), 14660-14669.
56. van Rijn, P.; Tutus, M.; Kathrein, C.; Mouglin, N. C.; Park, H.; Hein, C.; Schurings, M. P.; Boker, A., Ultra-thin self-assembled protein-polymer membranes: A new pore forming strategy. *Advanced Functional Materials* **2014**, *24* (43), 6762-6770.
57. Suci, P. A.; Klem, M. T.; Arce, F. T.; Douglas, T.; Young, M., Assembly of multilayer films incorporating a viral protein cage architecture. *Langmuir* **2006**, *22* (21), 8891-8896.
58. Kostianen, M. A.; Hiekkataipale, P.; de la Torre, J. A.; Nolte, R. J. M.; Cornelissen, J., Electrostatic self-assembly of virus-polymer complexes. *Journal of Materials Chemistry* **2011**, *21* (7), 2112-2117.

59. Kostiainen, M. A.; Kasyutich, O.; Cornelissen, J.; Nolte, R. J. M., Self-assembly and optically triggered disassembly of hierarchical dendron-virus complexes. *Nature Chemistry* **2010**, *2* (5), 394-399.
60. Liljestrom, V.; Seitsonen, J.; Kostiainen, M. A., Electrostatic self-assembly of soft matter nanoparticle cocrystals with tunable lattice parameters. *Acs Nano* **2015**, *9* (11), 11278-11285.
61. Mohanraj, V.; Chen, Y., Nanoparticles-a review. *Tropical journal of pharmaceutical research* **2006**, *5* (1), 561-573.
62. Schmid, G., *Nanoparticles: From theory to application*. John Wiley & Sons: **2011**.
63. Kulkarni, N.; Muddapur, U., Biosynthesis of metal nanoparticles: A review. *Journal of Nanotechnology* **2014**, 2014.
64. Hasan, S., A review on nanoparticles: Their synthesis and types. *Res. J. Recent Sci* **2015**, *2277*, 2502.
65. Tiwari, D. K.; Behari, J.; Sen, P., Application of nanoparticles in waste water treatment 1. **2008**.
66. Ravishankar Rai, V., Nanoparticles and their potential application as antimicrobials. **2011**.
67. Li, Y.; Kröger, M.; Liu, W. K., Nanoparticle geometrical effect on structure, dynamics and anisotropic viscosity of polyethylene nanocomposites. *Macromolecules* **2012**, *45* (4), 2099-2112.
68. Wei, H.; Hao, F.; Huang, Y.; Wang, W.; Nordlander, P.; Xu, H., Polarization dependence of surface-enhanced raman scattering in gold nanoparticle– nanowire systems. *Nano Letters* **2008**, *8* (8), 2497-2502.
69. Beydoun, D.; Amal, R.; Low, G.; McEvoy, S., Role of nanoparticles in photocatalysis. *Journal of Nanoparticle Research* **1999**, *1* (4), 439-458.
70. Welch, C. M.; Compton, R. G., The use of nanoparticles in electroanalysis: A review. *Analytical and bioanalytical chemistry* **2006**, *384* (3), 601-619.
71. Doria, G.; Conde, J.; Veigas, B.; Giestas, L.; Almeida, C.; Assunção, M.; Rosa, J.; Baptista, P. V., Noble metal nanoparticles for biosensing applications. *Sensors* **2012**, *12* (2), 1657-1687.

72. Zeng, S.; Yong, K.-T.; Roy, I.; Dinh, X.-Q.; Yu, X.; Luan, F., A review on functionalized gold nanoparticles for biosensing applications. *Plasmonics* **2011**, *6* (3), 491.
73. Kairdolf, B. A.; Qian, X.; Nie, S., Bioconjugated nanoparticles for biosensing, in vivo imaging, and medical diagnostics. *Analytical chemistry* **2017**, *89* (2), 1015-1031.
74. Mamaeva, V.; Sahlgren, C.; Lindén, M., Mesoporous silica nanoparticles in medicine—recent advances. *Advanced Drug Delivery Reviews* **2013**, *65* (5), 689-702.
75. Yildiz, I.; Shukla, S.; Steinmetz, N. F., Applications of viral nanoparticles in medicine. *Current Opinion in Biotechnology* **2011**, *22* (6), 901-908.
76. Zhang, L.; Gu, F.; Chan, J.; Wang, A.; Langer, R.; Farokhzad, O., Nanoparticles in medicine: Therapeutic applications and developments. *Clinical pharmacology & therapeutics* **2008**, *83* (5), 761-769.
77. Zhou, Y.; Peng, Z.; Seven, E. S.; Leblanc, R. M., Crossing the blood-brain barrier with nanoparticles. *Journal of controlled release* **2018**, *270*, 290-303.
78. Lohse, S. E.; Murphy, C. J., Applications of colloidal inorganic nanoparticles: From medicine to energy. *Journal of the American Chemical Society* **2012**, *134* (38), 15607-15620.
79. Kang, Y.; Zhou, L.; Li, X.; Yuan, J., B-cyclodextrin-modified hybrid magnetic nanoparticles for catalysis and adsorption. *Journal of Materials Chemistry* **2011**, *21* (11), 3704-3710.
80. Li, Y.; Fan, X.; Qi, J.; Ji, J.; Wang, S.; Zhang, G.; Zhang, F., Gold nanoparticles–graphene hybrids as active catalysts for suzuki reaction. *Materials Research Bulletin* **2010**, *45* (10), 1413-1418.
81. Astruc, D., *Nanoparticles and catalysis*. John Wiley & Sons: 2008.
82. Lam, E.; Hrapovic, S.; Majid, E.; Chong, J. H.; Luong, J. H., Catalysis using gold nanoparticles decorated on nanocrystalline cellulose. *Nanoscale* **2012**, *4* (3), 997-1002.
83. Elzoghby, A. O.; Hemasa, A. L.; Freag, M. S., Hybrid protein-inorganic nanoparticles: From tumor-targeted drug delivery to cancer imaging. *Journal of controlled release* **2016**, *243*, 303-322.

84. Sailor, M. J.; Park, J. H., Hybrid nanoparticles for detection and treatment of cancer. *Advanced Materials* **2012**, *24* (28), 3779-3802.
85. Molino, N. M.; Wang, S.-W., Caged protein nanoparticles for drug delivery. *Current Opinion in Biotechnology* **2014**, *28*, 75-82.
86. Abe, S.; Ueno, T., Design of protein crystals in the development of solid biomaterials. *Rsc Advances* **2015**, *5* (27), 21366-21375.
87. Deschaume, O.; De Roo, B.; Van Bael, M. J.; Locquet, J. P.; Van Haesendonck, C.; Bartic, C., Synthesis and properties of gold nanoparticle arrays self-organized on surface-deposited lysozyme amyloid scaffolds. *Chemistry of Materials* **2014**, *26* (18), 5383-5393.
88. Kowalski, A. E.; Huber, T. R.; Ni, T. W.; Hartje, L. F.; Appel, K. L.; Yost, J. W.; Ackerson, C. J.; Snow, C. D., Gold nanoparticle capture within protein crystal scaffolds. *Nanoscale* **2016**, *8* (25), 12693-12696.
89. Srivastava, S.; Samanta, B.; Jordan, B. J.; Hong, R.; Xiao, Q.; Tuominen, M. T.; Rotello, V. M., Integrated magnetic bionanocomposites through nanoparticle-mediated assembly of ferritin. *Journal of the American Chemical Society* **2007**, *129* (38), 11776-11780.
90. Zhang, L.; Bailey, J. B.; Subramanian, R. H.; Tezcan, F. A., Hyperexpandable, self-healing macromolecular crystals with integrated polymer networks. *Nature* **2018**, *557* (7703), 86-91.
91. Zhang, J. T.; Zhou, K.; Zhang, Y. J.; Du, M. M.; Wang, Q. B., Precise self-assembly of nanoparticles into ordered nanoarchitectures directed by tobacco mosaic virus coat protein. *Advanced Materials* **2019**, *31* (23), 9.
92. Nikitin, M. P.; Zdobnova, T. A.; Lukash, S. V.; Stremovskiy, O. A.; Deyev, S. M., Protein-assisted self-assembly of multifunctional nanoparticles. *Proceedings of the National Academy of Sciences* **2010**, *107* (13), 5827-5832.
93. Park, S. J.; Lazarides, A. A.; Mirkin, C. A.; Letsinger, R. L., Directed assembly of periodic materials from protein and oligonucleotide-modified nanoparticle building blocks. *Angewandte Chemie International Edition* **2001**, *40* (15), 2909-2912.
94. Wei, H.; Wang, Z. D.; Zhang, J.; House, S.; Gao, Y. G.; Yang, L. M.; Robinson, H.; Tan, L. H.; Xing, H.; Hou, C. J.; Robertson, I. M.; Zuo, J. M.; Lu, Y., Time-dependent, protein-directed

growth of gold nanoparticles within a single crystal of lysozyme. *Nature Nanotechnology* **2011**, *6* (2), 93-97.

95. Allred, D. B.; Sarikaya, M.; Baneyx, F.; Schwartz, D. T., Electrochemical nanofabrication using crystalline protein masks. *Nano Letters* **2005**, *5* (4), 609-613.

96. Dannhauser, P. N.; Platen, M.; Boning, H.; Schaap, I. A. T., Durable protein lattices of clathrin that can be functionalized with nanoparticles and active biomolecules. *Nature Nanotechnology* **2015**, *10* (11), 954-U194.

97. Suzuki, Y.; Cardone, G.; Restrepo, D.; Zavattieri, P. D.; Baker, T. S.; Tezcan, F. A., Self-assembly of coherently dynamic, auxetic, two-dimensional protein crystals. *Nature* **2016**, *533* (7603), 369-373.

98. Alberstein, R.; Suzuki, Y.; Paesani, F.; Tezcan, F. A., Engineering the entropy-driven free-energy landscape of a dynamic nanoporous protein assembly. *Nature Chemistry* **2018**, *10* (7), 732-739.

99. Du, M. M.; Zhu, K.; Wang, X.; Zhang, J. T.; Zhang, Y. J.; Dong, J. C.; Wu, L. L.; Qiao, Z.; Chen, G.; Wang, C. B., Precise fabrication of de novo nanoparticle lattices on dynamic 2d protein crystalline lattices. *Nano Letters* **2020**, *20* (2), 1154-1160.

100. Cheung-Lau, J. C.; Liu, D.; Pulsipher, K. W.; Liu, W. R.; Dmochowski, I. J., Engineering a well-ordered, functional protein-gold nanoparticle assembly. *Journal of Inorganic Biochemistry* **2014**, *130*, 59-68.

101. Okuda, M.; Eloi, J. C.; Jones, S. E. W.; Sarua, A.; Richardson, R. M.; Schwarzacher, W., Fe₃O₄ nanoparticles: Protein-mediated crystalline magnetic superstructures. *Nanotechnology* **2012**, *23* (41), 7.

102. Kunzle, M.; Eckert, T.; Beck, T., Binary protein crystals for the assembly of inorganic nanoparticle superlattices. *Journal of the American Chemical Society* **2016**, *138* (39), 12731-12734.

103. Zhang, L.; Bailey, J. B.; Subramanian, R. H.; Groisman, A.; Tezcan, F. A., Hyperexpandable, self-healing macromolecular crystals with integrated polymer networks (vol 560, e31, 2018). *Nature* **2018**, *560* (7719), 1.

104. Badia, A.; Carlini, R.; Fernandez, A.; Battaglini, F.; Mikkelsen, S. R.; English, A. M., Intramolecular electron-transfer rates in ferrocene-derivatized glucose-oxidase. *Journal of the American Chemical Society* **1993**, *115* (16), 7053-7060.
105. Xiao, Y.; Patolsky, F.; Katz, E.; Hainfeld, J. F.; Willner, I., "Plugging into enzymes": Nanowiring of redox enzymes by a gold nanoparticle. *Science* **2003**, *299* (5614), 1877-1881.
106. Jensen, P. S.; Chi, Q.; Grumsen, F. B.; Abad, J. M.; Horsewell, A.; Schiffrin, D. J.; Ulstrup, J., Gold nanoparticle assisted assembly of a heme protein for enhancement of long-range interfacial electron transfer. *Journal of Physical Chemistry C* **2007**, *111* (16), 6124-6132.
107. Bonk, S. M.; Lisdat, F., Layer-by-layer assembly of electro-active gold nanoparticle/cytochrome c multilayers. *Biosensors & Bioelectronics* **2009**, *25* (4), 739-744.
108. Wang, S. P.; Mamedova, N.; Kotov, N. A.; Chen, W.; Studer, J., Antigen/antibody immunocomplex from cdte nanoparticle bioconjugates. *Nano Letters* **2002**, *2* (8), 817-822.
109. Pantarotto, D.; Partidos, C. D.; Hoebeke, J.; Brown, F.; Kramer, E.; Briand, J. P.; Muller, S.; Prato, M.; Bianco, A., Immunization with peptide-functionalized carbon nanotubes enhances virus-specific neutralizing antibody responses. *Chemistry & Biology* **2003**, *10* (10), 961-966.
110. Nam, J. M.; Thaxton, C. S.; Mirkin, C. A., Nanoparticle-based bio-bar codes for the ultrasensitive detection of proteins. *Science* **2003**, *301* (5641), 1884-1886.
111. Ma, J.; Wong, H. F.; Kong, L. B.; Peng, K. W., Biomimetic processing of nanocrystallite bioactive apatite coating on titanium. *Nanotechnology* **2003**, *14* (6), 619-623.
112. Shinkai, M.; Yanase, M.; Suzuki, M.; Honda, H.; Wakabayashi, T.; Yoshida, J.; Kobayashi, T., Intracellular hyperthermia for cancer using magnetite cationic liposomes. *Journal of Magnetism and Magnetic Materials* **1999**, *194* (1-3), 176-184.
113. Weissleder, R.; Elizondo, G.; Wittenberg, J.; Rabito, C. A.; Bengel, H. H.; Josephson, L., Ultrasmall superparamagnetic iron-oxide - characterization of a new class of contrast agents for mr imaging. *Radiology* **1990**, *175* (2), 489-493.
114. Kapur, A.; Aldeek, F.; Ji, X.; Safi, M.; Wang, W. T.; Del Cid, A.; Steinbock, O.; Mattoussi, H., Self-assembled gold nanoparticle-fluorescent protein conjugates as platforms for sensing thiolate compounds via modulation of energy transfer quenching. *Bioconjugate Chemistry* **2017**, *28* (2), 678-687.

115. Wang, J.; Zhang, Y.; Jin, N.; Mao, C. B.; Yang, M. Y., Protein-induced gold nanoparticle assembly for improving the photothermal effect in cancer therapy. *Acs Applied Materials & Interfaces* **2019**, *11* (12), 11136-11143.
116. Xie, J. B.; Mei, L.; Huang, K.; Sun, Y. X.; Iris, A.; Ma, B. L.; Qiu, Y. N.; Li, J. J.; Han, G., A photo-inducible protein-inorganic nanoparticle assembly for active targeted tumour theranostics. *Nanoscale* **2019**, *11* (13), 6136-6144.
117. Valero, E.; Tambalo, S.; Marzola, P.; Ortega-Munoz, M.; Lopez-Jaramillo, F. J.; Santoyo-Gonzalez, F.; Lopez, J. D.; Delgado, J. J.; Calvino, J. J.; Cuesta, R.; Dominguez-Vera, J. M.; Galvez, N., Magnetic nanoparticles-templated assembly of protein subunits: A new platform for carbohydrate-based mri nanoprobos. *Journal of the American Chemical Society* **2011**, *133* (13), 4889-4895.
118. Ghosh, D.; Lee, Y.; Thomas, S.; Kohli, A. G.; Yun, D. S.; Belcher, A. M.; Kelly, K. A., M13-templated magnetic nanoparticles for targeted in vivo imaging of prostate cancer. *Nature Nanotechnology* **2012**, *7* (10), 677-682.
119. Shih, W. M.; Quispe, J. D.; Joyce, G. F., A 1.7-kilobase single-stranded DNA that folds into a nanoscale octahedron. *Nature* **2004**, *427* (6975), 618-621.
120. Yurke, B.; Turberfield, A. J.; Mills, A. P.; Simmel, F. C.; Neumann, J. L., A DNA-fuelled molecular machine made of DNA. *Nature* **2000**, *406* (6796), 605-608.
121. Yan, H.; Zhang, X. P.; Shen, Z. Y.; Seeman, N. C., A robust DNA mechanical device controlled by hybridization topology. *Nature* **2002**, *415* (6867), 62-65.
122. Mitchell, J. C.; Harris, J. R.; Malo, J.; Bath, J.; Turberfield, A. J., Self-assembly of chiral DNA nanotubes. *Journal of the American Chemical Society* **2004**, *126* (50), 16342-16343.
123. LaBean, T. H.; Yan, H.; Kopatsch, J.; Liu, F. R.; Winfree, E.; Reif, J. H.; Seeman, N. C., Construction, analysis, ligation, and self-assembly of DNA triple crossover complexes. *Journal of the American Chemical Society* **2000**, *122* (9), 1848-1860.
124. Wang, F.; Willner, B.; Willner, I., DNA nanotechnology with one-dimensional self-assembled nanostructures. *Current Opinion in Biotechnology* **2013**, *24* (4), 562-574.
125. Winfree, E.; Liu, F. R.; Wenzler, L. A.; Seeman, N. C., Design and self-assembly of two-dimensional DNA crystals. *Nature* **1998**, *394* (6693), 539-544.

126. Yan, H.; Park, S. H.; Finkelstein, G.; Reif, J. H.; LaBean, T. H., DNA-templated self-assembly of protein arrays and highly conductive nanowires. *Science* **2003**, *301* (5641), 1882-1884.
127. Feng, L. P.; Park, S. H.; Reif, J. H.; Yan, H., A two-state DNA lattice switched by DNA nanoactuator. *Angewandte Chemie-International Edition* **2003**, *42* (36), 4342-4346.
128. Seeman, N. C., DNA in a material world. *Nature* **2003**, *421* (6921), 427-431.
129. Han, D.; Pal, S.; Nangreave, J.; Deng, Z.; Liu, Y.; Yan, H., DNA origami with complex curvatures in three-dimensional space. *Science* **2011**, *332* (6027), 342-346.
130. Zhou, Y. B.; Gerchman, S. E.; Ramakrishnan, V.; Travers, A.; Muyldermans, S., Position and orientation of the globular domain of linker histone h5 on the nucleosome. *Nature* **1998**, *395* (6700), 402-405.
131. Durniak, K. J.; Bailey, S.; Steitz, T. A., The structure of a transcribing t7 rna polymerase in transition from initiation to elongation. *Science* **2008**, *322* (5901), 553-557.
132. Nishimasu, H.; Ran, F. A.; Hsu, P. D.; Konermann, S.; Shehata, S. I.; Dohmae, N.; Ishitani, R.; Zhang, F.; Nureki, O., Crystal structure of cas9 in complex with guide rna and target DNA. *Cell* **2014**, *156* (5), 935-949.
133. Li, X.; Yang, D. L.; Shen, L. Y.; Xu, F.; Wang, P. F., Programmable assembly of DNA-protein hybrid structures. *Chemical Research in Chinese Universities* **2020**, *36* (2), 211-218.
134. Zhang, F.; Nangreave, J.; Liu, Y.; Yan, H., Structural DNA nanotechnology: State of the art and future perspective. *Journal of the American Chemical Society* **2014**, *136* (32), 11198-11211.
135. Seeman, N. C., DNA nicks and nodes and nanotechnology. *Nano Letters* **2001**, *1* (1), 22-26.
136. Ke, Y.; Ong, L. L.; Shih, W. M.; Yin, P., Three-dimensional structures self-assembled from DNA bricks. *Science* **2012**, *338* (6111), 1177-1183.
137. Kaushik, M.; Kaushik, S.; Roy, K.; Singh, A.; Mahendru, S.; Kumar, M.; Chaudhary, S.; Ahmed, S.; Kukreti, S., A bouquet of DNA structures: Emerging diversity. *Biochemistry and biophysics reports* **2016**, *5*, 388-395.

138. Carroll, S. B.; Grenier, J. K.; Weatherbee, S. D., *From DNA to diversity: Molecular genetics and the evolution of animal design*. John Wiley & Sons: 2013.
139. Hong, C. A.; Eltoukhy, A. A.; Lee, H.; Langer, R.; Anderson, D. G.; Nam, Y. S., Dendrimeric sirna for efficient gene silencing. *Angewandte Chemie-International Edition* **2015**, *54* (23), 6740-6744.
140. Kim, K. R.; Kim, D. R.; Lee, T.; Yhee, J. Y.; Kim, B. S.; Kwon, I. C.; Ahn, D. R., Drug delivery by a self-assembled DNA tetrahedron for overcoming drug resistance in breast cancer cells. *Chemical Communications* **2013**, *49* (20), 2010-2012.
141. Rosenzweig, B. A.; Ross, N. T.; Tagore, D. M.; Jayawickramarajah, J.; Saraogi, I.; Hamilton, A. D., Multivalent protein binding and precipitation by self-assembling molecules on a DNA pentaplex scaffold. *Journal of the American Chemical Society* **2009**, *131* (14), 5020-5021.
142. Agback, P.; Baumann, H.; Knapp, S.; Ladenstein, R.; Hard, T., Architecture of nonspecific protein-DNA interactions in the sso7d-DNA complex. *Nature Structural Biology* **1998**, *5* (7), 579-584.
143. Rothmund, P. W. K., Folding DNA to create nanoscale shapes and patterns. *Nature* **2006**, *440* (7082), 297-302.
144. Zhang, C.; Tian, C.; Guo, F.; Liu, Z.; Jiang, W.; Mao, C., DNA-directed three-dimensional protein organization. *Angewandte Chemie-International Edition* **2012**, *51* (14), 3382-3385.
145. Malo, J.; Mitchell, J. C.; Venien-Bryan, C.; Harris, J. R.; Wille, H.; Sherratt, D. J.; Turberfield, A. J., Engineering a 2d protein-DNA crystal. *Angewandte Chemie-International Edition* **2005**, *44* (20), 3057-3061.
146. Padilla, J. E.; Colovos, C.; Yeates, T. O., Nanohedra: Using symmetry to design self assembling protein cages, layers, crystals, and filaments. *Proceedings of the National Academy of Sciences of the United States of America* **2001**, *98* (5), 2217-2221.
147. Bale, J. B.; Gonen, S.; Liu, Y. X.; Sheffler, W.; Ellis, D.; Thomas, C.; Cascio, D.; Yeates, T. O.; Gonen, T.; King, N. P.; Baker, D., Accurate design of megadalton-scale two-component icosahedral protein complexes. *Science* **2016**, *353* (6297), 389-394.
148. Butterfield, G. L.; Lajoie, M. J.; Gustafson, H. H.; Sellers, D. L.; Nattermann, U.; Ellis, D.; Bale, J. B.; Ke, S.; Lenz, G. H.; Yehdego, A.; Ravichandran, R.; Pun, S. H.; King, N. P.; Baker,

D., Evolution of a designed protein assembly encapsulating its own rna genome. *Nature* **2017**, 552 (7685), 415-420.

149. Mou, Y.; Yu, J.-Y.; Wannier, T. M.; Guo, C.-L.; Mayo, S. L., Computational design of co-assembling protein-DNA nanowires. *Nature* **2015**, 525 (7568), 230-233.

150. Brodin, J. D.; Auyeung, E.; Mirkin, C. A., DNA-mediated engineering of multicomponent enzyme crystals. *Proceedings of the National Academy of Sciences of the United States of America* **2015**, 112 (15), 4564-4569.

151. McMillan, J. R.; Brodin, J. D.; Millan, J. A.; Lee, B.; de la Cruz, M. O.; Mirkin, C. A., Modulating nanoparticle superlattice structure using proteins with tunable bond distributions. *Journal of the American Chemical Society* **2017**, 139 (5), 1754-1757.

152. Subramanian, R. H.; Smith, S. J.; Alberstein, R. G.; Bailey, J. B.; Zhang, L.; Cardone, G.; Suominen, L.; Chami, M.; Stahlberg, H.; Baker, T. S.; Tezcan, F. A., Self-assembly of a designed nucleoprotein architecture through multimodal interactions. *Acs Central Science* **2018**, 4 (11), 1578-1586.

153. Dutta, P. K.; Levenberg, S.; Loskutov, A.; Jun, D.; Saer, R.; Beatty, J. T.; Lin, S.; Liu, Y.; Woodbury, N. W.; Yan, H., A DNA-directed light-harvesting/reaction center system. *Journal of the American Chemical Society* **2014**, 136 (47), 16618-16625.

154. Kashiwagi, D.; Sim, S.; Niwa, T.; Taguchi, H.; Aida, T., Protein nanotube selectively cleavable with DNA: Supramolecular polymerization of "DNA-appended molecular chaperones". *Journal of the American Chemical Society* **2018**, 140 (1), 26-29.

155. Ryu, Y.; Hong, C. A.; Song, Y.; Beak, H.; Seo, B. A.; Lee, L. J.; Kim, H. S., Modular protein-DNA hybrid nanostructures as a drug delivery platform. *Nanoscale* **2020**, 12 (8), 4975-4981.

Chapter 2 : Hyperexpandable, self-healing macromolecular crystals with integrated polymer networks

2.1 Abstract

The formation of condensed matter typically involves a tradeoff between structural order and flexibility. As the extent and directionality of interactions between atomic or molecular components increase, materials generally become more ordered but less compliant, and vice versa. Nevertheless, high levels of structural order and flexibility are not necessarily mutually exclusive; there are many biological (such as microtubules,¹⁻² flagella,³ viruses⁴⁻⁵) and synthetic assemblies (for example, dynamic molecular crystals⁶⁻⁹ and frameworks¹⁰⁻¹³) that can undergo considerable structural transformations without losing their crystalline order and that have remarkable mechanical properties^{8,14-15} that are useful in diverse applications, such as selective sorption,¹⁶ separation,¹⁷ sensing,¹⁸ and mechanoactuation.¹⁹ However, the extent of structural changes and the elasticity of such flexible crystals are constrained by the necessity to maintain a continuous network of bonding interactions between the constituents of the lattice. Consequently, even the most dynamic porous materials tend to be brittle and isolated as microcrystalline powders,¹⁴ whereas flexible organic or inorganic molecular crystals cannot expand without fracturing. Owing to their rigidity, crystalline materials rarely display self-healing behavior.²⁰ Here we report that macromolecular ferritin crystals with integrated hydrogel polymers can isotropically expand to 180 percent of their original dimensions and more than 500 percent of their original volume while retaining periodic order and faceted Wulff morphologies. Even after the separation of neighboring ferritin molecules by 50 ångströms upon lattice expansion, specific molecular contacts between them can be reformed upon lattice contraction, resulting in the recovery of atomic-level periodicity and the highest-resolution ferritin structure reported so far. Dynamic bonding interactions between

the hydrogel network and the ferritin molecules endow the crystals with the ability to resist fragmentation and self-heal efficiently, whereas the chemical tailorability of the ferritin molecules enables the creation of chemically and mechanically differentiated domains within single crystals.

2.2 Introduction

Hydrogel polymers present a stark contrast to molecular crystals in that they lack structural order, but are highly elastic and adaptive, can expand considerably and self-heal when equipped with dynamic bonding functionalities.²¹⁻²² Previously, the isotropic swelling–contraction behavior of hydrogels has been used to modulate the lattice spacing of colloidal nanoparticle arrays,²³ and recently, to expand biological tissue samples and thus facilitate high-resolution fluorescence imaging.²⁴ In this study, we examine whether the mechanical properties of hydrogels could be endowed upon molecular crystals. That is, can crystal lattices that are formed by discrete molecules that are connected via specific bonding interactions be mechanically modulated through the integration of polymeric hydrogels? To create hydrogel-expandable molecular crystals, we surmised that the following design parameter conditions should be met: (1) lattices should be mesoporous to enable the hydrogel network to penetrate efficiently and uniformly into the crystals; (2) intermolecular interactions between the constituents of the lattices should be reversible and chemically specific (that is, contain directional and dynamic bonds), such that they disengage with ease during expansion and re-engage with high fidelity upon contraction; (3) interactions between the constituents of the lattice and the hydrogel network should be extensive to maintain the integrity of the crystal–polymer hybrid at all times and sufficiently dynamic to minimize the build-up of local strain and to enable self-healing.

With these parameters in mind, we arrived at hybrid materials composed of ferritin crystals integrated with the superabsorbent poly(acrylate–acrylamide) (p(Ac–Am)) copolymer hydrogels,

whose swelling–contraction behavior can be modulated by the ionic strength and pH.²⁵ Ferritin is a 24-meric, quasi-spherical protein with 432 symmetry, an outer diameter of 12 nm, an inner diameter of 8 nm, and a molecular weight²⁶ of more than 500,000 Da. Human heavy-chain ferritin forms highly ordered, face-centered cubic (*fcc*) crystals that routinely grow to more than 200 μm in size and diffract to less than 2.0 Å. The *fcc* lattice (**Figure 2.1a**) is characterized by a mesoporous network consisting of cube-shaped, 6-nm-wide chambers (**Figure 2.1b**) that are interconnected by smaller, octahedron-shaped cavities that taper to a pore size of about 2 nm at their narrowest (**Figure 2.1c**), thus fulfilling condition (1). The lattice is formed through highly specific, metal-mediated contacts between neighboring ferritin molecules (**Figure 2.1d**), which are promoted through the K86Q surface mutation to enable metal coordination²⁷. The absence of any other interprotein contacts means that the entire lattice bonding framework of ferritin molecules can be formed or broken via binding or removal of metal ions (such as Ca^{2+}), satisfying condition (2). Finally, ferritin bears a small negative charge, with a zeta potential ranging from -5.5 mV at pH 6.0 to -7.3 mV at pH 7.5 (**Figure 2.2a, b**). The exterior surface of ferritin presents a diffuse distribution of both negatively and positively charged residues (**Figure 2.2c**), which should enable uniform association with the p(Ac–Am) network through a combination of ionic and H-bonding interactions, thus fulfilling condition (3) (**Figure 2.1e**).

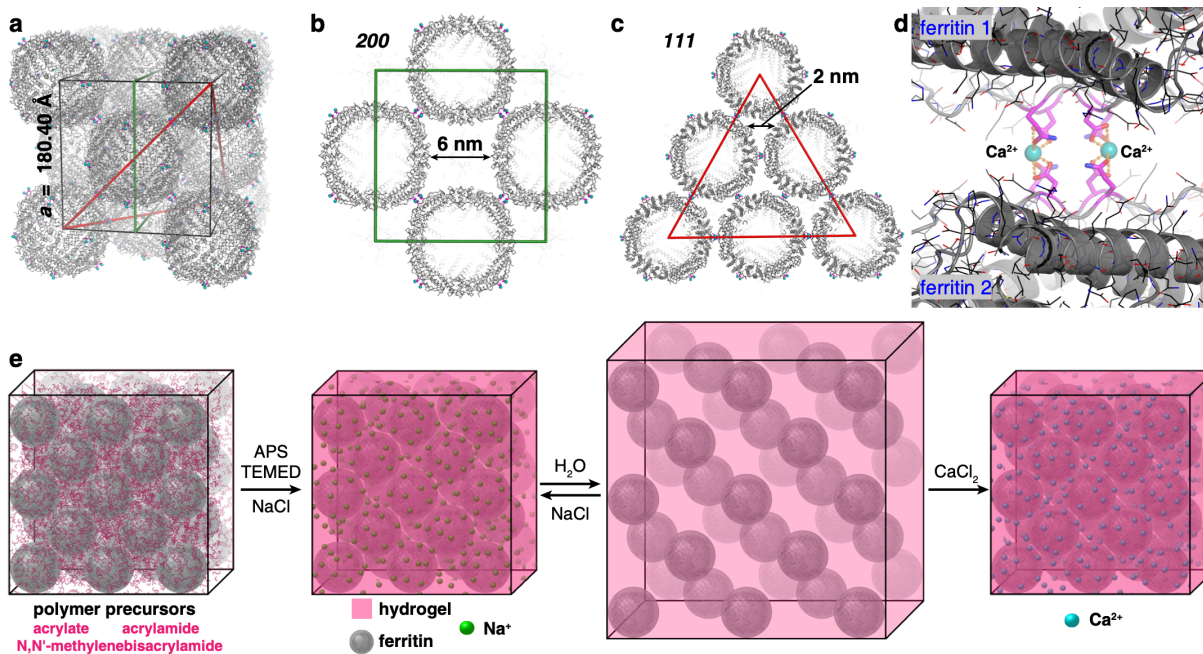


Figure 2.1 | Packing arrangement in ferritin crystals and their expansion–contraction mediated by the infused hydrogel network. a–c, The *fcc* packing arrangement of ferritin crystals (Protein Data Bank identifier, PDB ID, 6B8F). The unit cell, the 200 plane, and the 111 plane are outlined in black, green, and red, respectively. d, Ca-mediated intermolecular interactions between ferritin molecules in the lattice. Ca^{2+} ions (blue) are coordinated by two pairs of D84 and Q86 sidechains (magenta). e, Schematic representation of the formation, expansion and contraction of ferritin crystal–hydrogel hybrids.

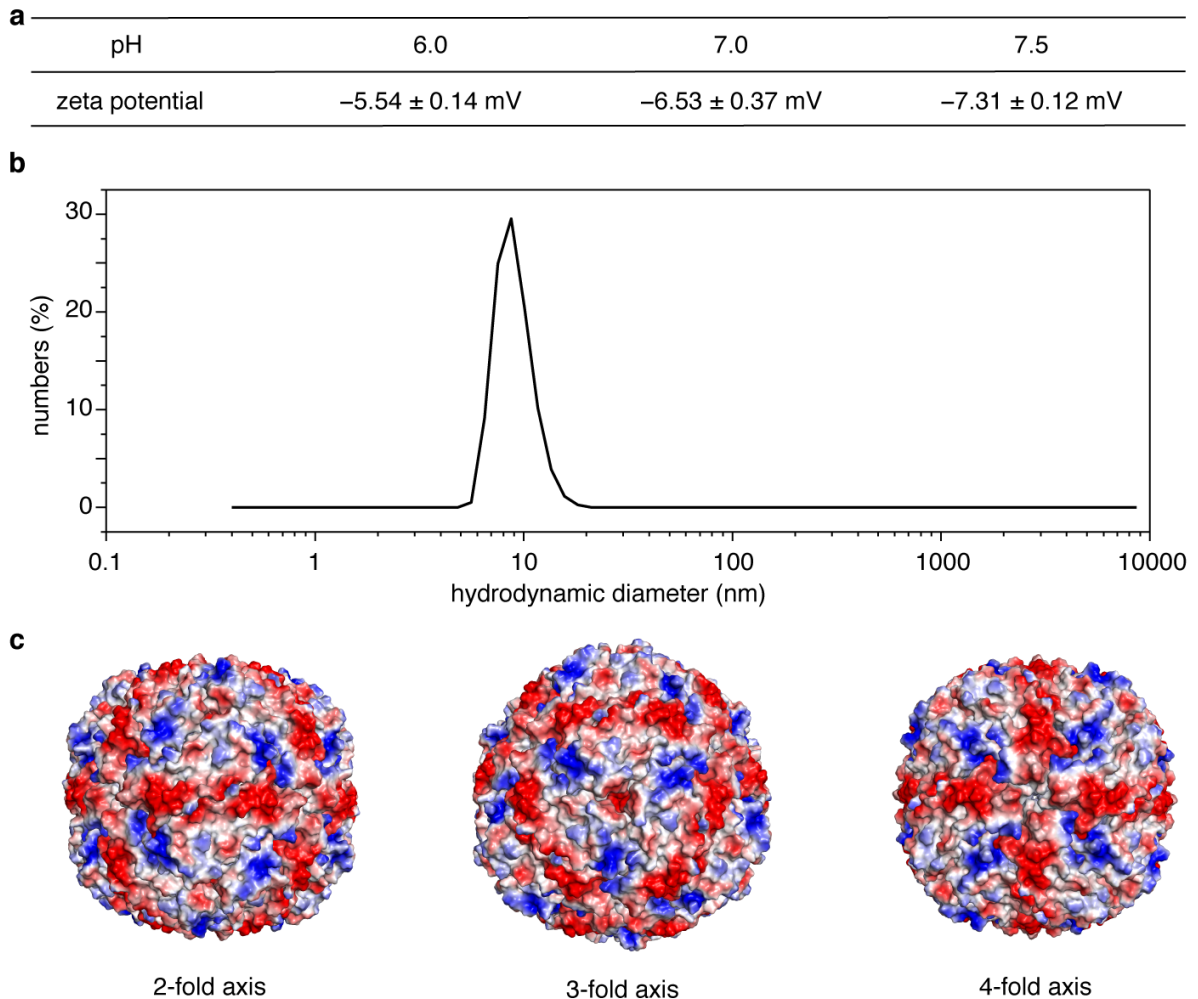


Figure 2.2 | Distribution of electrostatic charge on the surface of ferritin and size distribution of ferritin in solution. **a**, pH-dependent zeta potentials of ferritin, determined by dynamic-light-scattering measurements. **b**, Dynamic-light-scattering profile of ferritin (200 μ M) in a solution of 50 mM HEPES (pH 7.0). **c**, Representation of the electrostatic charge distribution on the ferritin surface, as viewed along the two-, three- and four-fold symmetry axes. Positive ($+5 k_B T/e$) and negative ($-5 k_B T/e$) charges are shown in blue and red, respectively. k_B , Boltzmann constant; e , electron charge.

2.3 Results

2.3.1 Polymer formation inside the crystal lattice

We first examined the efficiency of molecular diffusion and polymerization within ferritin crystals. Diffusion into single ferritin crystals was assessed using the fluorescent tracer rhodamine B by confocal fluorescence microscopy experiments. These experiments showed that a typical crystal (edge length, $l_{\text{edge}} = 50\text{--}250\ \mu\text{m}$) was completely infiltrated by rhodamine B (**Figure 2.3a**), which is considerably larger ($479\ \text{g mol}^{-1}$) than the Ac and Am molecules (both $71\ \text{g mol}^{-1}$), within 15 min. In a typical preparation of crystal–hydrogel hybrids, ferritin crystals were incubated with polymer precursors (8.625% sodium acrylate, 2.5% acrylamide and 0.2% N,N'-methylenebis(acrylamide), w/v) for at least 10 h to ensure their uniform distribution in the lattice interstices. This treatment caused no apparent damage to the crystals (see Supplementary Information for quantification of polymer precursor concentrations inside the crystals). Crystals were then transferred into a solution containing 1% (w/v) ammonium persulfate (APS) and 1% (v/v) tetramethylethylenediamine (TEMED) to initiate free-radical polymerization within the lattice, as well as 4 M sodium chloride (NaCl) to limit swelling during polymerization (**Figure 2.1e**). To assess the kinetics of polymerization inside the crystals, we added 0.3% (w/v) 8-hydroxypyrene-1,3,6-trisulfonic acid (pyranine) to the aforementioned co-monomer mixture. Pyranine has been reported to become covalently incorporated into the polymer backbone upon radical-mediated crosslinking and undergo a shift²⁸ in its emission maximum from 512 to 420 nm. Thus, the extent of *in crystallo* polymerization could be monitored through the decrease of green fluorescence intensity (emission wavelength $\lambda_{\text{emission}} = 500\text{--}550\ \text{nm}$, excitation wavelength $\lambda_{\text{excitation}} = 488\ \text{nm}$), indicating that hydrogel formation was complete in less than 2 min for a crystal with $l_{\text{edge}} = 70\ \mu\text{m}$ (**Figure 2.3b, c**; see **Figure 2.4** for polymer quantification via ^{19}F nuclear magnetic

resonance, NMR). Polymerization was promptly followed by intrusion of the aqueous NaCl solution into the crystal–hydrogel matrix, which was clearly visualized owing to the difference between the refractive indices of the salt solution ($n_D = 1.3676$) and the matrix ($n_D \approx 1.34$) (**Figure 2.3b**). The solvent permeation process typically finished within 10 min and was accompanied by a small but noticeable enlargement of the crystals ($\leq 5\%$ increase in l_{edge}) (**Figure 2.3c**).

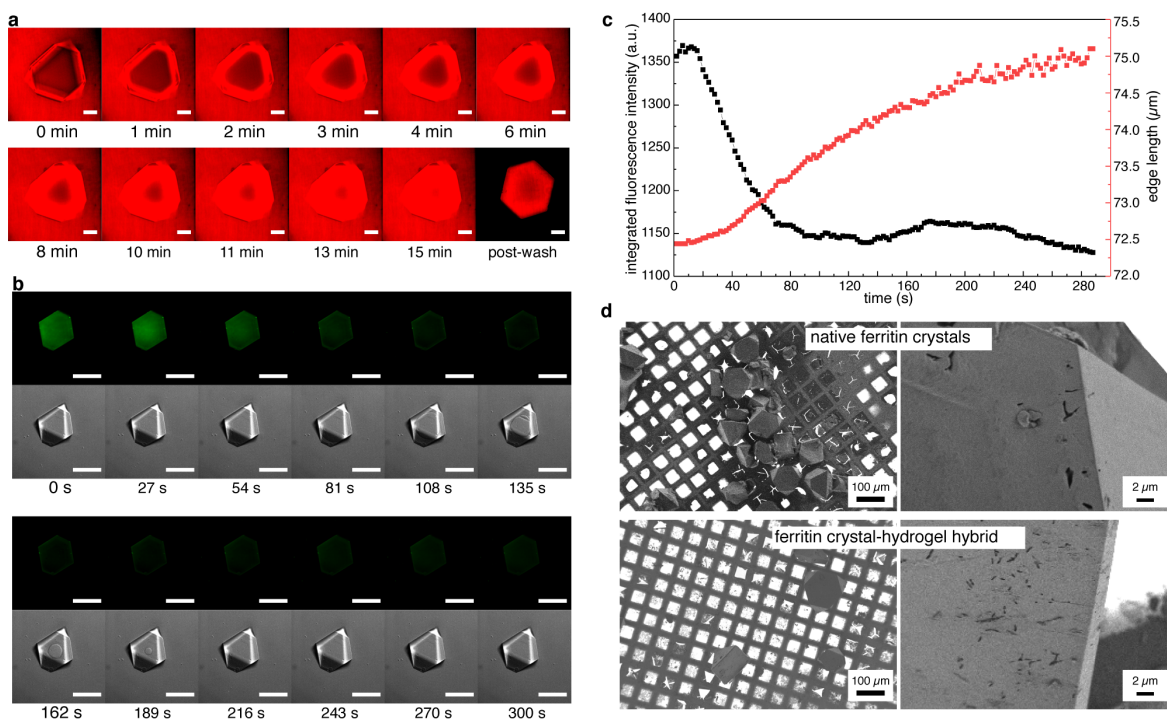


Figure 2.3 | Molecular diffusion and polymerization in ferritin crystals, monitored using confocal microscopy. a, Diffusion of rhodamine B into a ferritin crystal over 15 min. **b, c**, *in crystallo* polymerization of the hydrogel network, monitored through the decrease of integrated pyranine fluorescence (green fluorescence channel). The corresponding bright-field (DIC) images show the diffusion of the aqueous NaCl solution into the crystal. The ring-shaped diffusion front becomes evident at time $t=108$ s and disappears by $t=216$ s. The crystal expands by approximately 5% (edge length) during polymerization. Scale bars in **a** and **b** correspond to 100 μm . **d**, Scanning electron microscopy images of native ferritin crystals (top) and crystal–hydrogel hybrids (bottom).

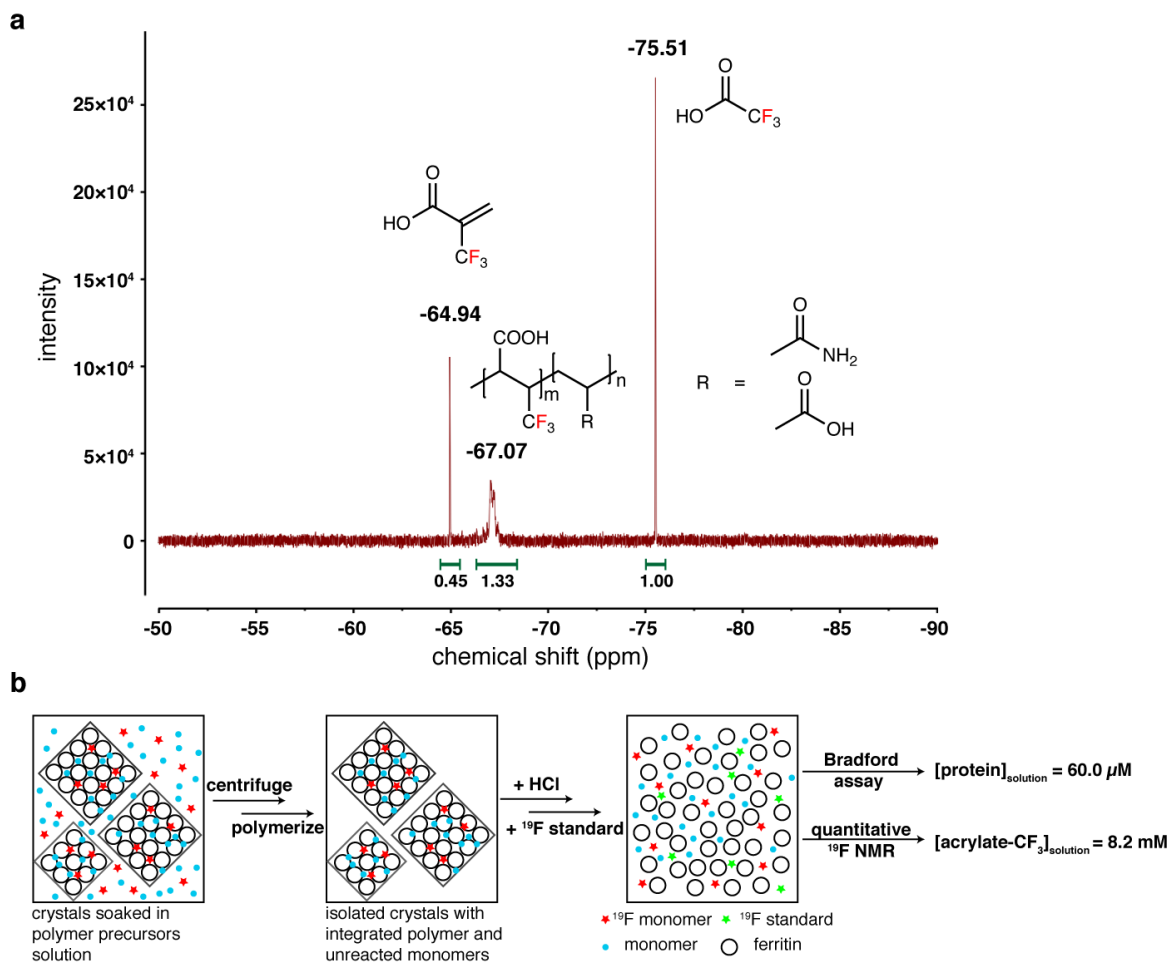


Figure 2.4 | Quantification of an acrylic acid analogue using ^{19}F NMR. **a**, ^{19}F -NMR spectrum, showing peak assignments for the trifluoroacetic acid standard, free 2-(trifluoromethyl)acrylic acid, and 2-(trifluoromethyl)acrylic acid incorporated into the polymer. **b**, Diagram illustrating the experimental protocol for the quantification of 2-(trifluoromethyl)acrylic acid uptake into the crystal lattice. The concentration of 2-(trifluoromethyl)acrylic acid in the crystal lattice (155.6 mM) is approximately the same as its concentration in the soaking solution (see Methods for details).

2.3.2 Characterization of the dynamic behavior of ferritin crystal-hydrogel hybrids

Full expansion of hydrogel-infused ferritin crystals was initiated by placing them in deionized water. As observed using light microscopy, the expansion of the crystals was highly isotropic and their sharply faceted, polyhedral morphologies were preserved even after they grew to $\geq 210\%$ of their original dimensions (**Figure 2.5a** and **Figure 2.6a** and **b** for additional examples), often without the appearance of any defects. The expansion kinetics was biphasic, with time constants $\tau_{\text{fast}} < 100$ s and $\tau_{\text{slow}} \gg 300$ s (**Figure 2.5a**). Isotropic growth continued indefinitely, until the edges of the materials were not discernible, but we typically stopped the process after < 10 min, when considerable expansion had already occurred. No substantial release of ferritin molecules from the lattices was evident during the first 50 min of expansion (**Figure 2.6c**). Addition of a concentrated monovalent salt solution (NaCl or KCl) led to rapid dehydration and isotropic contraction of the expanded crystals to nearly their original size (**Figure 2.5a** and **Figure 2.7a**). Recovery of the original crystal dimensions could be achieved by further addition of CaCl₂, owing to the ability of Ca²⁺ to both screen the negatively charged polymer backbone more effectively and to re-engage specific interactions between ferritin molecules. The same effect was observed with other divalent metal-ion salts (**Figure 2.7b**). The expansion–contraction cycle could be repeated at least eight times without apparent loss in amplitude and change in crystal morphology when a monovalent metal-salt solution was used to induce contraction (**Figure 2.8**). We observed that crystals contracted with CaCl₂ displayed considerably smaller expansion owing to the enhanced strength of the polymer network and protein–protein interactions. In control experiments, we examined other hydrogel formulations, including hydrogels that only contained polar but non-charged (pAm or poly-tris(hydroxymethyl)methyl(acrylamide)) or non-polar (poly-N-isopropylacrylamide) side-chains (**Figure 2.9**). All of these polymers led to either dissolution

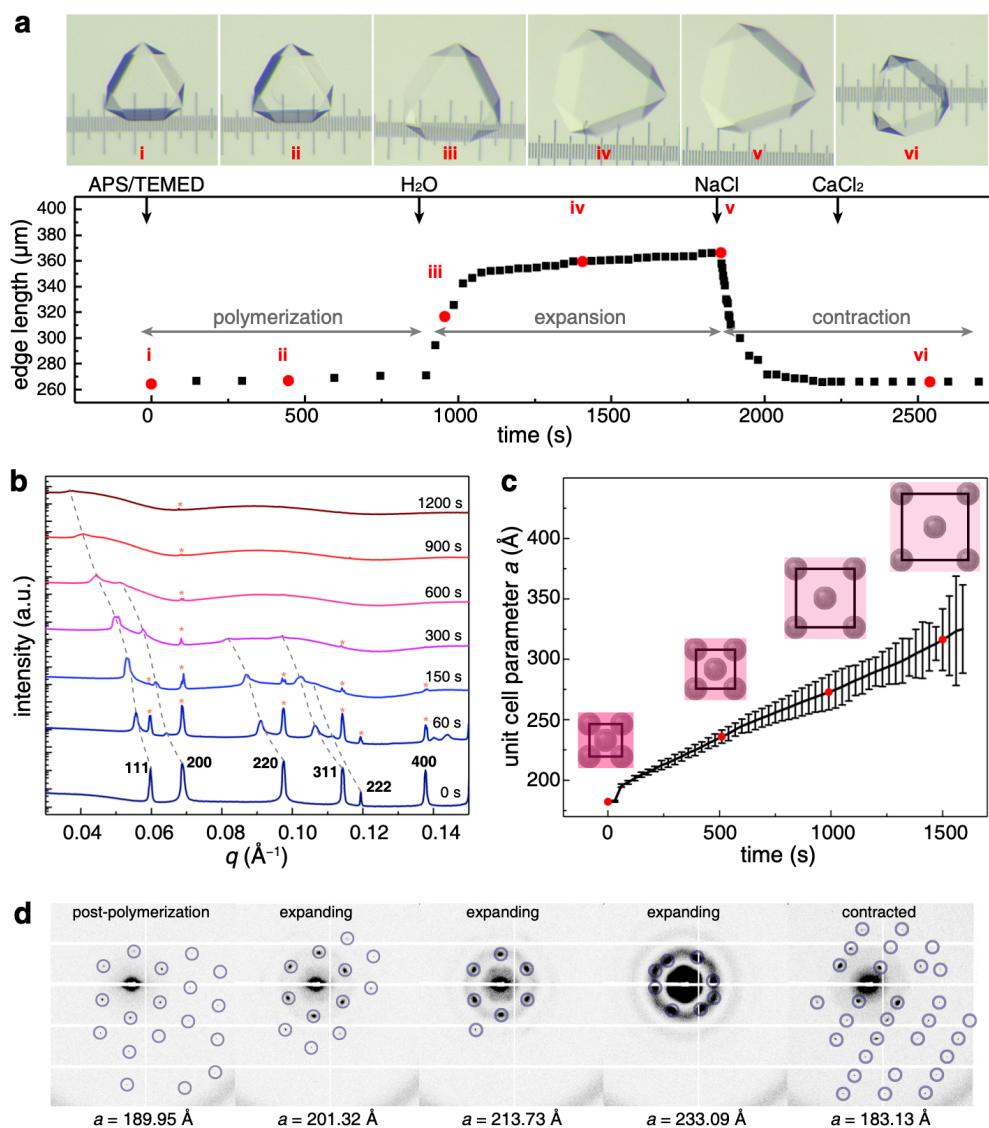


Figure 2.5 | Characterization of the expansion and contraction behaviour of ferritin crystal-hydrogel hybrids. **a**, Structural evolution of a ferritin crystal-hydrogel hybrid during the polymerization-expansion-contraction process. Black arrows indicate the addition of different solutions or water to the crystal. The numbered images (i-vi) in the top panels correspond to the selected time points shown as red circles in the bottom panel. The separation between the major ticks of the ruler is 100 μm . **b**, SAXS profiles of hydrogel-infused ferritin crystals during lattice expansion, plotted against the scattering vector length q . The progression of scattering peaks to lower angles is indicated with grey dashed lines. Peaks corresponding to the original lattice parameters (designated with red asterisks) are visible throughout the process. **c**, Changes in the unit-cell parameter a during lattice expansion, calculated from the SAXS profiles shown in **b**. The schematics correspond to the red circles and are drawn to scale. The error bars were determined from the full-widths at half-maximum of the scattering peaks. **d**, Expansion and contraction of a single crystal, monitored using SAXS.

or disintegration of crystals after initiation of *in crystallo* polymerization, suggesting a lack of substantial interactions between the functional groups on these polymers and on the ferritin surface.

Interestingly, pAc hydrogels promoted isotropic expansion of the crystals in the absence of Am co-monomers (**Figure 2.9**), indicating that carboxylate side-chains are the primary mediators of interactions with ferritin molecules. By contrast, treatment of ferritin crystals with pre-formed pAc polymers, which cannot diffuse into the lattice, led to crystal dissolution upon transfer into water (**Figure 2.9c**). Together, these observations confirm that (i) there are extensive non-covalent interactions between ferritin molecules and the p(Ac–Am) hydrogel matrix that preserve the structural integrity of even highly expanded crystals, and (ii) the hydrogel matrix continuously and uniformly pervades the entire lattice, thus promoting cooperative transmission of any lattice deformations to enable isotropic expansion–contraction. We investigated the expansion-related changes in the lattice arrangement of ferritin molecules using small-angle X-ray scattering (SAXS). Initial experiments entailed bulk measurements of a large number of ferritin crystals suspended in a capillary tube. **Figure 2.5b** shows the evolution of the ‘powder’ SAXS pattern of more than 100 single p(Ac–Am)-infused crystals upon the initiation of polymerization through the addition of APS/TEMED in a solution that contains no salt; thus, polymerization is immediately followed by expansion (see Methods for experimental details). The spectrum of the unexpanded crystals is indicative of an *fcc* lattice with a unit cell parameter of $a = 182.40 \text{ \AA}$. The isotropic growth of the unit cell is evident from the correlated shifts of the Bragg peaks to lower angles. The decay of the higher-angle peaks is considerably more rapid and is accompanied by the emergence of the ferritin form factor. This is consistent with the picture that as the crystal expands, the hydrogel matrix becomes less dense around the ferritin molecules, leading to their increased mobility. However, the (111) reflection is still evident after 20 min of expansion, which means

that some long-range periodic order is still present when the unit cell has grown to $a = 325 \text{ \AA}$ (Figure 2.5c) and the volume of the material has increased to 570% of its original value.

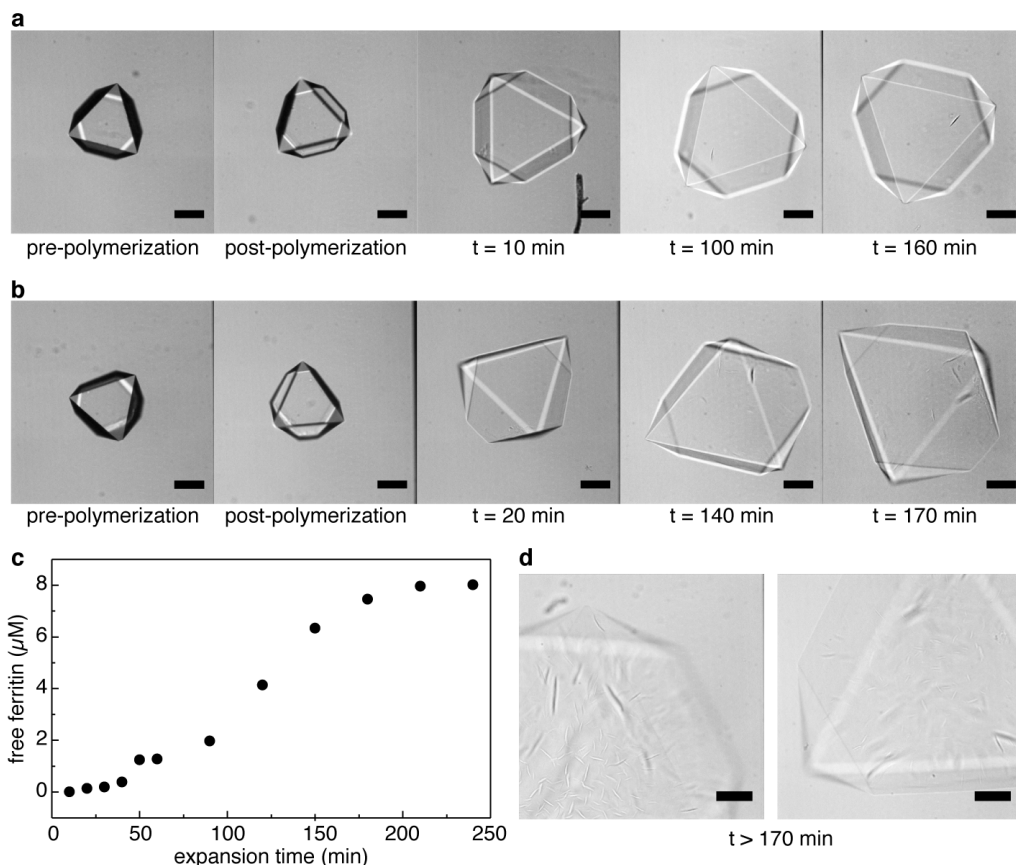


Figure 2.6 | Isotropic hyperexpansion of ferritin crystal–hydrogel hybrids. a, b, Continuous expansion of two different crystal–hydrogel hybrids in deionized water, monitored using confocal microscopy. Crystal facets are still discernible after expansion for more than 2 h. Scale bars correspond to $100 \mu\text{m}$. **c,** Ferritin release into the solution from expanding crystal–hydrogel hybrids ($n > 10,000$) over about 4 h. Negligible ferritin release is observed until about 1 h. Protein concentrations were determined using the Bradford assay. **d,** Confocal microscopy images of highly expanded crystal–hydrogel hybrids, showing the structural deterioration of the facets and the edges.

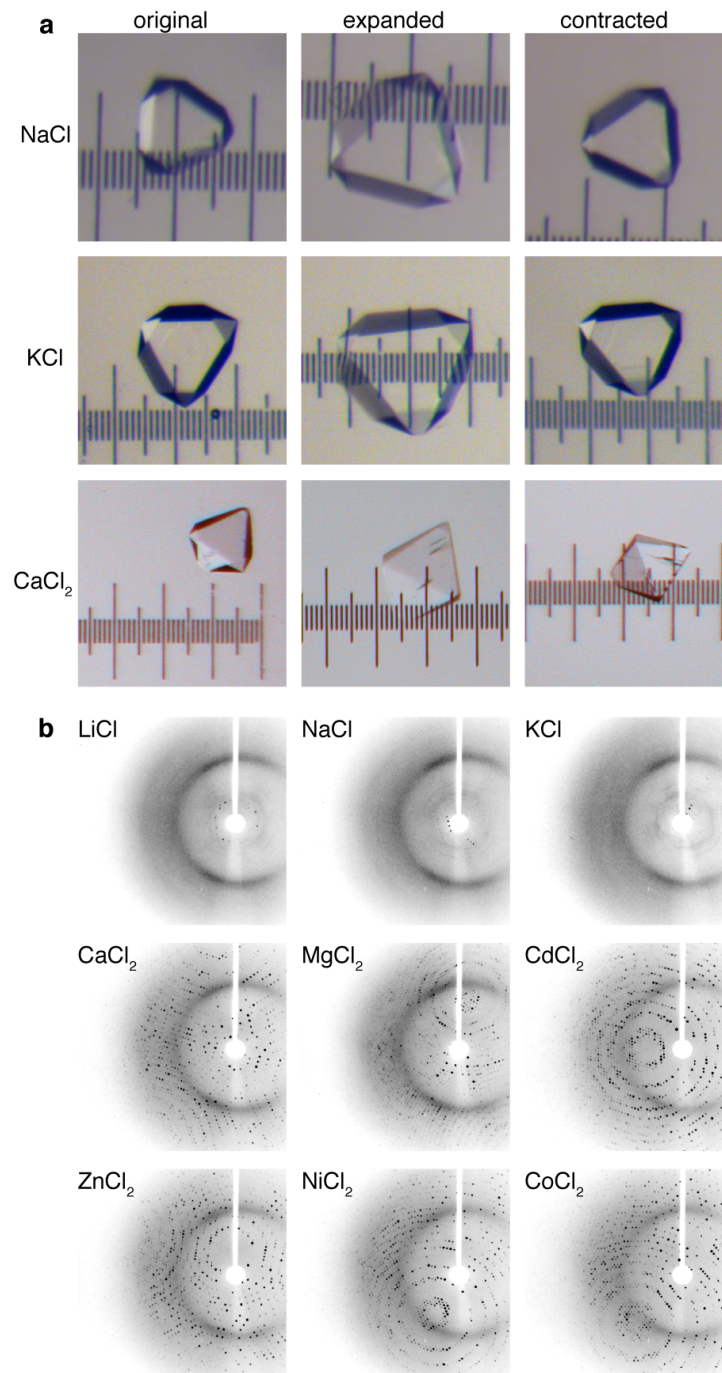


Figure 2.7 | Expansion and contraction behaviour of crystal–hydrogel hybrids in the presence of different metal ions. a, Light micrographs of the crystal–hydrogel hybrids at different stages of expansion and contraction in response to different metal ions. **b,** XRD patterns ($T = 273\text{ K}$) of expanded crystal–hydrogel hybrids, acquired upon contraction with different metal ions. Contraction with divalent cations (Ca, Mg, Cd, Zn, Ni and Co) reproducibly leads to the recovery of the full atomic-level order, whereas contraction with monovalent cations (Li, Na and K) only reinstates low-order diffraction peaks.

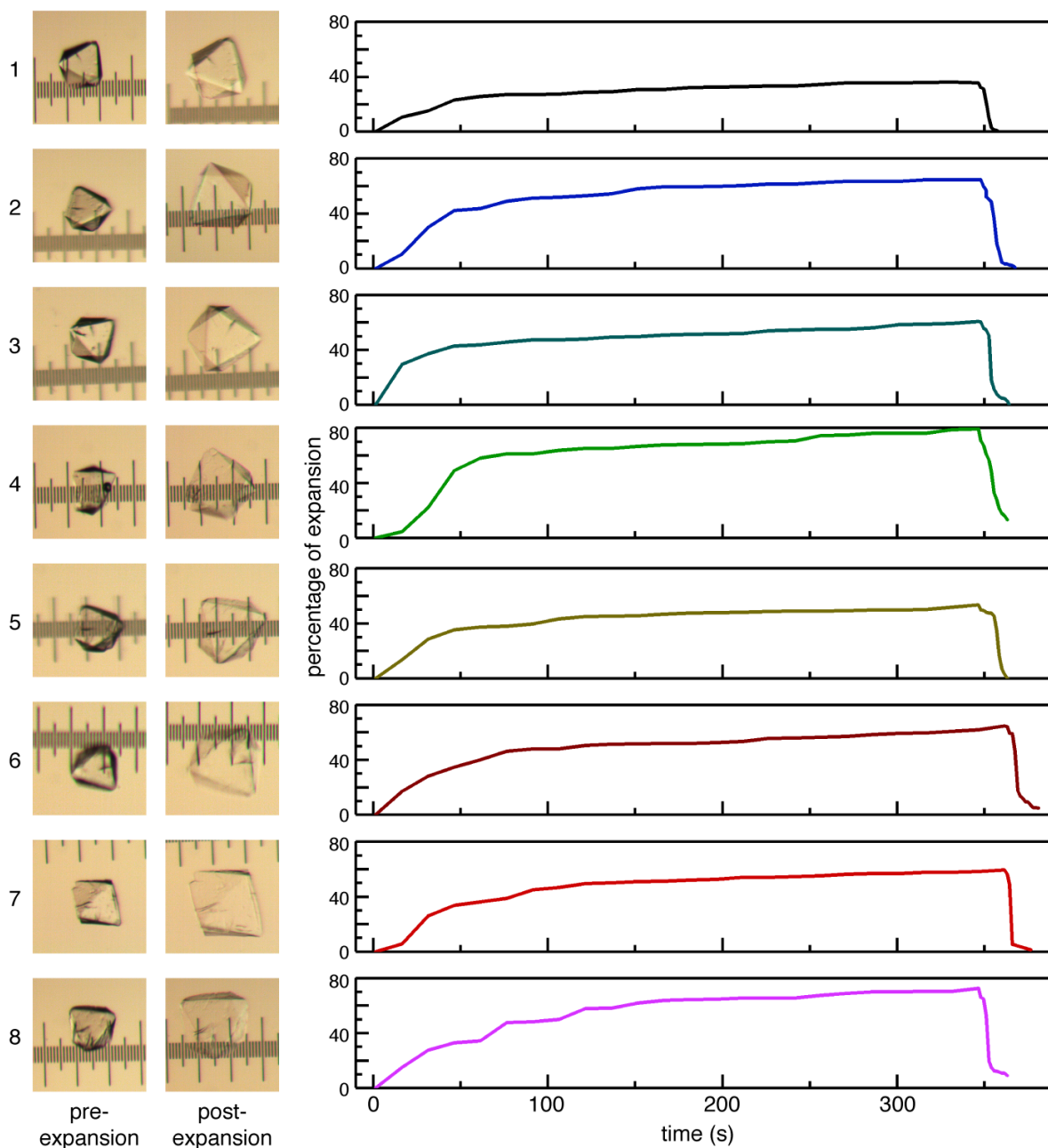


Figure 2.8 | Successive expansion–contraction cycles for a single ferritin crystal–hydrogel hybrid. Light micrographs of a hybrid crystal at pre- and post-expansion stages in each cycle are shown on the left, and the corresponding changes in edge length upon expansion–contraction are shown on the right. The separation between the major ticks of the ruler is $100\ \mu\text{m}$. The crystal expands to a lesser extent during the first expansion cycle, which we ascribe to residual CaCl_2 (which forms strong polymer–polymer and protein–protein interactions) remaining in the solution that is transferred on the loop along with the crystal. The subsequent variability in the rate and extent of expansion is attributed to the different amounts of residual NaCl transferred in each cycle.

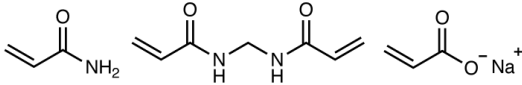
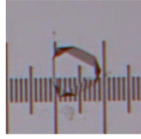
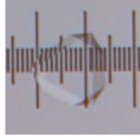
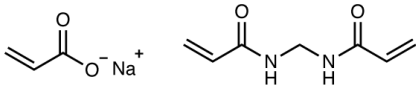
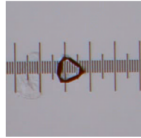
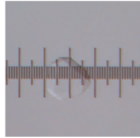
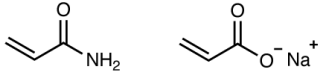
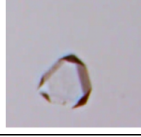

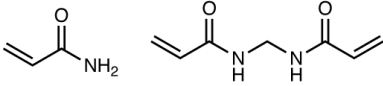
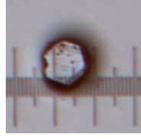
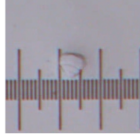
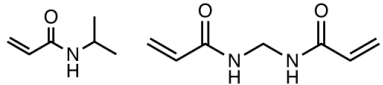
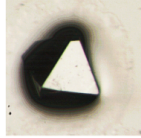
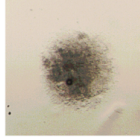
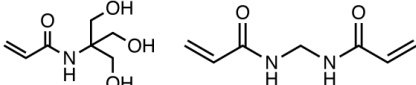
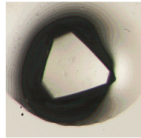
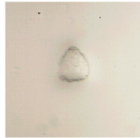
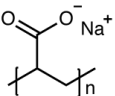
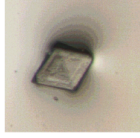
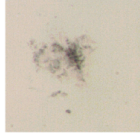
a	polymer precursors	chemical structure	post-polymerization	expanded
	-sodium acrylate -MBAm -acrylamide			
	-sodium acrylate -MBAm			
	-sodium acrylate -acrylamide			
b	polymer precursors	chemical structure	monomer infused	post-polymerization
	-acrylamide -MBAm			
	-N-isopropylacrylamide -MBAm			
	-TRIS-acrylamide -MBAm			
c	polymer	chemical structure	polymer soaked	hydration
	-sodium polyacrylate $M_w = \text{ca. } 2100$			

Figure 2.9 | Alternative hydrogel formulations. **a**, Alternative monomer combinations that yield successful in crystallo polymerization and crystal expansion. **b**, Monomer combinations that lead to crystal dissolution during polymerization. **c**, A crystal soaked in a solution containing polyacrylate (molecular weight, $M_w = 2,100$ Da) dissolves upon being transferred into water. The separation between the major ticks of the ruler is $100\ \mu\text{m}$. MBAm, N,N'-methylenebis(acrylamide).

2.3.3 Atomic-level structural characterization of ferritin crystal-hydrogel hybrids

To probe the reversibility of lattice expansion, we set up a microfluidic flow cell for single-crystal SAXS experiments (**Figure 2.10**), which circumvent the inherent issues associated with bulk measurements in a small capillary tube (such as sample heterogeneity and inefficient solvent diffusion). The SAXS data in Figure 2.3d indicate that a single-crystal lattice that has expanded by 27%—corresponding to a separation of 35 Å between neighboring ferritin molecules—can return to its original dimensions upon NaCl/CaCl₂-induced contraction. To examine whether this recovery also occurs at the level of atomic periodicity, we conducted high-angle, single-crystal X-ray diffraction (XRD) experiments at room temperature (**Figure 2.11a–c**). These experiments showed that crystals that expanded by up to 40% could fully regain their native diffraction pattern upon contraction with divalent metal-ion salts (**Figure 2.7b**). With such expanded and Ca-contracted crystals, we consistently obtained datasets with resolutions <1.15 Å at a synchrotron source at 100 K (**Table 1.1**). Interestingly, the resulting crystal structures revealed two different conformational states of the Ca²⁺-bridged ferritin–ferritin interfaces (**Figure 2.11d**): about 60% of these interfaces were found in the native configuration (as shown in **Figure 2.1d**, but with a well resolved Ca-coordinated water molecule), whereas the remaining 40% presented an alternative coordination mode for Ca²⁺, probably stemming from lattice rearrangements during contraction. Notably, the 1.06-Å-resolution crystal structure (R-factors, $R_{\text{work}} = 9.10\%$; $R_{\text{free}} = 10.26\%$; estimated coordinate error (dispersion precision indicator), 0.011 Å) is the highest-resolution ferritin structure reported until now. Our findings suggest that hydrogel infusion and the expansion–contraction process do not diminish XRD data quality and may actually improve it.

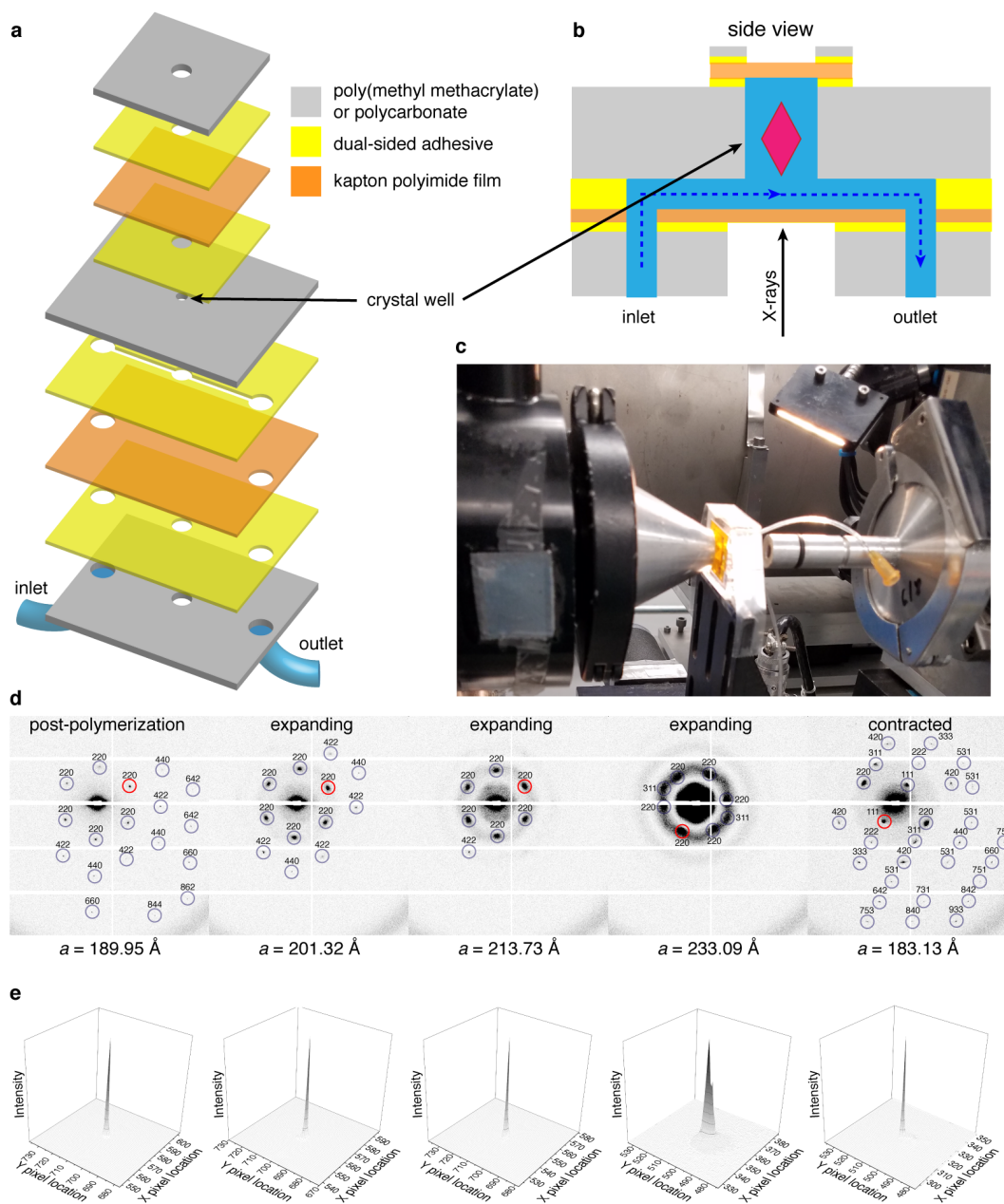


Figure 2.10 | SAXS imaging of a single crystal–hydrogel hybrid in a microfluidic chip. a, Schematic diagram of the microfluidic chip. The chip was constructed by Dr. Jake Bailey and Dr. Alex Groisman. **b,** Side-view representations of the microfluidic chip. **c,** Photograph of the microfluidic chip, mounted on beamline 4-2 at SSRL. **d,** Single-crystal SAXS diffraction patterns observed at different stages of crystal expansion and contraction. The Miller indices of each visible spot are indicated. Reflections with the highest signal-to-noise ratio ($I/\sigma I$) are circled in red. **e,** Spot profiles of the highest- $I/\sigma I$ reflections indicated in **d**.

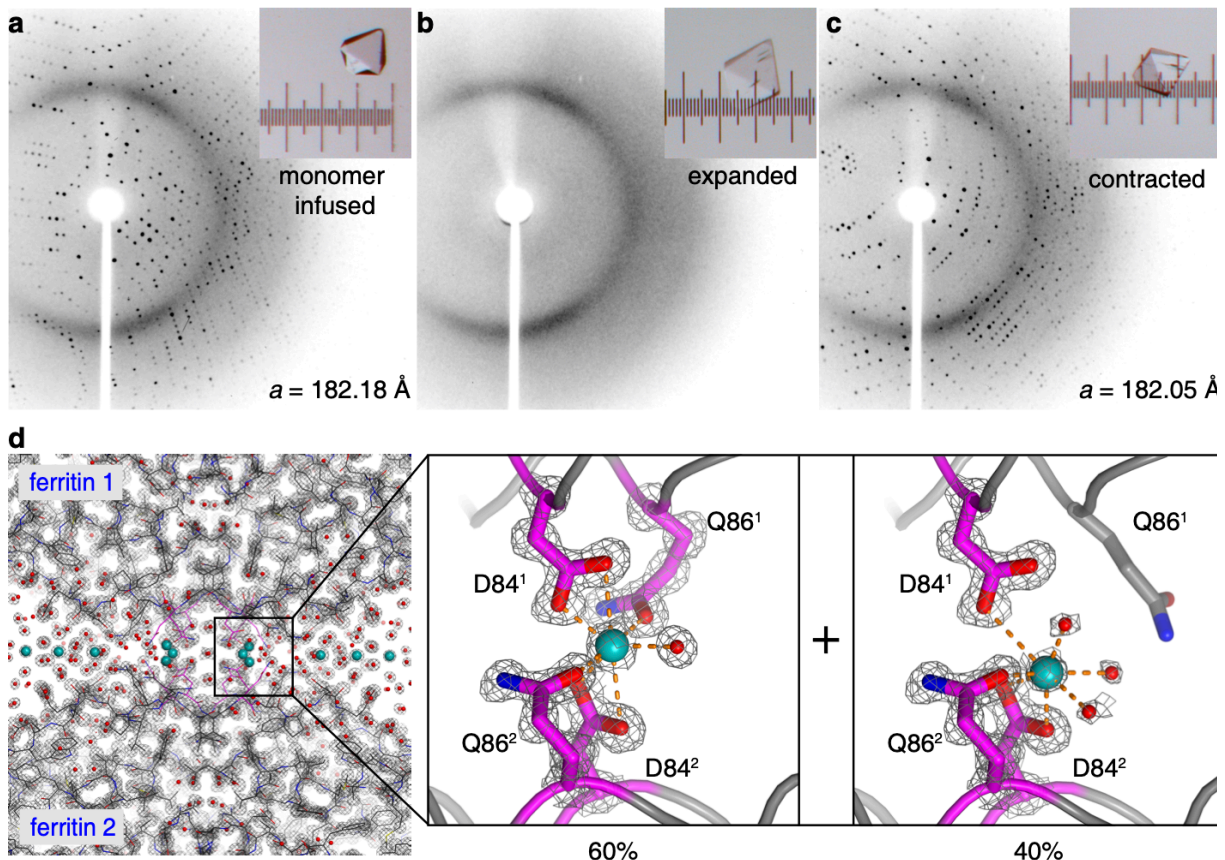


Figure 2.11 | Atomic-level structural characterization of ferritin crystal–hydrogel hybrids by XRD. **a–c**, XRD patterns (at temperature $T = 293 \text{ K}$) of a ferritin crystal infused with polymer precursors (**a**), after polymerization and expansion (**b**) and after contraction with CaCl_2 (**c**). Light micrographs of the crystal are shown in the insets; the separation between the major ticks of the ruler is $100 \mu\text{m}$. **d**, 1.06-\AA -resolution structure ($T = 100 \text{ K}$; PDB ID, 6B8F) of the contracted ferritin crystal–hydrogel hybrid, showing the electron density surrounding the Ca-mediated ferritin–ferritin interfaces and highlighting the two observed Ca coordination conformations. The electron density ($2F_o - F_c$) map (grey) is contoured at 1.5σ . Water molecules and Ca ions are shown as red and blue spheres, respectively.

Table 2.1 | X-ray data collection and refinement statistics.

	Crystal A (6B8F)	Crystal B (6B8G)
Data collection		
Space group	<i>F</i> 432	<i>F</i> 432
Cell dimensions		
<i>a</i> , <i>b</i> , <i>c</i> (Å)	180.40	179.95
α , β , γ (°)	90	90
Resolution (Å)	63.65-1.06	63.62-1.13
No. unique reflections	111189	92912
Multiplicity	14.0 (2.4)	32.2 (13.8)
<i>CC</i> 1/2	0.999 (0.897)	0.999 (0.628)
<i>R</i> merge	0.060 (0.222)	0.131 (1.131)
$\langle I / \sigma I \rangle$	24.8 (3.2)	19.1 (2.3)
Completeness (%)	99.0 (86.4)	100 (100)
Average mosaicity (°)	0.17	0.31
Total solvent content (%)	57.42	57.36
Interstitial solvent content (%)	39.72	39.62
Refinement		
<i>R</i> _{work} / <i>R</i> _{free}	0.0910/0.1026	0.1029/0.1213
No. atoms		
Protein	1687	1699
Ligand/ion	13	13
Water	340	372
<i>B</i> -factors (Å ²)		
Protein	8.51	9.81
Ligand/ion	10.19	11.96
Water	21.83	23.75
R.m.s. deviations		
Bond lengths (Å)	0.013	0.011
Bond angles (°)	1.317	1.241
MolProbity ⁴⁴ score	1.20	1.38
Clashscore	4.12	6.99
Ramachandran plot (%)		
Favored	98.82	98.82
Outliers	0.00	0.00
Rotamers (%)		
Favored	97.35	96.88
Poor	0.53	0.52
DPI (Å) ⁴⁵	0.011	0.015

2.3.4 Self-healing behavior and functionalization of ferritin crystal-hydrogel

Any local anisotropy developed during the expansion or contraction of the hydrogel matrix would be expected to cause dislocations in the embedded ferritin lattice. Indeed, exposure of hydrogel-infused crystals to rapid changes or temporary spatial gradients in NaCl or CaCl₂ concentrations frequently led to fracturing (see, for example, **Figure 2.11** inset). However, these materials showed a remarkable ability to self-heal, whereby the cracks were spontaneously and, in some cases, scarlessly sealed (**Figure 2.12a, b**), owing to the reversible bonding interactions of the hydrogel network with the protein molecules (**Figure 2.12c**). It is important to note that covalently crosslinked hydrogels like p(Ac–Am) do not typically self-heal unless they are modified with dynamic bonding functionalities.^{22,29} In the case of our materials, the role of such functional groups is fulfilled by the ferritin molecules, which act as interaction hubs for polymer chains. During expansion–contraction cycles, cracks tended to reoccur in the same loci in a given crystal. This observation suggests that the healed interfaces had not fully regained the original hydrogel crosslinking density of the bulk material, at least in the time scale (several minutes) of the experiments. Hydrogel integration substantially mitigated the brittleness of native ferritin crystals (**Figure 2.13a**). We observed no fragmentation, even in cases of substantial fracturing that propagated throughout the crystals, and fissures as wide as 20 μm could be closed to recover near-native crystal morphology (**Figure 2.12b**). The ferritin crystal–hydrogel hybrids had a reduced modulus of about 1 GPa, which is similar to that of ferritin crystals (**Figure 2.13b**), but several orders of magnitude higher than those of hydrogels.³⁰ The hybrids are also highly thermostable, maintaining their crystalline order at ≥80 °C (**Figure 2.13c**).

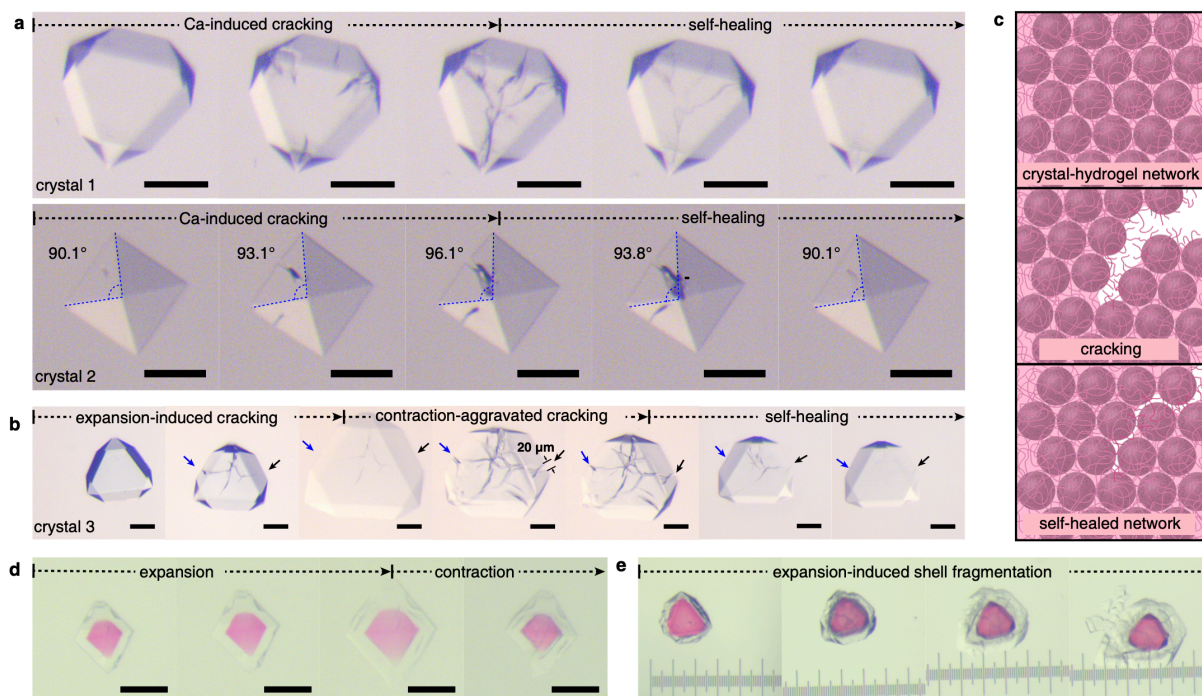


Figure 2.12 | Self-healing behavior and functionalization of ferritin crystal–hydrogel hybrids. **a**, Light microscopy images of crystal–hydrogel hybrids, showing the self-healing of cracks that appear during Ca-induced contraction. **b**, Extensive cracks can also appear during crystal expansion or during the initial stages of NaCl-induced contraction, but eventually self-heal. The arrows point to the termini of the major crack extending through the crystal. **c**, Schematic of crack formation and self-healing through the interactions between polymer strands and ferritin molecules. **d**, Isotropic expansion and contraction of a crystal-hydrogel hybrid with an expandable core and an expandable shell. **e**, Swelling-induced fragmentation of the shell of a crystal-hydrogel hybrid with a fixed core and expandable shell. All scale bars, as well as the separation between the major ticks of the ruler in **e**, correspond to a length of 100 μm.

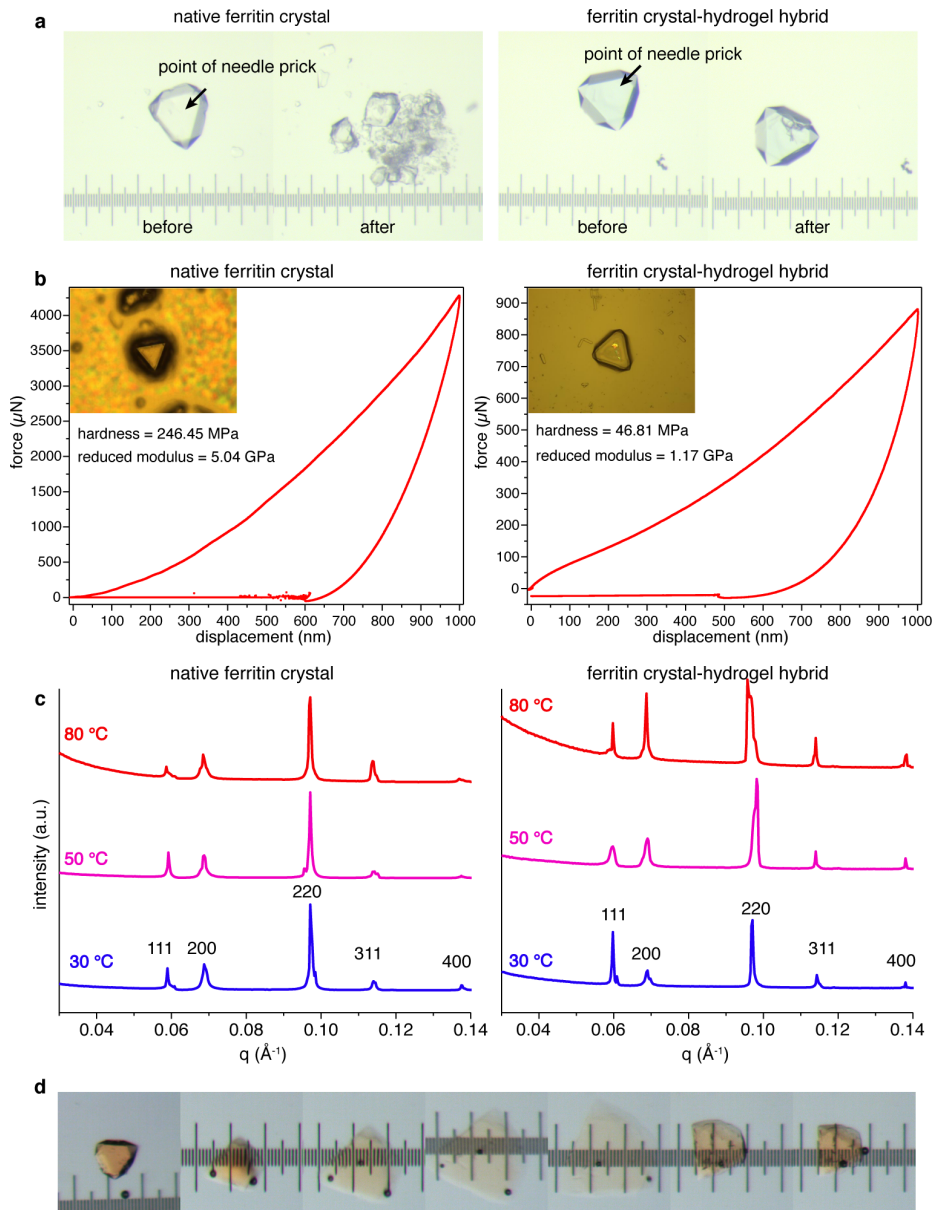


Figure 2.13 | Mechanical and thermal properties of ferritin crystal–hydrogel hybrids. **a**, Light-microscopy images showing the fragmentation of a native ferritin crystal and of a crystal–hydrogel hybrid upon application of external force with a needle at the location indicated with the arrow. The separation between the major ticks of the ruler is 100 μm . **b**, Temperature dependence of the SAXS profiles of native ferritin crystals and crystal–hydrogel hybrids. The small-angle reflections (that is, periodic order) in both samples are maintained at 80 $^{\circ}\text{C}$ (the maximal temperature experimentally attainable). **c**, Determination of the hardness and reduced modulus of native ferritin crystals and crystal–hydrogel hybrids using atomic force microscopy nanoindentation measurements. **d**, Light-microscopy images showing the expansion and contraction of a crystal–hydrogel hybrid containing Fe-loaded ferritin molecules. The separation between the major ticks of the ruler is 100 μm .

Owing to the inherent chemical tailorability of ferritin molecules, the crystal–hydrogel hybrids could be functionalized in different ways. They could be constructed from ferritin molecules with mineralized ferrihydrite in their interior cavity (**Figure 2.13d**), thus exploiting ferritin’s native function as a ferroxidase, or with fluorescent tags covalently attached to their exterior (**Figure 2.12d**). Additionally, spatially differentiated, core-shell crystals were created using a layer-by-layer growth method (**Figure 2.12d, e**). When infused with p(Ac–Am), such nanoparticle- or fluorophore-functionalized lattices displayed the same isotropic expansion–contraction behavior as non-functionalized ones. The layer-by-layer growth process was further modified whereby the core lattice domain (labelled with rhodamine groups) was first covalently fixed through the chemical crosslinking of ferritin molecules with glutaraldehyde, followed by the growth of an uncrosslinked, unlabeled shell layer and the incorporation of the p(Ac–Am) polymer into the composite lattice. Hydration of such ‘fixed core/expandable shell’ crystals led to complete fragmentation of the shell layer due to the strain generated at the mechanically mismatched core–shell interface, exposing the morphologically unaltered core layer (**Figure 2.12e**). These examples highlight the facility with which chemical and mechanical patterning are achieved in protein crystal–hydrogel hybrids.

2.4 Discussion

We have reported here a new form of materials that integrate macro-molecular protein crystals with synthetic polymer networks. These hybrids seamlessly combine the structural order and periodicity of crystals, the adaptiveness and tunable mechanical properties of polymeric networks and the chemical versatility of protein building blocks. Additionally, the ability to reversibly expand–contract crystal lattices and mobilize their protein components may provide a new means to improve XRD quality and explore otherwise inaccessible protein structural states

using three-dimensional protein crystallography. Protein crystals are often highly porous, sometimes containing up to 90% solvent, and are usually assembled through weak, non-covalent packing interactions; therefore, our approach should be applicable to other protein lattices. Their potential for generalizability, coupled with the chemical tailorability of synthetic polymers and the genetic mutability of proteins, should make protein crystal–hydrogel hybrids a rich medium for materials science.

2.5 Methods

2.5.1 Protein expression, purification and characterization.

The plasmid for the ΔC^* variant of human heavy-chain ferritin (HuHF), devoid of all native cysteine residues (C90E, C102A and C130A), was obtained via site-directed mutagenesis as previously described.³¹ Expression and purification of ΔC^* was performed according to the previously published protocol³² and reproduced in detail here. The plasmids of ΔC^* variant isolated from XL-1 Blue cells were transformed into BL21 (DE3) *E. coli* cells and plated on LB agar containing 100 $\mu\text{g}/\text{mL}$ ampicillin. Colonies or freezer stocks of BL21 containing ferritin variant pJexpress vectors were used to inoculate starter cell cultures (200 mL LB medium, 100 $\mu\text{g}/\text{mL}$ ampicillin). Cultures were incubated for 16 hours at 37 °C with shaking at 200 rpm prior to inoculating 1 L LB cultures (10 mL per flask) supplemented with 100 mg/L ampicillin. Cells were grown to $\text{OD}_{600} = 0.6\text{-}0.8$ at 37 °C. Overexpression of protein was induced by addition of isopropyl- β -D-1-thiogalactopyranoside (IPTG) to a total concentration of 1 mM. Cells were incubated at 37 °C for 3 h and harvested by centrifugation (6000 g, 10 min). Pellets were stored at -80 °C. Frozen cell pellets were thawed and resuspended in buffer (15 mM Tris, pH 7.4, 150 mM NaCl) with 1 mM phenylmethylsulfonyl fluoride (PMSF), 5 mM DTT, ~ 25 μM lysozyme. Cells were sonicated for 12 min on ice (59 s pulse on and 30 s pulse off), and the lysate was centrifuged

at 4 °C (12,000 g, 20 min). A second sonication was carried out for the cell pellet after centrifugation with addition of 1% (v/v) Triton X-100 on ice at the same conditions. All variants were isolated as intact 24 subunit cages from the lysate supernatants and further purified.

Ferritin variants were enriched to >80% purity by a heat treatment at 65 °C for 15 min and centrifugation (12,000 g, 10 min). The protein, found in the soluble fraction, was then exchanged into a buffered solution (15 mM Tris, pH 8.0), filtered, and purified using a Uno-Q anion exchange column (Bio-Rad) on a DuoFlow chromatography workstation (Bio-Rad) using a linear 0-1 M NaCl gradient. Ferritin cage fractions were eluted at around 400 mM NaCl. After combining all the fractions containing the protein together, the solution was concentrated to <5 mL for further purification with size exclusion column (SEC). We used a Sephacryl S-300 resin for the purification equilibrated with the buffer (15 mM Tris, pH 7.4, 150 mM NaCl). Protein purity was assessed via SDS-PAGE gel.

2.5.2 Determination of zeta potentials.

Purified ferritin was concentrated to about 200 µM and exchanged into a buffer solution containing 50 mM 2,2-Bis(hydroxymethyl)-2,2',2''-nitrilotriethanol (Bis-Tris) (pH 6.0), 50 mM 4-(2-hydroxyethyl)-1-piperazineethanesulfonic acid (HEPES) (pH 7.0) or 50 mM HEPES (pH 7.5) using an Amicon Ultra centrifugal filter unit (10 kDa cutoff). The zeta potentials of ferritin in the three different buffers were determined using a Zetasizer Nano ZS90 (Malvern Instruments). Experimental runs were performed to collect 12 datasets with a He–Ne laser at 633 nm.

2.5.3 Formation of crystal-hydrogel hybrids

Polymer precursor solution. 25 mM (HEPES; pH 7.0), 30 mM CaCl₂, 917 mM (8.625% w/v) sodium acrylate, 352 mM (2.5% w/v) acrylamide and 13 mM (0.2% w/v) N,N'-methylenebis(acrylamide). *Polymerization solution.* 4 M NaCl, 1% (w/v) APS and 1% (v/v)

TEMED. Octahedron-shaped ferritin crystals formed over 1–2 days in a buffered solution containing 25 mM HEPES (pH 7.0), 3–14.5 μ M protein (per 24meric ferritin cage) and 4.5–7.5 mM CaCl_2 . Once the ferritin crystals matured, the crystallization solution was replaced with the polymer precursor solution. Crystals were soaked for more than 10 h to ensure full infusion of the monomers into the ferritin crystals and were then individually transferred with a mounted CryoLoop (Hampton) to the polymerization solution for 5 min, initiating in crystallo polymerization. Alternatively, the crystallization solution was replaced with the polymerization solution for the bulk polymerization of many crystals at once.

2.5.4 Measurement of the rate of diffusion into ferritin crystals.

A large ferritin crystal was transferred with a mounted CryoLoop onto a glass slide, and 20 μ L of a solution containing 20 μ M (0.01 mg/ml) rhodamine B, 30 mM CaCl_2 and 25 mM HEPES (pH 7.0) was added to the crystal. The rhodamine diffusion process was monitored with a 10 \times air objective installed on a spinning-disk confocal Axio Observer inverted microscope (Zeiss) equipped with a pair of Quantum 5125C cameras (Roper), using a filter to collect light at 575–650 nm (red channel). Differential interference contrast (DIC) and fluorescence (564 nm excitation) images were captured at 1-s intervals with a 10-ms exposure. Images were collected in Slidebook 6 (Intelligent Imaging Innovations) and analyzed using Fiji (<http://fiji.sc/Fiji>).

2.5.5 Determination of in crystallo polymerization dynamics

Ferritin crystals were incubated in a polymer precursor solution supplemented with 5.7 mM (0.3%) pyranine (Sigma-Aldrich). After 12 h, an individual crystal was transferred onto a glass slide and polymerization was initiated by adding 10 μ L of the polymerization solution. Hydrogel polymerization throughout the crystal and the corresponding decrease of pyranine fluorescence were monitored with a 20 \times air objective on the confocal microscope as described

above, using a filter to collect light at 500–550 nm (green channel). DIC and fluorescence (488 nm excitation) images were captured at 1-s intervals with 100-ms (DIC) and 1-s (fluorescence) exposures.

2.5.6 Scanning electron microscopy of ferritin crystals

Native ferritin crystal and crystal–hydrogel hybrid samples were deposited onto glow-discharged, Formvar/ carbon-coated Cu grids (Ted Pella Inc.). Each grid was blotted with filter paper to remove excess liquid. Grids were mounted onto a STEM 12x v2 sample holder and imaged using a Sigma 500 scanning electron microscope (Zeiss) at an accelerating voltage of 1 kV using a 30- μ m aperture.

2.5.7 Polymer quantification with ^{19}F NMR

Large-scale crystallization of ferritin was carried out in a 24-well culture plate (Costar). 100 μ L of 25 μ M ferritin in 15 mM Tris (pH 7.4) and 150 mM NaCl) was combined with 100 μ L of a buffered solution containing 50 mM HEPES (pH 7.0) and 12 mM CaCl_2 . Crystals formed overnight and matured over 72 h. The solution in each well was replaced with 100 μ L of a polymer precursor soaking solution containing: 25 mM HEPES (pH 7.0), 30 mM CaCl_2 , 179.9 mM 2-(trifluoromethyl)acrylic acid, 744.8 mM sodium acrylate, 350.7 mM acrylamide and 20.4 mM N,N'-methylenebis(acrylamide). After soaking overnight, this solution was removed, and the crystals were washed with a buffered solution (25 mM HEPES, pH 7.0; 30 mM CaCl_2) to remove unincorporated monomers. Polymerization was initiated by replacing the washing solution with 100 μ L of the polymerization solution. After 10 min, the crystals were transferred into an Eppendorf tube and centrifuged at 2,000g for 60 s. The supernatant was decanted, and the crystals were resuspended in 1 ml D_2O . Concentrated HCl was added until the pH of the solution was approximately 4.0 to facilitate crystal decomposition. 705 μ L of this solution was transferred into

an NMR tube and supplemented with 4.6 mM trifluoroacetic acid. The ^{19}F -NMR spectrum was collected using a 300M Bruker AVA spectrometer with a ^{19}F probe (Figure 2.5). The peak at -64.94 ppm corresponds to free 2-(trifluoromethyl)acrylic acid, the cluster of peaks near -67.07 p.p.m. to 2-(trifluoromethyl)acrylic acid that has been incorporated into the polymer, and the peak at -75.51 ppm to the trifluoroacetic acid standard. From the integration of these peaks it was deduced that (a) the total concentration of 2-(trifluoromethyl)acrylic acid in the solution was 8.2 mM and (b) 74.7% of the monomeric precursor was incorporated into the polymer matrix inside the crystals. The protein concentration was determined to be 60.0 μM using the Bradford assay,³³ and the molar ratio of 2-(trifluoromethyl) acrylic acid to ferritin was calculated as 137:1. Given this ratio and the fact that each unit cell of the ferritin crystals contains four ferritin cages and has a volume of about 5832 nm³ ($a = 18$ nm), the concentration of 2-(trifluoromethyl)acrylic acid in the crystal lattice was calculated as 155.6 mM, which is very similar to its concentration (179.9 mM) in the soaking solution.

2.5.8 Monitoring crystal expansion-contraction using light microscopy

Single crystals were transferred with a mounted CryoLoop onto a glass slide with a microscopic ruler (OMAX). All images and videos were obtained on an SZX7 (Olympus) microscope equipped with an Infinity 1 charge-coupled device (CCD; Lumenera). For crystals that had not been polymerized, 10 μL of the polymerization solution was carefully added to minimize crystal movement. This solution was removed before water addition. For previously polymerized crystals, water (Milli-Q, 30 μL) was added and crystal expansion was observed over 5–20 min. To initiate crystal contraction, water was replaced with a solution containing either 4 M NaCl or 1 M CaCl_2 .

This expansion–contraction cycle could be repeated at least eight times for a crystal if NaCl was used to induce crystal contraction. Crystal size was determined by measuring the edge length of a facet relative to the microscopic ruler using the Fiji image processing package

2.5.9 Monitoring crystal expansion using confocal microscopy

Crystals containing polymer precursors were prepared as described above. One of these crystals was transferred onto a glass slide and imaged on a confocal microscope. After capturing an initial image, the crystal was polymerized in 10 μL of the polymerization solution, and its expansion in 30 μL water was monitored. DIC images were captured at different time intervals with a 100-ms exposure until the crystal was no longer visible.

2.5.10 Quantification of protein release during expansion

Large-scale crystallization of ferritin was carried out as described above. Once crystals fully matured, the well solution was replaced with 100 μL of the polymer precursor solution. After 12 h, the crystals were all combined into a single Eppendorf tube and 500 μL of the polymerization solution was added. Crystals were expanded by replacing the polymerization solution with 1 ml water. During this experiment, aliquots (100 μL) of the protein solution were removed and replaced with 100 μL of water, and each aliquot was used to determine the protein concentration using the Bradford assay.

2.5.11 Multi-crystal expansion monitored using SAXS

Crystals for multi-crystal small-angle X-ray scattering were prepared as described above and transferred into the polymer precursor solution. A large number ($n > 100$) of crystals were transferred to an Eppendorf tube. After the crystals had settled at the bottom, they were transferred, along with 50 μL of solution, into a 1.5-mm quartz capillary (Hampton). Crystals in capillaries were analyzed at beamline 5-ID-D of the Advanced Photon Source (Argonne National Laboratory).

Data were collected using collimated X-ray radiation (0.7293 Å, 17 keV) calibrated with both a glassy carbon standard and a silicon diffraction grating. After the sample was mounted on the instrument, a thin tube (with a diameter of 0.51 mm) was inserted into the capillary to facilitate the addition of 50 µL of solution with a syringe injector during X-ray exposure. The injected solution contained a more concentrated polymerization solution without NaCl (2% APS and 2% TEMED) in water. After the first exposure, the solution was injected, and an image with a 1-s X-ray exposure was collected every 30 s. Peaks corresponding to the original lattice were visible throughout the process, indicating that some of the crystals in the bulk sample did not expand. This is probably due to limited solvent diffusion or incomplete polymerization within the capillary tubes used for the SAXS experiments. It is important to note that in this procedure, ‘polymerized’ crystals immediately began expanding upon the commencement of data collection. The reason for this experimental strategy (instead of polymerization in a high-ionic-strength solution, followed by the initiation of expansion through lowering the ionic strength) is that it was not possible to sufficiently dilute the high-ionic-strength polymerization solution in the thin capillary tubes used for SAXS (which cannot accommodate addition of large volumes of solution) to enable expansion.

Scattered radiation was detected using a CCD area detector and one-dimensional scattering data were obtained through the azimuthal averaging of the two-dimensional data to produce plots of the scattering intensity as a function of the scattering vector length, $q = 4\pi\sin(\theta/\lambda)$, where θ is one-half of the scattering angle and λ is the wavelength of the X-rays used. Analysis of the one-dimensional data was performed using the powder diffraction processing software JADE (MDI) or Origin (OriginLab).

2.5.12 Multi-crystal SAXS at elevated temperatures

Large-scale crystallization of ferritin was performed as described above. The crystallization solution was removed, and ferritin crystals were resuspended in either the polymer precursor solution or a buffered solution containing 25 mM HEPES (pH 7.0) and 30 mM CaCl₂. After 72 h, the polymer precursor soaking solution was replaced with the polymerization solution. After 10 min, this was also replaced with a buffered solution containing 25 mM HEPES (pH 7.0), 4 M NaCl and 30 mM CaCl₂. Both samples, containing either native ferritin crystals or the crystal–hydrogel hybrids, were transferred into 1.5-mm quartz capillaries (Hampton). Data were collected at beamline 4-2 of SSRL using collimated X-ray radiation (1.1271 Å, 11 keV) calibrated with a silver behenate standard. The samples were heated using a custom-built thermal stage operating at 1 °C min⁻¹, and images with a 1-s X-ray exposure were collected every minute. Scattered radiation was detected using a Pilatus3 X 1M detector (Detectris) and processed as described above.

2.5.13 Single-crystal SAXS

Crystals containing the polymer precursors were prepared and polymerized using the polymerization solution as described above, and were analyzed at SSRL (beamline 4-2). Single crystals were harvested with a mounted CryoLoop and transferred into a 2 M NaCl solution in the 400- μ m-diameter central well of a custom-made microfluidic chip (**Figure 2.10a, 10b**). The microfluidic chip was sealed with a coverslip, attached to a syringe injector and mounted on beamline 4-2 at SSRL for data collection. Data were collected using collimated X-ray radiation (1.127 Å, 11 keV) calibrated with a silver behenate standard. Water was injected into the microfluidic chip at 1 μ L/s to initiate expansion, and 0.5-s-exposure images were taken every about 2.5 s for 4 min. After the data acquisition for crystal expansion was complete, the process was repeated—in the order 4 M NaCl, water, 1 M CaCl₂, water—to monitor repeated contraction and

expansion processes. Data were collected using a Pilatus3 X 1M detector (Detectris). The unit-cell parameters were determined by calculating the radial distance of individual reflections, after fitting the spot intensity to a two-dimensional Gaussian surface.

2.5.14 Single-crystal XRD at room temperature

Crystals containing polymer precursors were prepared and imaged using light microscopy as described above. A single crystal was transferred onto a MicroMount precision tool (MiTeGen) with a 100- μm aperture and sealed with a MicroRT capillary (MiTeGen). Data were acquired on an APEX II CCD diffractometer (Bruker) using Cu K α radiation (1.5418 Å) at 295 K. Three images (60-s exposure) were collected at rotation angles $\varphi = 0^\circ$, 60° and 120° . The crystal was removed from the instrument and soaked in 10 μL of the polymerization solution for 2 min. The crystal was transferred onto a microscopic ruler and 30 μL of water was added. Crystal expansion was measured over 3 min. This crystal was returned to the MicroMount with the MicroRT capillary and an identical three-image dataset was collected. This process was repeated using 30 μL of a 1 M CaCl₂ solution. After the crystal had contracted (1 min), another three-image dataset was collected. Images were analyzed with the Apex III software (Bruker).

2.5.15 Single-crystal XRD at 100 K

Crystal–hydrogel hybrids were prepared and imaged using light microscopy as described above. Two crystals were harvested, 30 μL of water was added, and crystal expansion was monitored over 5 min for both crystals. After 5 min, the water was removed and 30 μL of either a solution containing 1 M CaCl₂ (crystal A) or 4 M NaCl (crystal B) was added. Crystal B was re-expanded in 30 μL water. After 5 min, the water was replaced with 30 μL of a 1 M CaCl₂ solution to contract crystal B. After contraction, both crystals were cryoprotected in perfluoropolyether (Hampton) and frozen in liquid N₂. Single-crystal XRD data for the contracted ferritin crystals

were collected at 100 K at beamline 9-2 of SSRL using 0.98-Å radiation. The data were integrated using iMosflm³⁴ and scaled with Aimless³⁵ (Table 1.1). The structures for crystal A and crystal B were determined at resolutions of 1.06 Å and 1.13 Å, respectively. Molecular replacement was performed with Phaser³⁶ using the HuHF structure (PDB ID: 5CMQ) as a search model. Rigid-body, positional, anisotropic thermal and atom-occupancy refinements were carried out using Phenix.³⁷ Coot³⁸ was used for iterative manual model building. The interstitial solvent content was calculated by subtracting the solvent volume of each crystal from the volume of the inner cavity of ferritin (calculated using VOIDOO).³⁹ All figures were produced with Pymol.⁴⁰

2.5.16 Nanoindentation measurements of crystals

The mechanical properties of the native ferritin crystals and the crystal–hydrogel hybrids were determined using a Hysitron TI 950 Triboindenter test instrument (Bruker). All crystals were dried before the indentation experiments. A Berkovich probe (TI-0039, 142.3°, 100 nm tip radius) was used to determine the hardness and reduced modulus of the native crystals and crystal–hydrogel hybrids. Experiments were conducted in displacement control mode using a displacement of 1,000 nm.

2.5.17 Preparation of iron-loaded ferritin

Iron-loaded ferritin was prepared by adding 10.8 ml of 10 mM (NH₄)₂Fe(SO₄)₂ over 2 h to 144.8 ml of a vigorously stirring solution containing 1 μM ferritin, 15 mM Tris (pH 7.4) and 150 mM NaCl. Subsequently, the solution was stirred for an additional hour before being concentrated to about 3 ml using a 10-kDa Amicon membrane. A DG-10 column (Bio-Rad) was used to remove any unbound iron. The iron content was assessed using a 2-2'-bipyridine-based colorimetric assay⁴¹ and the protein concentration was determined using the Bradford assay. Each ferritin cage contained about 800 Fe atoms.

2.5.18 Formation of core-shell ferritin crystals

Expandable core/expandable shell crystals: Mature ferritin crystals were transferred to a buffered solution containing 25 mM HEPES (pH 7.0), 30 mM CaCl₂ and 1.9 mM (1 mg/ml) 5-(and 6)-carboxytetramethyl rhodamine succinimidyl ester (NHS-rhodamine; Thermo Fisher Scientific). After soaking for 12 h, an individual crystal was removed and washed three times in a buffered solution containing 25 mM HEPES (pH 7.0) and 30 mM CaCl₂ to remove unbound NHS-rhodamine. The crystal was transferred to a well containing 10 µL of 12.5 µM ferritin, 25 mM HEPES (pH 7.0) and 6 mM CaCl₂. A transparent layer of ferritin formed around the rhodamine-labelled ferritin crystal over 12 h (creating a red core and a transparent shell). This crystal was soaked in a polymer precursor solution and polymerized as described above to yield an expandable core/expandable shell crystal.

Fixed core/expandable shell crystals: Fixed core/expandable shell ferritin crystals were prepared similarly to the expandable core/expandable shell crystals described above. The only difference was that after the rhodamine labelling step, the crystal was transferred into a solution containing 2.5% (v/v) glutaraldehyde, 25 mM HEPES (pH 7.0) and 30 mM CaCl₂. After 12 h, the crystal was washed five times with water to remove unbound glutaraldehyde, followed by the epitaxial growth of the transparent layer of ferritin crystals on top of the core layer in a fresh crystallization solution containing 12.5 µM ferritin. This crystal was then soaked in a polymer precursor solution and polymerized as described above to yield a fixed core/expandable shell crystal.

2.6 Data availability

Crystal structures have been deposited in the Research Collaboratory for Structural Bioinformatics Protein Data Bank under accession codes 6B8F (ferritin–polymer hybrid crystal 1;

<https://www.rcsb.org/structure/6b8f>) and 6B8G (ferritin–polymer hybrid crystal 2; <https://www.rcsb.org/structure/6b8g>).

2.7 Acknowledgments

We thank the following colleagues for assistance: R. Alberstein for data processing; A. Rheingold, C. Moore and M. Gembicky for XRD; S. Weigand, T. Weiss and I. Rajkovic for SAXS; W.-J. Rappel for confocal microscopy; Z. Hu for performing the nanoindentation experiments. This work was primarily funded by the US Department of Energy, DOE (BES, Division of Materials Sciences, Biomolecular Materials Program, DE-SC0003844 to F.A.T.). Additional funding was provided by NSF (DMR-1602537 to F.A.T. for SAXS studies). Crystallographic data were collected at Stanford Synchrotron Radiation Lightsource (SSRL) and the Crystallography Facility of the University of California, San Diego. SAXS data were collected at SSRL and the Advanced Photon Source. SSRL and the Advanced Photon Source are supported by the DOE Office of Science, Office of Basic Energy Sciences under contracts DE-AC02-76SF00515 and DE-AC02-06CH11357, respectively.

Chapter 2 is reproduced, in part, with permission, from: Zhang, L., Bailey, J. B., Subramanian, R. H., Groisman, A., Tezcan, F. A. “Hyperexpandable, self-healing macromolecular crystals with integrated polymer networks” *Nature* **557**, 86–91 (2018). The dissertation author was the primary author on all reprinted materials.

2.8 References

1. Hawkins, T.; Mirigian, M.; Yasar, M. S.; Ross, J. L., Mechanics of microtubules. *Journal of Biomechanics* **2010**, *43* (1), 23-30.
2. Fletcher, D. A.; Mullins, D., Cell mechanics and the cytoskeleton. *Nature* **2010**, *463* (7280), 485-492.
3. Block, S. M.; Blair, D. F.; Berg, H. C., Compliance of bacterial flagella measured with optical tweezers. *Nature* **1989**, *338* (6215), 514-518.
4. Lewis, J. K.; Bothner, B.; Smith, T. J.; Siuzdak, G., Antiviral agent blocks breathing of the common cold virus. *Proceedings of the National Academy of Sciences of the United States of America* **1998**, *95* (12), 6774-6778.
5. Lok, S.-M.; Kostyuchenko, V.; Nybakken, G. E.; Holdaway, H. A.; Battisti, A. J.; Sukupolvi-Petty, S.; Sedlak, D.; Fremont, D. H.; Chipman, P. R.; Roehrig, J. T.; Diamond, M. S.; Kuhn, R. J.; Rossmann, M. G., Binding of a neutralizing antibody to dengue virus alters the arrangement of surface glycoproteins. *Nature Structural & Molecular Biology* **2008**, *15* (3), 312-317.
6. Kobatake, S.; Takami, S.; Muto, H.; Ishikawa, T.; Irie, M., Rapid and reversible shape changes of molecular crystals on photoirradiation. *Nature* **2007**, *446* (7137), 778-781.
7. Kim, T.; Al-Muhanna, M. K.; Al-Suwaidan, S. D.; Al-Kaysi, R. O.; Bardeen, C. J., Photoinduced curling of organic molecular crystal nanowires. *Angewandte Chemie-International Edition* **2013**, *52* (27), 6889-6893.
8. Panda, M. K.; Ghosh, S.; Yasuda, N.; Moriwaki, T.; Mukherjee, G. D.; Reddy, C. M.; Naumov, P., Spatially resolved analysis of short-range structure perturbations in a plastically bent molecular crystal. *Nature Chemistry* **2015**, *7* (1), 65-72.
9. Naumov, P.; Chizhik, S.; Panda, M. K.; Nath, N. K.; Boldyreva, E., Mechanically responsive molecular crystals. *Chemical Reviews* **2015**, *115* (22), 12440-12490.
10. Barthelet, K.; Marrot, J.; Riou, D.; Ferey, G., A breathing hybrid organic-inorganic solid with very large pores and high magnetic characteristics. *Angewandte Chemie-International Edition* **2002**, *41* (2), 291-294.

11. Sakata, Y.; Furukawa, S.; Kondo, M.; Hirai, K.; Horike, N.; Takashima, Y.; Uehara, H.; Louvain, N.; Meilikhov, M.; Tsuruoka, T.; Isoda, S.; Kosaka, W.; Sakata, O.; Kitagawa, S., Shape-memory nanopores induced in coordination frameworks by crystal downsizing. *Science* **2013**, *339* (6116), 193-196.
12. Rabone, J.; Yue, Y. F.; Chong, S. Y.; Stylianou, K. C.; Bacsá, J.; Bradshaw, D.; Darling, G. R.; Berry, N. G.; Khimiyak, Y. Z.; Ganin, A. Y.; Wiper, P.; Claridge, J. B.; Rosseinsky, M. J., An adaptable peptide-based porous material. *Science* **2010**, *329* (5995), 1053-1057.
13. Suzuki, Y.; Cardone, G.; Restrepo, D.; Zavattieri, P. D.; Baker, T. S.; Tezcan, F. A., Self-assembly of coherently dynamic, auxetic, two-dimensional protein crystals. *Nature* **2016**, *533* (7603), 369-373.
14. Serre, C.; Mellot-Draznieks, C.; Surble, S.; Audebrand, N.; Filinchuk, Y.; Ferey, G., Role of solvent-host interactions that lead to very large swelling of hybrid frameworks. *Science* **2007**, *315* (5820), 1828-1831.
15. Worthy, A.; Grosjean, A.; Pfrunder, M. C.; Xu, Y.; Yan, C.; Edwards, G.; Clegg, J. K.; McMurtrie, J. C., Atomic resolution of structural changes in elastic crystals of copper(ii) acetylacetonate. *Nature Chemistry* **2018**, *10* (1), 65-69.
16. Mason, J. A.; Oktawiec, J.; Taylor, M. K.; Hudson, M. R.; Rodriguez, J.; Bachman, J. E.; Gonzalez, M. I.; Cervellino, A.; Guagliardi, A.; Brown, C. M.; Llewellyn, P. L.; Masciocchi, N.; Long, J. R., Methane storage in flexible metal-organic frameworks with intrinsic thermal management. *Nature* **2015**, *527* (7578), 357-361.
17. Couck, S.; Denayer, J. F. M.; Baron, G. V.; Remy, T.; Gascon, J.; Kapteijn, F., An amine-functionalized mil-53 metal-organic framework with large separation power for CO₂ and CH₄. *Journal of the American Chemical Society* **2009**, *131* (18), 6326-6327.
18. Chen, Q.; Chang, Z.; Song, W.-C.; Song, H.; Song, H.-B.; Hu, T.-L.; Bu, X.-H., A controllable gate effect in cobalt(ii) organic frameworks by reversible structure transformations. *Angewandte Chemie-International Edition* **2013**, *52* (44), 11550-11553.
19. Ghosh, S.; Reddy, C. M., Elastic and bendable caffeine cocrystals: Implications for the design of flexible organic materials. *Angewandte Chemie-International Edition* **2012**, *51* (41), 10319-10323.
20. Commins, P.; Hara, H.; Naumov, P., Self-healing molecular crystals. *Angewandte Chemie-International Edition* **2016**, *55* (42), 13028-13032.

21. Tanaka, T.; Fillmore, D.; Sun, S. T.; Nishio, I.; Swislow, G.; Shah, A., Phase-transitions in ionic gels. *Physical Review Letters* **1980**, *45* (20), 1636-1639.
22. Phadke, A.; Zhang, C.; Arman, B.; Hsu, C.-C.; Mashelkar, R. A.; Lele, A. K.; Tauber, M. J.; Arya, G.; Varghese, S., Rapid self-healing hydrogels. *Proceedings of the National Academy of Sciences of the United States of America* **2012**, *109* (12), 4383-4388.
23. Holtz, J. H.; Asher, S. A., Polymerized colloidal crystal hydrogel films as intelligent chemical sensing materials. *Nature* **1997**, *389* (6653), 829-832.
24. Chen, F.; Tillberg, P. W.; Boyden, E. S., Expansion microscopy. *Science* **2015**, *347* (6221), 543-548.
25. Elliott, J. E.; Macdonald, M.; Nie, J.; Bowman, C. N., Structure and swelling of poly(acrylic acid) hydrogels: Effect of pH, ionic strength, and dilution on the crosslinked polymer structure. *Polymer* **2004**, *45* (5), 1503-1510.
26. Theil, E. C., Ferritin - structure, gene-regulation, and cellular function in animals, plants, and microorganism. *Annual Review of Biochemistry* **1987**, *56*, 289-315.
27. Lawson, D. M.; Artymiuk, P. J.; Yewdall, S. J.; Smith, J. M. A.; Livingstone, J. C.; Treffry, A.; Luzzago, A.; Levi, S.; Arosio, P.; Cesareni, G.; Thomas, C. D.; Shaw, W. V.; Harrison, P. M., Solving the structure of human h-ferritin by genetically engineering intermolecular crystal contacts. *Nature* **1991**, *349* (6309), 541-544.
28. Kaya, D.; Pekcan, O.; Yilmaz, Y., Direct test of the critical exponents at the sol-gel transition. *Physical Review E* **2004**, *69* (1), 016117.
29. Strandman, S.; Zhu, X. X., Self-healing supramolecular hydrogels based on reversible physical interactions. *Gels* **2016**, *2* (2), 16.
30. Denisin, A. K.; Pruitt, B. L., Tuning the range of polyacrylamide gel stiffness for mechanobiology applications. *Acs Applied Materials & Interfaces* **2016**, *8* (34), 21893-21902.
31. Huard, D. J. E.; Kane, K. M.; Tezcan, F. A., Re-engineering protein interfaces yields copper-inducible ferritin cage assembly. *Nature Chemical Biology* **2013**, *9* (3), 169-176.

32. Sontz, P. A.; Bailey, J. B.; Aln, S.; Tezcan, F. A., A metal organic framework with spherical protein nodes: Rational chemical design of 3d protein crystals. *Journal of the American Chemical Society* **2015**, *137* (36), 11598-11601.
33. Bradford, M. M., Rapid and sensitive method for quantitation of microgram quantities of protein utilizing principle of protein-dye binding. *Analytical Biochemistry* **1976**, *72* (1-2), 248-254.
34. Battye, T. G. G.; Kontogiannis, L.; Johnson, O.; Powell, H. R.; Leslie, A. G. W., Imosflm: A new graphical interface for diffraction-image processing with mosflm. *Acta Crystallographica Section D-Biological Crystallography* **2011**, *67*, 271-281.
35. Evans, P. R.; Murshudov, G. N., How good are my data and what is the resolution? *Acta Crystallographica Section D-Biological Crystallography* **2013**, *69*, 1204-1214.
36. McCoy, A. J.; Grosse-Kunstleve, R. W.; Adams, P. D.; Winn, M. D.; Storoni, L. C.; Read, R. J., Phaser crystallographic software. *Journal of Applied Crystallography* **2007**, *40*, 658-674.
37. Adams, P. D.; Afonine, P. V.; Bunkoczi, G.; Chen, V. B.; Davis, I. W.; Echols, N.; Headd, J. J.; Hung, L. W.; Kapral, G. J.; Grosse-Kunstleve, R. W.; McCoy, A. J.; Moriarty, N. W.; Oeffner, R.; Read, R. J.; Richardson, D. C.; Richardson, J. S.; Terwilliger, T. C.; Zwart, P. H., Phenix: A comprehensive python-based system for macromolecular structure solution. *Acta Crystallographica Section D-Structural Biology* **2010**, *66*, 213-221.
38. Emsley, P.; Cowtan, K., Coot: Model-building tools for molecular graphics. *Acta Crystallographica Section D-Structural Biology* **2004**, *60*, 2126-2132.
39. Kleywegt, G. J.; Jones, T. A., Detection, delineation, measurement and display of cavities in macromolecular structures. *Acta Crystallographica Section D-Biological Crystallography* **1994**, *50*, 178-185.
40. The pymol molecular graphics system version 1.3, <http://pomyl.Org/2/support.Html> (Schrödinger LLC).
41. Levi, S.; Luzzago, A.; Cesareni, G.; Cozzi, A.; Franceschinelli, F.; Albertini, A.; Arosio, P., Mechanism of ferritin iron uptake - activity of the h-chain and deletion mapping of the ferro-oxidase site - a study of iron uptake and ferro-oxidase activity of human-liver, recombinant h-chain ferritins, and of 2 h-chain deletion mutants. *Journal of Biological Chemistry* **1988**, *263* (34), 18086-18092.

Chapter 3 : Towards a comprehensive understanding of the material properties of polymer integrated crystals

3.1 Abstract

The scope of applications for a given material is dictated by its functional properties¹ (*e.g.*, chemical, physical, and mechanical),²⁻³ which in turn depend on the composition,⁴⁻⁶ interactions,⁷⁻⁸ and arrangement⁹⁻¹⁰ of its individual subcomponents.^{9,11} Compared to single-component materials, which possess a fixed set of properties after manufacture, hybrid materials (made from >one component) can circumvent this limitation.¹² Advantages of hybrid materials include 1) the possibility for complementary properties of the individual elements (minimizing disadvantages of each and/or maximizing the synergistic properties of all),¹³⁻¹⁵ 2) new emergent behaviors that cannot be achieved from single-component materials,^{9,16} and 3) high tunability of the bulk material properties by manipulating the composition, connectivity, and/or characteristics of each component.¹⁷⁻²¹ However, taking advantage of this enhanced complexity to achieve specialized materials for specific applications requires a comprehensive understanding of how the many factors underlying their macroscopic behavior work together. Previously, we combined rigid, fragile protein crystals with continuous, flexible polymer networks to create a new hybrid material—polymer integrated crystals (PIX)^{20,22}—which possess self-healing behavior and can reversibly expand (up to 500% by volume) and contract in response to changes in the ionic strength of the surrounding solution. In this chapter, we describe initial characterization of the scope of dynamic behaviors and material properties accessible to PIX by systematically varying both the protein and polymer components. We carried out experimental measurements in combination with molecular dynamics simulations to build a molecular-level understanding of the origin of bulk PIX behavior, including crystal packing, electrostatic interactions, and protein/polymer identity and density.

3.2 Introduction

The first proof-of-principle design for PIX (Chapter 2) involved the use of macromolecular ferritin crystals²³ (a highly porous cubic lattice) that had been infused with polyacrylate (pAc)-based polymers (specifically a 3:1 acrylate:acrylamide copolymer – poly(acrylate-co-acrylamide); p(Ac-Am)). Due to the swelling behavior of pAc-based polymers in different ionic strengths,²⁴ the resulting PIX were capable of expanding to 500% of their original volume without loss of crystallinity. Recently, it was also shown that the symmetry of the initial crystalline scaffold can influence the behavior of ferritin PIX, with an anisotropic *H32* packing leading to anisotropic and directional bending motions²² (as opposed to the isotropic expansion of *F432* cubic PIX) despite being composed of the same components. Inspired by these results, we sought to expand the scope of utility for PIX materials by investigating the behavior of PIX upon systematic variation of the polymer composition, ferritin surface charge, crystal packing, and identity of the crystallized protein. Here we characterized the consequences of these variables on the behavior of PIX using light microscopy, small angle X-ray scattering (SAXS), and coarse-grained and atomistic MD simulations to gain insight into the molecular-scale behavior that gives rise to macroscopic observables. Ultimately, this multidimensional screen over variable space is expected to define the range of material properties accessible to PIX and provide a methodological framework for future efforts to expand these analyses to other proteins and soft polymeric materials.

PIX, being multicomponent and multiphase systems, exhibit emergent bulk-scale properties that arise from their particular composition. When we first set out to construct PIX, we surmised that the following design parameters would be important for their function/behavior:²⁰

1. *Lattice structure*: appropriate crystalline scaffolds would be (meso)porous, forming a continuous volume through which the polymer precursors could be diffused, thus ensuring that the hydrogel network penetrates efficiently and uniformly throughout the crystal.
2. *Protein-protein interactions*: the requisite breaking and reforming of crystal contacts during expansion/contraction suggests that they should be reversible and specific, enabling their facile rupture and reformation. This is important for both enabling expansion (breakable contacts) as well as the eventual return to the final lattice packing.
3. *Protein-polymer interactions*: upon expansion, the interactions between polymer and protein must be sufficiently strong to ensure that crystallinity is maintained in the absence of direct protein-protein crystal contacts. Yet, the polymer network should also be dynamic enough to enable error correction and self-healing behavior to compensate for transient defects that form during the expansion/contraction processes.

As described below, we set out to study the impact of these parameters in systematic fashion. First, we designed a library of ferritin variants with different crystal contacts (to investigate packing effects) as well as different surface charges but identical *F432* symmetry (to modulate protein-polymer interactions). We then explored different polymer precursors, testing the dynamic behavior of the resulting PIX by tuning the composition and concentration of polymer chains in the final lattices. We further tested whether PIX can be formed using crystals of other proteins that have different symmetries, chemical compositions, and porosities. Finally, we conclude with preliminary molecular dynamics (MD) characterization of ferritin PIX lattices, using both all-atom and coarse-grained (CG) simulations to understand the protein-polymer interactions at both atomic and mesoscale resolutions.

3.3 Results and discussion

3.3.1 On the effects of ferritin packing on PIX behavior

In our original design, isotropic *fcc* symmetry crystals of Ca²⁺-bridged HuHF-ΔC* ferritin gave rise to isotropic expansion and contraction. In contrast, our recently reported *H32*-symmetry PIX exhibit anisotropic dynamic behavior, owing to their rhombic symmetry that is enabled by hydrophobic contacts mediated by covalently attached RAFT agents (¹⁵⁷C-HuHF).²² Both lattices rely on Ca²⁺ binding at the two-fold axis (residues 84D/86Q) of the ferritin cage as a primary crystal contact and have porosities of >50%, enabling complete infusion with polymer precursors. As both systems exhibited the same expansion and self-healing properties due to the use of the same p(Ac-Am) polymer, here we extended this analysis to additional ferritin lattices (**Figure 3.1**) spanning four different symmetries and three different types of protein-protein interactions.

For *F432* crystals, there are twelve Ca²⁺-mediated contacts distributed equally around each cage (**Figure 3.1a**). Our initial study showed that reformation of these calcium bridges during contraction readily occurred and commonly improved crystal quality. In some cases, the resolution (as determined by single-crystal X-ray diffraction) Ca²⁺-contracted PIX lattices exceeded that of the original crystal. However, in *H32* lattices, only six of these calcium contacts remain (defining the *ab* plane) (**Figure 3.1b**). The covalently attached RAFT agents form hydrophobic interactions along the *c* axis, creating asymmetry in both the packing and interaction strengths of protein-protein contacts within the crystal. This imbalance is further apparent in that the crystallinity of contracted *H32* PIX is sometimes worse than the initial crystal, likely reflecting the lower precision of hydrophobic contacts relative to metal coordination. Consequently, the different an/isotropic expansion behavior of *H32* and *F432* PIX (**Figure 3.2**) can be attributed to packing interactions.

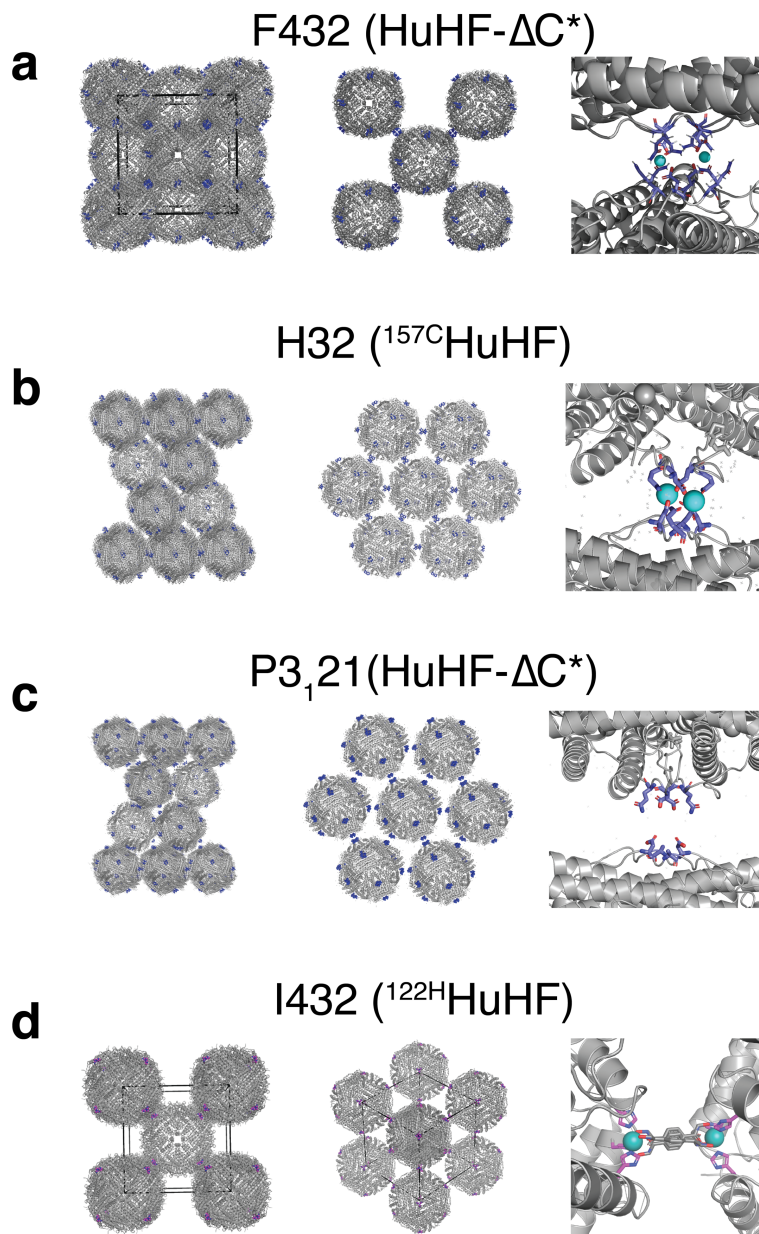


Figure 3.1 | Crystal lattice packing and protein-protein interaction in the lattice. **a**, *F432* packing of HuHF- ΔC^* and the calcium mediated protein-protein interaction between residue 84D and residue 86Q in all directions. **b**, *H32* packing of the RAFT-labeled ^{157}C HuHF variant, the 84D/86Q calcium-mediated crystal contact that defines the *a-b* plane. There is no metal coordination along the *c*-dimension, only weak hydrophobic interactions were observed. **c**, *P3₁21* packing of HuHF- ΔC^* and the non-covalent protein-protein interactions within the *a-b* plane. The absence of metal coordination at 84D/86Q is readily apparent. **d**, *I432* crystal packing of the ^{122}H HuHF ferritin variant. The right-most image shows the di-hydroxamate linker coordinated to two protein cages via Zn^{2+} ions at their 3-fold axes.

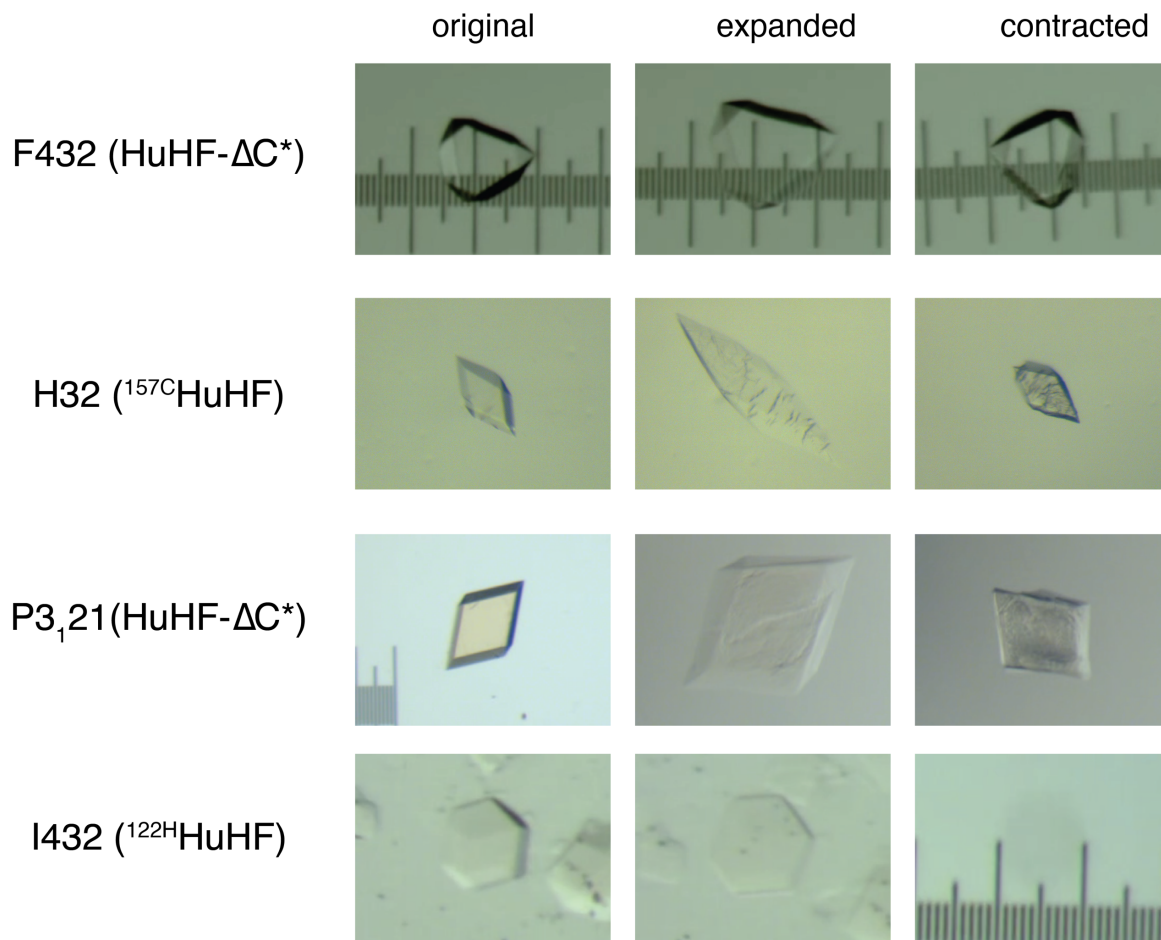


Figure 3.2 | Characterization of the expansion and contraction behavior of ferritin PIX. **a**, HuHF- ΔC^* crystallizes into *F*432 lattices with CaCl_2 . PIX made from these crystals expand and contract isotropically. **b**, RAFT-labeled ^{157}C HuHF variant instead forms *H*32-symmetry crystals due to anisotropic interactions on its surface. This anisotropy is reflected in the non-isotropic expansion/contraction behavior of PIX made from these crystals. **c**, *P*3₁21-symmetry crystals of HuHF- ΔC^* formed in the absence of CaCl_2 . Lacking any significant crystal contacts, these PIX expand and contract, but were unable to regain the molecular order of the initial lattices. **d**, ^{122}H HuHF ferritin crystallizes into *I*432 MOF-like frameworks via di-hydroxamate linkers. These PIX could expand but not contract, leading to crystal dissolution in all cases. The different expansion/contraction macroscopic behavior of each lattice is clearly visible by eye. The separation between the major ticks of the ruler is 100 μm .

To more closely compare to the original PIX, we next characterized HuHF- Δ C* crystallized into an alternate $P3_121$ space group; these crystals have no calcium contacts (**Figure 3.1c**). Rather, there are no obvious noncovalent contacts along the a - b plane (all ferritin-ferritin distances >3.0 Å)²², while small hydrophobic patches and salt-bridging (between E166/K119) comprise the interactions along the c -axis. This asymmetry is analogous to $H32$ packing, but now with the original protein component. Indeed, these $P3_121$ -symmetry PIX underwent anisotropic expansion (**Figure 3.2**) and were capable of contracting, but always resulted in disintegration, likely due to the very weak protein-protein interactions in the original crystal. As a final packing variant, we used a previously reported MOF-like ferritin crystal with body-centered cubic $I432$ symmetry (**Figure 3.1d**)²⁵. This ferritin (¹²²HuHF) has 3 histidine residues at each of the eight 3-fold symmetry axes (the corners of a cube), allowing coordination of a Zn^{2+} ion that has an open coordination site. Crystals then self-assemble via di-hydroxamate small-molecule linkers, which form bridging interactions with the zinc ions. This protein-MOF has a porosity of 56%, similar to the other crystal packing variants. As shown in **Figure 3.2**, PIX created with these lattices could expand, but could not be recovered from expansion. We believe this is due to leaching of the small-molecule linker during expansion, thus removing the possibility of reforming the MOF-like structure. We found that the original framework structure could not be recovered during contraction even when the solution was supplemented with excess linker, a limitation that we attribute to the slow kinetics of bonding between the metal ions and the chemical linkers.

To summarize, the behavior and fidelity of PIX expansion and contraction are dictated by both the crystal packing and the nature of the crystal contacts. Isotropic $F432$ -symmetry PIX readily expand and contract with ionic strength, but the degree of order in contracted PIX is further improved upon the addition of Ca^{2+} , which provide strong, fast, and precise interactions. In $H32$

packing, there are calcium contacts within the *ab* plane, but weaker, less specific hydrophobic interactions along the *c* axis. During expansion and contraction, the *ab* planes were more rigid and reformed more easily, creating a lamellar structure that displayed accordion-like dynamics and bending motions. However, this behavior was also associated with a somewhat reduced degree of ordering relative to the original PIX. *P3₁21* lattices, which only have weak noncovalent interactions both within the *ab* plane and along the *c* axis, are crystalline but not atomically ordered. These PIX underwent anisotropic expansion and contraction, but no longer diffracted afterwards, as the protein-protein interactions were too weak to facilitate recrystallization, though a few exhibited partial reformation (in small pieces), potentially templated by molecular imprints left on the polymer structure. Similarly, *I432* protein-MOF PIX could expand, but fractured during contraction, likely due to loss of the requisite di-hydroxamate linker, which prevented the reformation of bridging interactions between 3-fold axes. We found that even when the expansion solution was supplemented with additional metal and ligand, the poor solubility of the linker and slow kinetics of MOF crystallization proved incompatible with PIX behavior.

Finally, we note that both HuHF- ΔC^* variants above each only have a single mutation, meaning that the protein-polymer interactions are likely to be similar for all of them. All lattices have similar porosities (*F432*: 59.38%, *H32*: 54.67%, *P3₁21*: 59.37%, *I432*: 57.47%), and thus should have similar proportions of protein and polymer. As all PIX were infused with the same polymer (p(Ac-Am)), changes in behavior can be attributed to packing considerations. This endows PIX with a great level of control over their dynamic mechanical behavior through changes in symmetry or interaction that are achievable even by minor modification to the protein, where strong and precise protein-protein interactions promote orderly contraction. With the importance

of these contacts established, this naturally led us to the next topic: what is the impact of the strengths of different protein-polymer interactions on the physical properties of PIX?

3.3.2 On the effects of electrostatic interactions on PIX behavior

The interactions between protein and polymer are crucial for achieving the dynamic behavior of PIX, as the polymer both provides the driving force for expansion/contraction and preserves connections between the proteins in the expanded state to maintain crystallinity. In Chapter 2, we determined that the acrylate/acrylamide copolymer p(Ac-Am) provided the desired expansion behavior in the original PIX. However, we also determined that when only acrylamide (or other hydrophilic precursors such as N-[Tris(hydroxymethyl)methyl]acrylamide) was used, the protein crystals disintegrated during polymerization. To further characterize this relationship, we screened multiple additional polymer precursors (**Figure 3.3**), including two negative, two positive, two neutral, and two hydrophilic monomers.

To systematically study each precursor, *F432* HuHF- Δ C* crystals were used for all PIX trials, and polymerization was always done with 1% (w/v) APS and 1% (v/v) TEMED in 4 M NaCl solutions. While all PIX could be soaked with precursors, six of the eight candidates led to crystal disintegration during the polymerization process. The remaining non-acrylate precursor that successfully formed PIX is 2-(dimethylamino)ethyl methacrylate (DMAEMA), and these PIX could also undergo ionic-strength-dependent expansion and contraction (**Figure 3.4**). This is

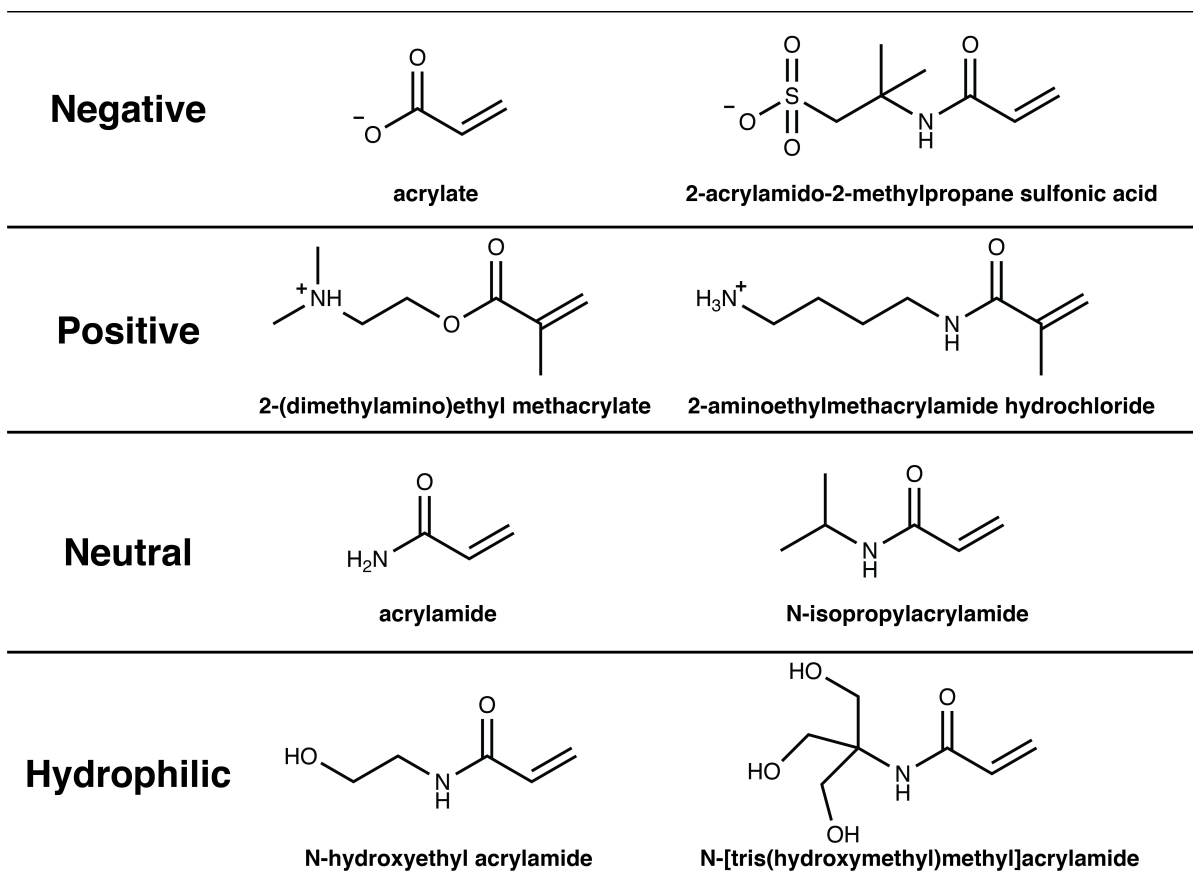


Figure 3.3 | Polymer precursors tested in this study.

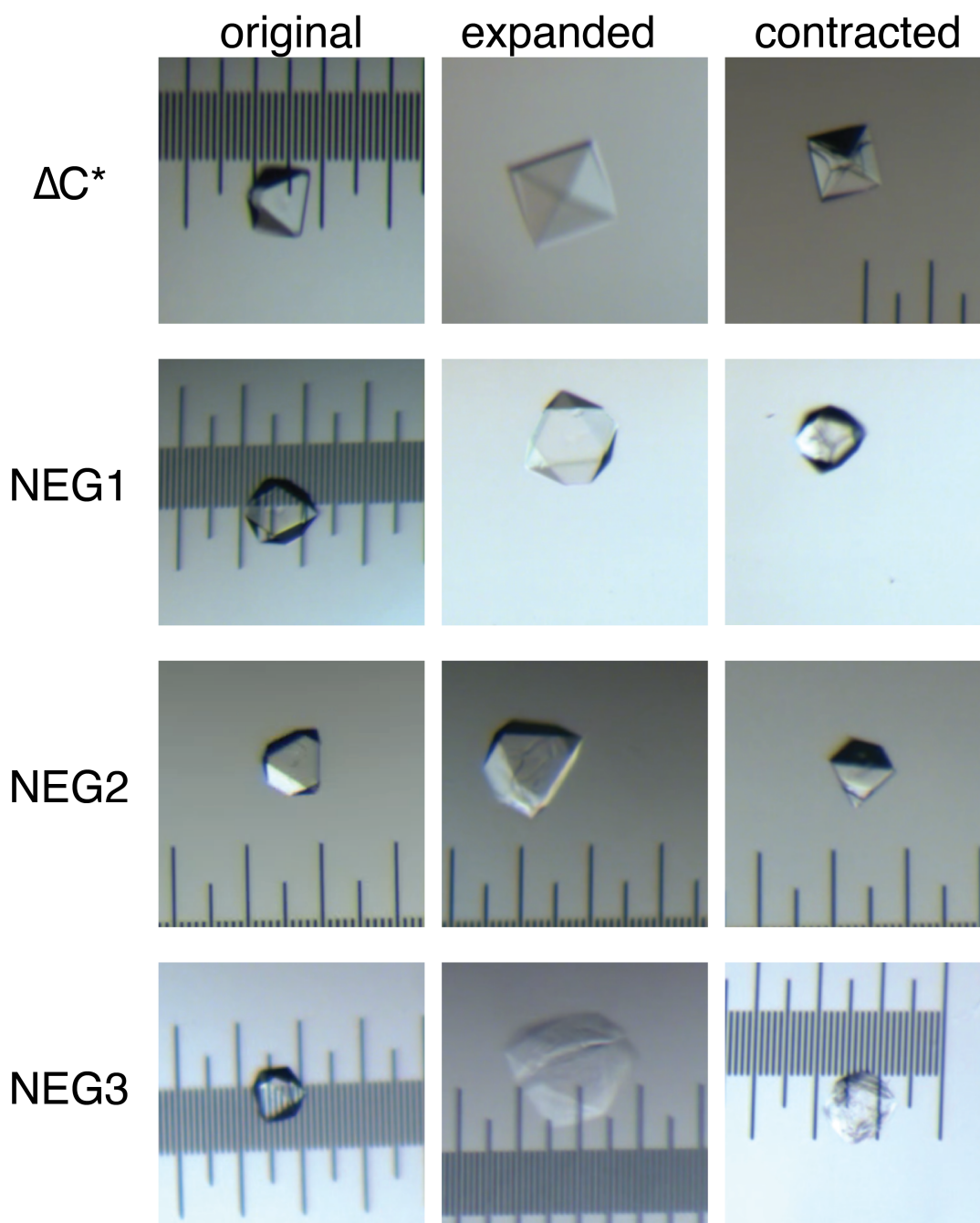


Figure 3.4 | Behavior of DMAEMA-based PIX. Light microscopy images of PIX constructed using DMAEMA and the three negatively charged ferritin variants and ΔC^* (also negatively charged). The three columns correspond to after polymerization (left), during expansion (middle), and after contraction (right). The separation between the major ticks of the ruler is 100 μm .

consistent with a charge-repulsion-mediated expansion mechanism (acrylate is negative, DMAEMA is positive), however it does not explain why the other two charged polymers cannot form PIX. The electrostatic polymer sidechain interactions with the protein surface should be similarly strong, unlike the hydrophilic and neutral precursors that should have relatively weak protein-polymer interactions, so the reason that these molecules lead to crystal dissolution is unclear. One remote possibility is that the two precursors that work (acrylate-acrylamide and DMAEMA) have carboxylate/carboxylate ester functional groups, while the remaining precursors instead have amide groups. This may lead to a loss of specific protein-polymer interactions that are essential for PIX formation, however future experiments are required to assess this hypothesis (such as using the carboxylate ester variants of the two remaining charged precursors or testing the amide variant of DMAEMA).

We next sought to evaluate the effect of protein surface charge on mediating protein-polymer interactions and overall PIX behavior. To do so, we generated six new ferritin variants with varying numbers of charge mutations to endow them with distinct surface charge distributions (**Figure 3.5**). Compared to the original HuHF- ΔC^* , which is slightly negatively charged ($pI = 5.2$), the HuHF variants NEG1, NEG2, and NEG3 are even more acidic. NEG2 is the most extreme, having seven additional negatively charged residues (168 per cage; $pI = 4.54$), NEG1 has three mutations (72 per cage; $pI = 4.86$), and NEG3 has its four mutations localized near the 4-fold axis. POS1, POS2, and POS3 are positively charged counterparts to the NEG variants. The properties of all variants are shown in **Figure 3.5** and **Table 3.1**. Unfortunately, POS1 and POS3 both formed inclusion bodies during overexpression, leading to very low yields during reconstitution of the cage. Consequently, these two variants were excluded from characterization.

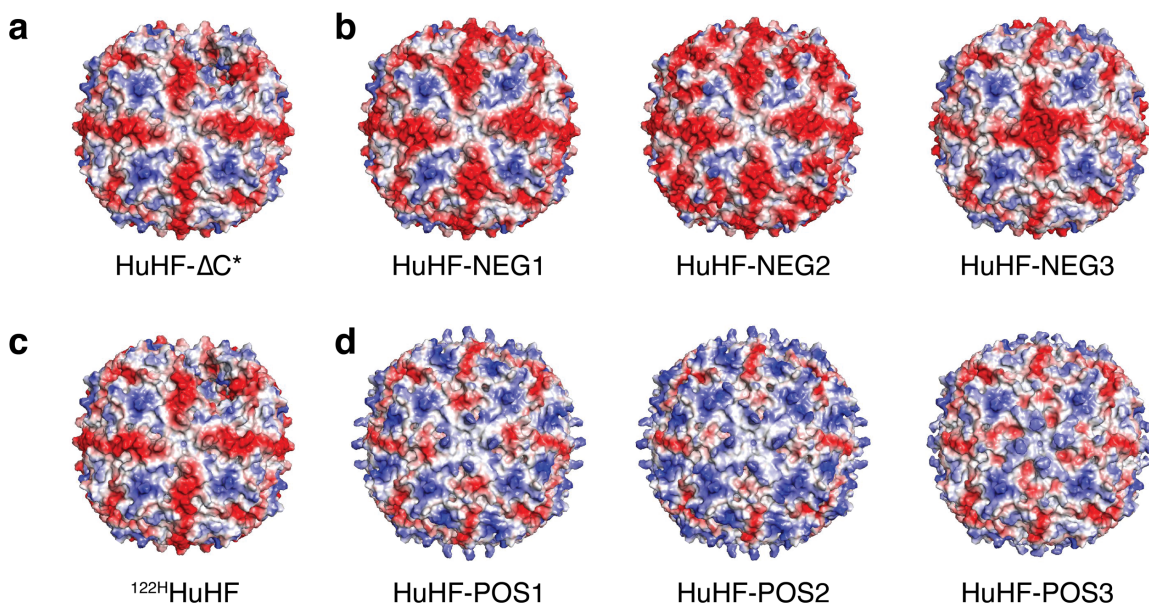


Figure 3.5 | Electrostatic maps of all ferritin variants, as viewed down the 4-fold axis. a, The native HuHF variant, devoid of all cysteines (ΔC^*). **b,** The negatively charged variants. **c,** The T122H HuHF variant for protein MOF. **d,** The positively charged variants. The protein surfaces are colored by charge, ranging from $+5 k_B T/e$ (blue) to $-5 k_B T/e$ (red).

Table 3.1 | Properties of ferritin variants used in this study.

	Protein variants	Mutations	Lattice symmetry	Packing interaction	pI	zeta potential
1	HuHF- ΔC^*	NONE	F432	metal binding Ca^{2+} non-covalent	5.12	1.13 ± 0.12 mV
2	T122H HuHF	T122H	I432	linker-mediated metal binding	5.12	N/A
3	HuHF-POS1	A18K, N25R, E90K, N109K, E162R	N/A	non-covalent	5.91	N/A
4	HuHF-POS2	A18K, E90K, N98R, A102K, H105K, N109K, D123K, E162R	F432	metal binding (Ca^{2+}) non-covalent	6.73	9.17 ± 1.24 mV
5	HuHF-POS3	E90K, E94R, G101R, E162R, G164R	N/A	metal binding (Ca^{2+})	5.91	N/A
6	HuHF-NEG1	A18E, A102E, H105E	F432	metal binding (Ca^{2+})	4.85	-8.22 ± 0.16 mV
7	HuHF-NEG2	R9D, A10E, R22E, A102E, H105E, Q112E, K119E	F432	metal binding (Ca^{2+})	4.54	-26.87 ± 0.60 mV
8	HuHF-NEG3	R90E, G159E, A160E, L165E	F432	metal binding (Ca^{2+})	5.06	-23.17 ± 0.40 mV

To explore the effect of surface charge in isolation, all HuHF variants were crystallized into diamond-shaped cubic *F*432 crystals (**Table 3.1, Figure 3.6**) and infused with the same 10% (w/v) acrylate monomers. The identical lattice parameters of all lattices were confirmed by SAXS (**Figure 3.6**). As shown in **Figure 3.7**, light microscope imaging clearly revealed that all NEG-variant PIX exhibited dynamic expansion/contraction behavior resembling that of HuHF- ΔC^* PIX. However, while the PIX based on the POS2 variant did expand slightly during the polymerization step (**Figure 3.9b**) and exhibited a solvent diffusion ring, they did not expand upon transfer into water, potentially indicating that the electrostatically favorable protein-polymer interactions may be too strong (or perhaps too neutrally charged), preventing expansion of the lattice via acrylate self-repulsion.

We next characterized the expansion rates of each NEG variant PIX using SAXS, using ΔC^* PIX as a reference. Due to the complex composition of PIX, the kinetics of molecular scale interactions (electrostatic, hydrogen bonds, van der Waals, metal coordination) cannot be disentangled. Instead, we determined an expansion rate (k , in $\text{\AA}/\text{s}$) via linear fit to the macroscale expansion of PIX, providing an intuitive quantitative parameter from a system design perspective (**Figure 3.8**). Each PIX variant was tested at two different polymer concentrations: 5.0% and 10.0% (w/v). HuHF- ΔC^* is somewhat negatively charged already; thus, as the concentration of polymer increases, so does the charge repulsion within the PIX, reflected by faster expansion rates (**Figure 3.8**). For all experiments, the X-ray beam was used as the radical initiator, creating the observed initial lag time, which is longer for lower polymer concentrations. 5–10% polymer led to relatively uniform expansion for all variants, with NEG2 exhibiting more variation, potentially due to instabilities associated with the very large total negative charge within the PIX.

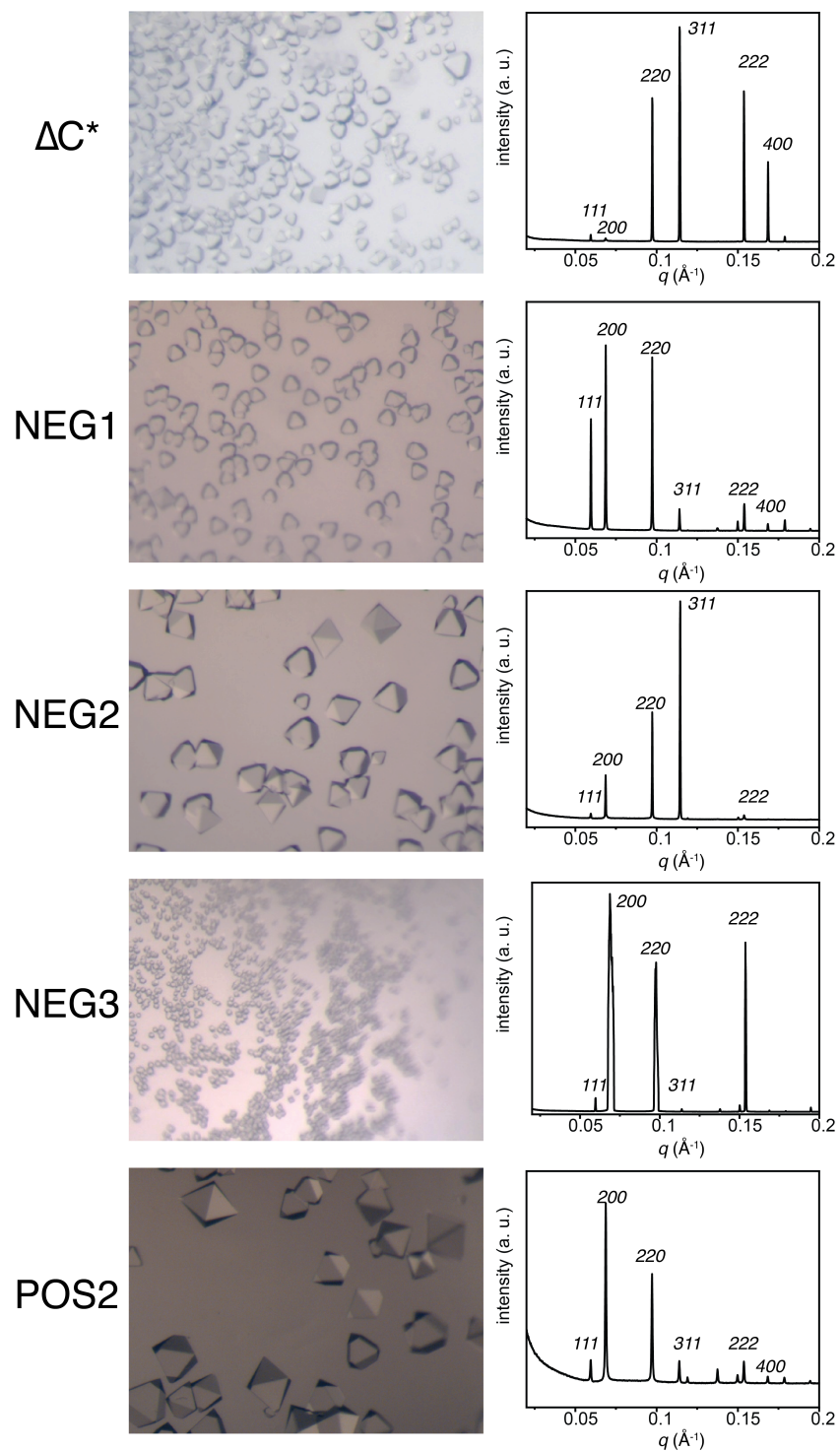


Figure 3.6 | Initial characterization of *F432* symmetry crystals for the different charged ferritin variants. For each variant, light microscopy images are shown at left, and corresponding SAXS patterns are shown at right.

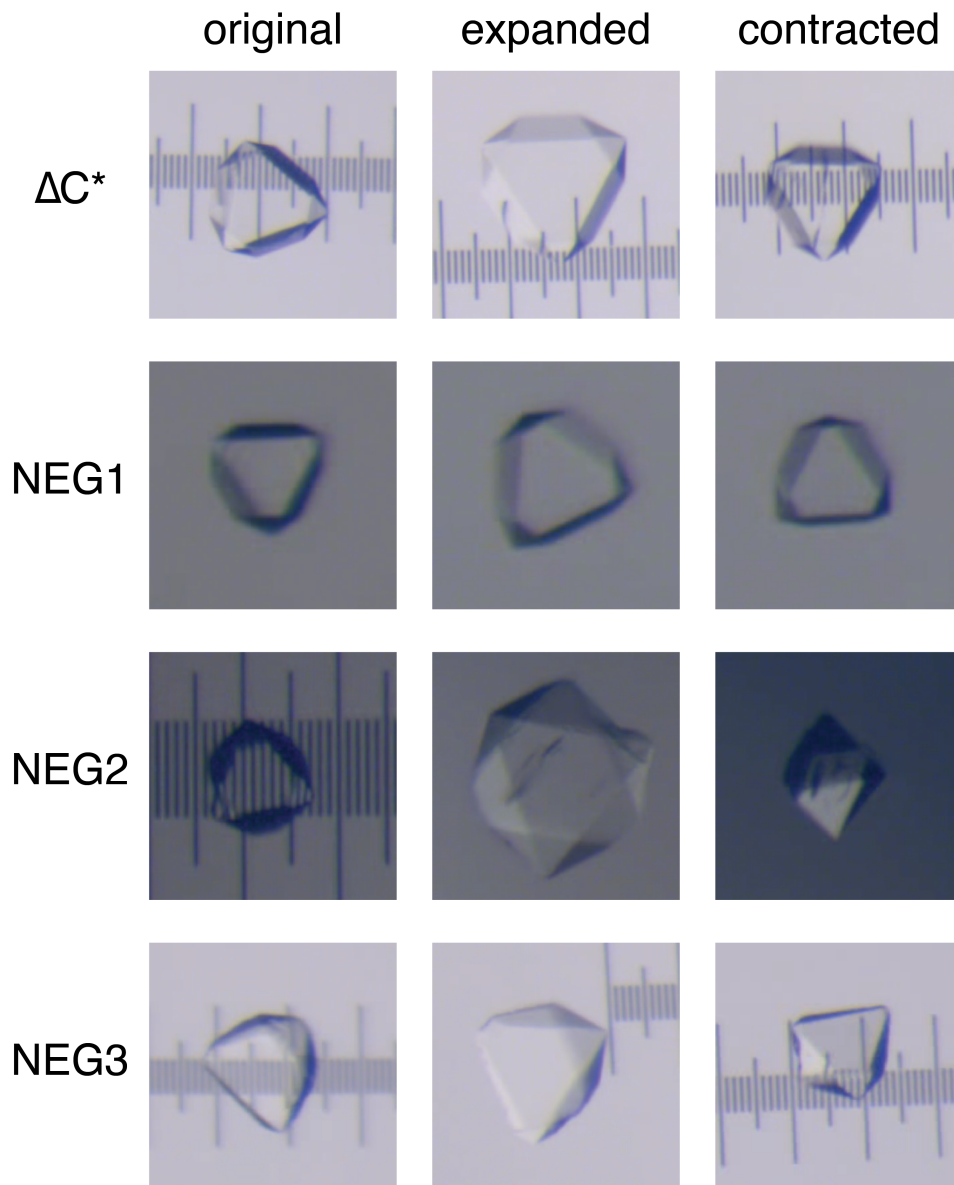


Figure 3.7 | Expansion behavior of *F432*-symmetry pAc-infused PIX constructed from different negatively charged ferritin variants. The three columns correspond to after polymerization (left), during expansion (middle), and after contraction (right). The separation between the major ticks of the ruler is 100 μm .

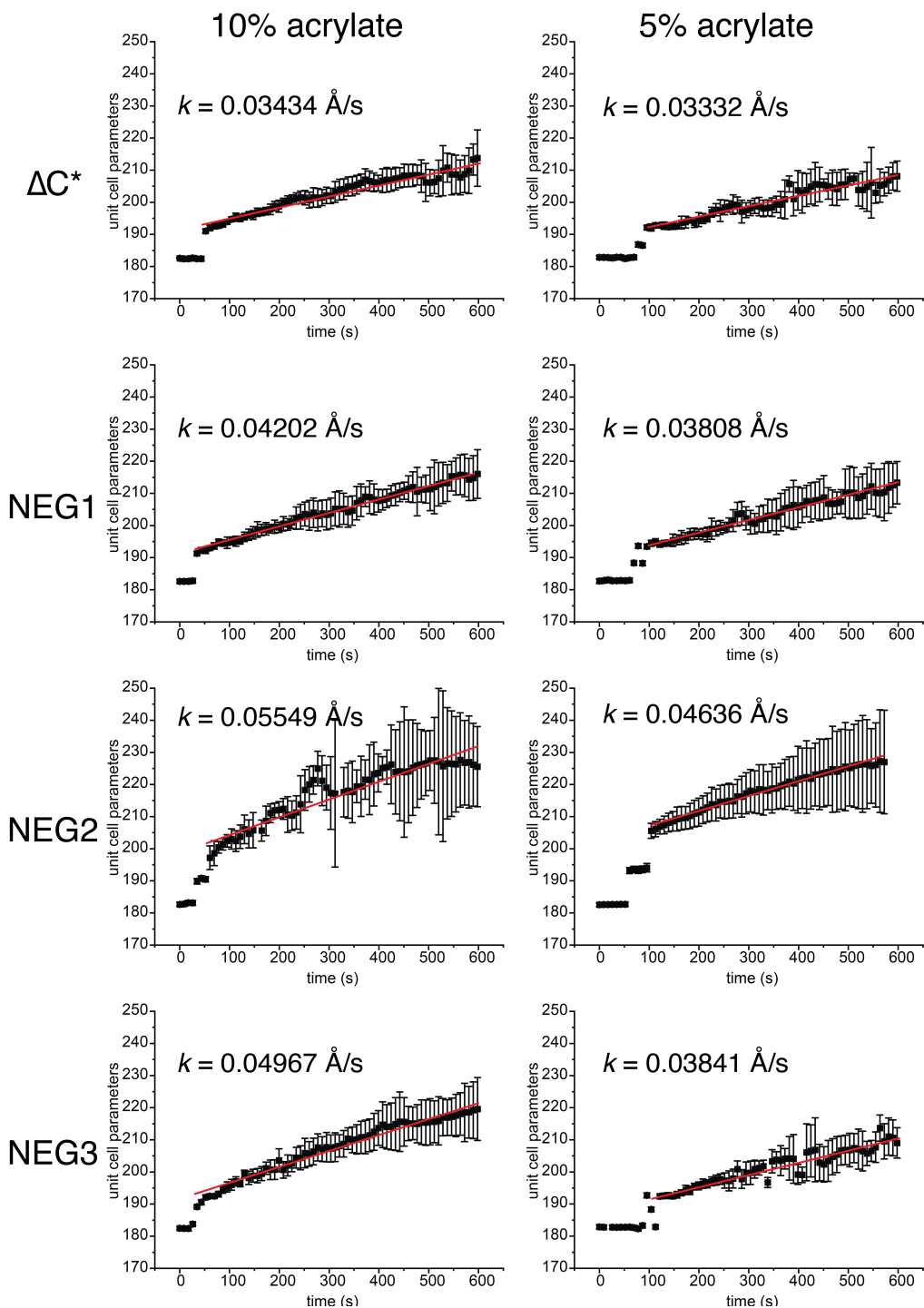


Figure 3.8 | Expansion behavior of negatively charged PIX variants, as determined by SAXS. Length of the cubic unit cell lattice parameter is plotted as a function of time, with the expansion rate k ($\text{\AA}/\text{s}$) corresponding to the slope of the linear fit (red lines) indicated for each sample. As radical initiation is induced by the X-ray beam (at $t = 0$ s), the initial delay observed in all samples reflects the polymerization step that precedes expansion. For this reason, lower polymer concentrations exhibit longer lag times. Only data during the expansion process was used for linear fitting.

We next sought to understand the relative importance of net charge versus localized charge for PIX expansion behavior. We observed that higher concentrations of negatively charged pAc polymer led to greater rates of expansion, and that when comparing within individual polymer concentrations, more negatively charged variants (*e.g.*, compare ΔC^* , NEG1, and NEG2) also expanded at faster rates. Both results are consistent with a charge-repulsion-based model of PIX expansion, where increasing the amount of negative charge of either the polymer or the protein leads to stronger responses in low ionic strength environments. Interestingly, though NEG3 has only one more negatively charged mutation than NEG1, PIX of the former swelled $\sim 18\%$ faster than the latter (and $\sim 45\%$ faster than ΔC^*) with 10% pAc, though their rates of expansion were comparable for 5% polymer PIX. Similarly, though the zeta potentials of NEG2 (with seven negative mutations) and NEG3 are very similar (**Table 3.1**), PIX of the former expanded more quickly than the latter at all polymer concentrations. Taken together, these observations indicate that mutations near the four-fold axes, which face the void space of the 6 nm chambers (where the polymer chains are expected to localize *in crystallo*), have a greater impact on the expansion rate per mutation than an isotropic distribution of negative charge (NEG3: +11.16%/mutation, NEG2: +8.80%/mutation, NEG1: +7.45%/mutation, relative to ΔC^* PIX with 10% polymer), though NEG2 still expands at the greatest absolute rate (61.59% faster than ΔC^* PIX with 10% polymer).

Interestingly, although 10% (w/v) pAc-infused POS2 PIX did not expand when placed into DI water, 0.1% (w/v) acrylate (*i.e.*, 9.9% (w/v) acrylamide)-infused POS2 PIX exhibited similar behavior to the negatively charged proteins, as evidenced by light microscopy and SAXS (**Figure 3.9**). POS2 has eight additional positively charged residues on its surface, which has two consequences that we attribute to the above behavior: significantly increased protein-protein repulsion and significantly stronger protein-acrylate interactions. This means that the polymer-

polymer repulsion that drives expansion in negatively charged PIX is mitigated due to the large number of acrylate sidechains that can be satisfied by salt bridges with the protein surface, interactions that only get stronger at low ionic strength. Acrylate concentrations as low as 1% produced similar behavior to 10%; expansion only occurred at acrylate concentrations around 0.1%. This low concentration of acrylate prevents charge neutralization between the polymer side chains and protein surface such that upon transfer into DI water, the crystals expanded, which we hypothesize to be driven by protein-protein like-charge repulsion instead of polymer-mediated expansion. However, these crystals did not retain their shape well and could not contract to their original state (**Figure 3.9**), likely due to the relatively weak polar (but not charged) protein-polymer interactions, which cannot preserve protein-protein connectivity and induce contraction.

In summary, we have systematically studied the effect of varying the surface charge of ferritin cages on the dynamic behavior of PIX. We observed that the total quantity, distribution, and sign of the protein charge can lead to dramatic changes in PIX expansion. Despite this varied behavior, all phenomena can be rationalized under our charge-repulsion based model of PIX expansion and contraction and new variants should be straightforward to conceptualize. Increasing the total amount of like-charge interactions (through higher concentrations of charged polymer or protein surface electrostatics) leads to more rapid expansion behavior, but may become less stable under extreme circumstances (*e.g.*, in the case of the very negatively charged NEG2 variant). Instead, more limited numbers of charge mutations can be placed at the 4-fold axes, where they face the cavities of the PIX lattice and interact more directly with the polymer sidechains, to more efficiently (per mutation) vary the PIX expansion rate. Additional experiments would more rigorously confirm these explanations, however, the fact that so many distinct behaviors fit neatly under a single molecular mechanism suggests that it is a robust model of the macroscale dynamics

of PIX. Preliminary MD simulations of PIX systems that give atomically detailed insights into these interactions will be discussed in Sections 3.5 and Section 3.6.

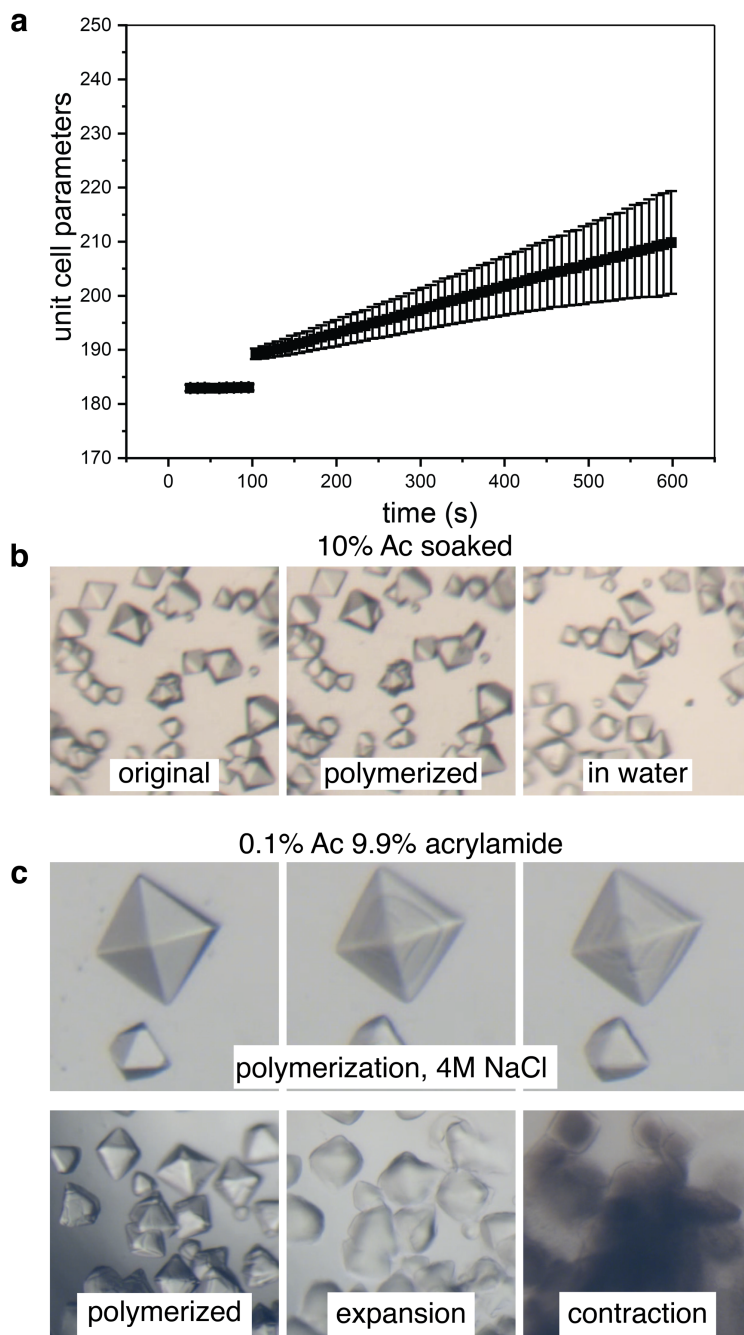


Figure 3.9 | Characterization of POS2 variant PIX. **a**, Expansion of pAm infused POS2 PIX, as quantified by SAXS. **b**, Light microscopy images of pAc infused POS2 PIX, which retain their shape but do not expand, and **c**, pAm infused POS2 PIX, which can expand but do not contract with high fidelity.

3.3.3 Exploring PIX formation with other proteins

Having now established that multiple different ferritin lattices can be used to construct PIX with tunable dynamic properties, we sought to explore a final experimental variable: the identity of the protein used to form the crystal lattice, which can provide different symmetries, porosities, and packing densities. We first tried a simple extension of the previous PIX by using horse spleen ferritin, which also crystallizes into *F432* lattices via metal (cadmium)-mediated protein-protein interactions at the 2-fold axis. However, Cd^{2+} ions formed precipitates with the polymer precursors, preventing their diffusion into the lattice, rendering the solution conditions required for crystallization unsuitable for PIX.

We tested seven other proteins that are known to readily crystallize into lattices with very different properties, including solvent content, protein-protein interactions, and protein shape and surface charge/isoelectric point. Illustrations of the protein surfaces (colored by charge) and lattice packing are shown in **Figure 3.10**, and further details about each crystal lattice are given in **Table 3.2**. As shown in **Figure 3.11**, three of the tightly packed proteins (lysozyme²⁶, proteinase K²⁶, and enterococcal surface protein (partial N-terminal region, ESP405)) were successfully soaked in polymer precursors under varying conditions (all soaking solutions contain 25–50% mother liquor). However, lysozyme and proteinase K crystals both dissolved quickly during the polymerization process. ESP405 dissolved slowly during polymerization (1% APS/TEMED, 4 M NaCl) and much more rapidly after transfer to water. We attribute the fragility of these PIX to poor permeation of the polymer precursors throughout the crystals, as their tight packing (<40% solvent content) likely prevented the formation of a robust hydrogel network such as those found in ferritin PIX. Consistent with this hypothesis, streptavidin crystals, which have a slightly higher solvent content,

successfully formed polymers throughout its channels, but dissolved upon transfer to water, indicating that the protein-polymer interactions are too weak to preserve the PIX structure.

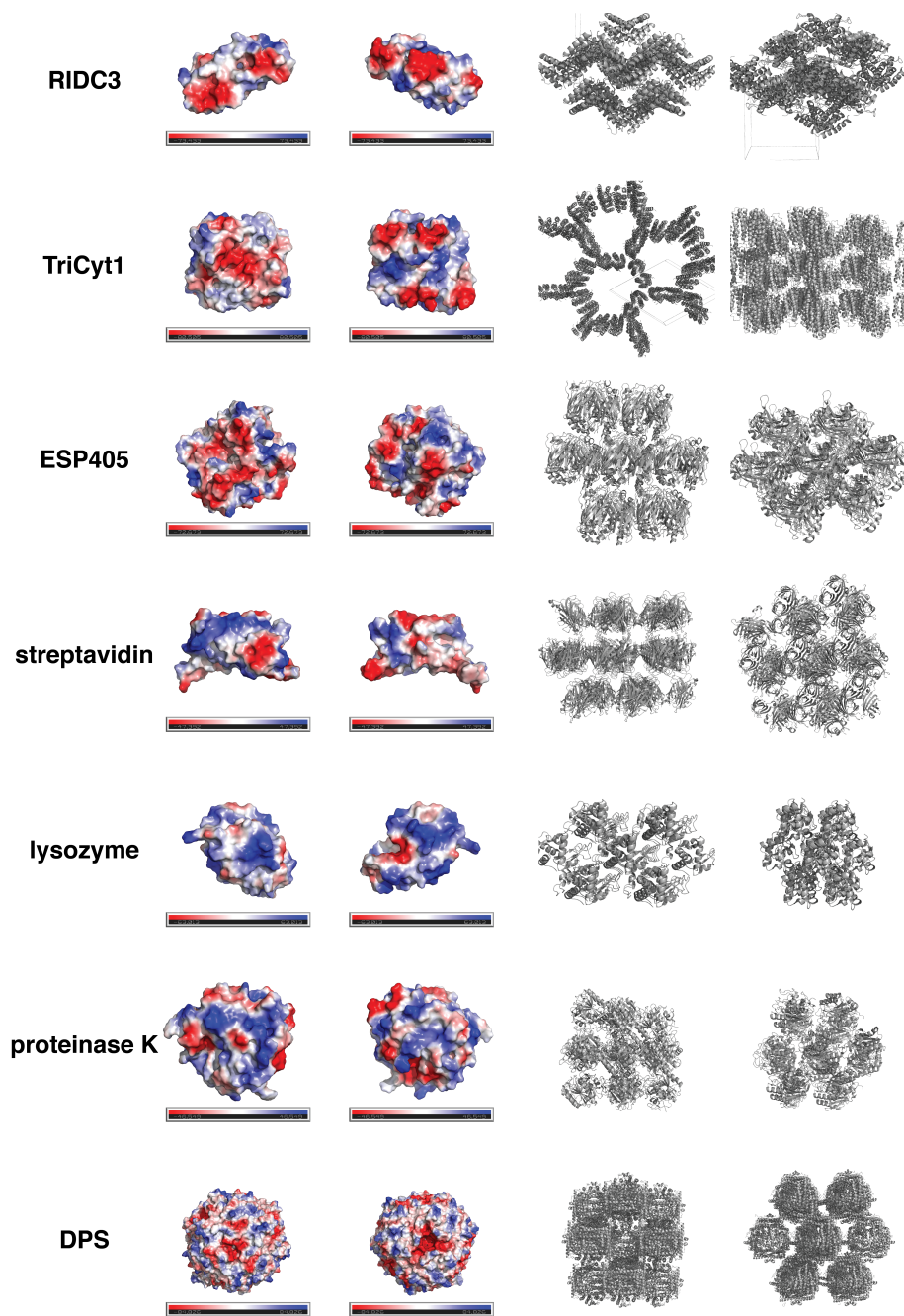


Figure 3.10 | Alternative proteins explored as new scaffolds for PIX. Electrostatic potential surfaces for each alternative protein (two orientations) are shown at left, colored by charge: $+5 k_B T/e$ (blue) to $-5 k_B T/e$ (red). The 3D packing of each protein in their crystal lattices are shown at right in two different orientations, highlighting their distinct symmetries, molecular densities, and shapes/porosities of the solvent channels.

Table 3.2 | Crystal packing information for all other proteins tested as new scaffolds for PIX.

	Protein	Solvent Content (porosity)	Lattice symmetry	Packing interaction	pI
1	RIDC3	42.92%	P2 ₁ 2 ₁ 2	non-covalent	5.7
2	TriCyt1	68.32%	P321	non-covalent	5.68
3	ESP405	37.26%	P1	non-covalent	4.89
4	Streptavidin	46.67%	I4 ₁ 22	non-covalent	6.04
5	lysozyme	40.18%	P4 ₃ 2 ₁ 2	non-covalent	10.7
6	proteinase K	40.93%	P4 ₃ 2 ₁ 2	non-covalent	7.80
7	DPS	53.00%	P2 ₁ 2 ₁ 2	non-covalent	5.53
8	HoSF	61.70%	F432	Cd-metal binding	5.36

Surprisingly, we found that PIX constructed from the protein RIDC3,²⁷ which packs into a low-porosity crystal (42.92% solvent content), could indeed reversibly expand and contract following soaking and polymerization (**Figure 3.11**). Thus, porosity is not the sole variable of importance for judging the suitability of protein lattices for new PIX. Looking more closely at the crystal structure, we observed that RIDC3 has a layered structure (with smaller channels connecting the layers) that enables lamellar polymer formation reminiscent of the ferritin *H32*-symmetry PIX. Moreover, RIDC3 has several positive sidechains facing into the solvent channels that can form favorable interactions with the acrylate groups of the polymer, in contrast with streptavidin, whose solvent channels are lined with negatively charged residues. This observation

is again consistent with a charge-centric mechanism of protein-polymer interactions, which must be of sufficient strength to preserve the crystallinity of PIX during expansion yet not so strong as to neutralize the polymer charge. Of course, well-connected solvent channels are also necessary to form the continuous hydrogel network. This is reflected by the behavior of another four-helix bundle variant (TriCyt1),²⁸ which has a solvent content >50% and well-connected solvent channels, whose PIX could also expand and contract (**Figure 3.11**). Finally, DPS,²⁹ another spherical protein resembling ferritin (but about half the diameter), forms a highly porous and well-connected lattice when crystallized with very high concentrations of polymeric precipitating agents. As these crystals do not exhibit any other obvious impediments to PIX formation, we hypothesize that these agents occupy the void space in the lattices, preventing intrusion of the polymer precursors and thus precluding the formation of PIX. This limitation is inherent to the crystallization condition, and would require either screening for alternative conditions (and/or a different lattice) to be utilized instead. While additional experiments are required to definitely confirm this hypothesis (*e.g.*, testing ferritin PIX in the presence of such precipitants), these results further implicate the necessity of uninhibited transport of polymer precursor throughout the lattices to enable correct polymer formation, which may not be dictated by crystal packing/porosity alone.

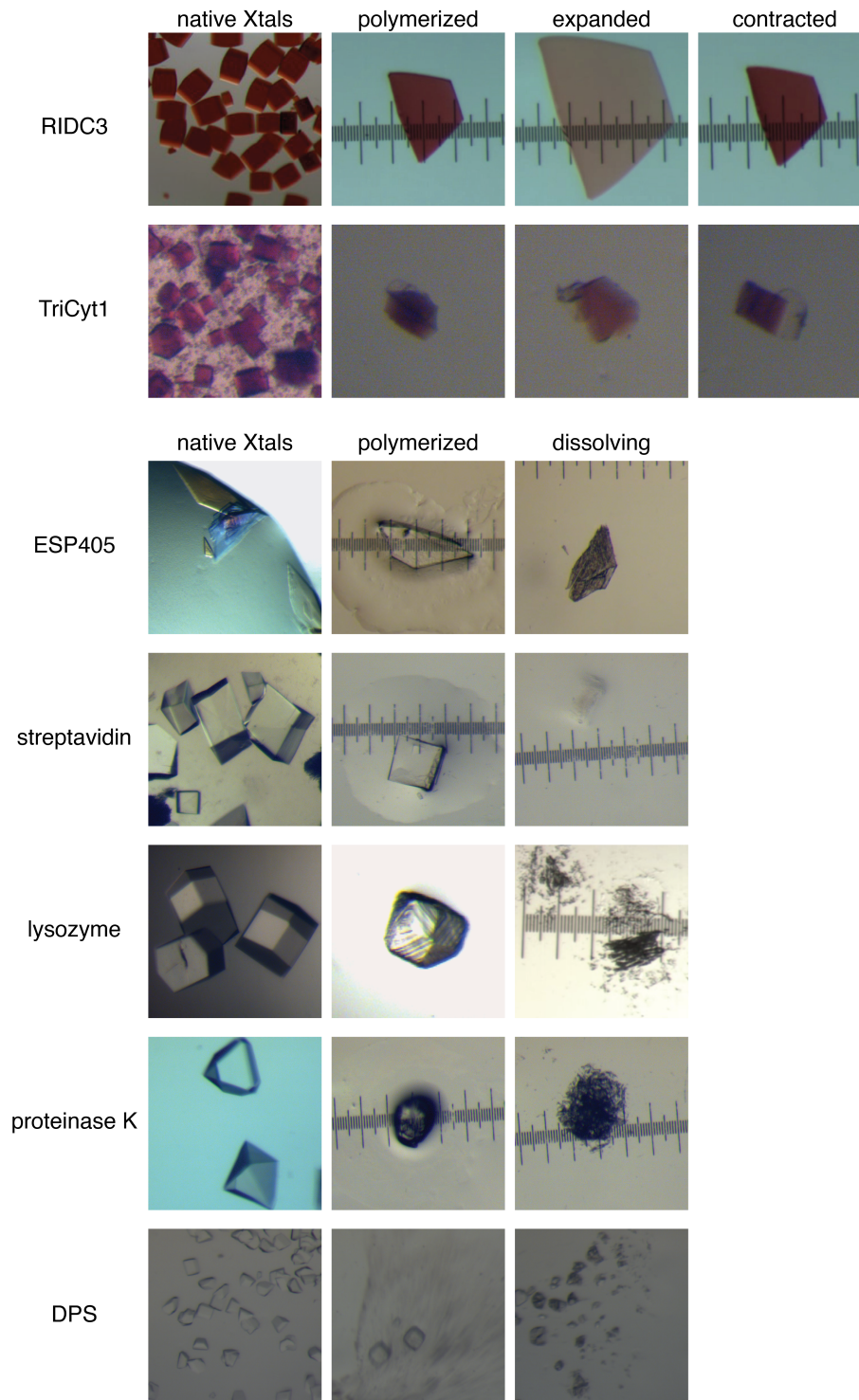


Figure 3.11 | Light microscopy images of the different protein crystals tested for the systematic variation of protein scaffold. Image columns are labeled according to the different behaviors of each PIX, which varied widely depending on choice of protein crystal. While PIX formed from the two cytochrome *cb*₅₆₂ variants (top two rows) could expand and contract once, all others failed to achieve the dynamic behavior of ferritin PIX.

In summary, multiple protein variants that crystallize into very different lattices indeed exhibited highly variable tolerance for PIX synthesis. We determined that low porosity crystals are generally not well-suited for PIX, which probably reflects the inability of the polymer precursors to permeate throughout the lattices well enough to form continuous polymer chains, leading to dissolution early on. This effect may also manifest due to the presence of excessive quantities of crowding agents required for crystallization of some proteins (*e.g.*, DPS), as these molecules occupy the void volume of even highly porous crystals, reducing the effective volume accessible to polymer precursors. However, tightly packed crystals can still be utilized if there are regions of continuous volumes for the polymer network to form, as seen in the layered structure of RIDC3 PIX. Our results suggest that moderate numbers of positive protein sidechains along the solvent channels are important for protein-polymer interactions, leading to dynamic PIX (RIDC3, TriCyt1) when present, or dissolution upon transfer to water (streptavidin) when absent. The above patterns all consistently point to solvent channel continuity and sufficiently strong protein-polymer interactions as two critical variables to consider when developing new PIX.

3.3.4 Atomistic simulations of ferritin cages in the presence of polymer chains

As described in Section 3.3.2 (and to some extent in Section 3.3.4), there is a very clear connection between PIX expansion behavior and the strength of protein-polymer interactions, which appear to be primarily charge-based. However, thus far our measurements have been limited to the macroscopic observables of 1) whether a PIX variant expands or not, 2) the rate of change in lattice spacing during its expansion, and 3) whether it can contract. To explore the relationship between these macroscale behaviors and the protein-polymer interactions, we turned to atomistic MD simulations (in collaboration with Felipe Jimenez-Angeles and Monica Olvera de la Cruz at Northwestern University) to gain insight into their nature at molecular resolution. As a reference,

we carried out two simulations of single HuHF- ΔC^* ferritin cages in solution with 10% polymer, one with neutrally charged polyacrylamide (pAm), and the other with the negatively charged p(Ac-Am) copolymer. This amounts to 54 polymer chains (20 repeating units each) for a single ΔC^* cage. Each system was fully solvated by (extended) simple point charge water to yield cubic periodic boxes of ≈ 20 nm side length and neutralized, with a final NaCl concentration ≈ 50 mM. In total, the two systems contained 791,910 (pAm) and 787,917 atoms (p(Ac-Am)), and 10 ns of sampling was obtained for both.

Snapshots of the p(Ac-Am) simulations, which reflects the composition of our previously reported PIX, are shown in **Figure 3.12a** (at 0, 2.5, 5, and 10 ns), with protein cage shown as dark gray cylinders, unbound polymer chains shown as light gray lines, and polymer chains having *any* subunits within 5 Å of the protein shown as magenta sticks. Visual assessment of the trajectory revealed a qualitative but noticeable accumulation of p(Ac-Am) chains onto the protein surface over time. We observed that upon binding, individual p(Ac-Am) chains could rearrange to form new contacts with different residues, but never fully dissociated from the surface, indicating strong protein-polymer interactions. Closer inspection of the protein-polymer interactions identified them as primarily electrostatic in nature, with salt bridges forming predominantly with arginine 9 (Arg9; **Figure 3.12b**) and secondarily with the nearby Arg43 and Arg79, which together form a cluster of guanidinium sidechains at the ends of each 2-fold interface (approximately halfway between the 4-fold and 3-fold axes of the cage). Due to its other intra-protein interactions (orange dashed lines), the positioning of the Arg9 sidechain seems most amenable to forming salt bridging contacts (green dashed lines) with the acrylate groups (**Figure 3.12b**), confirming the anticipated presence of strong protein-polymer interactions.

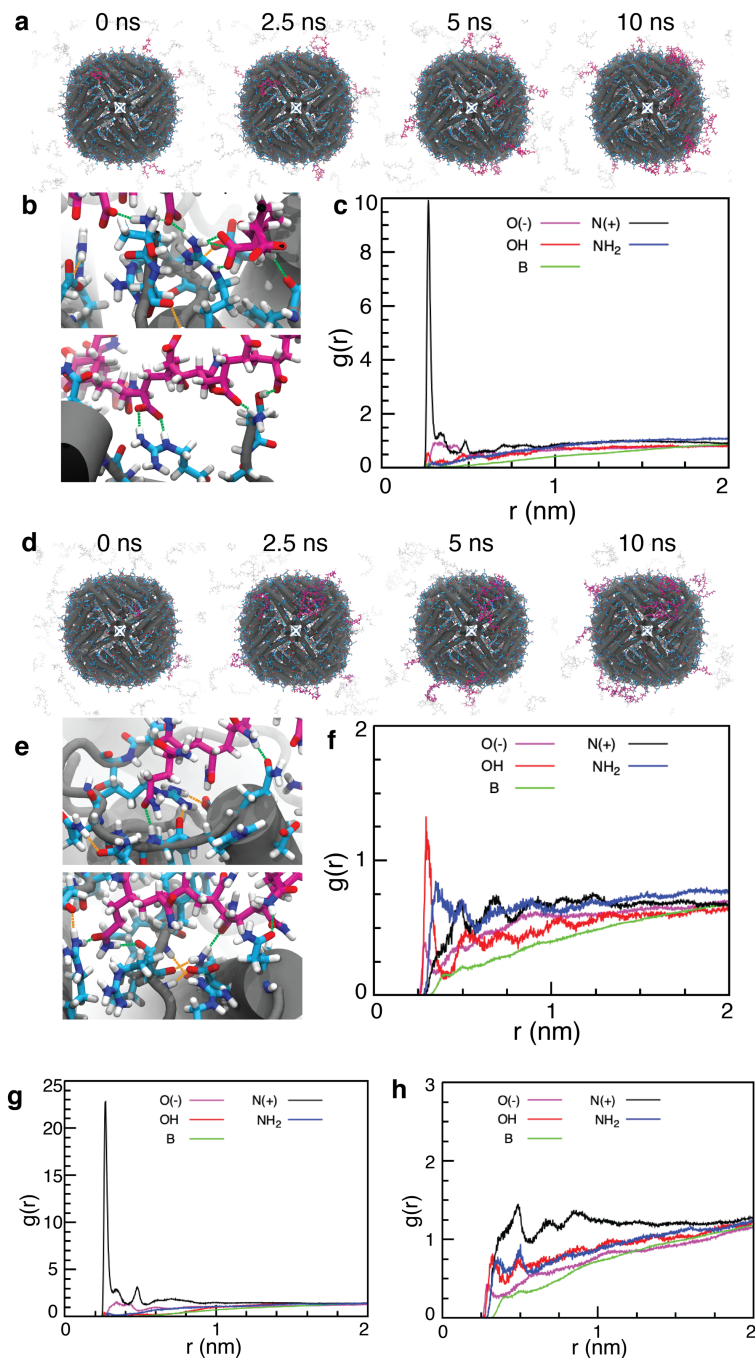


Figure 3.12 | Atomistic MD simulations of HuHF- ΔC^* in the presence of polymer chains. **a**, Snapshots of HuHF- ΔC^* with pAc. **b**, Close-ups of the inter- and intra-molecular interactions (green and orange dashes, respectively) between the polymer and the protein in **a**. **c**, Radial distribution functions of the polymer with respect to the O(-): negatively charged carboxylate sidechains N(+): positively charged lysine and arginine residues, OH, NH₂ polar amino acids, B: backbone. **d**, **e**, **f**, The analogous information as in **a-c**, but for HuHF- ΔC^* with pAm. Radial distribution functions of pAc (**g**) and pAm (**h**) with positively charged protein cage POS2 are shown at bottom, highlighting the strength of protein-pAc electrostatic interactions (**g**).

We quantified these interactions through the use of radial distribution functions (RDFs), which shows the density (normalized to bulk) of a species of interest as a function of distance from another (reference) set of atoms or molecules. RDFs can alternatively be viewed as probability distributions, with higher densities indicating more probable molecular configurations (*i.e.*, they are inversely related to the free energy as a function of distance). This relationship is given by:

$$g(r) = e^{\left(-\frac{W(r)}{kT}\right)} \quad (3.1)$$

Where $g(r)$ is the density of the species of interest at distance r , $W(r)$ is the effective pairwise interaction (*i.e.*, potential of mean force), and kT is the thermodynamic temperature (approximately 0.593 kcal/mol at 298 K. Values of $g(r) > 1$ indicate favorable interactions (*i.e.*, the species is more localized at that distance than at bulk), while $g(r) < 1$ indicates the converse. Thus, in this case, the larger the value of $g(r)$, the more favorable a particular protein-polymer interaction is.

Calculated RDFs (using p(Ac-Am) sidechains as the $r = 0$ reference) are shown in **Figure 3.12c**. This RDF is dominated by a very large peak (nearly 10x bulk density) at a distance of about 2.7 Å from the positively charged amine groups of arginine and lysine residues (“N(+)”), consistent with salt bridge geometries. In contrast, the traces for other protein groups, such as negatively charged carboxylate sidechains (“O(-)”), neutral polar interactions (“OH” and “NH2”), and the backbone all failed to accumulate p(Ac-Am) above bulk density (**Figure 3.12c**), confirming that the protein-p(Ac-Am) interactions are indeed electrostatic in nature. Comparing next to the pAm simulations, we similarly observed a qualitative increase in bound pAm chains over time (**Figure 3.12d**), however unlike the p(Ac-Am) interactions, pAm chains were highly mobile and formed relatively short-lived contacts with the protein surface. As pAm has polar sidechains but is neutrally charged, we anticipated that the protein-pAm interactions would instead be mediated by hydrogen bonding. Indeed, close inspection of protein-pAm interactions revealed

this to be the case, with hydrogen bonding observed between pAm and the protein sidechains and backbone (**Figure 3.12e**), though we note that Arg9 and Arg43 still appeared to be very common contact points for polymer binding. The relative weakness of protein-pAm interactions was corroborated by the corresponding RDFs (**Figure 3.12f**; pAm sidechains as the $r = 0$ reference), in which only the polar OH protein groups achieved a density peak greater than 1.0x at approximately 3.0 Å protein-pAm separation, more indicative of hydrogen bonding geometries. The smaller density peaks for pAm quantitatively demonstrate that the free energies of protein-acrylamide interactions are significantly reduced relative to pAc, consistent with weaker, more dynamic interactions between acrylamide sidechains and the protein surface.

To further evaluate the role of electrostatics, we repeated the above simulations after substituting HuHF- ΔC^* with the POS2 variant, which has 8 additional positive sidechains per monomer (POS2 full cage net charge = $-96e$, ΔC^* full cage net charge = $-240e$). We obtained qualitatively similar results for both RDFs (**Figure 3.12g, h**), indicating that the general patterns of polymer binding remained unchanged. We observed that the first p(Ac-Am)-O(-) peak at 2.7 Å was significantly larger for POS2 (nearly 23x bulk density; **Figure 3.12g**), reflecting a larger number interactions between the negatively charged polymer and positively charged sidechains on the protein. For pAm, the most prevalent acrylamide interaction was N(+) protein groups instead of OH (**Figure 3.12h**), but this may be a statistical effect associated with the greater number of Arg/Lys sidechains on POS2. As hydrogen bonds can interact with most all polar protein groups, the distribution of interactions can be expected to correlate with the relative population of different protein sidechains that are available for pAm interactions.

In brief, these atomistic simulations have provided a quantitative and molecularly detailed picture of protein-polymer interactions that are a crucial element of PIX. We found that charged

interactions dominate for acrylate-based polymers due to the formation of very strong electrostatic interactions with positively charged protein residues (primarily arginine). In contrast, the electrically neutral (but polar) acrylamide sidechains primarily form weaker hydrogen bonding interactions with the protein surface. Thus, while both polymers readily associate with the protein surface, the dynamism of pAm-based PIX is consistent with their experimentally observed fragility and inability to preserve lattice ordering during expansion and contraction, while strong salt-bridging protein-acrylate interactions at charged patches on the protein ensure robust protein-polymer connectivity during all stages of PIX expansion/contraction despite the overall negative charge of HuHF- ΔC^* cages. These observations were corroborated by analogous simulations with POS2, which showed enhanced (stronger) charge-based contacts for p(Ac-Am) but more subtle shifts for (still weak) pAm interactions arising from the different distribution of sidechains on the protein surface. These results are fully consistent with our electrostatics-based mechanisms for PIX behavior and provide fresh insight into how new protein/polymer pairs may be engineered to tune the properties of ferritin PIX and/or create new PIX with exciting new attributes. However, much more still remains to be explored, including new polymers, proteins (and their variants), solution conditions, and protein-protein interactions. Ultimately, achieving predictive power over PIX materials will require close collaboration of experiment and theory to understand both the behavior of PIX and how it can be tuned to achieve specific functions.

3.3.5 Coarse-grained simulations of ferritin PIX in the presence of polymer chains

Having established the importance of electrostatics for the behavior of PIX in the previous section, this final section describes preliminary coarse-grained (CG) MD simulations of complete PIX lattices carried out to gain insight into their meso-to-macroscale behavior. For these simulations, the well-established MARTINI forcefield³⁰ was used to describe the protein and

polymer residues, which were represented using two CG beads each: one for the backbone and one for the sidechain. CG p(Ac-Am) polymers have a 3:1 ratio of acrylate:acrylamide sidechain beads to match the experimental polymer composition. The resulting CG models for the polymer chains and ferritin cage are shown in **Figure 3.13a, b**. To construct the PIX simulations, four CG ferritin cages were first placed to match their corresponding positions in the HuHF- ΔC^* F432 unit cell. CG polymers were then introduced randomly to the simulation box (a total of 1080 monomers per ferritin cage, 4320 monomers total), followed by solvation with (polarizable) MARTINI waters and ions. A representative snapshot of a final system is shown in **Figure 3.13c**. All CG simulations were carried out for 500 ns to ensure full equilibration of each system and sufficient sampling to obtain well-converged RDFs with per-residue specificity.

To evaluate the accuracy of this CG representation, we recreated the CG equivalent of our atomistic HuHF- ΔC^* -p(Ac-Am) simulations above: one full cage and 54 p(Ac-Am) chains of 20 repeating units each. RDFs of the CG models are qualitatively very close to the atomistic simulations (**Figure 3.13d, e**), showing the same strong N(+) peak of about 10x bulk density, now shifted to approximately 5 Å separation due to the simplified representation of the protein/polymer sidechains. This CG artifact is what also gives rise to the slight apparent increase in structuring (defined peaks and valleys) for the other traces as well. Nevertheless, the close qualitative agreement with our all-atom simulations indicates that CG PIX simulations have the potential to be very informative, as they enable access to longer simulation time and length without sacrificing much accuracy.

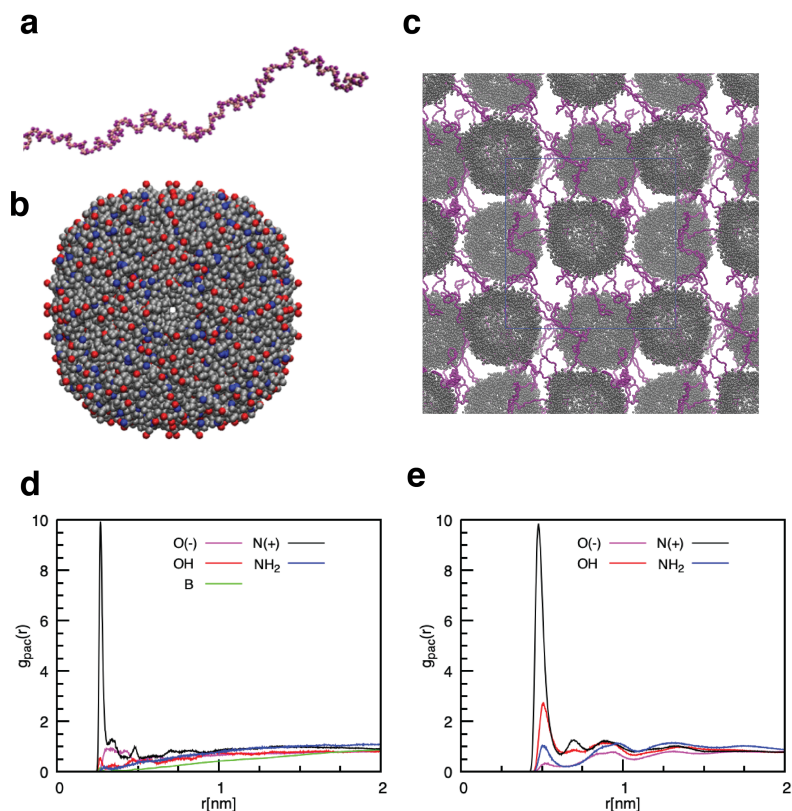


Figure 3.13 | Coarse-grained MD modeling of ΔC^* -based PIX. CG MARTINI models for the polymers (a) and ferritin cages (b). c, Render of fully constructed PIX simulation, comprising the ferritin lattice with added polymers. Polymer-protein RDFs for the CG model (d) and the all-atom representations (e). Protein atoms are labeled as O(-): negatively charged carboxylate sidechains, N(+): positively charged lysine and arginine residues, OH/NH₂: polar amino acids, B: backbone.

Table 3.3 Polymer chain compositions in coarse-grained simulation

Polymer composition	
N	Nmol
15	288
30	144
60	72
120	36
240	18
480	9

Next, we set out to study the relative magnitudes of different protein-polymer interactions in the context of the complete PIX system described above (four HuHF- ΔC^* cages in the presence of p(Ac-Am) chains). To do so, we used the magnitude of $g(r)$ at the first peak in the protein-polymer RDF (*i.e.*, the closest approach distance; r_c) as a quantitative measure of the effective interaction strength between the specified polymer and protein groups. This is shown in the RDF between p(Ac-Am) and arginine sidechains (**Figure 3.14a**), which have favorable electrostatic interactions ($r_c \approx 5 \text{ \AA}$, $g(r_c) \approx 5.5$). We calculated individual RDFs between all amino acid sidechains and the p(Ac-Am) groups and extracted their $g(r_c)$ values, as shown in **Figure 3.14b**. It was immediately apparent that arginine (R) residues form the strongest interactions, exceeding lysine (K) by about twofold. Though both residues are positively charged, the ability of guanidinium groups to form bidentate contacts with the carboxylate groups of pAc (seen in **Figure 3.12**) likely account for this difference. As expected, the negatively charged amino acids aspartate (D) and glutamate (E) have very weak interactions with p(Ac-Am) ($g(r_c) < 1$). We also note that the neutral polar amino acids glutamine (Q), serine (S), and threonine (T) have favorable p(Ac-Am) interactions ($g(r_c) > 1$) due to hydrogen bonding interactions. Somewhat surprisingly, nonpolar valine (V) residues also form relatively strong interactions ($g(r_c) > 2$) arising from short-ranged noncovalent contacts with the polymer backbone. Taken together, these results further support the hypothesis that protein-polymer interactions in PIX are primarily electrostatic and are further supplemented by weaker hydrogen bonding and noncovalent contacts. Future simulations using pAm would provide additional molecular-level insight into the behavior of pAm-based PIX.

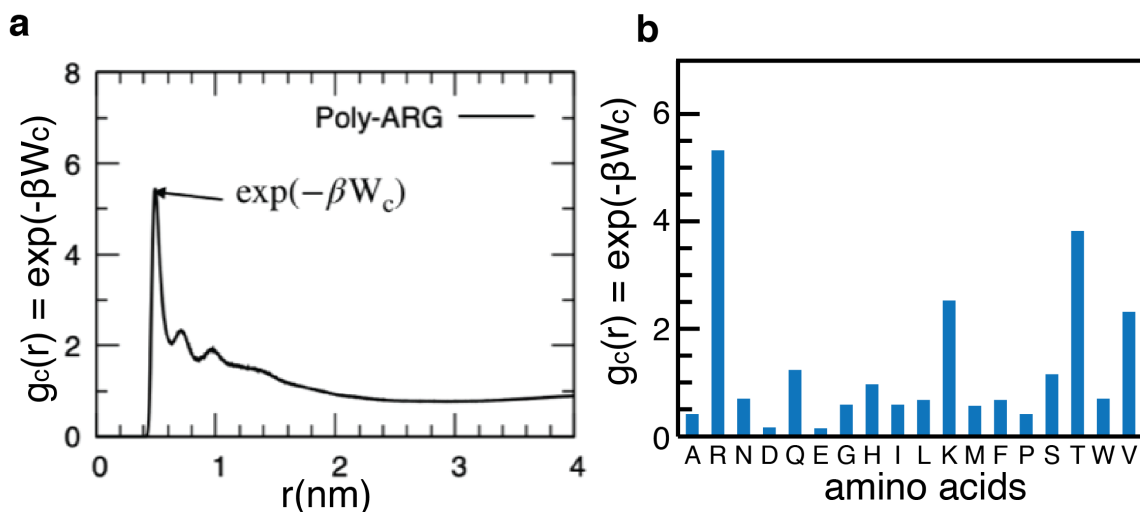


Figure 3.14 | Analysis of protein-polymer interactions in coarse-grained MD simulations. **a**, Radial distribution function $g(r) = \exp[-\beta W(r)]$ for acrylate sidechains with respect to the positively charged amino acid arginine (R). **b**, Interaction parameter $g(r_c)$ between acrylate sidechains and all possible ferritin amino acids. Larger values of $g(r_c)$ indicate stronger interactions.

As the use of simulations affords full control over the parameters of our system, we next explored the effect(s) of polymer chain length on the protein-polymer interactions. Keeping the total number of monomers (4320) constant for all systems, we varied the polymer lengths ($N = 15$ –480 monomers) and adjusted the total number of polymer chains (**Table 3.3**). Snapshots of PIX systems with $N = 15$, 240, and 480 are shown in **Figure 3.15**. We observed that polymer length had a significant effect in preserving the crystalline order of the ferritin cages. Short polymer chains ($N = 15$) were sufficient to prevent a collapse into close-packing of the cages (which occurred in the complete absence of polymer), but failed to prevent major distortions of the lattice (**Figure 3.15a**). In contrast, the longer polymer chains largely preserved the original cage positions in the *F432* lattice (**Figure 3.15b, c**), indicating an essential role of the polymer chains in maintaining the crystallinity of PIX. This is fully consistent with our previously attributed importance of protein-polymer interactions to enabling the ordered expansion/contraction behavior of PIX.

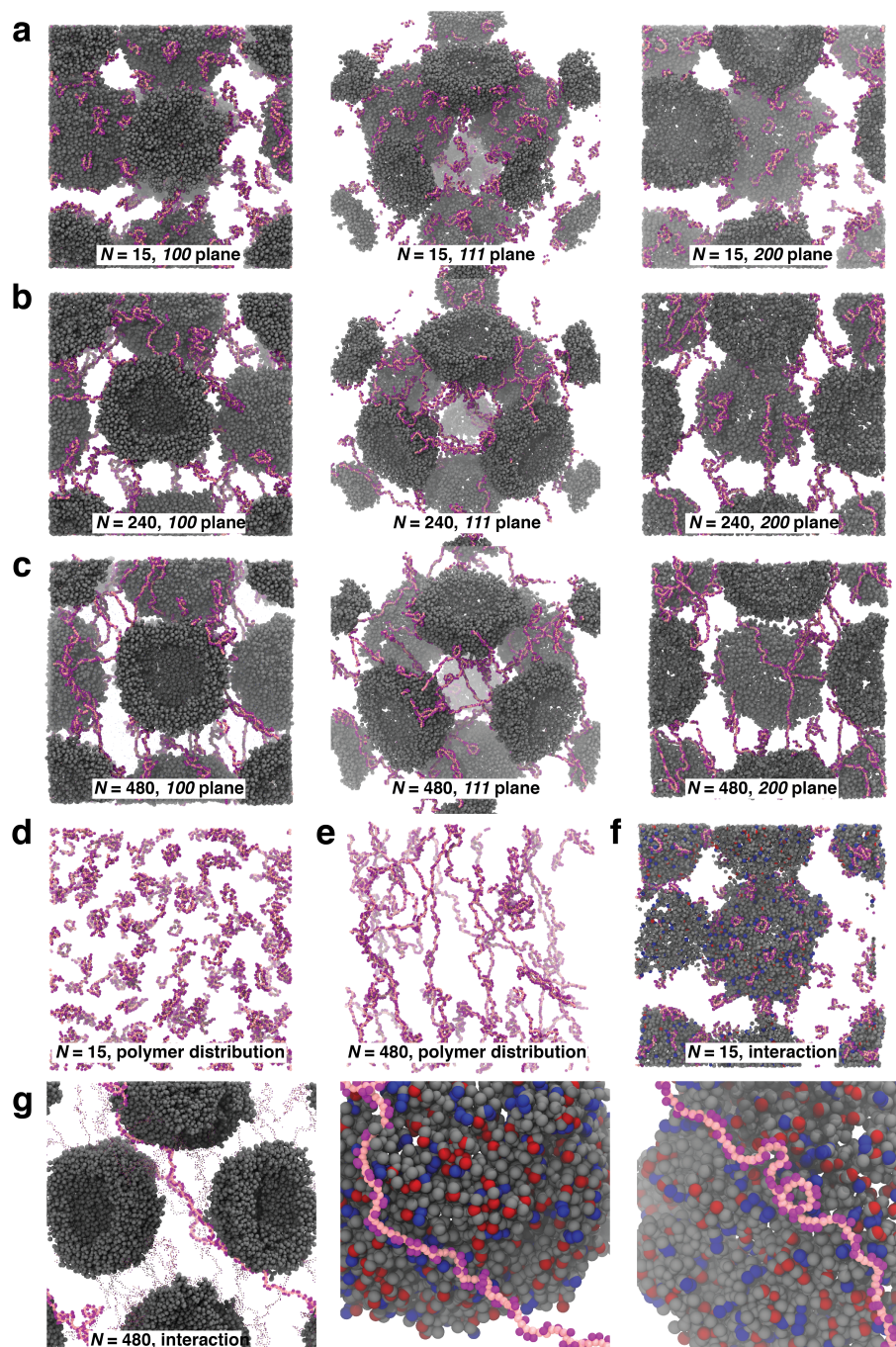


Figure 3.15 | Coarse-grained MD simulations of PIX lattices with various polymer lengths. Snapshots of CG PIX simulations viewed along the 100 (left), 111 (middle), and 200 (right) crystal planes when the polymer length $N = 15$ (a), $N = 240$ (b), and $N = 480$ (c). Distribution of polymer chains in the PIX unit cell when $N = 15$ (d) and $N = 480$ (e). Both chain lengths were well-dispersed, but only $N = 480$ polymers were observed to bridge between ferritin cages. f, Polymer-protein interactions on the ferritin surface for $N = 15$ polymer chains. g, Polymer-protein interactions when $N = 480$; a single polymer chain is highlighted (left). Detailed views of these interactions for ferritin cages 1 (middle) and 2 (right) shown in g. Red spheres represent negatively charged amino acids. Blue spheres represent positively charged amino acids.

The greater stability of the PIX lattice for longer polymer chains is reminiscent of gel transitions in other crosslinked polymeric networks. We quantified this transition by evaluating the diffusion coefficient (D) of the CG polymers (see Methods) as a function of their length. As expected, $D(N)$ decreased as N increased, eventually stabilizing for polymers of $N > 100$ monomers (**Figure 3.16**). When free in solution, the p(Ac-Am) diffusion coefficient in the long-length limit was *ca.* 10×10^7 cm²/s, but an order of magnitude lower when inside PIX (*i.e.*, when able to form interactions with the proteins) for lengths as low as $N = 60$ monomers (**Figure 3.16**). As the p(Ac-Am) chain length reached $N > 240$ monomers, D dropped nearly to zero, providing strong evidence of a gel transition that imparts structural integrity to PIX during expansion and contraction.

Finally, we present some preliminary results for POS2-pAm PIX simulations. Snapshots of equilibrated POS2-pAm PIX are shown in **Figure 3.17** for polymer lengths of $N = 30$ and 480. Somewhat unexpectedly, we found that these lattices were unstable regardless of polymer length, in contrast with experimental results showing that at least one round of expansion is possible. This may be due to the lack of electrostatic interactions afforded by acrylamide groups, which instead create weak, diffuse interactions across the whole protein surface, as well as the increased protein-protein charge repulsion. It is possible that the magnitude of polar interactions between pAm and POS2 proteins is underestimated, leading to lattice distortion, but additional simulations (including all-atom MD) would be required to more firmly identify the origins of this disagreement between theory and experiment.

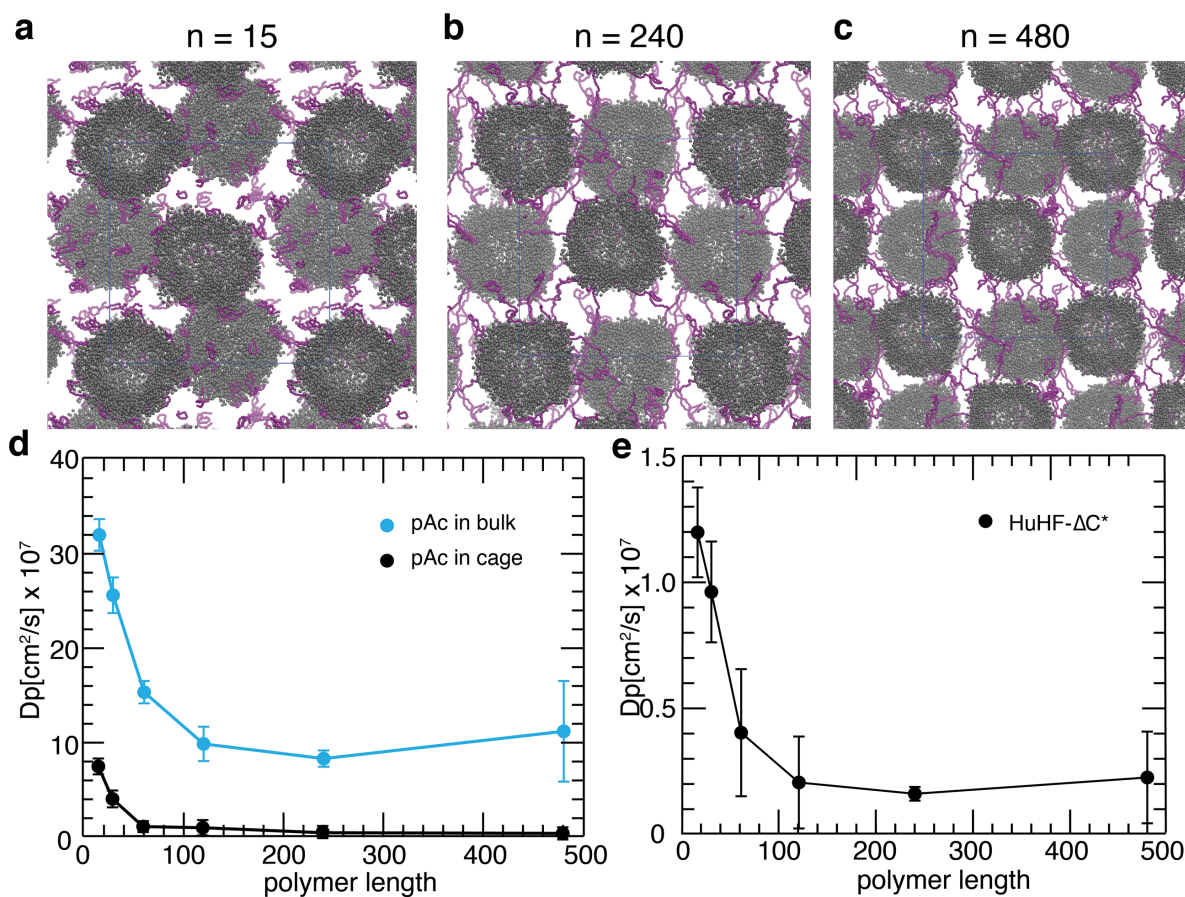


Figure 3.16 | Analysis of the effect of polymer chain length in coarse-grained MD simulations. Snapshots of the PIX simulation unit cell for negatively charged HuHF- ΔC^* cages and pAc copolymer (negatively charged) after 500 ns of molecular dynamics simulation for polymer lengths of $N = 15$ (a), $N = 240$ (b), and $N = 480$ (c). **d**, Polymer diffusion coefficient as a function of chain length when the polymer is freely dissolved in bulk solution (blue trace) or inside the ferritin PIX (black trace); only the latter was found to exhibit a gel transition for $N > 240$ monomers. **e**, Ferritin diffusion coefficient in presence of polymers of different lengths.

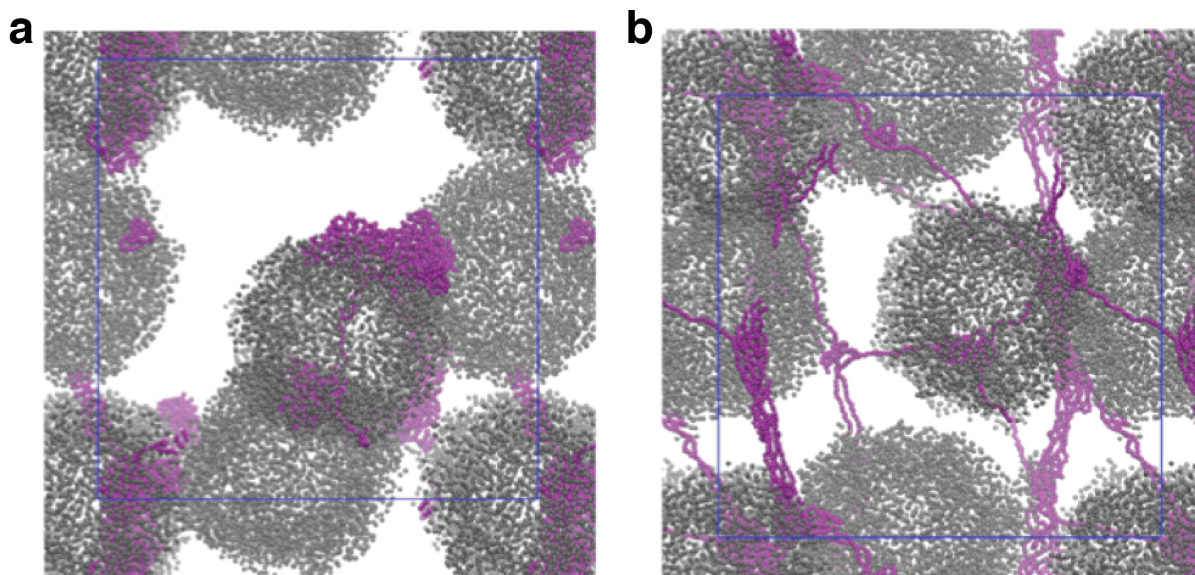


Figure 3.17 | Coarse-grained MD simulations of positively charged cage (POS2)-pAc PIX. Snapshots of the PIX lattice simulation box after 100 ns of sampling, for polymer chain lengths of $N = 30$ (**a**) and $N = 480$ (**b**). As noted above, only long polymer chains were found to be capable of bridging between ferritins, a characteristic expected to be important for the ability of PIX to remain crystalline during expansion as well as mediating robust contraction.

3.4 Conclusions

Here we have initiated a systematic investigation of several variables on the macroscopic behavior of PIX and connected these observations to molecularly detailed pictures obtained via MD simulations. Our findings underscore the principal importance of crystal packing, the need for a well-connected continuous solvent network throughout the crystal, and sufficiently strong (preferably charge-based) protein-polymer interactions with polymer chains long enough to bridge between proteins even in the expanded state. PIX are only stable when the solvent channels enable the formation of a continuous polymer network, while protein packing determines the degree of isotropy during expansion and contraction. Strong protein-polymer interactions are critical to preserve crystallinity in the expanded state and are essential for contraction, as these serve as bridges between proteins in the absence of direct protein-protein interactions. Atomistic and CG simulations highlight the nature of the protein-polymer interactions (to residue-level specificity), which is consistent with our charge-based models of PIX behavior. Together, all of these factors determine the compatibility of different protein and polymer species, which is borne out by our experimental characterization of these variables. While additional experimental and computational investigations will surely provide increasingly detailed parameters for the construction of new PIX, the results presented in this chapter are highly encouraging, as they are fully consistent with an intuitive understanding of how protein and polymer properties affect PIX that should render these materials highly predictable and tunable for different applications.

3.5 Methods

3.5.1 Design of ferritin variants

The quasi-spherical shape of HuHF is particularly advantageous for a systematic investigation of PIX design. We first proposed a library of ferritin variants that differ in 1) lattice packing symmetry, b) mode of protein-protein interactions, c) overall surface charge and specific charge distribution. The eight designed variants are listed in **Table 3.1**. The selected mutations were based on: 1) the location of the residues (distributed over the cage surface or localized to the 4-fold axis), 2) no interference with protein-protein interaction that would disrupt protein cage formation, 3) a favorable value of $\Delta\Delta G$ from calculations.

Among all the protein variants, HuHF- ΔC^* serves as the standard reference in the present study since it was used in all proof-of-principle studies. HuHF-POS1 and POS2 possess diffuse distributions of positive-charge mutations across their surfaces, while POS3 has its mutations concentrated within patches around the C_4 symmetry axes. HuHF-NE1, NEG2, and NEG3 follow the same design principle, but with negatively charged mutations. The POS2 variant was originally adapted from the literature³¹, however after purification we determined that it did not yield *F432* crystals. We hypothesized that an Arg mutation at position 25 was incompatible with the requisite crystal contacts, so we reverted this position to the native residue (asparagine) in the POS2 variant used here, which was successfully crystallized into *F432* crystals. The final variant, ^{T122H}HuHF, contains tris-His motifs at the C_3 symmetry axes capable of stably binding zinc ions in tetrahedral geometry, leaving one coordination site open to anchor each end of the bidentate hydroxamate-based organic linkers that connect the framework in a body-centered cubic 3D lattice.

3.5.2 Purification of ferritin variants

All tested ferritin variants are listed in **Table 3.1**. POS1 and POS3 formed inclusion bodies during overexpression, leading to very low yields during reconstitution of the cages. Consequently, only the remaining six ferritin variants were used for this study. For the five variants ΔC^* , NEG1, NEG2, NEG3, and T122H HuHF, the same expression and purification protocols were used with minor modification, as described below. POS2 required significant changes to the protocols.

*Negative ferritin variant expression, isolation and purification:*²⁵ Plasmids (pJexpress vector) containing each variant were amplified in and isolated from XL-1 Blue cells (via Mini-Prep), transformed into BL21 (DE3) *E. coli* cells via heat shock, and plated onto LB agar containing 100 μ g/mL ampicillin. Colonies or freezer stocks of BL21 cells containing ferritin variant plasmids were used to inoculate starter cell cultures (200 mL LB medium, 100 μ g/mL ampicillin) that were incubated for 16 hours at 37 °C with shaking at 200 rpm and used to inoculate 1 L LB cultures (10 mL starter culture per flask) supplemented with 100 mg/L ampicillin. Cells were grown at 37 °C to an OD₆₀₀ of 0.6-0.8. Overexpression of the protein was induced by addition of isopropyl β -D-1-thiogalactopyranoside (IPTG) to a total concentration of 1 mM and the cells were incubated at 37 °C for 3 h prior to collection by centrifugation (6000 \times g for 10 min). Pellets were stored at -80 °C. Frozen cell pellets were thawed and resuspended in buffer (15 mM Tris (pH 7.4), 150 mM NaCl) with 1 mM phenylmethylsulfonyl fluoride (PMSF), 5 mM DTT, and ~25 μ M lysozyme. Cells were sonicated for 12 min on ice (59 s pulse on, 30 s pulse off), and the lysate was clarified by centrifugation (12,000 \times g, 20 min, 4 °C). After collection of the supernatant by decanting, the cell pellet was resuspended in buffered 1% (v/v) Triton X-100 solution and sonicated again (on ice, same parameters). All variants were isolated as intact 24 subunit cages from the lysate supernatants and further purified.

Ferritin variants were enriched to >80% purity by heat treatment at 65 °C for 15 min and centrifugation (12,000×g, 10 min) to separate the precipitated contaminants. All variants were confirmed to be present in the clarified supernatant. This solution was then exchanged into a buffered solution (15 mM Tris (pH 8.0)), filtered, and purified using a Uno-Q anion exchange column (Bio-Rad) on a DuoFlow chromatography workstation (Bio-Rad) using a linear 0-1 M NaCl gradient. ΔC^* , ^{1122}H uHF, NEG1, and NEG3 eluted at around 400 mM NaCl, NEG2 eluted at slightly higher salt concentrations, around 450 mM NaCl. After combining the fractions of greatest purity (as determined by SDS-PAGE), this protein solution was concentrated to <5 mL for further purification via size exclusion column (SEC) using a Sephacryl S-300 resin equilibrated with buffer (15 mM Tris (pH 7.4), 150 mM NaCl). Protein purity was assessed via SDS-PAGE.

POS2 ferritin variant expression, isolation, and purification: The expression and purification procedures for the POS2 variant significantly diverge from the above methods. Originally adapted from reference 31, our final protocol is detailed below. Briefly, the expression of POS2 differs from the other variants in that: 1) when the OD_{600} reached ~0.2, IPTG was added (0.25 mM final concentration) to induce overexpression of POS2, and 2) thawing and resuspension of frozen cell pellets required buffers containing higher concentrations of NaCl to stabilize the protein cages in solution (*e.g.*, 50 mM Tris (pH 7.5), 1 M NaCl). Sonication was carried out as described above to lyse the resuspended cell pellets.

After sonication, RNase was added to the protein solution (~20 μM final concentration) and incubated at 37 °C for 3 h to degrade all RNA in the solution, a step we found to be necessary to ensure binding of POS2 to cation-exchange resins. This solution was then heat treated in a water bath at 65 °C for 15 min to induce denaturation and precipitation of most other contaminants. The soluble fraction containing POS2 was separated by centrifugation (12,000×g, 10 min). Ammonium

sulfate was then added to this clarified solution until reaching a concentration of 70% (w/v), at which point POS2 precipitates out to separate it from most remaining impurities. Following centrifugation (12,000×g, 10 min), the isolated protein pellet was fully dissolved into a solution of 50 mM MES (pH 6) and 0.5 M NaCl, filtered, loaded onto a Uno-S cation exchange column (BioRad) on a DuoFlow chromatography workstation (BioRad), and eluted using a linear 0.5-2 M NaCl gradient. Following assessment of the eluted fractions by SDS-PAGE, only highly pure (>95% purity) fractions were collected and combined without further purification. The resulting solution was transferred into dialysis tubing (6,000-8,000 Dalton molecular weight cut-off (Thermo Fisher)) and allowed to dialyze against a buffer of 50 mM Tris (pH 7.5) and 1 M NaCl. We note that the POS2 variant is unstable in low ionic strength conditions and will precipitate out shortly after isolation. Freshly purified POS2 should be aliquoted and flash frozen into liquid nitrogen as soon as possible after dialysis.

The isolation, labeling, and crystallization of the ferritin variant ^{157}C HuHF (labeled with RAFT reagent) can be found in our recently published paper (ref. 22).

3.5.3 Crystallization of ferritin variants

The crystallization conditions for all ferritin variants are listed in **Table 3.4**. All crystal trays were set up at room temperature (298 K) unless otherwise specified.

Table 3.4 Crystallization conditions for ferritin variants

variant	protein* concentration	protein buffer	reservoir	volume**
ΔC^* (F432)	25 μ M	15 mM Tris *pH 7.4) 150 mM NaCl	25 mM HEPES (pH 7.0) 10 mM CaCl ₂	5 μ L : 5 μ L
ΔC^* (P3,21)	25 μ M	50 mM Tris (pH 7.5) 1 M NaCl	100 mM HEPES (pH 7.0) 300 mM NH ₄ Ac, 50% MPD	5 μ L : 5 μ L
NEG1	25 μ M	15 mM Tris (pH 7.4) 150 mM NaCl	25 mM HEPES (pH 7.0) 15 mM CaCl ₂	5 μ L : 5 μ L
NEG2	25 μ M	15 mM Tris (pH 7.4) 150 mM NaCl	25 mM HEPES (pH 7.0) 13 mM CaCl ₂ , 1 M NaCl	5 μ L : 5 μ L
NEG3	25 μ M	50 mM Tris (pH 7.4) 150 mM NaCl	25 mM HEPES (pH 7.0) 15 mM CaCl ₂ , 100 mM NaCl	5 μ L : 5 μ L
POS2	25 μ M	50 mM Tris (pH 7.4) 1 M NaCl	25 mM HEPES (pH 7.0) 80 mM CaCl ₂ , 1.2 M NaCl	5 μ L : 5 μ L
RAFT- ¹⁵⁷ C _{HuHF}	25 μ M	50 mM MES (pH 5.0) 12 mM CaCl ₂	25 mM HEPES (pH 7.0) 80 mM CaCl ₂ , 1.2 M NaCl	5 μ L : 5 μ L

* as 24mer

** volume of protein solution : volume of reservoir

3.5.4 Acquisition of all non-ferritin proteins

RIDC3 was expressed and purified by Rohit Subramaniam following the protocol in reference 27. TryCyt1²⁸ was expressed and purified by Albert Kakkis following the protocol in reference 28. ESP405 was provided by Lindsey Spiegelman. Streptavidin was expressed and purified by Lisa Olshansky.³² DPS was expressed and purified by Jie Zhu following the protocol in reference 29. Lysozyme, proteinase K, and horse spleen ferritin were purchased from Millipore Sigma and used without further purification.

3.5.5 Crystallization of all non-ferritin proteins

We used sitting drop vapor diffusion in 24-well trays at room temperature (298 K) to crystallize all proteins. The volume of the reservoir solution was 500 μL for all wells unless otherwise specified. The crystallization conditions for all non-ferritin proteins are listed in **Table 3.5**. In all cases, the protein was first dissolved with the specified buffer to the final concentration specified in the table. 1–5 μL of protein solution was then deposited onto the pedestal of each well and an equal volume of reservoir solution was added to each drop without mixing.

Table 3.5 Crystallization conditions of other protein variants

variant	protein concentration	protein buffer	reservoir	volume
RIDC3	1 mM	0.2 M Bis-Tris (pH 6.5)	40 % PPG 400, 0.2 M (NH ₄) ₂ SO ₄ , 0.1 M Tris (pH 8.0), 2 mM ZnCl ₂	1 μL : 1 μL
TriCyt1	3 mM	20 mM HEPES (pH 7.5) 1 eq. Zn	45% MPD, 200 mM MgCl ₂ 20 mM HEPES (pH 8.5)	1 μL : 1 μL
ESP405	7.5 mg/mL	10 mM Tris (pH 7.0) 10 mM NaCl	0.2 M NH ₄ Ac (pH 7.0) 16% PEG 3350	1 μL : 1 μL
streptavidin	10 mg/mL	DI water	2.6 M (NH ₄) ₂ SO ₄ , 0.1 M sodium acetate (pH 4.0)	2 μL : 2 μL
lysozyme	20 mg/mL	DI water	1 M NaCl, 100 mM NaAc (pH 4.5) 10% w/v NaCl	2 μL : 2 μL
proteinase K	20 mg/mL	50 mM Tris-HCl (pH 7.5) 1 mM CaCl ₂	50 mM Tris-HCl (pH 6.5), 10 mM CaCl ₂ , 1.2 M NaNO ₃	2 μL : 2 μL
DPS	20 mg/mL	50 mM Tris (pH 8.0) 100 mM NaCl, 0.1 mM EDTA	1.55 M sodium formate, 100 mM NaCl, 15% PEG 8000, 50 mM Tris (pH 8.0)	2 μL : 2 μL
HoSF	10 mg/mL	DI water	1.2 M (NH ₄) ₂ SO ₄ , 80 mM CdSO ₄	2 μL : 2 μL

3.5.6 PIX formation using ferritin variants

ΔC^* , *NEG1*, *NEG2*, and *NEG3*: All four of these variants readily formed *F432* crystals under the conditions reported in **Table 3.4**. After crystallization (using either 24-well trays or 12-well macrotrays), the supernatant was gently pipetted out and replaced with buffered solutions (25 mM HEPES (pH 7.0), 30 mM CaCl_2) supplemented with polymer precursors (5% or 10% w/v). For the precursors 2-acrylamido-2-methylpropane sulfonic acid and 2-aminoethylmethacrylamide hydrochloride, excess NaOH was added to adjust the pH of the solution to 7.0. The crystals were soaked in the precursor solutions for at least 24 hours to ensure complete diffusion of monomers into the protein lattice. For small scale crystallization (24-well trays), 20 μL of precursor solution was used for soaking, while for large scale crystallization (12-well macrotrays), 200 μL of solution was used. Large scale crystallization was primarily employed to generate the very large numbers of crystals required for SAXS experiments.

POS2: The *POS2* ferritin variant was crystallized in 24-well sitting drop crystal trays (small scale) as described in **Table 3.4**. 10% acrylate and 10% acrylamide stock solutions containing 100 mM CaCl_2 were prepared and used to generate soaking solutions with different concentrations of each monomer (for example, to prepare a 1% acrylate/9% acrylamide solution, 10 μL of acrylate stock and 90 μL acrylamide stock were mixed together). 20 μL of the resulting solutions were added to the crystals in the pedestal of each sitting drop well for soaking.

$^{112}\text{H}u\text{HF-MOF}$: The soaking solutions for the ferritin-MOF crystals contained the polymer precursors, 50% concentrations of all reagents found in the reservoir solution, and supplemented with 5 mM di-hydroxamate linker prior to addition to each pedestal.

Polymerization: After soaking the crystals in monomer mixtures for at least >24 hours, *in situ* polymerization of the hydrogel within the lattice was typically (*e.g.*, for light microscopy

experiments) initiated by transfer of individual crystals into solutions of 1% (w/v) ammonium persulfate (APS) and 1% (v/v) TEMED in 4 M NaCl. For SAXS experiments however, polymerization was instead initiated upon irradiation of the sample by the X-ray beam; no further initiator/accelerator was added unless otherwise specified.

3.5.7 PIX formation using non-ferritin proteins

For all non-ferritin protein crystals, the aqueous monomer mixture (17.3% acrylate, 5% acrylamide and 0.4% Bis-acrylamide, w/v) was mixed 1:1 with the corresponding reservoir solution for each protein crystallization condition (**Table 3.5**) in order to stabilize the crystals during soaking. After soaking, intact crystals were directly transferred into solutions of the APS/TEMED/NaCl mixture described above to initiate polymerization and synthesize the PIX.

3.5.8 Determination of zeta potentials

Purified ferritin variants were concentrated to about 50 μM and exchanged into DI water using an Amicon Ultra centrifugal filter unit (10 kDa cutoff) to mimic the solution conditions during PIX expansion. The zeta potentials of ferritin in the three different buffers were measured using a Zetasizer Nano ZS90 (Malvern Instruments) equipped with a 633 nm He–Ne laser. Twelve datasets were collected for each measurement; the averages and standard deviations of the zeta potentials for all variants tested are reported in **Table 3.1**.

3.5.9 Monitoring PIX dynamics using light microscopy

For most experiments, one to several PIX were directly transferred via mounted CryoLoop into 30 μL drops of the desired solution placed on a glass slide equipped with a microscopic ruler (OMAX). When very large numbers of crystals were required for observation, manual transfer is not possible. Instead, the crystallization solution (supernatant) was gently removed from the pedestal, carefully replaced with the desired one, and then imaging was performed on the entire

well. All images were collected using an SZX7 (Olympus) microscope equipped with an Infinity 1 charge-coupled device (CCD; Lumenera). For more detailed steps of monitoring PIX dynamics using light microscopy, we refer the reader to Section 2.5.8.

3.5.10 Monitoring PIX dynamics using SAXS

To prepare PIX samples for SAXS measurements in capillaries, large-scale crystallization of ferritin in macrotrays was first performed as described in Section 3.5.6 to produce large quantities of crystals. Next, the crystallization solution (supernatant) was removed and the crystals were resuspended in a buffered solution of 25 mM HEPES (pH 7.0) containing either polymer precursors or 30 mM CaCl₂. After 72 h, the samples containing monomer-soaked crystals were transferred into 1.5-mm quartz capillaries (Hampton). Data were collected at beamline 4-2 of SSRL using collimated X-ray radiation (1.1271 Å, 11 keV) calibrated with a silver behenate standard. The images with a 1-s X-ray exposure were collected every minute. Scattered radiation was detected using a Pilatus3 X 1M detector (Detectris) and processed as described above.

3.5.11 MD simulations

Atomistic simulations: Molecular dynamics simulations were employed to gain insight into the nature of mechanical coupling between protein and polymer components within ferritin PIX (and why specific combinations produce stable expandable PIX while others do not) by providing a molecularly detailed picture of their interactions. We first investigated three systems at atomistic resolution: a full ΔC^* cage (negatively charged) in the presence of either negatively charged p(Ac-Am) or electrically neutral pAm polymers, and a full POS2 cage (positively charged) in the presence of pAm chains. All three systems were solvated in 20×20×20 nm water boxes and neutralized with NaCl. Atomistic simulations (using the GROMOS force field and SPC/E waters)³³⁻³⁵ account for the detailed structure of molecules but are computationally expensive and

were sampled for only 10 ns, just long enough to characterize the intermolecular interactions between individual ferritin cages and polymer chains.

Coarse-grained simulations: In order to study models of entire PIX lattices, we turned to the MARTINI³⁰ coarse-grained force field, a well-parameterized lower-resolution potential that allows simulations to achieve longer time and length scales at computational costs significantly lower than atomistic simulations.^{30,36-39} For these simulations, waters were represented using a polarizable model consisting of a positive site and a negative site connected to a central bead and forming an angle θ . This pseudo-molecule represents an aggregate formed by four water molecules. Using this polarizable MARTINI water model, the effective dielectric constant of the bulk solution is $\epsilon_{\text{eff}} \approx 80$, in agreement with the experimental value.

The MARTINI force field preserves the overall molecular structure of each CG model by mapping groups of four atoms onto single beads and then connecting them using spring potentials. The short-range interactions between the beads were modeled using the Lennard-Jones potential:

$$u_{ij}^{sr}(r) = 4\epsilon_{ij} \left[\left(\frac{\sigma_{ij}}{r} \right)^{12} - \left(\frac{\sigma_{ij}}{r} \right)^6 \right] \quad (3.2)$$

Where σ_{ij} and ϵ_{ij} are the force field parameters. The electrostatic interactions between charged groups are through the Coulomb potential, given by:

$$u_{ij}^{el}(r) = \frac{q_i q_j}{4\pi \epsilon_0 \epsilon_r r} \quad (3.3)$$

where q_i and q_j are the particles charges, ϵ_0 is the vacuum permittivity, and ϵ_r is the dielectric constant (assumed to be equal to 2.5). Particle types were designated according to the notation of the MARTINI force-field, which have standard values of the nonbonded parameters.

All polymer and protein monomeric units were represented using two MARTINI beads each. Acrylate monomers are modeled using a hydrophobic bead (sC1) representing the C-C

backbone atoms and a charged bead (Qa) representing the charged $\text{O}=\text{C}-\text{O}^-$ group. Similarly, acrylamide monomers were constructed as two beads, one representing the backbone atoms (sC1) and a second bead representing the polar $\text{O}=\text{C}-\text{NH}$ group. The polymer chains were constructed by connecting N monomers to their neighbors using spring potentials. The p(Ac-Am) copolymers were built to match the 3:1 stoichiometry of the experimental conditions. The CG ferritin cages were built using the atomic coordinates taken from experimental X-ray diffraction (PDB ID: 6B8F) that were then mapped onto the MARTINI topology for amino acids. These cages have a net charge of $-96e$ whereas the net charge of the POS2 cage is $+48e$; e is the positive elementary charge.

Models of the PIX lattices were built by placing four ferritin cages in a *fcc* cell with the simulation box side lengths L adjusted to match the experimental dimensions. N_p polymers were randomly added into the simulation box, and the remaining void volume was filled with N_+ cations, N_- anions, and N_w water molecules. Following the experimental conditions, we maintained a constant 1080 monomers per cage. The number of polymer chains and their lengths were adjusted to preserve the total number of monomers (4320 for four cages in the PIX unit cell), as follows: $N_p = 9, 18, 36, 72, 144, 288$ and $N = 480, 240, 120, 60, 30, 15$, respectively. The p(Ac-Am) copolymers were built using 3240 acrylate and 1080 acrylamide monomers. For all systems, cations were added to neutralize the negative charge of the system, and 200 additional ion pairs were introduced (~ 50 mM NaCl). The final ΔC^* -p(Ac-Am) system contained $N_+ = 3824$ and $N_- = 200$ ions; the POS2-pAm system contained $N_+ = 3824$ and $N_- = 200$ ions.

3.6 Acknowledgments

We thank the following colleagues for assistance: S. Weigand, T. Weiss and I. Rajkovic for SAXS. This work was primarily funded by the Army Research Office. Crystallographic data were collected at Stanford Synchrotron Radiation Lightsource (SSRL) and the Crystallography

Facility of the University of California, San Diego. SAXS data were collected at SSRL, SSRL is supported the DOE Office of Science, Office of Basic Energy Sciences under contracts DE- AC02-76SF00515.

Author contributions: L. Z. and F. A. T. conceived the work and designed the experiments. F-J. A. and M. O. designed and carried out the molecular dynamics simulations. L. Z. and R. G. A. wrote the manuscript and performed data analysis and molecular visualization.

Chapter 3, in part, is currently being prepared for submission for publication: Zhang, L., Jimenez-Angeles, F., Alberstein, R. G., Olvera de la Cruz, M., Tezcan, F. A. “Towards a comprehensive understanding of the material properties of polymer integrated crystals”. The dissertation author was the primary investigator and author of this manuscript.

3.7 References

1. Kohn, K. P.; Underwood, S. M.; Cooper, M. M., Connecting structure-property and structure-function relationships across the disciplines of chemistry and biology: Exploring student perceptions. *Cbe-Life Sciences Education* **2018**, *17* (2), 15.
2. Barthelat, F.; Yin, Z.; Buehler, M. J., Structure and mechanics of interfaces in biological materials. *Nature Reviews Materials* **2016**, *1* (4), 16.
3. Humphrey, J. D.; Dufresne, E. R.; Schwartz, M. A., Mechanotransduction and extracellular matrix homeostasis. *Nature Reviews Molecular Cell Biology* **2014**, *15* (12), 802-812.
4. King, N. P.; Bale, J. B.; Sheffler, W.; McNamara, D. E.; Gonen, S.; Gonen, T.; Yeates, T. O.; Baker, D., Accurate design of co-assembling multi-component protein nanomaterials. *Nature* **2014**, *510* (7503), 103-108.
5. Bale, J. B.; Gonen, S.; Liu, Y. X.; Sheffler, W.; Ellis, D.; Thomas, C.; Cascio, D.; Yeates, T. O.; Gonen, T.; King, N. P.; Baker, D., Accurate design of megadalton-scale two-component icosahedral protein complexes. *Science* **2016**, *353* (6297), 389-394.
6. He, X. M.; Aizenberg, M.; Kuksenok, O.; Zarzar, L. D.; Shastri, A.; Balazs, A. C.; Aizenberg, J., Synthetic homeostatic materials with chemo-mechano-chemical self-regulation. *Nature* **2012**, *487* (7406), 214-218.
7. Gonen, S.; DiMaio, F.; Gonen, T.; Baker, D., Design of ordered two-dimensional arrays mediated by noncovalent protein-protein interfaces. *Science* **2015**, *348* (6241), 1365-1368.
8. Sakai, F.; Yang, G.; Weiss, M. S.; Liu, Y. J.; Chen, G. S.; Jiang, M., Protein crystalline frameworks with controllable interpenetration directed by dual supramolecular interactions. *Nature Communications* **2014**, *5* (1), 1-8.
9. Brodin, J. D.; Auyeung, E.; Mirkin, C. A., DNA-mediated engineering of multicomponent enzyme crystals. *Proceedings of the National Academy of Sciences of the United States of America* **2015**, *112* (15), 4564-4569.
10. Padilla, J. E.; Colovos, C.; Yeates, T. O., Nanohedra: Using symmetry to design self assembling protein cages, layers, crystals, and filaments. *Proceedings of the National Academy of Sciences of the United States of America* **2001**, *98* (5), 2217-2221.

11. Goodsell, D. S.; Olson, A. J., Structural symmetry and protein function. *Annual Review of Biophysics and Biomolecular Structure* **2000**, *29*, 105-153.
12. Kickelbick, G., (Ed.), Hybrid materials: Synthesis, characterization, and applications. *John Wiley & Sons* **2007**.
13. Pelegri-O'Day, E. M.; Lin, E. W.; Maynard, H. D., Therapeutic protein-polymer conjugates: Advancing beyond pegylation. *Journal of the American Chemical Society* **2014**, *136* (41), 14323-14332.
14. Huang, X.; Patil, A. J.; Li, M.; Mann, S., Design and construction of higher-order structure and function in proteinosome-based protocells. *Journal of the American Chemical Society* **2014**, *136* (25), 9225-9234.
15. Shin, H.; Jo, S.; Mikos, A. G., Biomimetic materials for tissue engineering. *Biomaterials* **2003**, *24* (24), 4353-4364.
16. Yan, H.; Park, S. H.; Finkelstein, G.; Reif, J. H.; LaBean, T. H., DNA-templated self-assembly of protein arrays and highly conductive nanowires. *Science* **2003**, *301* (5641), 1882-1884.
17. Cobo, I.; Li, M.; Sumerlin, B. S.; Perrier, S., Smart hybrid materials by conjugation of responsive polymers to biomacromolecules. *Nature Materials* **2015**, *14* (2), 143-159.
18. Moatsou, D.; Li, J.; Ranji, A.; Pitto-Barry, A.; Ntai, I.; Jewett, M. C.; O'Reilly, R. K., Self-assembly of temperature-responsive protein-polymer bioconjugates. *Bioconjugate Chemistry* **2015**, *26* (9), 1890-1899.
19. Phadke, A.; Zhang, C.; Arman, B.; Hsu, C.-C.; Mashelkar, R. A.; Lele, A. K.; Tauber, M. J.; Arya, G.; Varghese, S., Rapid self-healing hydrogels. *Proceedings of the National Academy of Sciences of the United States of America* **2012**, *109* (12), 4383-4388.
20. Zhang, L.; Bailey, J. B.; Subramanian, R. H.; Groisman, A.; Tezcan, F. A., Hyperexpandable, self-healing macromolecular crystals with integrated polymer networks. *Nature* **2018**, *557* (7719), 86-91.
21. Holtz, J. H.; Asher, S. A., Polymerized colloidal crystal hydrogel films as intelligent chemical sensing materials. *Nature* **1997**, *389* (6653), 829-832.

22. Han K., Bailey J. B., Zhang L., and Tezcan F. A., Anisotropic dynamics and mechanics of macromolecular crystals containing lattice-patterned polymer networks. *Journal of the American Chemical Society* **2020**, *142* (45), 19402-19410.
23. Lawson, D. M.; Artymiuk, P. J.; Yewdall, S. J.; Smith, J. M. A.; Livingstone, J. C.; Treffry, A.; Luzzago, A.; Levi, S.; Arosio, P.; Cesareni, G.; Thomas, C. D.; Shaw, W. V.; Harrison, P. M., Solving the structure of human h-ferritin by genetically engineering intermolecular crystal contacts. *Nature* **1991**, *349* (6309), 541-544.
24. Elliott, J. E.; Macdonald, M.; Nie, J.; Bowman, C. N., Structure and swelling of poly(acrylic acid) hydrogels: Effect of pH, ionic strength, and dilution on the crosslinked polymer structure. *Polymer* **2004**, *45* (5), 1503-1510.
25. Sontz, P. A.; Bailey, J. B.; Aln, S.; Tezcan, F. A., A metal organic framework with spherical protein nodes: Rational chemical design of 3d protein crystals. *Journal of the American Chemical Society* **2015**, *137* (36), 11598-11601.
26. Liu, Y. X.; Wang, X. J.; Ching, C. B., Toward further understanding of lysozyme crystallization: Phase diagram, protein-protein interaction, nucleation kinetics, and growth kinetics. *Crystal Growth & Design* **2010**, *10* (2), 548-558.
27. Subramanian, R. H.; Smith, S. J.; Alberstein, R. G.; Bailey, J. B.; Zhang, L.; Cardone, G.; Suominen, L.; Chami, M.; Stahlberg, H.; Baker, T. S.; Tezcan, F. A., Self-assembly of a designed nucleoprotein architecture through multimodal interactions. *Acs Central Science* **2018**, *4* (11), 1578-1586.
28. Kakkis, A.; Gagnon, D.; Esselborn, J.; Britt, R. D.; Tezcan, F. A., Metal-templated design of chemically switchable protein assemblies with high-affinity coordination sites. *Angewandte Chemie-International Edition*, **2020**, *132*(49), 22124-22128
29. Grant, R. A.; Filman, D. J.; Finkel, S. E.; Kolter, R.; Hogle, J. M., The crystal structure of dps, a ferritin homolog that binds and protects DNA. *Nature Structural Biology* **1998**, *5* (4), 294-303.
30. Marrink, S. J.; Risselada, H. J.; Yefimov, S.; Tieleman, D. P.; de Vries, A. H., The martini force field: Coarse grained model for biomolecular simulations. *Journal of Physical Chemistry B* **2007**, *111* (27), 7812-7824.
31. Kunzle, M.; Eckert, T.; Beck, T., Binary protein crystals for the assembly of inorganic nanoparticle superlattices. *Journal of the American Chemical Society* **2016**, *138* (39), 12731-12734.

32. Olshansky, L.; Huerta-Lavorie, R.; Nguyen, A. I.; Vallapurackal, J.; Furst, A.; Tilley, T. D.; Borovik, A. S., Artificial metalloproteins containing co4o4 cubane active sites. *Journal of the American Chemical Society* **2018**, *140* (8), 2739-2742.
33. Scott, W. R. P.; Hunenberger, P. H.; Tironi, I. G.; Mark, A. E.; Billeter, S. R.; Fennen, J.; Torda, A. E.; Huber, T.; Kruger, P.; van Gunsteren, W. F., The gromos biomolecular simulation program package. *Journal of Physical Chemistry A* **1999**, *103* (19), 3596-3607.
34. Berendsen, H. J. C.; Grigera, J. R.; Straatsma, T. P., The missing term in effective pair potentials. *Journal of Physical Chemistry* **1987**, *91* (24), 6269-6271.
35. Chatterjee, S.; Debenedetti, P. G.; Stillinger, F. H.; Lynden-Bell, R. M., A computational investigation of thermodynamics, structure, dynamics and solvation behavior in modified water models. *Journal of Chemical Physics* **2008**, *128* (12), 124511.
36. Yesylevskyy, S. O.; Schafer, L. V.; Sengupta, D.; Marrink, S. J., Polarizable water model for the coarse-grained martini force field. *Plos Computational Biology* **2010**, *6* (6), e1000810.
37. Rossi, G.; Monticelli, L.; Puisto, S. R.; Vattulainen, I.; Ala-Nissila, T., Coarse-graining polymers with the martini force-field: Polystyrene as a benchmark case. *Soft Matter* **2011**, *7* (2), 698-708.
38. Vogele, M.; Holm, C.; Smiatek, J., Coarse-grained simulations of polyelectrolyte complexes: Martini models for poly(styrene sulfonate) and poly(diallyldimethylammonium). *Journal of Chemical Physics* **2015**, *143* (24), 243151.
39. Jimenez-Angeles, F.; Kwon, H. K.; Sadman, K.; Wu, T.; Shull, K. R.; de la Cruz, M. O., Self-assembly of charge-containing copolymers at the liquid-liquid interface. *Acs Central Science* **2019**, *5* (4), 688-699.

Chapter 4 : Polymer integrated protein crystals as a general platform for controlled protein encapsulation and release

4.1 Abstract

Crystalline materials have great potential for use as porous biocompatible scaffolds for the immobilization of functional (macro)molecules. In contrast to other porous structures, crystalline lattices present several advantages, most principally that their equivalent pores are uniformly distributed throughout the lattice and provide unique chemical environments that can be tuned with atomic precision. The immobilization of proteins into porous materials has attracted great attention, with an eye toward applications including controlled catalysis, long-term storage (and release), chemical separation, and drug delivery. However, the rigidity of porous crystalline materials and the difficulty in chemically tailoring these materials limit the types/sizes and the controlled uptake/release of guest molecules. In this chapter, we demonstrate that protein macromolecules of various shapes, sizes, and chemical compositions can be immobilized within hyperexpandable polymer integrated crystals (PIX), a class of hybrid materials capable of controlled volumetric variations up to 500% of their initial size. The capability of PIX to reversibly expand in response to changes in ionic strength—coupled with the chemical properties of the embedded polymer matrix—allows PIX to efficiently encapsulate large macromolecules that otherwise cannot penetrate into the crystalline lattice. We demonstrate that the encapsulation of protein molecules can be controlled by tuning the degree of expansion. Large proteins with molecular weights greater than 30 kDa (*e.g.*, green fluorescent protein, streptavidin, and catalase) can only be encapsulated in ferritin PIX upon >140% expansion of the unit cell followed by the subsequent salt-induced contraction to lock the protein cargo inside the lattice. Smaller proteins (*e.g.*, lysozyme) are found to penetrate into the lattice even at less than 5–10% expansion, likely enabled by favorable

electrostatic interactions between the negatively charged polymer and the positively charged protein. The entrapped macromolecular cargo can then be released by re-expansion of the PIX by decreasing the ionic strength of the environment. Thus, PIX provide a novel encapsulation platform capable of controllably trapping and releasing diverse macromolecular cargo, uniquely combining the advantages of porous, crystalline frameworks and polymer-based systems as pharmaceutical encapsulation/delivery platforms.

4.2 Introduction

The immobilization of nanoscale protein molecules into macroscopic materials has been utilized in a wide range of applications (*e.g.*, molecular storage,¹⁻² catalysis,³⁻⁶ vaccine delivery,⁷⁻⁹ and biosensing¹⁰⁻¹¹). Immobilization serves to improve the stability of the encapsulated protein in challenging environments while retaining native protein activity (and in some cases enhance the catalytic properties of the target protein).¹²⁻¹⁸ For example, synthetic polymers have been shown to be capable of stabilizing proteins in organic solvents.¹⁹ Traditional methods for immobilization include proteins binding into preformed matrices, soaking proteins into a gel or matrix, and co-crystallization of the target protein molecules within high-porosity frameworks.^{17, 20-23} While historically successful, soaking and co-crystallization are inherently limited by both the pore and inter-pore channel sizes of the template scaffolds, and the processing steps must be individually optimized for each cargo.^{2, 24-25} Furthermore, once encapsulated, the cargo proteins are commonly crosslinked to the material in order to prevent leakage. However, such treatments preclude the possibility of controlled release and have the side effect of constraining molecular dynamics, which can reduce native protein activity.^{3, 26-27} In one report,²⁸ which achieved protein immobilization by co-crystallizing a metal-organic framework (MOF) in the presence of the target protein, excessive bonding between the protein and MOF was observed, reducing protein activity.

Addressing this problem required multiple post-synthetic steps to replace the MOF coating with a covalent organic framework, which led to fewer protein-framework interactions, increasing protein mobility and activity.²⁸⁻²⁹ While the modularity of framework materials presents an attractive strategy for protein encapsulation, such a system requires multiple processing steps and must be custom tuned for each target of interest.^{22,26,29-30} Consequently, a universal crystalline platform for protein immobilization would, in theory, require that the material (1) possesses high porosity for high-capacity loading,^{7,9,23,31} (2) maintain protein stability during encapsulation and utilization,³²⁻³⁴ (3) provide a fluid environment to achieve minimally encumbered protein movement,³⁵⁻³⁷ and (4) be capable of selective capture and release of the target protein cargo in a stimuli-responsive manner.^{5,8,38-39} Our recent reports⁴⁰⁻⁴¹ (described also in Chapter 2) on the development of hydrogel-infused macromolecular protein crystals (polymer infused crystals; PIX) indicated that this material would fulfill these requirements.

In our initial study (Chapter 2), we used the 24-meric, quasi-spherical protein ferritin, which crystallizes into *fcc* (*F432* symmetry) crystals through Ca^{2+} -mediated interactions at the C_2 symmetric, two-fold axis interfaces.⁴⁰ The *fcc* lattice possesses two types of cavities: a 6 nm cube-shaped chamber bridged by smaller (narrowest diameter: 2 nm), tetrahedron-shaped pores, and connected by small channels. Together, these form a continuous 3D volume into which small molecules can be diffused. When an 8.625% / 2.5% (w/v) aqueous solution of acrylate/acrylamide was soaked into preformed crystals and polymerized within the framework, the interconnected polymer network and noncovalent protein-polymer interactions enabled the resultant PIX to reversibly expand to >500% by volume (driven by electrostatic charge repulsion of the acrylate groups of the polymer) and contract back to their original state without a loss in crystalline order, simply by changing the ionic strength of the solution surrounding the PIX. One consequence of

this construction is that PIX are likely to be significantly more capable of sorption of larger cargo (after expansion), owing to the larger pore sizes, and should avoid the limitations of their transport into and out of the PIX scaffold, owing to the material's ability to dynamically change the scale of its channels and pores. This creates the potential for the capture and passive retention of large cargo too big to diffuse out of a contracted lattice.

4.3 Results and Discussion

4.3.1 Encapsulation of GFP within ferritin PIX

Cubic Ca²⁺-bridged ferritin crystals consist of *ca.* 39% void space (solvent content: 59.38%).⁴⁰ During expansion, this results in a 170–240% increase in the pore diameters, as depicted in **Figure 4.1a, b**. In the expanded state, the void volume exceeds 85% of the crystal lattice, creating not only pores >10 nm in diameter, but also significantly larger inter-pore channels, providing the opportunity for uptake of large biomolecules via diffusion into the material (**Figure 4.1c**). As this expansion/contraction process is controlled by the ionic strength of the solution, expanded crystals that have taken up the target protein can subsequently be contracted to immobilize the cargo within the pores. The PIX can be stored and later re-expanded to release the encapsulated protein. In other words, the free vs. fixed state of the target molecules can be controlled in a stimuli-responsive manner, while providing a native aqueous environment to ensure high protein activity. By extension, tuning the degree of PIX expansion creates pores and channels of specific sizes, which would enable selective encapsulation of proteins of different sizes via size-exclusion (**Figure 4.1c**).

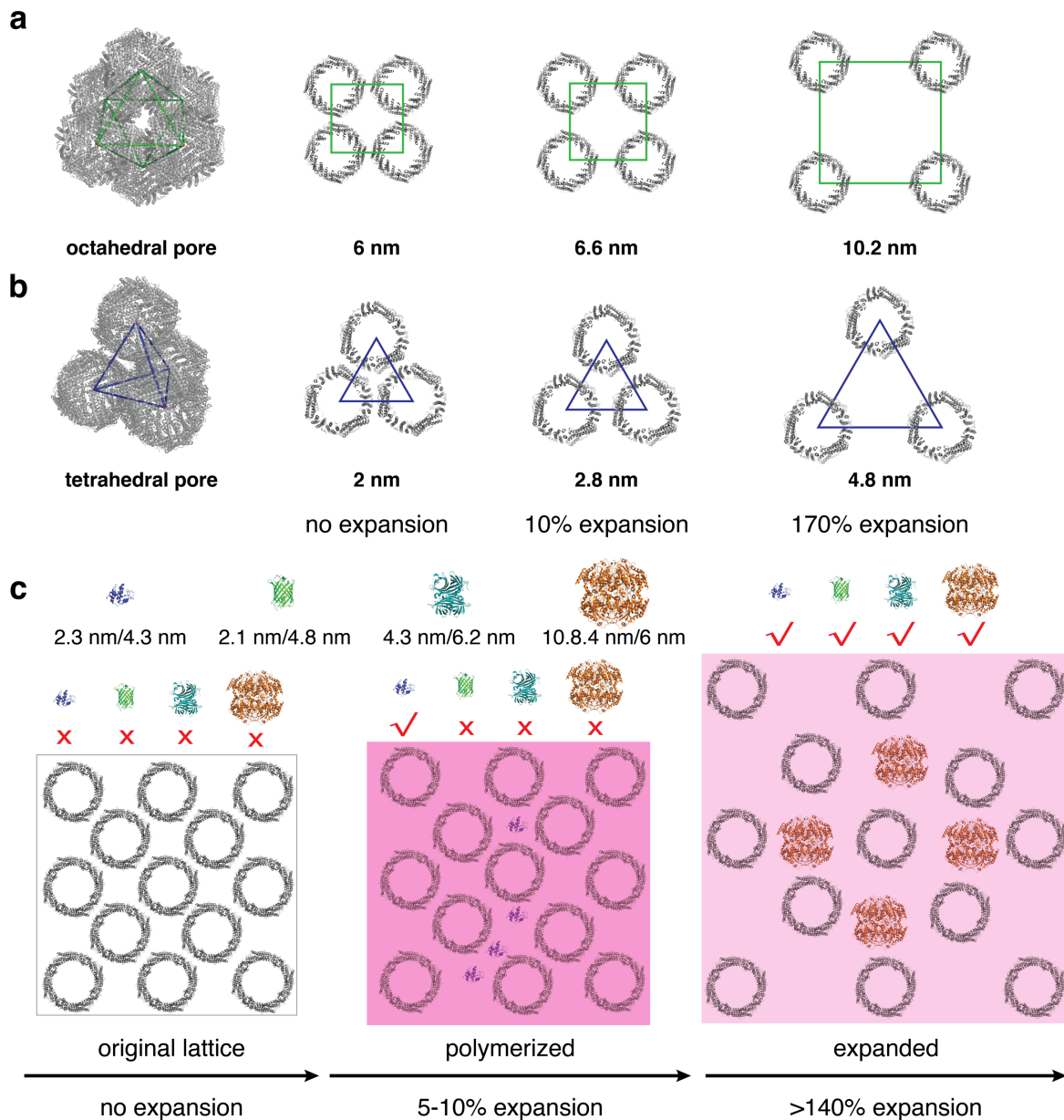


Figure 4.1 | Schematic representation of protein immobilization using PIX. a, Octahedral pores in PIX at different stages of expansion. **b,** Tetrahedral pores in PIX at different stages of expansion. **c,** Cartoon illustrating the potential encapsulation of a series of proteins with varying sizes and chemical compositions, the numbers indicate the narrowest/widest dimensions of each protein.

As a proof-of-principle, we first characterized the ability of ferritin PIX to uptake and encapsulate monomeric superfolder green fluorescent protein (GFP).⁴² GFP exhibits a robust fluorescent signal that can easily be detected by confocal microscopy and UV-Vis absorbance ($\epsilon = 28000 \text{ M}^{-1} \text{ cm}^{-1}$ at 488 nm) measurements. The size of monomeric GFP is approximately 5 nm at the widest, which is slightly smaller than the 6-nm cubic chamber but much larger than the 2-nm tetrahedral pores of the PIX (**Figure 4.1c**). Expansion of fully polymerized PIX was initiated upon transfer of individual PIX into solutions containing varying concentrations of GFP (50–400 μM) in salt-free buffer. We allowed free GFP to diffuse into the PIX over timescales ranging from 10 minutes to 3 hours, then added sodium chloride and/or calcium chloride directly into the solution to initiate contraction of the PIX and entrap the cargo. Confocal imaging of GFP-encapsulated PIX revealed bright fluorescence intensity throughout the crystal (**Figure 4.2a**), indicating internalization of the GFP. 3D slices at different focal planes within single crystals, which revealed plane-dependent geometric shapes of uniform fluorescence, confirmed that GFP encapsulation is not superficial (**Figure 4.2b**). When expansion of the PIX is prevented by CaCl_2 (“control”), only trace amounts of GFP was found nonspecifically bound to the surface, indicating that GFP cannot diffuse into the unexpanded lattice (**Figure 4.2c**, **Figure 4.3**). To characterize uptake, time-course soaking experiments were carried out on PIX expanded in the presence of 200 μM GFP. After contraction with CaCl_2 and transfer to a GFP-free solution, the fluorescence intensity within PIX (as determined by integrating confocal microscopy images) revealed a signal intensity maximum between 30–60 min (**Figure 4.2d**). Repeat trials revealed that while GFP encapsulation was achieved with high reproducibility, there were variations in the timeframe for maximum encapsulation. In some cases, the intensity maxima occurred as early as 10 min (**Figure 4.3**). This suggests that variations in experimental conditions and/or expansion behavior of

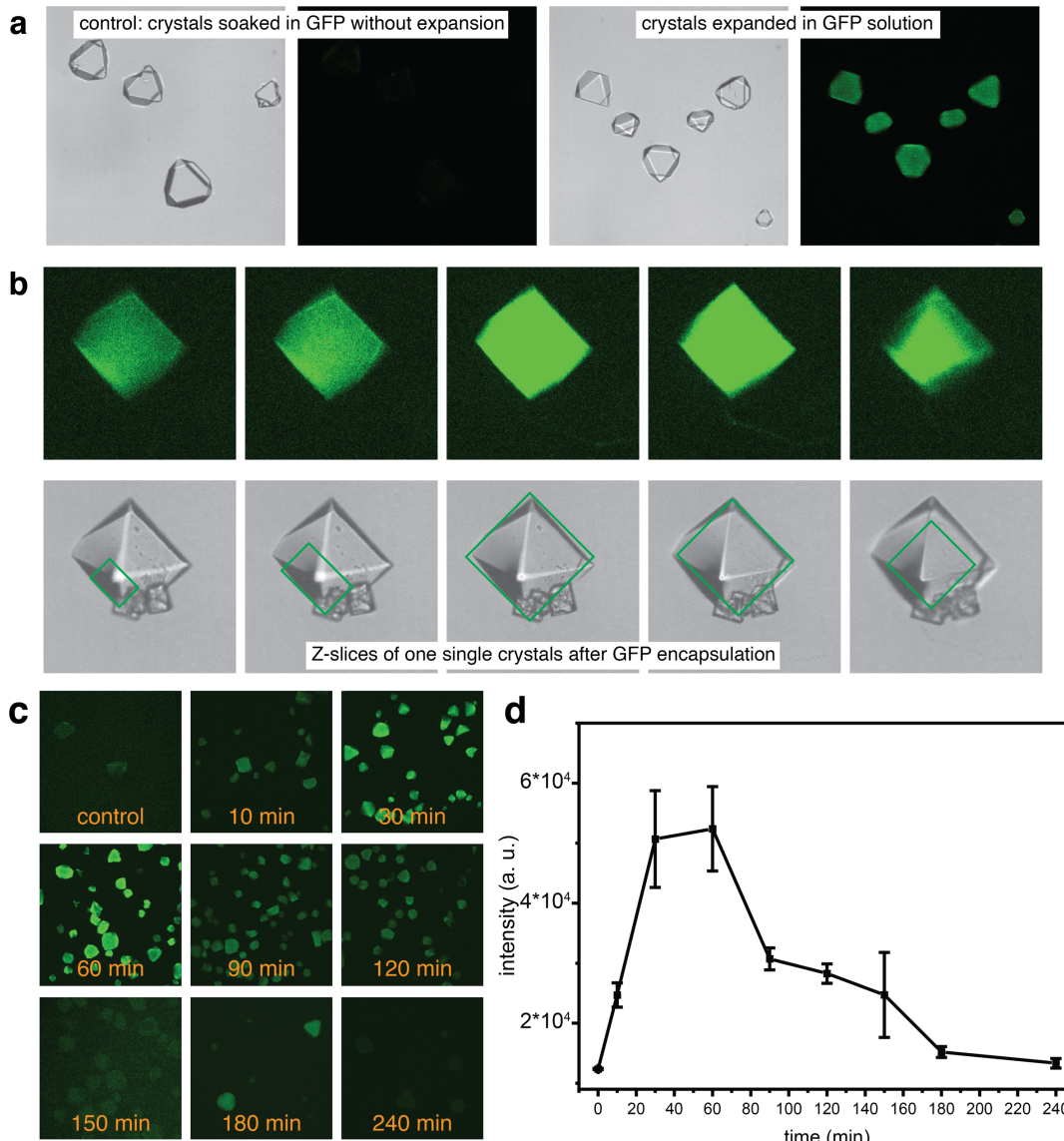


Figure 4.2 | Encapsulation of GFP within PIX. **a**, Bright-field and fluorescence confocal microscopy images of PIX after GFP encapsulation (left: non-expanded control (PIX soaked in GFP solution supplemented with CaCl₂), right: PIX expanded in GFP solution). **b**, Confocal profiles of a single PIX after GFP encapsulation at multiple z-heights. **c**, Fluorescence images of GFP-encapsulated PIX after soaking for different lengths of time. **d**, Fluorescence intensity as a function of time for GFP encapsulation by PIX.

individual PIX is responsible for the differential uptake rate of PIX. Due to the low ionic strength of the soaking solution, the non-covalently linked PIX eventually expand beyond the point of reversibility after approximately 1 hour of expansion, preventing ordered contraction and entrapment of GFP inside the lattice. This is consistently observed in all experiments, as reflected in the long-term decay of the fluorescence for longer soaking times (**Figure 4.3**), and the poor shape recovery of contracted PIX (and associated drop in fluorescence of encapsulated cargo) can be visualized in **Figure 4.3**. After >3 hours, PIX could not be contracted to any extent, even with the addition of CaCl₂; only crystal fragments and protein precipitates were observed. The inability of PIX to properly re-contract after over-expansion (>60 min) is primarily responsible for the lower fluorescence at longer soaking times. Photobleaching is unlikely to be a concern, as the GFP is only imaged at each time point, not continuously.

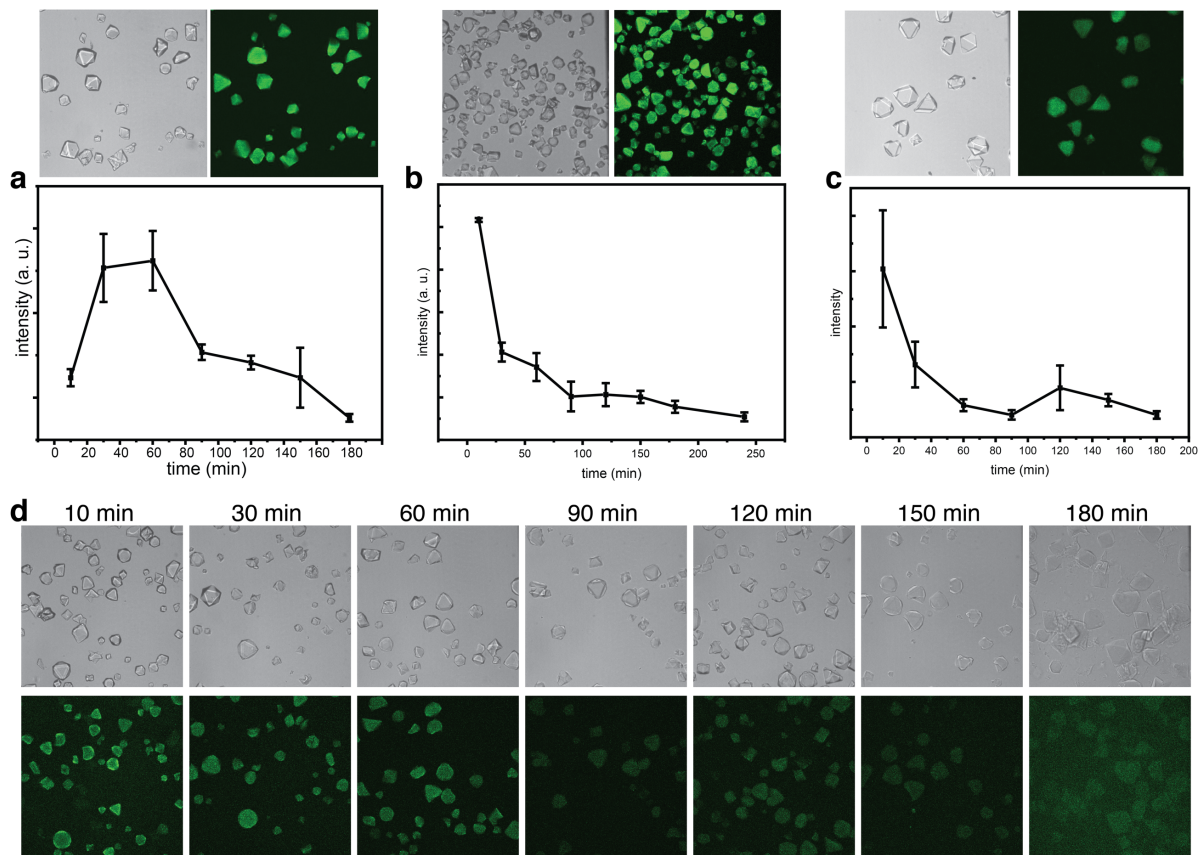


Figure 4.3 | Time-dependent encapsulation of GFP by PIX. **a–c**, Fluorescence intensity time-course analysis of GFP encapsulation by large PIX at pH 8 (**a**), small PIX at pH 8 (**b**), and large PIX at pH 6 (**c**). Each subsection shows a bright-field image (top left), fluorescence image (top right), and the integrated fluorescence intensity as a function of soaking time (bottom). **d**, DIC images (top) and fluorescence images (bottom) of GFP-encapsulated PIX after soaking for different lengths of time.

4.3.2 Characterization of pH effects on GFP encapsulation by PIX

We next addressed the effect of pH on the encapsulation of GFP within PIX. In these PIX, the isoelectric point (pI) of ferritin is 5.2, making it slightly negatively charged at neutral pH and matching the high negative charge of p(Ac-Am), which is responsible for the salt-dependent expansion-contraction behavior of PIX. Thus, PIX in higher pH environments should have an increased negative charge that promotes crystal expansion but may also affect the uptake of the target. We observed that the encapsulation of GFP (pI = 5.9) decreased as pH increased from 6 to 9 (**Figure 4.4**). We hypothesized that the reduced efficiency was due to increased negative charge repulsion from both the ferritin units and polymer network. To corroborate this hypothesis, we generated a more negatively charged ferritin variant (pI = 4.54) and repeated the experiments. Indeed, we observed a further reduced ability to encapsulate GFP at all pH values ≥ 7 (**Figure 4.5**) due to the greater negative charge of the lattice. The decreased stability of GFP at pH values below 6 prevented characterization beyond this lower limit.

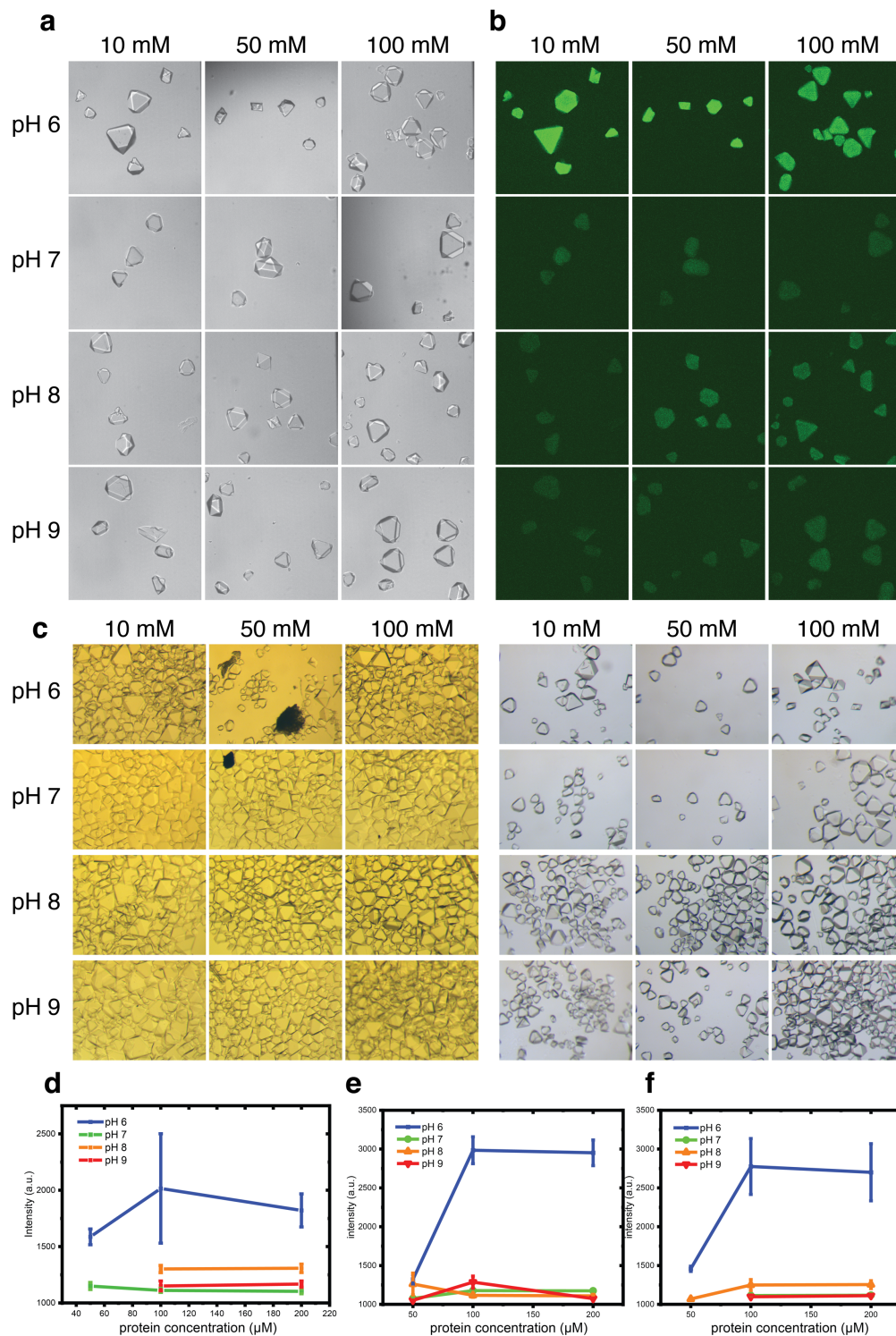


Figure 4.4 | Optimization of GFP encapsulation. **a**, DIC and **b**, fluorescence images of PIX after GFP encapsulation. **c**, Light microscope images of PIX soaking in GFP. Fluorescence intensity analysis of PIX at different pH and protein concentrations with buffer concentrations of 10 mM (**d**), 50 mM (**e**), and 100 mM (**f**), respectively. Buffers: MES (pH 6), HEPES (pH 7), Tris (pH 8), CHES (pH 9).

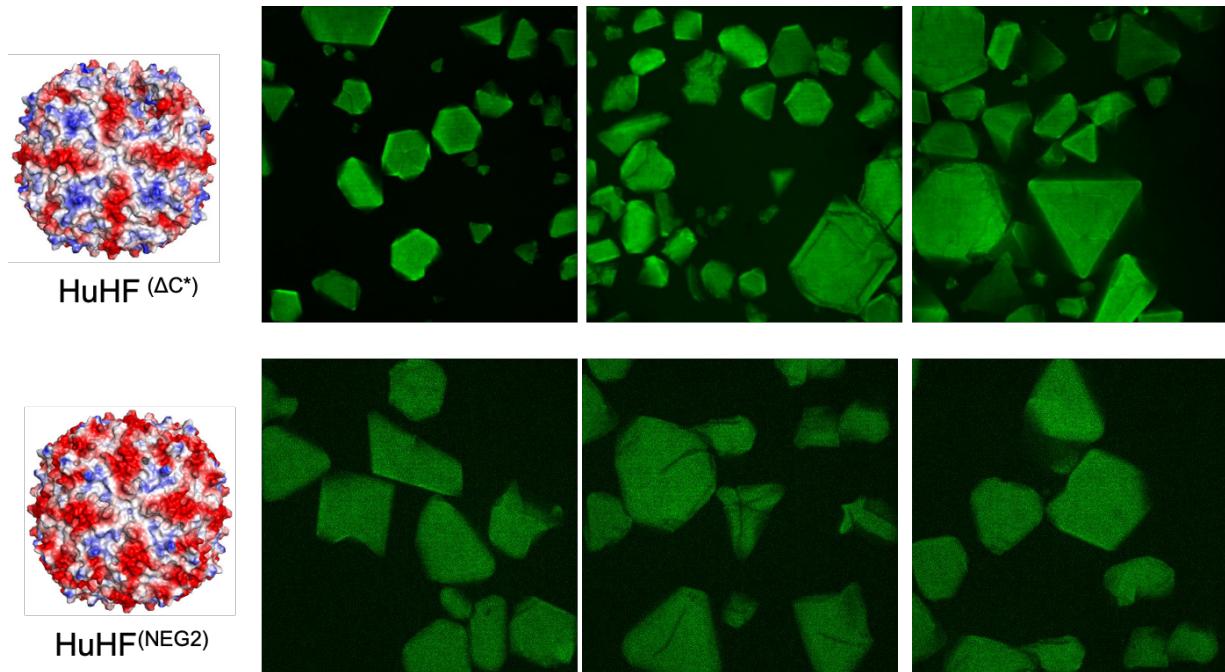


Figure 4.5 | Confocal profiles of GFP-encapsulated PIX constructed from different ferritin variants. a, ΔC^* HuHF. b, NEG2 (a more negatively charged variant).

4.3.3 Quantification of cargo loading within GFP-encapsulated PIX

To further optimize and quantify the loading efficiency of GFP into PIX, we first transferred GFP-loaded PIX (soaked for 60 min in 200 μM GFP) into deionized water and allowed them to dissolve. We then performed quantitative HPLC and UV-Vis measurements to measure the concentrations of both GFP and ferritin in the resulting solutions, detailed steps can be found in the Methods section. By standardizing against a 1.11 mM ferritin cage concentration (the packing density of *fcc* ferritin crystals) inside fully contracted PIX, GFP concentrations within the PIX were calculated to range from 120 to 180 μM , varying somewhat from sample to sample. This workflow and results are depicted in **Figure 4.6** and **Figure 4.7**. As cargo is taken up via diffusion, the density of encapsulated protein is limited by the surrounding concentration of the target (200 μM in this case). Thus, the uptake of cargo by diffusion by PIX (defined as $[\text{encapsulated cargo}]/[\text{cargo in solution}]$) is as high as 90%, though we note that 180 μM represents only 16.1% occupancy of all void spaces in the PIX lattice. The loading efficiency in the experiment was between 0.46% to 0.69% (w/w) assuming the polymer concentration equals the concentration of monomers used in soaking. Given that the diffusion uptake mechanism of PIX should primarily be concentration-limited, we attempted to achieve greater occupancy of the lattice void spaces with higher GFP concentrations, however we found that >200 μM GFP failed to lead to greater quantities of protein being encapsulated. Despite this, we note that highly soluble biomolecules such as those found in biologic formulations may be well-suited to the large loading capacity of PIX. In addition to improving the total quantity of encapsulated cargo, further optimization of the PIX expansion procedure, solution conditions, and/or chemical properties of the PIX or cargo could potentially increase the loading efficiency.

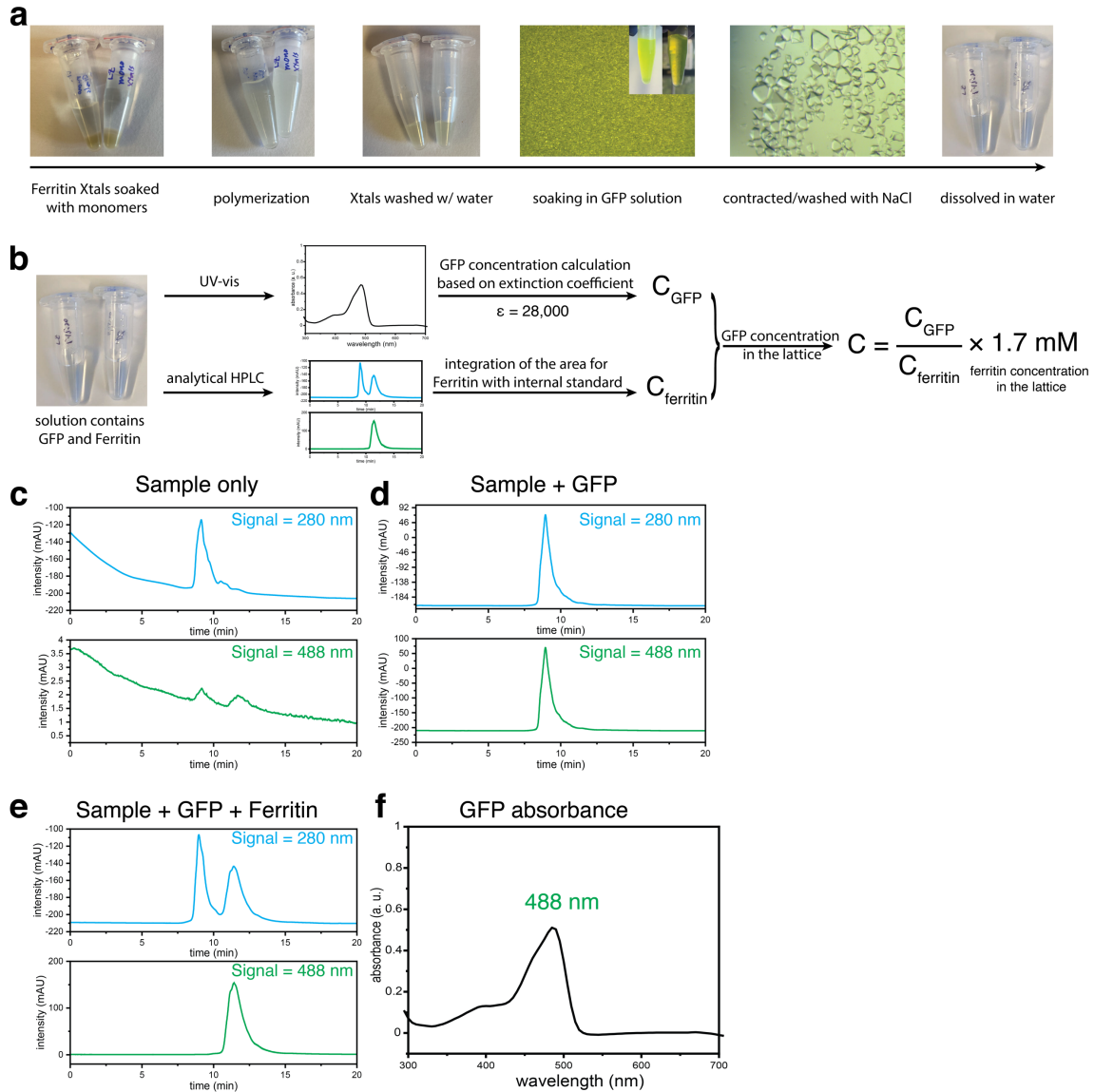
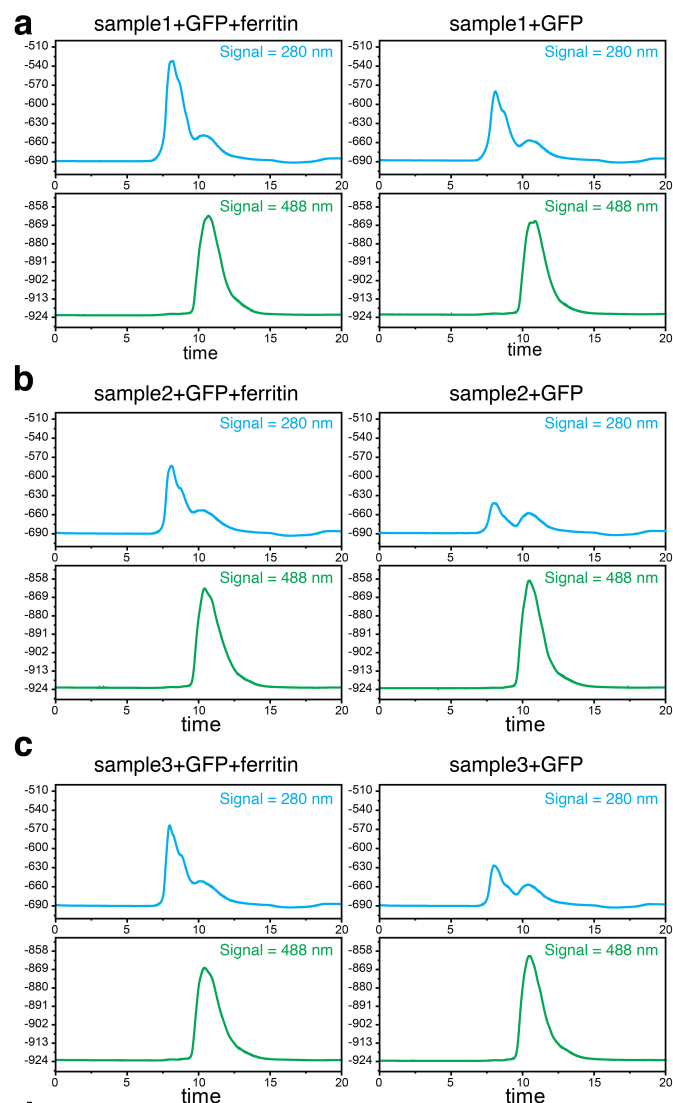


Figure 4.6 | Workflow for the quantification of ferritin and GFP in PIX via HPLC and UV-Vis absorption. **a**, Experimental steps of sample preparation for quantification. **b**, Method employed for calculating the GFP concentration encapsulated within PIX lattices. **c**, Representative HPLC traces of dissolved PIX samples; absorption was measured at 280 nm and 488 nm. **d**, The same sample as **c** in the presence of GFP of known concentration (internal standard). **e**, The same sample as **d** with added ferritin of known concentration (internal standard). **f**, UV-Vis spectrum of GFP, showing the absorption peak at 488 nm.



	$C_{\text{ferritin, soln}}$	$C_{\text{GFP, soln}}$	$C_{\text{GFP, lattice}}$
sample1	535 μM	2.4 μM	120 μM
sample2	220 μM	1.2 μM	146 μM
sample3	222 μM	1.5 μM	180 μM

* The concentration of ferritin in lattice is 1113.93 μM

Figure 4.7 | Quantification of encapsulated GFP concentration within PIX via quantitative HPLC and UV-Vis measurements. a, b, c, HPLC traces for three repeat samples at 280 nm and 488 nm. d, Calculated quantities of GFP encapsulated (quantified by UV-Vis) inside PIX lattices for the three samples shown above.

4.3.4 Controlled release of GFP from PIX

We previously showed in Chapter 2 that PIX are capable of undergoing repeated cycles of expansion and contraction while maintaining the structural integrity of the lattice.⁴⁰⁻⁴¹ We surmised that after one round of expansion and contraction in a solution containing a protein of interest (encapsulation), the PIX could be transferred into a new solution, where re-expansion of the lattices would lead to controlled release, making PIX suitable for delivery applications (**Figure 4.8a**). To assess this hypothesis, we first placed GFP-loaded PIX into deionized water, re-expanded them for different lengths of time (to release the cargo), then re-contracted them (to prevent further release), and transferred these PIX to a new solution for confocal microscopy imaging. Both fluorescence imaging (**Figure 4.8b**) and total fluorescence intensity (**Figure 4.8c**) revealed an immediate drop in GFP concentration—relative to a 0-min expansion control—in as little as 10 min, indicating that the cargo is rapidly released into the solution upon PIX expansion. The remaining GFP slowly releases over extended periods of additional expansion, concluding with the eventual dissolution of the crystals after three hours (**Figure 4.8c**). However, this quantity represents a very small fraction of the total GFP released. In summary, all of the data presented above are consistent with our modeled mechanism of protein encapsulation by PIX, in which GFP molecules are expected to freely migrate into and out of the expanded PIX lattices (so long as the structural integrity of the scaffold is preserved), while the contracted lattices prevent GFP intrusion and release.

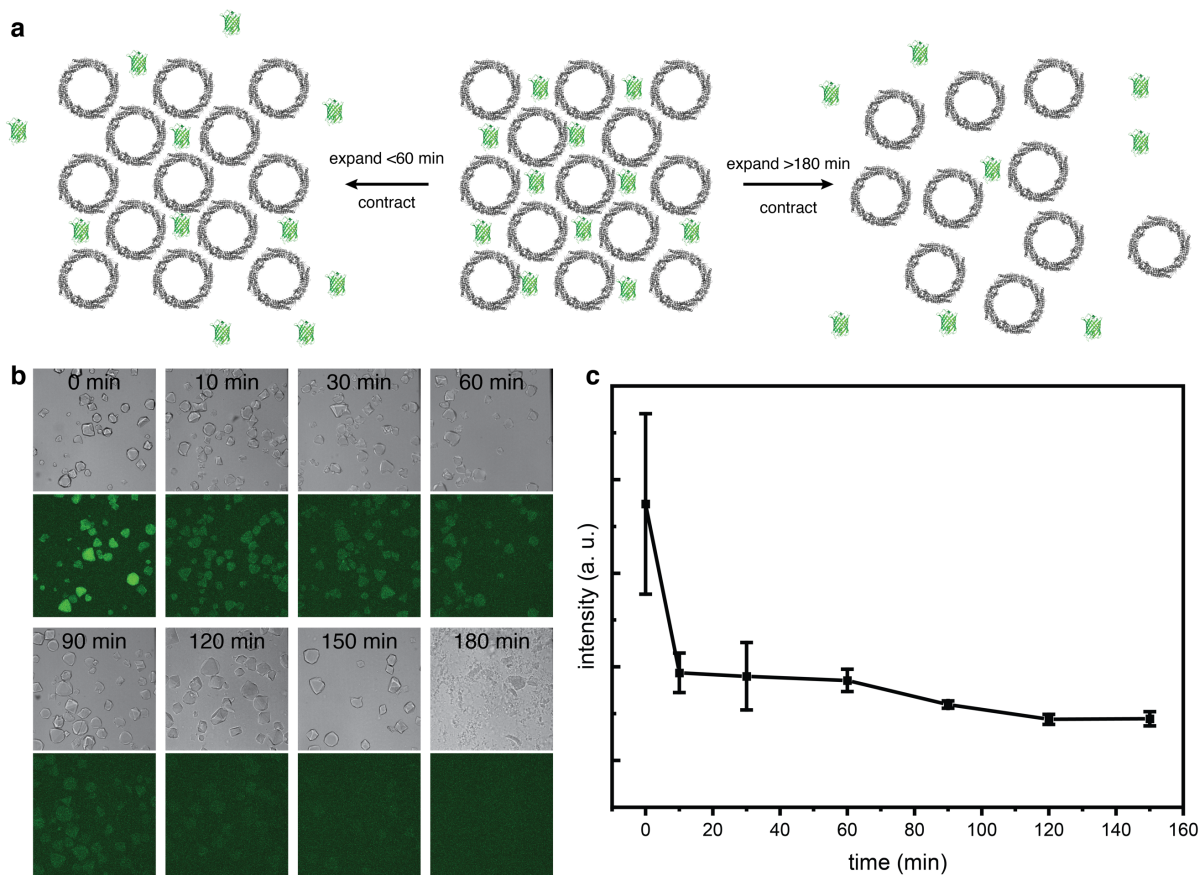


Figure 4.8 | Cargo release from GFP-loaded PIX. a, Cartoon depiction of successful GFP encapsulation (left) vs poor encapsulation by over-expanded PIX (right). **b,** Confocal images (top: bright field, bottom: fluorescence) of PIX after releasing GFP for different lengths of time. Fully loaded PIX are shown in the 0 min images. **c,** Fluorescence intensity time course analysis of the images shown in a.

4.3.5 Size-selective encapsulation of other proteins within PIX

We then sought to demonstrate that PIX can incorporate proteins of different sizes and identities (**Figure 2c**). Of particular interest was the uptake of proteins between the different size cutoffs imposed by the octahedral cavities, lattice channels, and tetrahedral pores, as these should be sequentially admitted with increasing expansion. To test this capability, we carried out additional encapsulation experiments on proteins of increasing diameter: monomeric lysozyme⁴³ (2.3 x 4.3 nm), tetrameric streptavidin⁴⁴ (4.3 x 6.2 nm), and the enzymatically active tetrameric catalase⁴⁵ (6 x 10.8 nm). All cargo proteins were rendered fluorescent by rhodamine labeling via NHS chemistry (NHS-rhodamine, Thermo-Fisher catalog #46406), which forms covalent crosslinks with surface-exposed lysine sidechains (all of the proteins tested here have at least one), to facilitate characterization by confocal microscopy. Lysozyme, notably smaller than both pores but larger than the widest channel of the contracted state, was indeed unable to permeate native ferritin crystals (**Figure 4.9a**). However, after polymerization (conversion of ferritin crystals into PIX), lysozyme was found to diffuse into the PIX lattice (**Figure 4.9b**), likely enabled by the 5–10% expansion that occurs during polymerization, highlighting the flexibility yet stringent size exclusion properties of PIX. The uptake of lysozyme may also be facilitated by electrostatic interactions. The pI of lysozyme is 10.7, making it positively charged in the buffer conditions tested, and thus attractive to the PIX material, however, further characterization is needed to confirm this behavior. Expansion and contraction of the PIX did not lead to any apparent increase in the encapsulation efficiency of lysozyme (**Figure 4.9c**), though confocal image slices through the 3D crystal volume again confirmed a uniform distribution of fluorescent cargo throughout the PIX lattice (**Figure 4.9d**). As seen with the similarly sized GFP, streptavidin can be encapsulated only upon a complete expansion and contraction cycle of the PIX (**Figure 4.10**). For catalase,

which can barely fit within the expanded octahedral pores, a small amount of the protein was detected inside PIX, however the total quantities were lower relative to smaller targets (**Figure 4.10**). Time-course experiments on the encapsulation of streptavidin and catalase revealed qualitatively similar behavior as for GFP, reaching a maximum at some point during expansion before falling off (due to the over-expansion and eventual disintegration of the PIX). Taken together, our results indicate that PIX are indeed capable of loading proteins of varying sizes, segregating them into size classes that are intuitively determinable from the model of PIX expansion and contraction. A slight (5–10%) expansion enables permeation of the smallest targets, moderate expansion enables the uptake of targets <10 nm, and extensive expansion (>140%) can manage low-efficiency sorption of very large targets on the order of the largest expanded lattice pores. This demonstrates that PIX can be used for robust encapsulation of different molecular targets of varying size and can controllably release them in a stimuli-responsive fashion, making them attractive for immobilization, stabilization, and delivery applications.

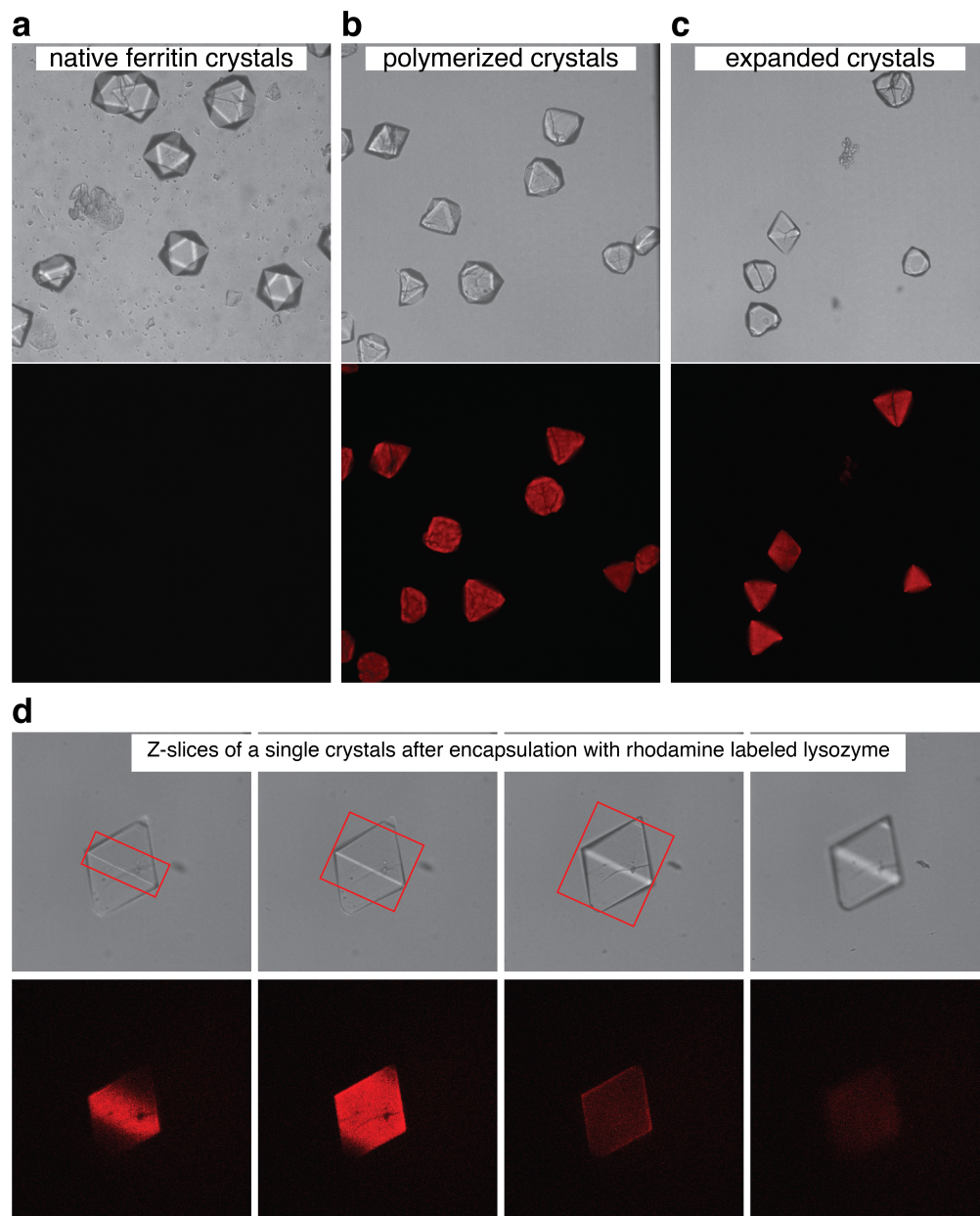


Figure 4.9 | Confocal profiles of lysozyme-encapsulated PIX. **a**, Native ferritin crystals soaked with lysozyme did not show any fluorescence (no uptake of cargo). **b**, Polymerized PIX soaked with lysozyme do appear fluorescent, indicating uptake of lysozyme (likely due to the 5-10% expansion of the PIX lattice). **c**, PIX after expansion and contraction (encapsulation) in the same lysozyme solution. **d**, Bright-field (top) and fluorescence (bottom) images of z-slices of a single PIX after encapsulation of lysozyme.

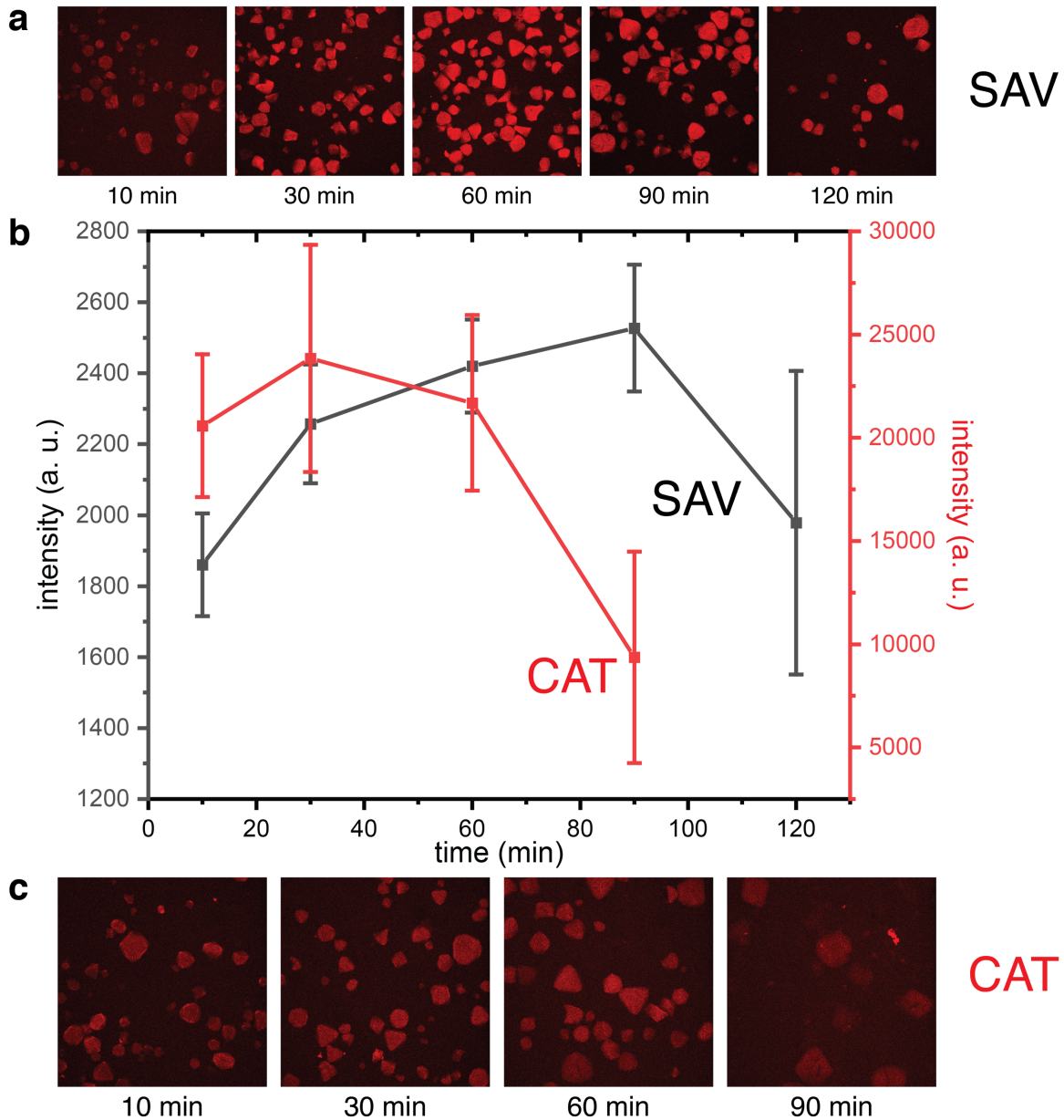


Figure 4.10 | Characterization of streptavidin and catalase encapsulation within PIX. a, Confocal profiles of rhodamine-labeled streptavidin inside PIX after soaking for different lengths of time. **b,** Fluorescence intensity time course analysis for PIX when soaked in each protein solution. **c,** Confocal profiles of rhodamine-labeled catalase inside PIX after soaking for different lengths of time. The fluorescence intensities shown in **b** correspond to the images shown in **a** and **c**.

4.4 Conclusions

In summary, we have created a new platform that can selectively encapsulate protein molecules based on their size and charge. For positively charged lysozyme molecules, the interaction between the protein and the negatively charged PIX network increases the encapsulation rate, yet the passive diffusion of negatively charged GFP leads to an overall encapsulation of up to 90% of the concentration in solution, so charge may affect kinetics more than total loading of the cargo. Furthermore, the uptake of molecules exhibited clear size-dependent behavior, which is readily rationalized from our model of PIX expansion behavior, making this material straightforward and intuitive to apply to new proteins of interest. The long-term storage and controlled release of the target molecules demonstrates that PIX are a suitable platform for potential applications encompassing macromolecular encapsulation and storage as well as controlled release. Due to the size-based mechanism of cargo entrapment by PIX, proteins of varying sizes and chemical compositions can be readily immobilized within a single platform. Thus, unlike methods such as co-crystallization, which can require extensive optimization of crystallization conditions for each target protein, PIX represent a dynamic scaffold that is agnostic to the nature of its cargo. With further investigations into alternate PIX compositions (different protein and/or polymer identities), PIX may achieve near-universal capabilities for macromolecular encapsulation. The versatility and tunability afforded by the modularity of PIX highlights their promise as a novel hybrid material with a wide range of potential uses: in addition to controlled cargo release (delivery), the uniform chemical environments of the framework pores may be suitable for long-term storage of macromolecules and/or enzymatic catalysis in confined spaces, and the PIX as a whole also exhibits chemo-mechanical deformations that implies their utility as actuators or artificial muscles.

4.5 Methods

4.5.1 GFP expression and purification

The gene for monomeric superfolder GFP⁴² was provided by Dr. Suckjoon Jun's group. The gene was incorporated into the plasmid vector pJexpress through restriction enzyme ligation. Restriction enzyme sites NdeI (5') and XhoI (3') were first added to the gene through PCR amplification. Then, the restriction enzymes NdeI and XhoI were used to digest the gene following the protocol of New England Biolabs (NEB). The resulting gene fragments were separated using a spin column with a 30 kDa cut-off. T4 ligase was used for the ligation of the GFP gene into the plasmid following the protocol of NEB. The final vector was transformed into XL1-Blue cells via heat-shock and subjected to sequencing, which confirmed successful insertion of the gene.

For GFP expression, isolation, and purification, we adapted protocols from previously published literature.⁴⁶ Protein plasmids isolated from XL-1 Blue cells were transformed into BL21 (DE3) *E. coli* cells and plated onto LB agar containing 100 µg/mL ampicillin. Colonies or freezer stocks of BL21 containing GFP-pJexpress vectors were used to inoculate starter cell cultures (200 mL LB medium, 100 µg/mL ampicillin). Cultures were incubated for 16 hours at 37 °C with shaking at 200 rpm prior to inoculating 1 L LB cultures (10 mL per flask) supplemented with 100 µg/mL ampicillin. Cells were grown to OD₆₀₀ = 0.6-0.8 at 37 °C and protein expression was then induced by addition of isopropyl β-D-1-thiogalactopyranoside (IPTG) to a final concentration of 1 mM. Cells were incubated at 37 °C for 4 h and yielded bright green solutions, confirming the expression of GFP. The cells were harvested by centrifugation (6,000×g, 10 min). Pellets were stored at -80 °C. Frozen cells were thawed and resuspended in a buffer solution containing 50 mM Tris (pH 8.0), 20 mM EDTA, and 50 mM NaCl. The cells were then lysed by sonication (in an

ice-bath) for 12 min total, with 30 s pulse on and 59 s off. Resulting cell debris was removed by centrifugation at 4 °C at 12,000×g for 20 min. Next, ammonium sulfate was directly added to the solution to purify the GFP by precipitation. At 40% saturated ammonium sulfate, the GFP remains soluble, and precipitated impurities were removed by centrifugation at 12,000×g. Upon reaching 65% ammonium sulfate, bright green precipitates formed and were separated by centrifugation at 12,000×g. The resulting pellet was then dissolved into a minimal volume of 50 mM Tris (pH 8.0), subjected to size exclusion chromatography (SEC) using Sephacryl-300 resin, and followed by anion exchange chromatography (Q column, Bio-Rad) to further purify the protein, collecting only peak fractions (as determined by UV-vis absorbance 488 nm) at the end of each purification step. The protein eluted from the Q column at approximately 110 mM NaCl in 50 mM Tris (pH 8.0). The purity of the final GFP solution was confirmed by SDS-PAGE.

4.5.2 Rhodamine labeling of streptavidin, catalase, and lysozyme

Streptavidin⁴⁴ (offered by the Borovik Lab), catalase (catalase from bovine liver, Sigma C40), and lysozyme (lysozyme from chicken egg white, Sigma L6876) were dissolved in 50 mM HEPES (pH 8.0) to a final protein concentration of 10 mg/mL. Separately, N-Hydroxysuccinimide (NHS)-rhodamine was dissolved in DMF to a concentration of 10 mg/mL. This NHS-rhodamine stock was added to the protein solution (1:999 v/v; 10 µg/mL NHS-rhodamine) and stirred at 4 °C overnight. Unreacted rhodamine in solution was removed by buffer exchange using a 10DG column (Bio-Rad). The final concentration of the protein was determined via Bradford assay.⁴⁷

4.5.3 Formation of polymer integrated crystals

Ferritin crystals were first crystallized in the presence of CaCl₂ (**Table 3.1**). After 2 days, the matured crystals were soaked in the monomer mixture solution (8.625% acrylate, 2.5% acrylamide, and 0.2% bis-acrylamide; w/v) for >48 hours. The crystals from one entire macrotray

were collected and transferred into an eppendorf tube. After settling to the bottom of the tube, the soaking solution supernatant was removed by pipetting. A solution of 1% APS/TEMED in 4 M NaCl was added to initiate the polymerization inside the crystal lattice to create PIX.

4.5.4 Protein encapsulation within PIX

Following polymer formation inside the lattice, the resulting PIX were washed with DI water twice to remove excess NaCl, then washed once with buffered solutions containing different concentrations of GFP (50 μ M, 100 μ M, 200 μ M or 400 μ M in different buffers (see **Figure 4.4**)) or other protein (100 μ M streptavidin, 100 μ M lysozyme, 100 μ M catalase in 10 mM MES (pH 6)) and allowed to soak in the same protein solution. After soaking for specific lengths of time (ranging from 10 min to 4 hours), the PIX were contracted with aqueous solutions of 5 M NaCl and 1 M CaCl₂, then washed with excess CaCl₂ solution to remove any remaining proteins free in solution or loosely absorbed to the surface of the PIX.

For the non-expanding control experiment, PIX were soaked in GFP solutions containing 1 M CaCl₂ to ensure that no expansion occurred.

4.5.5 Confocal microscopy imaging of protein-encapsulated PIX

GFP- (or rhodamine-labeled protein)-encapsulated PIX were transferred onto a glass slide. Imaging was performed with a 10 \times air objective installed on a spinning-disk confocal Axio Observer inverted microscope (Zeiss) equipped with a pair of Quantum 5125C cameras (Roper), using a filter to collect light at 500–550 nm (green channel for GFP) or 575–600 nm (red channel for rhodamine). Differential interference contrast (DIC) and fluorescence (488 nm excitation for green channel, 564 nm for red channel) images were captured with a 100-ms exposure. Images

were collected using Slidebook 6 (Intelligent Imaging Innovations) and analyzed with Fiji (<http://fiji.sc/Fiji>).

4.5.6 Protein release from PIX

After soaking PIX in a GFP solution for 30–60 min, a 5 M NaCl solution was added to induce contraction of the PIX, no calcium chloride was used in this step. The PIX were washed with excess NaCl solution to remove any free GFP. For release, the PIX were soaked in water, and aliquots containing PIX were taken at different time points, contracted with NaCl, and washed with 1 M CaCl₂ prior to confocal imaging. Excess DI water was added to the PIX aliquots, leading to complete dissolution within 4 hours prior to protein quantitation via UV-Vis and HPLC.

4.5.7 Quantification of total encapsulated GFP via UV-Vis absorbance

UV-Vis spectra were taken of PIX dissolved into DI water and the absorbance at 488 nm (corresponding to the GFP absorbance maximum) was used to calculate the concentration of GFP in solution, using an extinction coefficient of $\epsilon = 28,000 \text{ M}^{-1}\text{cm}^{-1}$.

4.5.8 Quantitation of protein concentrations in PIX via HPLC

After dissolving the PIX in water and sterile filtering through a 0.22 μm cutoff syringe filter, 40 μL aliquots of each sample were mixed with 5 μL ferritin, GFP, or both at known concentration(s), and water was added to reach a final volume of 50 μL . This creates an internal standard for the HPLC signal intensity. 20 μL of each PIX sample (with and without the extra protein) were injected for HPLC analysis. The workflow for the quantification and the calculation process of protein concentrations is depicted in **Figure 4.6**.

4.6 Acknowledgments

We thank the following colleagues for assistance: R. Alberstein for data processing; W.-J. Rappel for confocal microscopy; Borovik lab for providing streptavidin; Suckjoon Jun's group for the gene of monomeric superfolder GFP.

Chapter 4, in part, is currently being prepared for submission for publication: Zhang, L., Han, K., Na, Y., Tezcan, F. A. "Polymer integrated protein crystals as a general platform for controlled protein encapsulation and release". The dissertation author was the primary investigator and author of this manuscript.

4.7 References

1. Chen, Y. C.; Smith, T.; Hicks, R. H.; Doekhie, A.; Koumanov, F.; Wells, S. A.; Edler, K. J.; van den Elsen, J.; Holman, G. D.; Marchbank, K. J.; Sartbaeva, A., Thermal stability, storage and release of proteins with tailored fit in silica. *Scientific Reports* **2017**, *7*, 8.
2. Abe, S.; Ijiri, H.; Negishi, H.; Yamanaka, H.; Sasaki, K.; Hirata, K.; Mori, H.; Ueno, T., Design of enzyme-encapsulated protein containers by in vivo crystal engineering. *Advanced Materials* **2015**, *27* (48), 7951-7956.
3. Margolin, A. L.; Navia, M. A., Protein crystals as novel catalytic materials. *Angewandte Chemie-International Edition* **2001**, *40* (12), 2204-2222.
4. Shieh, F. K.; Wang, S. C.; Yen, C. I.; Wu, C. C.; Dutta, S.; Chou, L. Y.; Morabito, J. V.; Hu, P.; Hsu, M. H.; Wu, K. C. W.; Tsung, C. K., Imparting functionality to biocatalysts via embedding enzymes into nanoporous materials by a de novo approach: Size-selective sheltering of catalase in metal-organic framework microcrystals. *Journal of the American Chemical Society* **2015**, *137* (13), 4276-4279.
5. Dutta, S., Exoskeleton for biofunctionality protection of enzymes and proteins for intracellular delivery. *ADVANCED Nanobiomed research* **2020**, 2000010.
6. Majewski, M. B.; Howarth, A. J.; Li, P.; Wasielewski, M. R.; Hupp, J. T.; Farha, O. K., Enzyme encapsulation in metal-organic frameworks for applications in catalysis. *Crystengcomm* **2017**, *19* (29), 4082-4091.

7. Basu, S. K.; Govardhan, C. P.; Jung, C. W.; Margolin, A. L., Protein crystals for the delivery of biopharmaceuticals. *Expert Opinion on Biological Therapy* **2004**, 4 (3), 301-317.
8. Slowing, II; Trewyn, B. G.; Lin, V. S. Y., Mesoporous silica nanoparticles for intracellular delivery of membrane-impermeable proteins. *Journal of the American Chemical Society* **2007**, 129 (28), 8845-8849.
9. Caruso, F.; Trau, D.; Mohwald, H.; Renneberg, R., Enzyme encapsulation in layer-by-layer engineered polymer multilayer capsules. *Langmuir* **2000**, 16 (4), 1485-1488.
10. Roy, J. J.; Abraham, T. E.; Abhijith, K. S.; Kumar, P. V. S.; Thakur, M. S., Biosensor for the determination of phenols based on cross-linked enzyme crystals (clec) of laccase. *Biosensors & Bioelectronics* **2005**, 21 (1), 206-211.
11. Laothanachareon, T.; Champreda, V.; Sritongkham, P.; Somasundrum, M.; Surareungchai, W., Cross-linked enzyme crystals of organophosphate hydrolase for electrochemical detection of organophosphorus compounds. *World Journal of Microbiology & Biotechnology* **2008**, 24 (12), 3049-3055.
12. Chen, Y., Jiménez-Ángeles, F., Qiao, B., Krzyaniak, M.D., Sha, F., Kato, S., Gong, X., Buru, C.T., Chen, Z., Zhang, X. and Gianneschi, N.C., Insights into the Enhanced catalytic activity of cytochrome c when encapsulated in a metal-organic framework. *Journal of the American Chemical Society*, **2020** 142(43), pp.18576-18582..
13. Ayala, M.; Horjales, E.; Pickard, M. A.; Vazquez-Duhalt, R., Cross-linked crystals of chloroperoxidase. *Biochemical and Biophysical Research Communications* **2002**, 295 (4), 828-831.
14. Schmid, A.; Dordick, J. S.; Hauer, B.; Kiener, A.; Wubbolts, M.; Witholt, B., Industrial biocatalysis today and tomorrow. *Nature* **2001**, 409 (6817), 258-268.
15. Li, M., Qiao, S., Zheng, Y., Andaloussi, Y.H., Li, X., Zhang, Z., Li, A., Cheng, P., Ma, S. and Chen, Y., Fabricating covalent organic framework capsules with commodious microenvironment for enzymes. *Journal of the American Chemical Society*, **2020** 142(14), pp.6675-6681.
16. Fernandez-Lafuente, R., Stabilization of multimeric enzymes: Strategies to prevent subunit dissociation. *Enzyme and Microbial Technology* **2009**, 45 (6-7), 405-418.
17. Hanefeld, U.; Gardossi, L.; Magner, E., Understanding enzyme immobilisation. *Chemical Society Reviews* **2009**, 38 (2), 453-468.

18. Heater, B.; Yang, Z. F.; Lee, M.; Chan, M. K., In vivo enzyme entrapment in a protein crystal. *Journal of the American Chemical Society* **2020**, *142* (22), 9879-9883.
19. Panganiban, B.; Qiao, B. F.; Jiang, T.; DelRe, C.; Obadia, M. M.; Nguyen, T. D.; Smith, A. A. A.; Hall, A.; Sit, I.; Crosby, M. G.; Dennis, P. B.; Drockenmuller, E.; de la Cruz, M. O.; Xu, T., Random heteropolymers preserve protein function in foreign environments. *Science* **2018**, *359* (6381), 1239-1243.
20. Sheldon, R. A., Enzyme immobilization: The quest for optimum performance. *Advanced Synthesis & Catalysis* **2007**, *349* (8-9), 1289-1307.
21. Hashimoto, T.; Ye, Y. X.; Matsuno, A.; Ohnishi, Y.; Kitamura, A.; Kinjo, M.; Abe, S.; Ueno, T.; Yao, M.; Ogawa, T.; Matsui, T.; Tanaka, Y., Encapsulation of biomacromolecules by soaking and co-crystallization into porous protein crystals of hemocyanin. *Biochemical and Biophysical Research Communications* **2019**, *509* (2), 577-584.
22. Wei, T. H.; Wu, S. H.; Huang, Y. D.; Lo, W. S.; Williams, B. P.; Chen, S. Y.; Yang, H. C.; Hsu, Y. S.; Lin, Z. Y.; Chen, X. H.; Kuo, P. E.; Chou, L. Y.; Tsung, C. K.; Shieh, F. K., Rapid mechanochemical encapsulation of biocatalysts into robust metal-organic frameworks. *Nature Communications* **2019**, *10*, 8.
23. Mehta, J.; Bhardwaj, N.; Bhardwaj, S. K.; Kim, K. H.; Deep, A., Recent advances in enzyme immobilization techniques: Metal-organic frameworks as novel substrates. *Coordination Chemistry Reviews* **2016**, *322*, 30-40.
24. Volodkin, D. V.; Larionova, N. I.; Sukhorukov, G. B., Protein encapsulation via porous caco3 microparticles templating. *Biomacromolecules* **2004**, *5* (5), 1962-1972.
25. Hudson, S.; Cooney, J.; Magner, E., Proteins in mesoporous silicates. *Angewandte Chemie-International Edition* **2008**, *47* (45), 8582-8594.
26. Wang, H. R.; Han, L.; Zheng, D.; Yang, M. F.; Andaloussi, Y. H.; Cheng, P.; Zhang, Z. J.; Ma, S. Q.; Zaworotko, M. J.; Feng, Y. F.; Chen, Y., Protein-structure-directed metal-organic zeolite-like networks as biomacromolecule carriers. *Angewandte Chemie-International Edition* **2020**, *59* (15), 6263-6267.
27. Liang, K.; Ricco, R.; Doherty, C. M.; Styles, M. J.; Bell, S.; Kirby, N.; Mudie, S.; Haylock, D.; Hill, A. J.; Doonan, C. J.; Falcaro, P., Biomimetic mineralization of metal-organic frameworks as protective coatings for biomacromolecules. *Nature Communications* **2015**, *6*(1), 1-8.

28. Li, M. M.; Qiao, S.; Zheng, Y. L.; Andaloussi, Y. H.; Li, X.; Zhang, Z. J.; Li, A.; Cheng, P.; Ma, S. Q.; Chen, Y., Fabricating covalent organic framework capsules with commodious microenvironment for enzymes. *Journal of the American Chemical Society* **2020**, *142* (14), 6675-6681.
29. Huo, J.; Aguilera-Sigalat, J.; El-Hankari, S.; Bradshaw, D., Magnetic mof microreactors for recyclable size-selective biocatalysis. *Chemical Science* **2015**, *6* (3), 1938-1943.
30. Huang, S. M.; Kou, X. X.; Shen, J.; Chen, G. S.; Ouyang, G. F., "Armor-plating" enzymes with metal-organic frameworks (mofs). *Angewandte Chemie-International Edition* **2020**, *59* (23), 8786-8798.
31. Shen, S. H.; Wu, Y. S.; Liu, Y. C.; Wu, D. C., High drug-loading nanomedicines: Progress, current status, and prospects. *International Journal of Nanomedicine* **2017**, *12*, 4085-4109.
32. Sheldon, R. A.; van Pelt, S., Enzyme immobilisation in biocatalysis: Why, what and how. *Chemical Society Reviews* **2013**, *42* (15), 6223-6235.
33. Shieh, F.-K.; Wang, S.-C.; Yen, C.-I.; Wu, C.-C.; Dutta, S.; Chou, L.-Y.; Morabito, J. V.; Hu, P.; Hsu, M.-H.; Wu, K. C. W.; Tsung, C.-K., Imparting functionality to biocatalysts via embedding enzymes into nanoporous materials by a de novo approach: Size-selective sheltering of catalase in metal-organic framework microcrystals. *Journal of the American Chemical Society* **2015**, *137* (13), 4276-4279.
34. Ye, C.; Chi, H., A review of recent progress in drug and protein encapsulation: Approaches, applications and challenges. *Materials Science & Engineering C-Materials for Biological Applications* **2018**, *83*, 233-246.
35. Renggli, K.; Baumann, P.; Langowska, K.; Onaca, O.; Bruns, N.; Meier, W., Selective and responsive nanoreactors. *Advanced Functional Materials* **2011**, *21* (7), 1241-1259.
36. Qiao, L.; Liu, Y.; Hudson, S. P.; Yang, P. Y.; Magner, E.; Liu, B. H., A nanoporous reactor for efficient proteolysis. *Chemistry-a European Journal* **2008**, *14* (1), 151-157.
37. Lin, J. L.; Wang, Z. K.; Xu, Z. Y.; Wei, L.; Zhang, Y. C.; Wang, H.; Zhang, D. W.; Zhou, W.; Zhang, Y. B.; Liu, Y.; Li, Z. T., Water-soluble flexible organic frameworks that include and deliver proteins. *Journal of the American Chemical Society* **2020**, *142* (7), 3577-3582.

38. Ma, Y.; Zhao, Y.; Bejjanki, N. K.; Tang, X.; Jiang, W.; Dou, J.; Khan, M. I.; Wang, Q.; Xia, J.; Liu, H.; You, Y.-Z.; Zhang, G.; Wang, Y.; Wang, J., Nanoclustered cascaded enzymes for targeted tumor starvation and deoxygenation-activated chemotherapy without systemic toxicity. *Acs Nano* **2019**, *13* (8), 8890-8902.
39. Han, Y. J.; Stucky, G. D.; Butler, A., Mesoporous silicate sequestration and release of proteins. *Journal of the American Chemical Society* **1999**, *121* (42), 9897-9898.
40. Zhang, L.; Bailey, J. B.; Subramanian, R. H.; Tezcan, F. A., Hyperexpandable, self-healing macromolecular crystals with integrated polymer networks. *Nature* **2018**, *557* (7703), 86-91.
41. Han, K., Bailey, J. B., Zhang, L., & Tezcan, F. A, Anisotropic dynamics and mechanics of macromolecular crystals containing lattice-patterned polymer networks. *Journal of the American Chemical Society* **2020**, *142* (45), 19402-19410.
42. Ke, N.; Landgraf, D.; Paulsson, J.; Berkmen, M., Visualization of periplasmic and cytoplasmic proteins with a self-labeling protein tag. *Journal of Bacteriology* **2016**, *198* (7), 1035-1043.
43. Su, C. K.; Chiang, B. H., Partitioning and purification of lysozyme from chicken egg white using aqueous two-phase system. *Process Biochemistry* **2006**, *41* (2), 257-263.
44. Olshansky, L.; Huerta-Lavorie, R.; Nguyen, A. I.; Vallapurackal, J.; Furst, A.; Tilley, T. D.; Borovik, A. S., Artificial metalloproteins containing co4o4 cubane active sites. *Journal of the American Chemical Society* **2018**, *140* (8), 2739-2742.
45. Kirkman, H. N.; Gaetani, G. F., Catalase - a tetrameric enzyme with 4 tightly bound molecules of nadph. *Proceedings of the National Academy of Sciences of the United States of America-Biological Sciences* **1984**, *81* (14), 4343-4347.
46. Zhou, X. P.; Shi, Q. H.; Xing, X. H.; Sun, Y., Rapid purification of enhanced green fluorescent protein from escherichia coli. *Chinese Journal of Chemical Engineering* **2006**, *14* (2), 229-234.
47. Bradford, M. M., Rapid and sensitive method for quantitation of microgram quantities of protein utilizing principle of protein-dye binding. *Analytical Biochemistry* **1976**, *72* (1-2), 248-254.

46. Zhou, X. P.; Shi, Q. H.; Xing, X. H.; Sun, Y., Rapid purification of enhanced green fluorescent protein from Escherichia coli. *Chinese Journal of Chemical Engineering*. **2006**, *14* (2), 229-234.
47. Bradford, M. M., Rapid and sensitive method for quantitation of microgram quantities of protein utilizing principle of protein-dye binding. *Analytical biochemistry*. **1976**, *72* (1-2), 248-254.